

**JAERI - M**  
**91-138**

REACTOR ENGINEERING DEPARTMENT ANNUAL REPORT

(APRIL 1, 1990-MARCH 31, 1991)

September 1991

Department of Reactor Engineering

日 本 原 子 力 研 究 所  
Japan Atomic Energy Research Institute

JAERI-Mレポートは、日本原子力研究所が不定期に公刊している研究報告書です。  
入手の問合わせは、日本原子力研究所技術情報部情報資料課（〒319-11茨城県那珂郡東海村）あて、お申しこしください。なお、このほかに財団法人原子力弘済会資料センター（〒319-11 茨城県那珂郡東海村日本原子力研究所内）で複写による実費頒布をおこなっております。

JAERI-M reports are issued irregularly.

Inquiries about availability of the reports should be addressed to Information Division  
Department of Technical Information, Japan Atomic Energy Research Institute, Tokai-mura, Naka-gun, Ibaraki-ken 319-11, Japan.

©Japan Atomic Energy Research Institute, 1991

編集兼発行 日本原子力研究所  
印刷 いばらき印刷(株)

Reactor Engineering Department Annual Report  
(April 1, 1990 - March 31, 1991)

Department of Reactor Engineering  
Tokai Research Establishment  
Japan Atomic Energy Research Institute  
Tokai-mura, Naka-gun, Ibaraki-ken

(Received July 31, 1991)

This report summarizes the research and development activities in the Department of Reactor Engineering during the fiscal year of 1990 (April 1, 1990 - March 31, 1991).

The major Department's programs promoted in the year are the assessment of the high conversion light water reactor, the design activities of advanced reactor system and development of a high energy proton linear accelerator for the engineering applications including TRU incineration.

Other major tasks of the Department are various basic researches on the nuclear data and group constants, the developments of theoretical methods and codes, the reactor physics experiments and their analyses, fusion neutronics, radiation shielding, reactor instrumentation, reactor control/diagnosis, thermohydraulics, technology assessment of nuclear energy and technology developments related to the reactor physics facilities.

The cooperative works to JAERI's major projects such as the high temperature gas cooled reactor or the fusion reactor and to PNC's fast reactor project also progressed.

The activities of the Research Committee on Reactor Physics are also summarized.

---

Board of Editors for Annual Report:

T. Hiraoka (Chief Editor), M. Nakagawa (Associated Chief Editor), F. Akino, S. Fujisaki, H. Gotoh, K. Hasegawa, Y. Ikeda, H. Nakashima, M. Okazaki, T. Osugi, S. Sasaki, O. Sato, N. Suzuki (Editorial Assistant)

Keywords: Reactor Engineering Department Annual Report, Advanced Reactor System, Nuclear Data, Group Constants, Reactor Physics, Thermohydraulics, Fusion Neutronics, Radiation Shielding, Reactor Instrumentation, Reactor Control/Diagnosis

平成2年度原子炉工学部年報

日本原子力研究所東海研究所原子炉工学部

(1991年7月31日受理)

平成2年度における原子炉工学部の研究活動状況を取りまとめた。原子炉工学部において、まとまった規模で行われた活動は、高転換軽水炉の検討評価、新型炉概念設計研究及び TRU消滅処理のための大強度陽子線形加速器の計画である。基礎基盤研究としては、核データと群定数、炉理論とコード開発、炉物理の実験と解析、核融合ニュートロニクス、放射線遮蔽、原子炉計測・計装、原子炉制御・診断、伝熱流動、核エネルギー技術評価及び炉物理施設技術開発等がある。また、高温ガス炉及び核融合等原研のプロジェクトへ協力する研究も含まれている。さらに、動燃事業団との高速炉の共同研究も進められた。炉物理に関する研究委員会活動もまとめられている。

---

東海研究所：〒319-11 茨城県那珂郡東海村白方白根2-4

原子炉工学部年報編集委員会：

平岡 徹（委員長）、中川 正幸（副委員長）、秋濃 藤義、藤崎 伸吾、五藤 博、長谷川 和男、池田裕二郎、中島 宏、岡崎 元昭、大杉 俊隆、佐々木 忍、佐藤 治、鈴木 昇（事務局）

## Contents

Foreword .....	00
1. Nuclear Data and Group Constants .....	1
1.1 Activation Cross Section Measurements at Neutron Energy from 13.3 MeV to 15.0 MeV for Ru, Pd, Cd, Tb and Re .....	2
1.2 Measurements of Long-Lived Activation Cross Sections at 14 MeV Energy Region .....	5
1.3 Thermal Reactor Benchmark Calculation for JENDL-3 .....	8
1.4 JENDL-3 Based Data Library for the Continuous Energy Monte Carlo Code VIM .....	11
2. Theoretical Method and Code Development .....	13
2.1 Applicability of Avery's Coupled Reactor Theory to Estimate of Subcriticality of TCA Test Region .....	14
2.2 Hexagonal Lattice Geometry for Monte Carlo Calculations ....	17
2.3 A Three-Dimensional Plotting Code for Monte Carlo Geometry .	20
2.4 Development of Burnup Calculation Code for Boiling Water Reactor Core .....	23
2.5 Development of Intellectual Reactor Design System IRDS .....	26
2.6 Interactive Interface on a Workstation for Reactor Design Codes .....	29
2.7 THYDE-W: Reactor Coolant System Analysis Code .....	32
3. Reactor Physics Experiment and Analysis .....	35
3.1 Benchmark Experiments for Metallic-Fueled LMFBR at FCA .....	36
3.2 Reactivity Worth Measurements in Metallic-Fueled Core FCA XVI-1 .....	38
3.3 Reaction Rate Measurements in Metallic-Fueled Core FCA XVI-1 .....	40
3.4 Doppler Worth Measurement in Metallic-Fueled Core FCA XVI-1 .....	43
3.5 Control Rod Reactivity Worth Measurement in Metallic-Fueled Core FCA XVI-1 .....	46
3.6 Fuel Expansion and Displacement Worth Measurement in Metallic-Fueled Core FCA XVI-1 .....	49
3.7 Analysis on FCA-HCLWR Core Using JENDL-3 .....	52
3.8 Measurement of the Void Reactivity Worth of HTTR Mockup Control Rod Holes in the VHTRC-1 Core .....	55

4. Advanced Reactor System Design Studies .....	58
4.1 A Concept of Advanced Fast Breeder Reactor with Instantaneous Negative Temperature Coefficient .....	59
4.2 Th/U-233 Fueled Boiling Water Breeder Reactor .....	62
4.3 Performance of Double Flat Core HCLWR with TRU Mixed Fuel ..	64
4.4 An Analysis of Heterogeneity in the Fuel Assembly of Tight Pitch Lattice .....	67
4.5 Design Study of the SPWR (System-integrated PWR) .....	70
4.6 Daily Load Following Analysis of SPWR .....	73
5. Fusion Neutronics .....	75
5.1 Measurement and Analysis of Low Energy Neutron Spectrum in a Large Cylindrical Iron Assembly Bombarded by D-T Neutrons ..	76
5.2 Neutronics Experiment and Analysis on a Tungsten Slab Assembly Bombarded with D-T Neutrons .....	79
5.3 Self-Shielding Effect in Analysis of TOF Experiment on Iron Slab .....	82
5.4 Post-Analysis of Phase-IIIA Experiment of JAERI/USDOE Collaborative Program on Fusion Neutronics .....	85
5.5 Phase-IIIB Experimental Results of JAERI/USDOE Collaborative Program .....	88
5.6 Experimental Verification of the Current Data and Methods for Induced Radioactivity and Decay Heat Calculation in D-T Fusion Reactors .....	91
5.7 International Comparison on Measuring Techniques of Tritium Production Rate for Fusion Neutronics Experiments ---Summary of Additional Questionnaire and Result for ANL Samples--- .....	94
5.8 Characteristics of a 40 mm Diameter NE213 Scintillation Counter for In-System Gamma-ray Spectrum Measurement .....	97
5.9 14 MeV Neutron Generation Characteristics of FNS Rotating Target .....	100
5.10 Calculational Benchmark for Deep Penetration of 14 MeV Neutrons in Iron .....	103
6. Radiation Shielding .....	106
6.1 Development of a Microcalorimeter for Measuring Absolute Intensity of Synchrotron Radiations (II) .....	107
6.2 Bulk Shielding Calculation of High Energy Electron Accelerators with Line Source Assumptions .....	110

6.3	Attenuation Factors of Neutron and Secondary Gamma-ray Dose Equivalents for Typical Neutron Sources in Shielding Materials .....	112
7.	Reactor and Nuclear Instrumentation .....	115
7.1	Development of a High-Sensitive Ionization Chamber for High Temperature Gas Cooled Reactors .....	116
7.2	High-Temperature Out-Pile Tests of N-type Thermocouples ....	119
7.3	Development of Fuel Failure Detection System for High Temperature Gas Cooled Reactor .....	122
7.4	The Ultraviolet Irradiation Effects of Pure Silica Core Optical Fiber .....	125
7.5	New Candidate for the Residual Defect in a Silicon Surface Barrier Detector .....	127
7.6	An Analytical Expression for the Distribution of Time Intervals Between Successive Detection Pulses of Neutrons from Spontaneous Fissions .....	130
7.7	Detection Efficiency for Neutrons from Spontaneous Fissions and ( $\alpha$ , n) Reactions .....	133
7.8	A New Method for Measurement of Magnetic Field by Utilizing Diamagnetic Materials .....	136
8.	Reactor Control, Diagnosis and Robotics .....	139
8.1	Dynamic Identification Experiment of "Mutsu" Reactor by Using Pseudo Random Binary Signal .....	140
8.2	Application of Layered Neural Networks to Anomaly Diagnosis .....	142
8.3	Study of a Modeling Method for Nonlinear Reactor Noise .....	144
8.4	Search for Chaotic Character of Reactor Noise Signals .....	147
8.5	Detection of Sodium Boiling by Means of Acoustic Noise Analysis .....	150
8.6	On a Study of Robust Control Based on $H^\infty$ Control Theory ....	151
8.7	Development of Telerobotic Systems for Reactor Dismantlement .....	153
8.8	Kinematic Analysis of Robot Manipulator Using Optimization Technique .....	154
9.	Heat Transfer and Fluid Dynamics .....	155
9.1	Investigation on Long-Term Core Cooling Behaviors after Reflood Phase of PWR LBLOCA .....	156
9.2	Investigation on Flow Pattern in Cold Leg during PWR	



Reflow Phase by Using CCTF Data .....	159
9.3 Refill Behavior in the Simulated PWR under Combined ECC Injection Mode .....	162
9.4 Investigation of Water Break-through and Core Cooling Behaviors under Intermittent ECC Water Delivery to Upper Plenum during Reflood Phase in PWRs with Combined-Injection Type ECCS .....	165
9.5 Analysis of SCTF/CCTF Counterpart Test Results .....	168
9.6 Development of a Driver Program for Assessment of Constitutive Equations for Two Fluid Model Code: MINI-TRAC .....	171
9.7 A Study of Interfacial Friction Model for Upward Flow in Vertical Pipe at Low Mass Velocity .....	174
9.8 Assessment of Model in Two-Fluid Model Code for Slug Flow and Annular Flow in Horizontal Tube with MINI-TRAC Code ...	177
9.9 Improvement of Numerical Treatment of Convection Term in TRAC-PF1 Code at Transition from Single Phase Flow to Two Phase Flow .....	180
9.10 Effect of Rod Pitch on Critical Heat Flux .....	183
9.11 Effect of Axial Power Distribution on Critical Heat Flux of HCPWR .....	186
9.12 Safety Evaluation of Reactivity Initiated Accidents for Double-Flat-Core Type HCLWR .....	189
9.13 Discussion on Differences between Calculated Results with 1-D and 3-D Models on 0.5% Small Break LOCA at Vessel Bottom of Double-Flat-Core Type HCLWR .....	192
10. Nuclear Energy Systems Analysis and Assessment .....	195
10.1 Development of Integrated Energy-Economy-Environment Model System .....	196
10.2 Preliminary Analysis on CO <sub>2</sub> Emission Reduction in Japanese Energy System by MARKAL Model .....	198
10.3 An Analysis on the Role of HCLWR from the Viewpoint of Long-Term Fuel Cycle .....	201
10.4 A Study on Broad Economic Impact of Nuclear Power .....	204
10.5 CO <sub>2</sub> Emission Coefficient of Nuclear Power and Process Heat Utilization .....	206
10.6 Study on Cycle Simulation of the UT-3 Thermochemical Hydrogen Production Process .....	208

11. Development of Proton Linear Accelerator and Transmutation	
Target System .....	210
11.1 A Progress in the High Intensity Proton Linear Accelerator Development .....	211
11.2 Study on a High Brightness Ion Source for the Basic Technology Accelerator .....	214
11.3 Design Study on a Radio Frequency Quadrupole for the Basic Technology Accelerator .....	217
11.4 Study on a Drift Tube Linac of the Basic Technology Accelerator .....	220
11.5 Analysis of Time Evolution Process of Spallation Products .	223
11.6 Conceptual Design Study on the TRU Incineration System Driven by a Proton Accelerator ---The Metal Fuelled Core--- .....	226
11.7 Conceptual Design Study on the TRU Incineration System Driven by a Proton Accelerator ---The Molten Salt Core--- .	229
11.8 Integral Experiment on a Lead Bulk System Bombarded with High Energy Protons .....	232
12. Facility Operation and Technique Development .....	235
12.1 Operation Report of FCA .....	236
12.2 Operation Report of VHTRC .....	237
12.3 Operation Report of FNS .....	238
13. Activities of the Research Committee on Reactor Physics .....	240
Publication List .....	244
Author Index .....	252
Appendix I Department of Reactor Engineering Organization Chart ..	257
Appendix II Abbreviations .....	259

## Foreword

The annual research activities of the Department of Reactor Engineering, Japan Atomic Energy Research Institute, during the period of April 1990 - March 1991, i.e. fiscal year 1990 in Japan are presented in this report. The research activities of the Department had covered the broad area including fission reactor physics, fusion reactor physics, shielding, reactor instrumentation and control, thermohydraulics, nuclear energy systems analysis and intense accelerator technology.

The total number of people working in the department was 121. JAERI funded expenditures during the period amounted to about 1182 million yen, excluding nuclear fuel costs and personnel expenses. A considerable amount of funding was also provided by research contrasts with external organizations; Science and Technology Agency (STA) for non-destructive measurement technology of transuranic elements (TRU) and for large scale reflood test program and thermal hydraulic demonstration test in HCLWR and Power Reactor and Nuclear Fuel Development Corporation (PNC) for fast reactor physics.

The research activities were conducted in the following 9 laboratories:

- Reactor System Laboratory,
- Fast Reactor Physics Laboratory,
- Thermal Reactor Physics Laboratory,
- Reactor Instrumentation Laboratory,
- Reactor Control Laboratory,
- Heat Transfer and Fluid Flow Laboratory,
- Fusion Reactor Physics Laboratory,
- Nuclear Energy Technology Assessment Laboratory and
- Shielding Laboratory

with the support of Reactor Physics Facility Operation Division, the Research Committee on Reactor Physics and the Research Committee on Advanced Reactor.

The major research and development projects to which the research programs in the department are closely related are;

- (1) Development of technology for partitioning and transmutation of nuclear wastes (OMEGA Program),
- (2) Development of high conversion light water reactors,
- (3) Development of very high temperature gas-cooled reactors

(VHTR),

- (4) Design study of advanced reactors, and
- (5) Engineering research for fusion reactors.

Use of intense proton linear accelerators for the incineration of transuranium elements TRU such as Np, Am and Cm contained in spent fuels is studied. Design study of a TRU fueled subcritical reactor driven by the accelerator has been in progress. Development of intense proton linear accelerator was initiated. The incineration of TRU by reactors has also been investigated.

The research activity on a high conversion light water reactor (HCLWR), has been extended with purpose to investigate a possibility and to establish the reactor concept as an advanced light water reactor for the next generation. Investigations of a basic idea for the high conversion boiling water reactor have been initiated, in which the higher values are anticipated for both the conversion ratio and fuel burn-up under the condition of the negative coolant void coefficient. Thermo-hydraulic performances of the tight lattices were fully investigated under pressurized water reactor conditions. The role of HCLWR in fuel cycle was analysed from view point of uranium resource saving.

Efforts for VHTR development have continued in the field of reactor physics, reactor instrumentation and reactor control. Critical experiment was successfully proceeded on the Very High Temperature Reactor Critical Assembly (VHTRC) with 2-6% enriched uranium fuel elements. Performance tests of coated particle fuel failure detection system have been successfully developed.

In the design studies of the advanced reactor system, some basic ideas have been conceived. A conceptual design of the System Integrated Pressurized Water Reactor (SPWR) is continued as a medium size power reactor with highly passive safety features. A very small reactor using coated particle fuels has also been studied for use in space.

Concerning the fusion reactor physics the third stage FNS experiments on the lithium oxide system of annular geometry was performed under a collaborative research program between US-DOE and JAERI. The program will provide important experimental data for validation calculation methods of fusion blanket design. Activation cross section measurements for the structural materials of the fusion reactors have been conducted. Benchmark test of the JENDL-3 nuclear data library has also been extensively done.

Addressing R&D of LMFBR, the measurements of the Doppler effect in the high temperature range using the core oscillation started at FCA.

In the area of instrumentation and control technology, the research interest has moved to establish an intelligent robotics technology with emphasis on recognition of objects in extreme environment using the sensor devices withstanding the high radiation level. Self-tuning fuzzy control of a mobile robot is also studied.

Several other significant achievements have been made. These include nondestructive measuring technique of TRU in waste drums, Intellectual Reactor Design System (IRDS) and the standardized intelligent shielding analysis code package.

Yoshihiko Kaneko, Director  
Department of Reactor Engineering

## 1. Nuclear Data and Group Constants

Main activities on nuclear data are related to activation cross section measurements for fusion reactor materials and benchmark calculations for the third version of Japanese Evaluated Nuclear Data Library (JENDL-3).

Continuous efforts have been devoted to the systematic measurements of neutron activation cross sections around 14 MeV by using FNS facility in the framework of the JAERI/USDOE collaboration program. The measurements are performed for short-lived isotopes of Ru, Pd, Cd, Tb and Re for which are considered as fusion reactor structure materials. The present cross sections measured at eight energy points between 13 and 15 MeV are valuable, because of few other experimental data in this energy region. Furthermore, the production cross sections at 14.8 MeV by D-T neutron source are measured for long-lived isotopes of Al,  $^{81}\text{Ni}$ , Cu, Nb, Mo, Ag,  $^{151}\text{Eu}$ ,  $^{153}\text{Eu}$ , Tb, Dy, Hf, W, Re and Bi. These measured data are compared with the other experimental data and the evaluated data such as JENDL-3 and REAC-ECN3.

Benchmark calculations for TRX-1 thermal reactor core are conducted to investigate prediction accuracy of the JENDL-3 nuclear data and neutron codes for effective multiplication factor and reaction rates. Eight codes from six organizations participate under the thermal reactor integral test working group in Japanese Nuclear Data Committee. The group cross section library for each code is produced on the basis of the nuclear data file JENDL-3. The continuous energy Monte Carlo code VIM and the library have been improved so as to treat the tabulated fission spectrum based on Madland-Nix formula. The  $k_{\text{eff}}$  obtained with the four deterministic codes CASMO, SRAC, TGBLA and WIMS-E are well agreed with the experiment, and on the other hand, the VIM solving accurately three dimensional configuration underestimates it. This is mainly caused by the difference of leakage rate between the deterministic and Monte Carlo codes.

In addition to the present results, the general applicability of JENDL-3 to fission, fusion and shielding calculations have been investigated in detail and the results have been presented at International Conference on Nuclear Data for Science and Technology, 13 - 17 May, 1991, Juelich, F.R. Germany.

(Hideki Takano)

# 1.1 Activation Cross Section Measurements at Neutron Energy from 13.3 MeV to 15.0 MeV for Ru, Pd, Cd, Tb and Re

C. Konno and Y. Ikeda

A program on systematic measurements of neutron activation cross sections around 14 MeV has been underway at FNS since 1985<sup>1)</sup>. More than two hundreds reactions have been subjected so far. The reaction cross sections measured in 1990 for the elements of Ru, Pd, Cd, Tb and Re are shown in Table 1.1.1. The experimental procedure and data processing method were the same as that adopted in the previous study<sup>1)</sup>. Since samples of natural abundance were used, some of products of (n,p) reactions were contaminated by the contributions via (n,np) reactions in the adjacent nuclide.

Figures 1.1.1 to 1.1.6 show measured activation cross sections for  $^{96}\text{Ru}(n,2n)^{95}\text{Ru}$ ,  $^{96}\text{Ru}(n,p)^{96\text{m}+g}\text{Tc}$ ,  $^{102}\text{Pd}(n,2n)^{101}\text{Pd}$ ,  $^{112}\text{Cd}(n,p)^{112}\text{Ag}$ ,  $^{159}\text{Tb}(n,p)^{159}\text{Gd}$  and  $^{187}\text{Re}(n,p)^{187}\text{W}$ , respectively, along with data in the literature. Data of this work covered rather a wide energy range showing trends of reaction excitation functions. The data were in reasonable agreement within experimental errors with data reported recently.

## Reference

- 1) Ikeda Y., et al.: "Activation Cross Section Measurements for Fusion Reactor Structural Materials at Neutron Energy from 13.3 to 15.0 MeV Using FNS Facility", JAERI 1312 (1988).

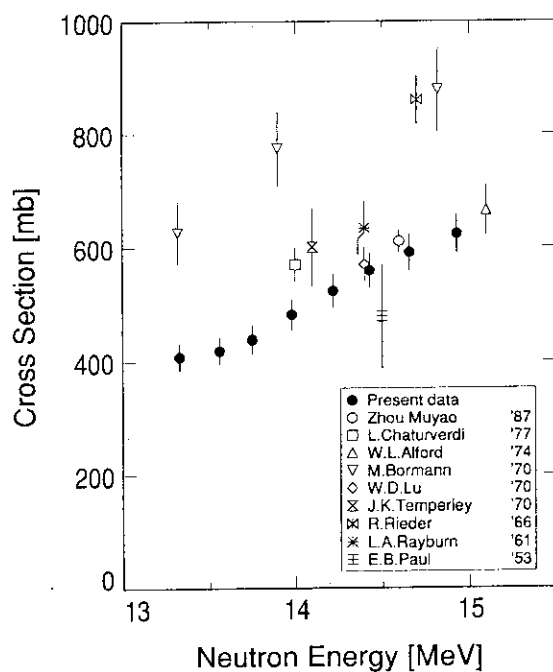
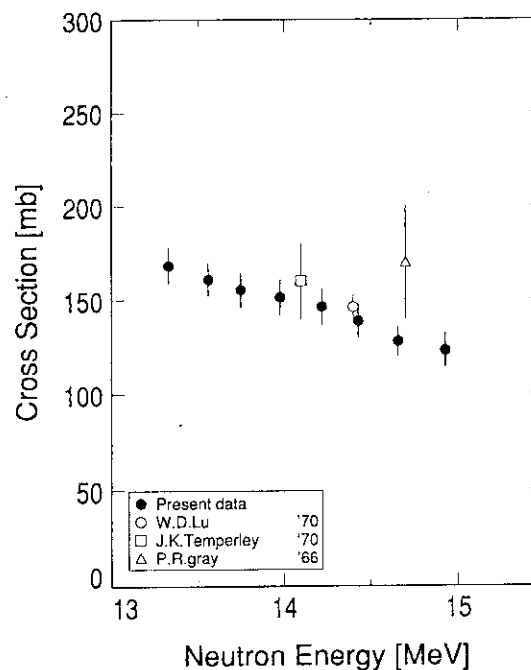
Table 1.1.1 Measured reactions

Target Nucleus	Natural Abundance[%]	Reaction	Product	Half-life	Gamma-ray Energy[keV]	Branching Ratio[%]	Q-value [MeV]
$^{96}\text{Ru}$	5.50	(n,2n)	$^{95}\text{Ru}$	$1.65 \pm 0.02$ h	336.40	$71 \pm 1$	-10.694
$^{96}\text{Ru}$	5.50	(n,np)	$^{95\text{m}}\text{Tc}$	$20.0 \pm 0.1$ h	765.76	$93 \pm 1$	-7.390
$^{96}\text{Ru}$	5.50	(n,np)	$^{95\text{g}}\text{Tc}$	$61 \pm 2$ d	204.12	$66.2 \pm 2.5$	-7.351
$^{96}\text{Ru}$	5.50	(n,p)	$^{96\text{m}+g}\text{Tc}$	$4.35 \pm 0.4$ d	778.22	$99.1 \pm 0.1$	0.528
$^{99}\text{Ru}$	12.70	(n,p)	$^{99\text{m}}\text{Tc}$	$6.007 \pm 0.002$ h	140.51	$89.0 \pm 0.2$	0.346
$^{102}\text{Pd}$	1.00	(n,2n)	$^{101}\text{Pd}$	$8.47 \pm 0.06$ h	296.29	$18 \pm 1$	-10.568

Table 1.1.1 Measured reactions (Continued)

Target Nucleus	Natural Abundance[%]	Reaction	Product	Half-life	Gamma-ray Energy[keV]	Branching Ratio[%]	Q-value [MeV]
$^{102}\text{Pd}$	1.00	(n,np)	$^{101\text{m}}\text{Rh}$	$4.34 \pm 0.01$ d	306.77	$87 \pm 1$	-7.961
$^{105}\text{Pd}$	22.20	(n,p)	$^{105}\text{Rh}$	$35.47 \pm 0.08$ h	318.90	$19 \pm 1$	0.215
$^{106}\text{Pd}$	27.30	(n,p)	$^{106\text{m}}\text{Rh}$	$130 \pm 2$ m	450.80	$24.4 \pm 0.4$	-2.896
$^{108}\text{Pd}$	26.70	(n, $\alpha$ )	$^{105}\text{Ru}$	$4.44 \pm 0.02$ h	469.37	$17.8 \pm 0.6$	2.062
$^{106}\text{Cd}$	1.25	(n,2n)	$^{105}\text{Cd}$	$56.0 \pm 0.5$ m	961.84	$4.7 \pm 0.3$	-2.013
$^{106}\text{Cd}$	1.25	(n,np)	$^{105}\text{Ag}$	$41.29 \pm 0.07$ d	443.00	$17.1 \pm 1.7$	-7.345
$^{106}\text{Cd}$	1.25	(n,p)	$^{106\text{m}}\text{Ag}$	$8.5 \pm 0.1$ d	450.97	$28.4 \pm 1.2$	0.492
$^{110}\text{Cd}$	12.50	(n,p)	$^{110\text{m}}\text{Ag}$	$252.2 \pm 0.3$ d	657.75	$94.4 \pm 0.6$	-2.229
$^{112}\text{Cd}$	24.10	(n,p)	$^{112}\text{Ag}$	$3.14 \pm 0.02$ h	617.40	$42 \pm 5$	-3.176
$^{113}\text{Cd}$	12.20	(n,p)	$^{113}\text{Ag}$	$5.37 \pm 0.05$ h	298.40	9.0	-1.181
$^{159}\text{Tb}$	100.00	(n,p)	$^{159}\text{Gd}$	$18.56 \pm 0.08$ h	363.30	10	-0.192
$^{185}\text{Re}$	37.40	(n,2n)	$^{184\text{m}}\text{Re}$	$169 \pm 8$ d	920.93	$8.3 \pm 0.3$	0.983
$^{185}\text{Re}$	37.40	(n,2n)	$^{184\text{g}}\text{Re}$	$38.0 \pm 0.5$ d	903.28	$38 \pm 1$	1.171
$^{187}\text{Re}$	62.60	(n, $\alpha$ )	$^{184}\text{Ta}$	$8.7 \pm 0.1$ h	414.01	$74 \pm 1$	7.262
$^{187}\text{Re}$	62.60	(n,p)	$^{187}\text{W}$	$23.85 \pm 0.08$ h	479.53	21	-0.530

\* Data are taken from Table of Isotopes, 7th Edition

Fig. 1.1.1 Cross section of  $^{96}\text{Ru}(n,2n)^{95}\text{Ru}$ Fig. 1.1.2 Cross section of  $^{96}\text{Ru}(n,p)^{96\text{m+g}}\text{Tc}$



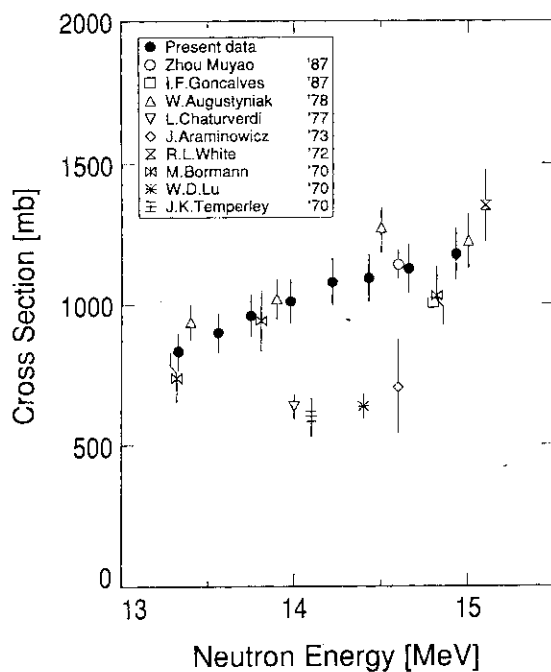


Fig. 1.1.3 Cross section of  $^{102}\text{Pd}(n,2n)^{101}\text{Pd}$

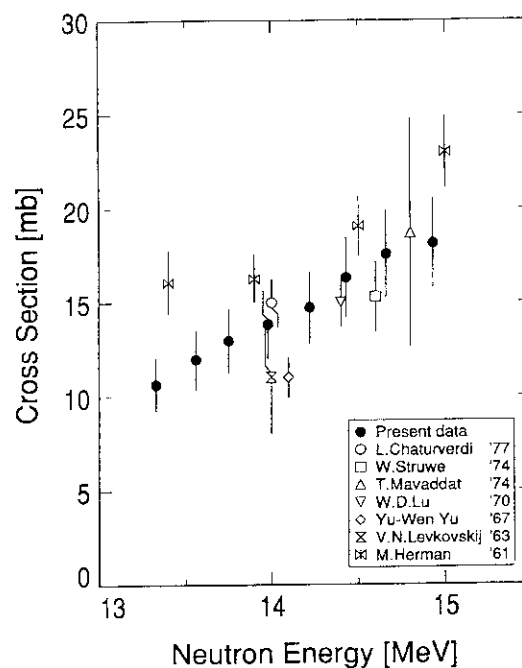


Fig. 1.1.4 Cross section of  $^{112}\text{Cd}(n,p)^{112}\text{Ag}$

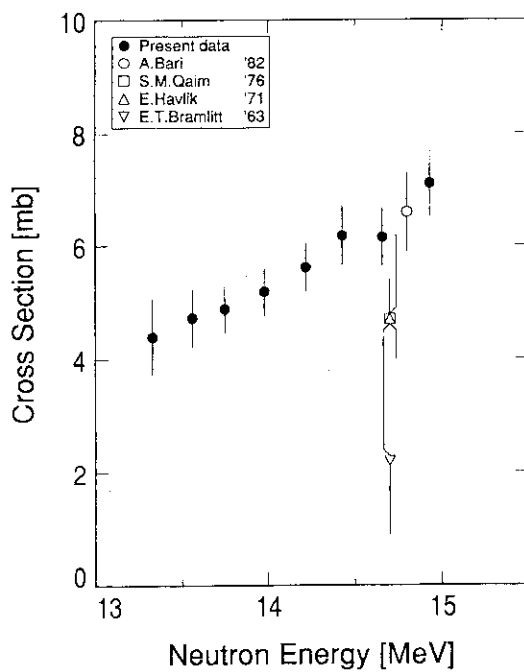


Fig. 1.1.5 Cross section of  $^{159}\text{Tb}(n,p)^{159}\text{Gd}$

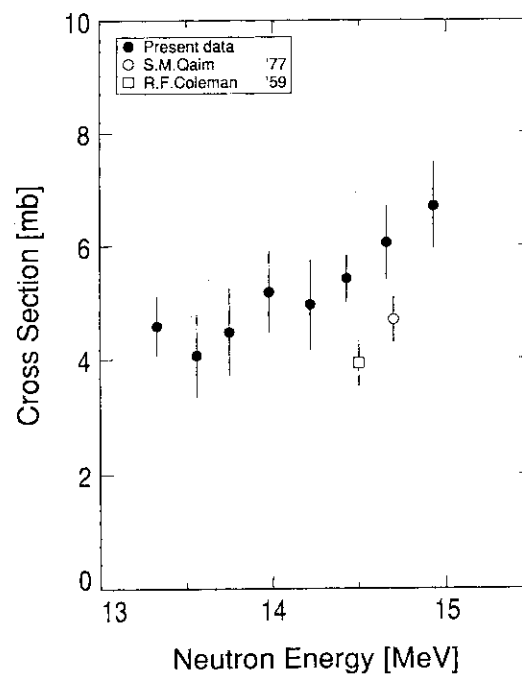


Fig. 1.1.6 Cross section of  $^{187}\text{Re}(n,p)^{187}\text{W}$

## 1.2 Measurements of Long-lived Activation Cross Sections at 14 MeV Energy Region

Y. Ikeda, A. Kumar<sup>\*</sup> and C. Konno

The production cross sections of long-lived radioactivities in the structural materials for 14 MeV neutrons are the key elements from a view point of the waste disposal assessment in the D-T fusion reactor. It has been strongly requested to measure systematic data from the fusion reactor application point of view. In this context, an experiment to measure long-lived activation cross sections at 14 MeV has been conducted in the framework of the JAERI/USDOE collaborative program on fusion neutronics.

Fourteen reactions measured are given in Table 1.2.1 along with associated decay properties of the reaction products. Samples of Al,  $^{61}\text{Ni}$ , Cu, Nb, Mo, Ag,  $^{151}\text{Eu}$ ,  $^{153}\text{Eu}$ , Tb, Dy, Hf, W, Re and Bi were irradiated with D-T neutronics for 32 hours. It resulted in  $1.7 \times 10^{17}$  neutrons of total neutron yield at the target. The foil packages were placed at angles of  $0^\circ$ ,  $45^\circ$  and  $90^\circ$  with respect to the incident  $d^+$  beam, the distances of which was about 50 mm from the D-T source. Neutron flux at each sample was determined with the  $^{93}\text{Nb}(n,2n)^{92}\text{Nb}$  reaction rate. The neutron fluence at the samples was estimated to be  $0.8 - 2.0 \times 10^{15} / \text{cm}^2$ . At more than 1.7 year after irradiation,  $\gamma$ -ray counting has started by using a high detection efficiency Ge detector. The reaction rates of concerned were derived from  $\gamma$ -ray peak counts with necessary corrections. The cross sections were preliminary obtained by using neutron fluxes determined, where a cross section value of 455 mb for  $^{93}\text{Nb}(n,2n)^{92}\text{Nb}$  reaction around 14 MeV was used.

In Table 1.2.2, present data are summarized along with data available in the literature and IAEA-CRP<sup>1)</sup>. Some topics of this measurement are given as follows;

- (1) The reaction cross sections for  $^{27}\text{Al}(n,2n)^{26}\text{Al}$ ,  $^{63}\text{Cu}(n,\alpha)^{60\text{m}}\text{Co}$ ,  $^{94}\text{Mo}(n,p)^{94\text{m}}\text{Nb}$ ,  $^{109}\text{Ag}(n,2n)^{108\text{m}}\text{Ag}$ ,  $^{151}\text{Eu}(n,2n)^{150\text{m}}\text{Eu}$ ,  $^{153}\text{Eu}(n,2n)^{152\text{m}}\text{Eu}$ ,  $^{159}\text{Tb}(n,2n)^{158\text{m}}\text{Tb}$ ,  $^{179}\text{Hf}(n,2n)^{178\text{m2}}\text{Hf}$  and  $^{209}\text{Bi}(n,2n)^{208}\text{Bi}$  were close to the data reported in the literature.
- (2) Present measurement for  $^{61}\text{Ni}(n,np)^{60\text{m}}\text{Co}$  gave considerably larger cross section for this reaction than data in JENDL-3 and REAC-ECN3<sup>2)</sup>.

---

<sup>\*</sup> University of California, Los Angeles, Los Angeles CA 90024-1579 USA

However, from the reaction systematics, our data seemed reasonable.

- (3) The present measurement for  $^{93}\text{Nb}(n,n')^{93\text{m}}\text{Nb}$  gave an excellent agreement with a recent evaluation by Odano<sup>3)</sup>, while the present data were slightly larger than the data by Ryves<sup>4)</sup>, which has ever been only the available experimental data at 14 MeV region.
- (4) For the first time, experimental data for  $^{158}\text{Dy}(n,p)^{158\text{m}}\text{Tb}$ ,  $^{182}\text{W}(n,n'\alpha)^{178\text{m}}\text{Hf}$  and  $^{187}\text{Re}(n,2n)^{186\text{m}}\text{Re}$  were given by the present measurement.

The counting of activities are still underway to arrive at better statistics.

#### References

- 1) INDC(NDS)-232/L: "Activation Cross Sections for the Generation of Long-Lived Radionuclides of Importance in Fusion Reactor Technology", Proc. of an IAEA Consultants' Meeting, Argonne National Laboratory, 11th - 12th, Sept. 1989.
- 2) Gruppelaar H., et al.: ECN-207 (1988).
- 3) Odano N., Iwasaki S. and Sugiyama K.: "Evaluation of Cross Sections for the Dosimetry Reactions of Niobium", Proc. Int. Conf. on Nuclear Data, at Julich Germany, May 13-17, 1991.
- 4) Ryves T.B. and Kolkowski T.: J. Phys. G: Nucl. Phys. 7, 52 (1981).
- 5) Meadows J.W., et al.: "A Search for Activation Produced by Fast-Neutron Irradiations of Copper, Silver, Europium, Terbium and Hafnium", Proc. of an IAEA Consultants' Meeting, Argonne National Laboratory, 11th - 12th, Sept. 1989.

Table 1.2.1 List of reactions measured and associated decay data of products

	Reaction	Half-Life	Abundance	$\gamma$ -ray Energy(keV)	$\gamma$ -ray branching
1	$^{27}\text{Al}(n,2n)^{26}\text{Al}$	$(7.16 \pm 0.32) \times 10^5 \text{ y}$	100	1808.65	$99.76 \pm 0.04$
2	$^{61}\text{Ni}(n, np)^{60\text{m}} + \text{gCo}$	5.217 y	88.84 <sup>a)</sup>	1332.5	99.98
3	$^{63}\text{Cu}(n, \alpha)^{60\text{m}} + \text{gCo}$	5.217 y	69.1	1332.5	99.98
4	$^{93}\text{Nb}(n, n')^{93\text{m}}\text{Nb}$	$13.6 \pm 0.3 \text{ y}$	100	30.4	(K/L+M+...0.12)
5	$^{94}\text{Mo}(n, p)^{94}\text{Nb}$	$(2.03 \pm 0.16) \times 10^5 \text{ y}$	9.3	871.10	100.0
6	$^{109}\text{Ag}(n, 2n)^{108\text{m}}\text{Ag}$	$127 \pm 7 \text{ y}$	48.17	434.0	90.5
7	$^{151}\text{Eu}(n, 2n)^{150\text{m}}\text{Eu}$	$35.8 \pm 1.0 \text{ y}$	97.7 <sup>a)</sup>	333.96	$94. \pm 3$
8	$^{153}\text{Eu}(n, 2n)^{152\text{m}} + \text{gEu}$	$13.2 \pm 0.3 \text{ y}$	99.92 <sup>a)</sup>	344.3	$27.2 \pm 0.4$
9	$^{159}\text{Tb}(n, 2n)^{158\text{m}} + \text{gTb}$	$150 \pm 30 \text{ y}$	100	944.2	$43 \pm 3$
10	$^{158}\text{Dy}(n, p)^{158\text{m}} + \text{gTb}$	$150 \pm 30 \text{ y}$	0.1	944.2	$43 \pm 3$
11	$^{179}\text{Hf}(n, 2n)^{178\text{m}}\text{Hf}$	$31 \pm 1 \text{ y}$	13.7	325.56	$94.1 \pm 0.3$
12	$^{182}\text{W}(n, n')^{178\text{m}}\text{Hf}$	$31 \pm 1 \text{ y}$	26.3	325.56	$94.1 \pm 0.3$
13	$^{187}\text{Re}(n, 2n)^{186\text{m}}\text{Re}$	$2 \times 10^5 \text{ y}$	62.6	137.0 <sup>b)</sup>	10.0
14	$^{209}\text{Bi}(n, 2n)^{208}\text{Bi}$	$(3.68 \pm 0.04) \times 10^5 \text{ y}$	100	2614.47 <sup>c)</sup>	100.0

a) Enriched  $^{61}\text{Ni}$  (88.84%),  $^{151}\text{Eu}$  (97.70%) and  $^{153}\text{Eu}$  (99.92%) sample were used.

b) Natural background subtraction was needed.

c) Decay of ground state of  $^{186}\text{Re}$  to  $^{186}\text{Os}$ .

Table 1.2.2 Cross sections measured for long-lived activation

Reaction	Present Work		References	
	$E_n(\text{MeV})$	Cross Section (mb)	$E_n(\text{MeV})$	Cross Section (mb)
$^{27}\text{Al}(n, 2n)^{26}\text{Al}$	14.8	$47 \pm 5$	14.7	$40.6 \pm 4.4$
	14.5	$30 \pm 7$	14.8	$35 \pm 7$
	14.1	$19 \pm 10$	14.5	16.2
$^{61}\text{Ni}(n, np)^{60\text{m}} + \text{gCo}$			14.1	19.0
	14.8	$50.5 \pm 8.2$	14.5	18
			14.1	17.4
$^{63}\text{Cu}(n, \alpha)^{60\text{m}} + \text{gCo}$	14.8	$40.4 \pm 2.3$	14.8	$40.1 \pm 1.2$
	14.5	$43.8 \pm 2.5$		
$^{93}\text{Nb}(n, n')^{93\text{m}}\text{Nb}$	14.8	$43 \pm 9$	14.1	$36 \pm 4$
	14.5	$44 \pm 9$		
$^{94}\text{Mo}(n, p)^{94}\text{Nb}$	14.8	$58 \pm 17$	14.8	$53.1 \pm 5.3$
	14.5	$48 \pm 20$		
	14.1	$44 \pm 18$		
$^{109}\text{Ag}(n, 2n)^{108\text{m}}\text{Ag}$	14.8	$212 \pm 11$	14.77	$230 \pm 7$ *-1)
			14.56	$263 \pm 20$ *-2)
			14 - 15	$665 \pm 73$ *-3)
$^{151}\text{Eu}(n, 2n)^{150\text{m}}\text{Eu}$			14.9	$191 \pm 7$ *-4)
	14.8	$1276 \pm 64$	14.9	$208 \pm 37$ *-5)
	14.5	$1170 \pm 59$	14.77	$1219 \pm 28$ *-1)
$^{153}\text{Eu}(n, 2n)^{152\text{m}} + \text{gEu}$	14.1	$1215 \pm 53$	14 - 15	$1325 \pm 94$ *-3)
			14.8	$1127 \pm 55$ *-4)
			14.9	$1090 \pm 84$ *-5)
$^{159}\text{Tb}(n, 2n)^{158\text{m}} + \text{gTb}$	14.8	$1659 \pm 83$	14.7	$1270 \pm 149$
	14.5	$1533 \pm 77$	14.8	$1180 \pm 150$
	14.1	$1326 \pm 75$	14.8	$1712 \pm 155$ *-4)
$^{158}\text{Dy}(n, p)^{158\text{m}} + \text{gTb}$			14.77	$1544 \pm 42$ *-1)
	14.8	$100 \pm 80$	14 - 15	$1442 \pm 60$ *-3)
	14.5	$6.3 \pm 0.6$	14.9	$1740 \pm 145$ *-5)
$^{179}\text{Hf}(n, 2n)^{178\text{m}}\text{Hf}$			14.7	$1542 \pm 138$
	14.8	$(1.4 \pm 0.8) \times 10^{-2}$	14.77	$1968 \pm 56$ *-1)
			14.8	$1600 \pm 88$ *-4)
$^{182}\text{W}(n, n')^{178\text{m}}\text{Hf}$	14.8	$135 \pm 65$	14 - 15	$1930 \pm 49$ *-3)
			14.7	1801
			14.8	1930
$^{187}\text{Re}(n, 2n)^{186\text{m}}\text{Re}$			14.5	10.7
	14.8	$2450 \pm 260$	14.8	$5.9 \pm 0.6$ *-6)
			14	2.9 *-7)
$^{209}\text{Bi}(n, 2n)^{208}\text{Bi}$			14.9	$6.0 \pm 0.3$ *-4)
	14.8		14.5	0.176
			14.1	693
			14.5	$605 \pm 258$
			14-15	$591 \pm 122$ *-3)
			14.1	2176
			14.5	2340

\* Measurement, evaluation or calculation performed for CRP:

\*-1); IAE Beijing

\*-2); Debrecen

\*-3); IRK, Vienna

\*-4); ANL/LANL/JAERI - Ref. 5)

\*-5); KRI Leningrad

\*-6); Harwell

\*-7); Oxford/LANL

## 1.3 Thermal Reactor Benchmark Calculation for JENDL-3

H. Akie, H. Takano and K. Kaneko<sup>\*</sup>

Light water reactors (LWRs) are now the most reliable nuclear energy system, and will be major energy resources for a long term in the future. On this point of view, a lot of design studies for advanced LWRs are being made actively; In the studies the accurate prediction of nuclear characteristics is one of the most important problems. In the present work, a benchmark calculation for thermal reactors was made with the newly evaluated nuclear data library JENDL-3, for the purpose of testing the reliability of nuclear data and neutronics calculation codes. This research activity has been done by the thermal reactor integral test working group in the Japanese Nuclear Data Committee.

The experiment analysed in this benchmark was the TRX-1 core<sup>1)</sup>, with water moderated lattice of 1.3% enriched uranium metal rods. The benchmark calculations were carried out with the JENDL-3 library by using the following codes; CASMO, SRAC, TGBLA, MGCL-ANISN, PHOENIX-P, VIM, VMONT and WIMS-E. A continuous energy Monte Carlo code VIM is possible to solve the three dimensional full core configuration of TRX-1. For these reasons, the VIM result was taken as a reference of the calculated results. The results compared are the infinite and effective multiplication factors ( $k_{\infty}$  and  $k_{\text{eff}}$ ) and several reaction rates measured in the experiment. A neutron spectrum with fine energy structure and infinite dilution and effective cross sections of important nuclides were also compared to investigate the sources of the differences between the calculated results.

Table 1.3.1 summarizes the calculated results for multiplication factors and reaction rates. The ratio of calculation to experiment (C/E) values are shown in this table except for  $k_{\infty}$ s. The  $k_{\text{eff}}$  values predicted by the codes are agreed with the experiment within the error of 0.8%. The largest difference between VIM and WIMS-E is about 1%. The over-estimations of the reaction rate ratios for  $\delta$ -28 are found for all the calculated results. However, the experimental error of the measurement of this reaction rate ratio is also large (more than 4%). The effective cross sections and the neutron spectra are compared in Table 1.3.2 and

---

\* The Japan Research Institute, Ltd., Tokyo

Fig. 1.3.1, respectively. The good agreements between the calculated results are seen both in the cross section and in the spectrum.

Furthermore, the C/E value for  $k_{eff}$  calculated with JENDL-2 by using the SRAC system was 0.9939, and the difference from the value calculated with JENDL-3(0.9956) was small.

#### Reference

- 1) Cross Section Evaluation Working Group: "Benchmark Specifications", ENDF-202(BNL-19302) (1974).

Table 1.3.1 Calculated results with JENDL-3 for multiplication factors and reaction rate ratios in TRX-1  
(calculation/experiment values except for  $k_{\infty}$ )

	CASMO	SRAC	TGBLA	WIMS-E	VIM
$k_{\infty}$	1.1783	1.1828	1.1784	1.1817	1.1826±0.0022
$k_{eff}$	0.9994	0.9956	0.9949	1.0020	0.9924±0.0016
$\rho$ -28	1.021	1.019	1.026	1.003	1.022
$\delta$ -25	0.976	0.980	0.975	0.975	0.986
$\delta$ -28	1.048	1.067	1.050	1.042	1.072
$C^*$	0.996	0.995	1.000	0.987	0.998

$\rho$ -28 : the ratio of epithermal to thermal U-238 capture

$\delta$ -25 : the ratio of epithermal to thermal U-235 fission

$\delta$ -28 : the ratio of U-238 fission to U-235 fission

$C^*$  : the ratio of U-238 capture to U-235 fission

Table 1.3.2 Effective cross sections in the fuel region  
in TRX-1(barns)

Energy range	Fast	Resonance	Thermal	One group
<<U-235 fission>>				
CASMO	1.379E+00	2.002E+01	3.037E+02	7.815E+01
SRAC	1.379E+00	2.036E+01	3.037E+02	7.809E+01
TGBLA	1.379E+00	2.010E+01	3.061E+02	7.928E+01
VIM	1.379E+00	2.052E+01	3.024E+02	7.845E+01
<<U-238 capture>>				
CASMO	1.337E-01	1.723E+00	1.559E+00	8.093E-01
SRAC	1.360E-01	1.717E+00	1.560E+00	8.080E-01
TGBLA	1.358E-01	1.733E+00	1.570E+00	8.198E-01
VIM	1.370E-01	1.724E+00	1.555E+00	8.123E-01

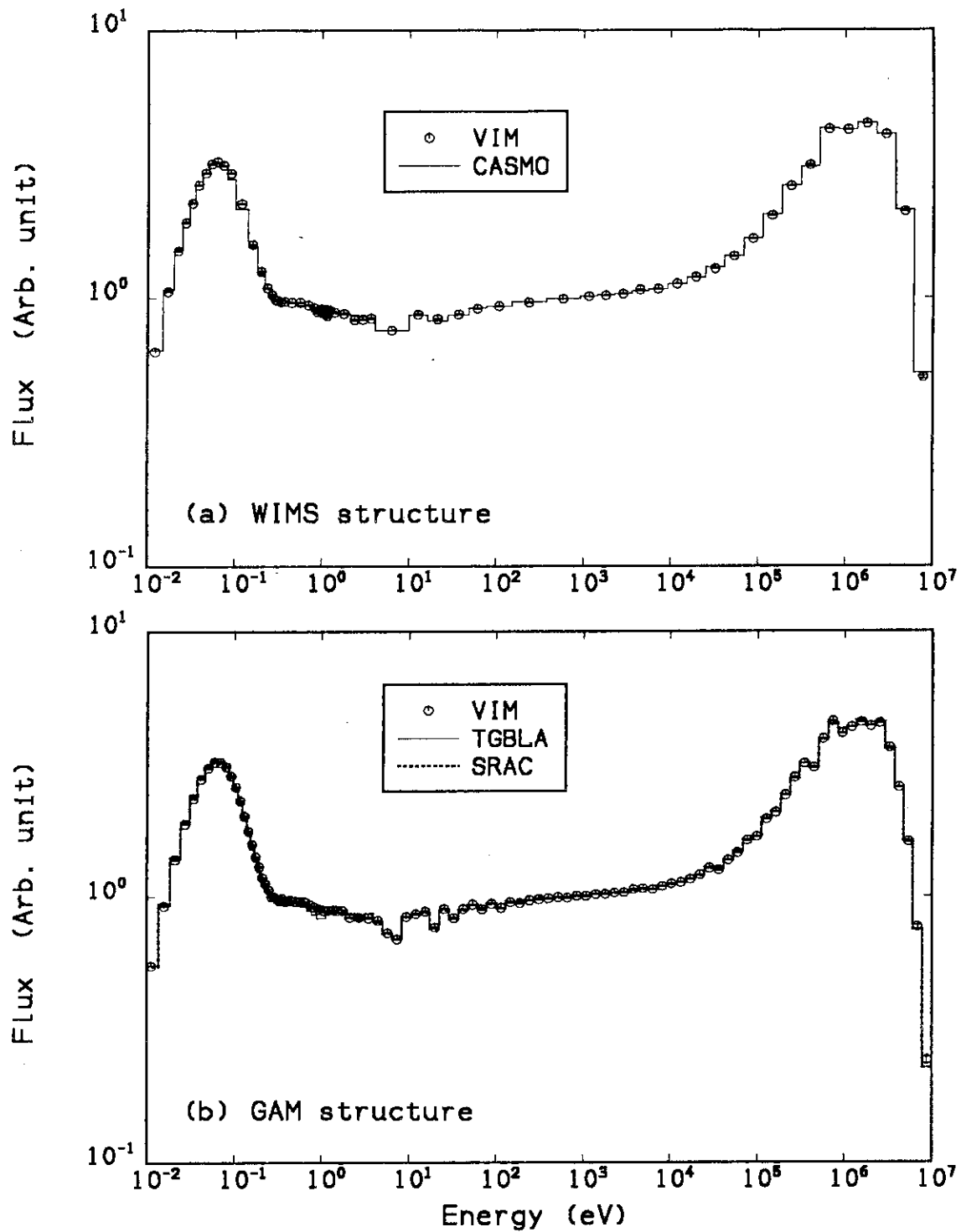


Fig. 1.3.1 Comparison of neutron spectrum in the TRX-1 cell calculated with (a) WIMS type and (b) GAM type energy structures

#### 1.4 JENDL-3 Based Data Library for the Continuous Energy Monte Carlo Code VIM

H. Akie, H. Takano and K. Kaneko\*

The nuclear data library for the continuous energy Monte Carlo code VIM<sup>1)</sup> has been produced based on the evaluated nuclear data file JENDL-3. The Monte Carlo method is suitable to accurately describe a complicated geometry. Furthermore, the continuous energy Monte Carlo method precisely calculates resonance absorption. For these reasons, the results obtained by the VIM code is considered as reference data in the benchmark calculation of JENDL-3.

By using the data processing system<sup>2)</sup>, the VIM library was generated for about 30 nuclides based on JENDL-3:

Heavy nuclides; Th-232, uranium and plutonium isotopes and Am-241,  
moderator or coolant; H, O-16, C-12 and Na-23,  
absorber; B-10, and

structural nuclides and others; B-11, N-14, F-19, Al-27, Si, Cr,  
Mn-55, Fe, Ni, Cu and Mo.

Point energy cross section data files were first generated for these nuclides by using the codes LINEAR<sup>3)</sup>, RECENT<sup>3)</sup>, and SIGMA<sup>3)</sup>. The ACER-J code<sup>2)</sup> was used to treat these point energy data to create a master file of the VIM library. This code was improved based on the module ACER in the NJOY code system<sup>4)</sup>. A probability table for the unresolved resonance cross section was created with U3R-J<sup>2)</sup>, which is a modified version of the U3R code<sup>5)</sup>. The result obtained with U3R-J was also compiled in the master file, and the nuclear data library for the VIM code was produced by processing this master file.

In the original VIM code, a fission spectrum can be presented only as a distribution function of Maxwellian, evaporation or Watt spectrum. However, the fission spectra of the nuclides U-233, U-234, U-235, U-238, Pu-239 and Pu-240 are evaluated as a tabulated form in JENDL-3. The improvement was made for the VIM code and the VIM library editing code BANDIT so as to treat the tabulated fission spectrum.

The benchmark calculations were made to test the reliability of the new data library for thermal and fast reactor systems. The result of

---

\* The Japan Research Institute, Ltd., Tokyo



the thermal reactor benchmark is compared in Table 1.4.1 with the result obtained with the JENDL-2 library for the U-235 and Pu-239 fueled cores; ORNL and PNL series<sup>6)</sup>, and the benchmark cores collected by McNeany and Jenkins<sup>7)</sup>. The multiplication factors calculated with JENDL-3 are slightly underestimated for U-235 fuel cores, and are in good agreement with experiments for Pu-239 fuel cores.

#### References

- 1) Prael R.E. and Milton L.J.: "A User's Manual for the Monte Carlo Code VIM", FRA-TM-84 (1976).
- 2) Mori T., et al.: Private communication.
- 3) Cullen D.E.: UCEL-50400, Vol.17, Part A - C (1979).
- 4) McFarlane R.E., et al.: LA-7584-M(ENDF-272) (1978).
- 5) Otter J.M., et al.: "U3R: A Code to Calculate Unresolved Resonance Cross Section Probability Table", AI-AEC-13024 (1972).
- 6) Cross Section Evaluation Working Group: "Benchmark Specifications", ENDF-202(BNL-19302) (1974).
- 7) McNeany S. and Jenkins D.: Nucl. Sci. Eng., 65, 441 (1978).

Table 1.4.1 Effective multiplication factors  
calculated by VIM

Library	JENDL-2	JENDL-3
<<U-235 cores>>		
M&J-13	0.995±0.004	0.997±0.003
M&J-14	1.001±0.006	0.995±0.004
M&J-15	0.989±0.006	0.996±0.003
ORNL-1	0.998±0.005	0.997±0.004
ORNL-2	0.999±0.005	0.993±0.004
ORNL-3	0.995±0.004	0.987±0.003
ORNL-4	1.000±0.004	0.988±0.003
ORNL-10	0.987±0.005	0.992±0.003
<<Pu-239 cores>>		
PNL-1	1.023±0.006	1.005±0.003
PNL-2	1.019±0.007	0.997±0.005
PNL-3	1.002±0.005	0.988±0.004
PNL-4	1.010±0.006	1.005±0.004
PNL-5	1.009±0.005	1.004±0.005
M&J : McNeany and Jenkins cores		

## 2. Theoretical Method and Code Development

The major portion in this chapter is related to theoretical work and code development in reactor physics.

A numerical study was performed to verify an experimental estimate of subcriticality of which method was based on Avery's coupled reactor theory. Upon modifying the definition of the coupled coefficients, it was shown that the estimate using only the measurable quantities is not applicable to a general coupled system.

Hexagonal lattice geometry becomes available as a geometry treated as lattice in a Monte Carlo code. The speed-up compared with non-lattice treatment is remarkable as shown in a sample calculation of an FBR lattice.

A 3-D plotting code for Monte Carlo codes has been developed. It provides bird-eye view and cross sectional view. It serves to constructing and debugging the input data to describe a complicated 3-D geometry.

Following to the requirement for feasibility study on HCLWR of boiling water type, improvements to the core burnup code COREBN to be applicable to HCLWR of boiling water type have been achieved. An iterative procedure to determine thermohydraulic condition and power distribution under the Hailing strategy is realized owing to the improvements.

Continuous effort is devoted to the development of IRDS (Intellectual reactor design system). Installation of SUN workstations changed the stage of development from system design into practical programming. Key technologies developed are construction of Design Data Base with object oriented structure, visualization by graphic display of the structure of reactor components and also the corresponding simulation model. An intellectual interface on the workstation for design codes has been realized. Display on menu windows supported by an expert system will help intellectual use of the codes.

Consecutive improvements on the THYDE code performed in recent years made the code comprehensive. The code provides static thermohydraulics design, dynamics analysis including LOCA for LWRs of boiling water type and pressurized water type and even for HWRs.

(Keichiro Tsuchihashi)

## 2.1 Applicability of Avery's Coupled Reactor Theory to Estimate of Subcriticality of TCA Test Region

T. Kugo

In order to examine the validity of the method to estimate the subcriticality of an unknown test region using only measurable quantities on the basis of Avery's coupled reactor theory<sup>1)</sup>, we analyze experiments<sup>2)</sup> constructed in Tank-type Critical Assembly (TCA) and evaluate the subcriticality of the test region by numerical study.

Avery proposed that a small reactivity in a coupled reactor system composed of two regions can be approximately expressed by

$$\rho = \frac{\Delta_1 \Delta_2}{\Delta_1 + \Delta_2} \left( -\frac{\delta \Delta_1}{\Delta_1} - \frac{\delta \Delta_2}{\Delta_2} + \frac{\delta k_{12}}{k_{12}} + \frac{\delta k_{21}}{k_{21}} \right) \quad (2.1.1).$$

Coupling coefficient,  $k_{ij}$ , is defined as the expected value that a current generation fission neutron in a region  $j$  gives rise to the next generation in a region  $i$ . The quantity,  $\Delta_i$ , is defined as  $1 - k_{ii}$ .

The TCA experiments<sup>2)</sup> were performed with coupled reactor systems as shown in Fig. 2.1.1. A disturbance was imposed only in the driver region by inserting a fuel rod. Therefore, the second, third and fourth terms in the parentheses of the R.H.S. of Eq.(2.1.1) were assumed to be negligible and the reactivity  $\rho$  could be expressed by

$$\rho = \frac{\Delta_1 \Delta_2}{\Delta_1 + \Delta_2} \left( -\frac{\delta \Delta_1}{\Delta_1} \right) \quad (2.1.2),$$

where the driver and test regions were denoted as the region 1 and 2, respectively. From Eq.(2.1.2), the subcriticality of the test region,  $\Delta_2$ , could be estimated by only measurable quantities,  $\rho$ ,  $\Delta_1$  and  $\delta \Delta_1$ . However, this assumption was suspicious, and then the validity was examined by comparing the multiplication factors of the test region,  $k_{22}$ , evaluated by the following two formulas;

$$k_{22} = 1 + \frac{\Delta_1 \rho}{\rho + \delta \Delta_1} \quad (2.1.3),$$

and

$$k_{22} = 1 + \frac{(\Delta_1 + \delta\Delta_1)\rho}{\rho + \Delta_1 \left( \frac{\delta\Delta_1}{\Delta_1} + \frac{\delta\Delta_2}{\Delta_2} - \frac{\delta k_{12}}{k_{12}} - \frac{\delta k_{21}}{k_{21}} \right)} \quad (2.1.4).$$

Equation (2.1.3) is derived from Eq.(2.1.2) and Eq.(2.1.4) is used for an accurate estimate. Here, the coupling coefficient is defined as

$$k_{ij} = \frac{\int_{V_i} dr \sum_g v \Sigma_f^g(r) \phi_j^g(r)}{\frac{1}{k} \int_{V_j} dr \sum_g v \Sigma_f^g(r) \phi_j^g(r)} \quad (2.1.5),$$

where the neutron flux distribution of the next generation,  $\phi_j^g(r)$ , is originated from the fission source distribution of the current generation in the region  $j$ . On the other hand, Avery defined it as;

$$k_{ij} = \frac{\int_{V_i} dr \sum_g v \Sigma_f^g(r) \phi_j^g(r)}{\int_{V_j} dr \sum_g v \Sigma_f^g(r) \phi_j^g(r)} \times \frac{\int_{V_i} dr \sum_{g'} \chi^{g'} \phi^{*g'}(r) \sum_g v \Sigma_f^g(r) \phi_j^g(r)}{\int_{V_i} dr \sum_{g'} \chi^{g'} \phi^{*g'}(r) \sum_g v \Sigma_f^g(r) \phi_j^g(r)} \times k \quad (2.1.6),$$

where the adjoint flux,  $\phi^{*g}(r)$ , was introduced as the weighing function. It is usually used as the measure of the amount of progeny induced by the succeeding fission<sup>3)</sup>. However, it must be excluded from the present discussion limited only the relation between succeeding two generations.

For the numerical study, we choose the coupled reactor systems where the dimensions of the test regions are  $17 \times 17$  and  $17 \times 11$  pitches. The former is a symmetric system and the latter a typical case of an asymmetric one. Followings are found from the results. (1) All coupling coefficients change, although the disturbance is inserted into the driver region. (2) For the case of the strongly coupled system where the gap width is 0 or 3 pitches, the terms assumed to be unchangeable can not be ignored. (3) For the case of the asymmetric weakly coupled system, the numerator of the second term of R.H.S. of Eq.(2.1.3) mainly causes the deviations of the subcriticality and the terms assumed to be unchangeable become to be ignored. However, the denominator of the second term of R.H.S. of Eq.(2.1.3) becomes as small as one cent in reactivity, the uncertainty of measurement of reactivity, therefore, will cause a serious error on the estimate of the subcriticality. (4) The estimate using only measurable quantities is valid only for the symmetric weakly coupled

system where the subcriticality of the test region is very small within a few dollars in reactivity, as shown in Table 2.1.1.

Consequently, it is concluded that the estimate using only the measurable quantities is not applicable to a general coupled system.

#### References

- 1) Yamamoto Y., et al.: Proc. 1989 Fall Meeting of At. Energy Society of Japan, C52, (1989), (in Japanese).
- 2) Avery R.: Proc. 2nd Int. Conf. Peaceful Uses At. Energy, 12, 182, (1958).
- 3) Komata M.: Nucl. Sci. Eng. 38, 193, (1969).

Table 2.1.1 Comparison of multiplication factor of test region

Test Region Width(Pitch)	Gap Width (Pitch)	$k_{22}$ (I)	$k_{22}$ (II)	Deviation (I)-(II)
17	0	0.9248	0.8783	0.0466
17	3	0.9611	0.9397	0.0214
17	6	0.9876	0.9841	0.0036
17	9	0.9957	0.9963	-0.0005
11	0	0.8785	0.7962	0.0823
11	3	0.8921	0.8562	0.0359
11	6	0.8341	0.8800	-0.0459
11	9	1.0313	0.8834	0.1479

(I): Multiplication factor of test region evaluated by Eq.(2.1.3)  
 (II): that by Eq.(2.1.4)

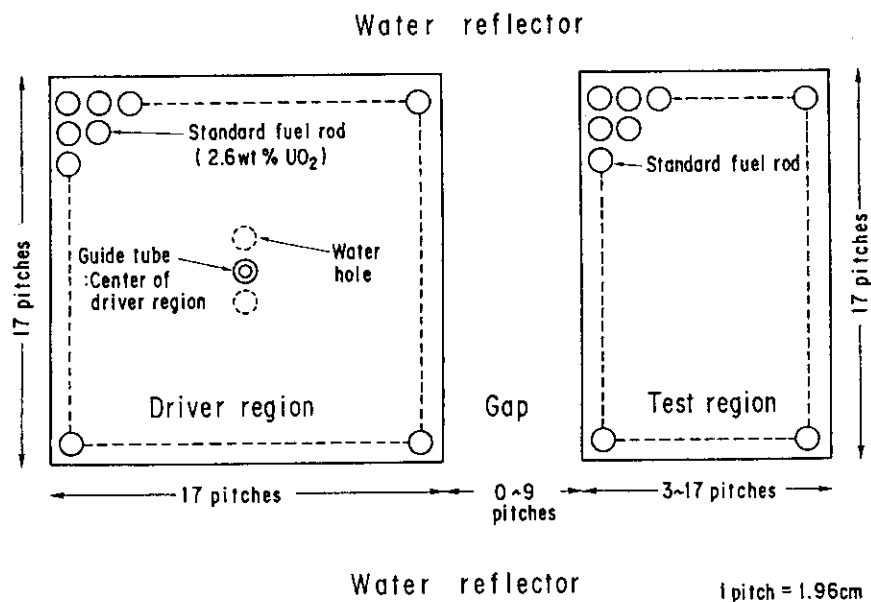


Fig. 2.1.1 Horizontal cross section view of two region coupled reactor system in TCA

## 2.2 Hexagonal Lattice Geometry for Monte Carlo Calculations

M. Nakagawa, T. Mori and M. Sasaki<sup>\*</sup>

Capability to treat lattice geometry is quite useful in a reactor calculation because a reactor core consists of nearly identical fuel cells. It makes possible to describe only once the cells of any structure that appears more than once in a geometry. The amount of input data to be provided and the amount of computer memory needed by problems that have a lot of geometrical repetition are reduced. In conventional scalar codes, however, problems would not run any faster than before. The situation is different in a vectorized code which is run on vector supercomputers<sup>1)</sup>. It can significantly reduce a computation time in addition to the benefits mentioned above. Hexagonal lattice geometry often appears in a reactor core calculation. A full lattice model can treat more accurately a fuel subassembly composed of several types of fuel pins and control rods compared with a unit cell model. As well known, the Monte Carlo method has a great advantage in a detailed description of such geometry

A method is proposed to treat a hexagonal lattice for a Monte Carlo calculation. The present method<sup>2)</sup> has a flexibility in geometry description and is particularly suitable for a vectorized code using the combinatorial geometry (CG). Any combination of CG and lattices is possible in these codes. A problem geometry is generally described in the laboratory coordinate system through particle tracking calculations. Positions and flight directions of particles are expressed in the Cartesian coordinate. When a particle enters a lattice, the coordinates of particles are at first transformed to those fixed to the cell array, then the code searches in which cell the particles exist. These coordinates are again transformed into those fixed to cells. As a result, all particles can be tracked in the cell coordinate system as far as those are in the lattice cell. When a particle goes out from a lattice, the coordinate system is inversely transformed.

Cells which are rotationally symmetry with respect to the axis of hexagonal prism can be reduced to the same geometry as the reference cell by transformation. If some cells existing in different lattices are the

---

<sup>\*</sup> Japan Research Institute Ltd., Tokyo

same type cell, all those can be treated as if they were a single cell in the particle tracking. Thus, the number of particles simultaneously processed increases much and the gain by the vectorization becomes higher.

To assess the present method, eigenvalue problems for infinitely repeated lattices are solved. The model fuel subassemblies are composed of  $\text{PuO}_2\text{-UO}_2$  fuel and cladding, a wrapper tube and sodium as illustrated in Fig. 2.2.1. The smaller subassembly has 19 fuel pins (3 layers) and the larger does 91 fuel pins (6 layers). The Monte Carlo calculations were carried out in both vector and scalar modes for the lattice and non-lattice geometries. The problems were also solved by a collision probability method code SLAROM<sup>3)</sup>.

The calculated results are shown in Table 2.2.1. The speedups are about a factor of 24 for the lattice geometries and a factor of 20.5 for the non-lattice. In the 19 pin case, the computation time by the lattice geometry is half compared with that by the non-lattice. Such a difference would become larger if the number of pins increases. It should be noted that the computation time for the 91 pins is shorter than that for the 19 pins. On the other hand, the computation time by the collision probability method rapidly increases with the number of pins though the calculated eigenvalues agree very well between both methods.

#### References

- 1) Nakagawa M., Mori T. and Sasaki M.: Nucl. Sci. Eng. 107, 58-66 (1991).
- 2) Nakagawa M., Mori T. and Sasaki M.: Annals of Nucl. Energy, 18, 467-477 (1991).
- 3) Nakagawa M. and Tsuchihashi K.: "SLAROM: a Code for Cell Homogenization Calculation of Fast Reactor", JAERI 1294 (1984).

Table 2.2.1 Hexagonal lattice problems<sup>a</sup>

Number of fuel pins	19 (3 layers)		91 (6 layers)
	Lattice	Non lattice	
Monte Carlo method			
$k_{eff}$	1.2815	1.2817	1.3493
FSD(%) <sup>b</sup>	±0.048	±0.052	±0.042
Scalar/vector	23.9	20.5	24.1
CPU time(s) <sup>c</sup>	245	469	216
Collision probability method			
$k_{eff}$	1.2814		1.3489
CPU time(s)	264		503

- <sup>a</sup> batch size = 10 000 particle/batch.  
total number of batches = 17.  
The calculations were carried out on the FACOM VP-2600 supercomputer.
- <sup>b</sup> fractional standard deviation(%).
- <sup>c</sup> computation time (in second) for 170 000 particles.

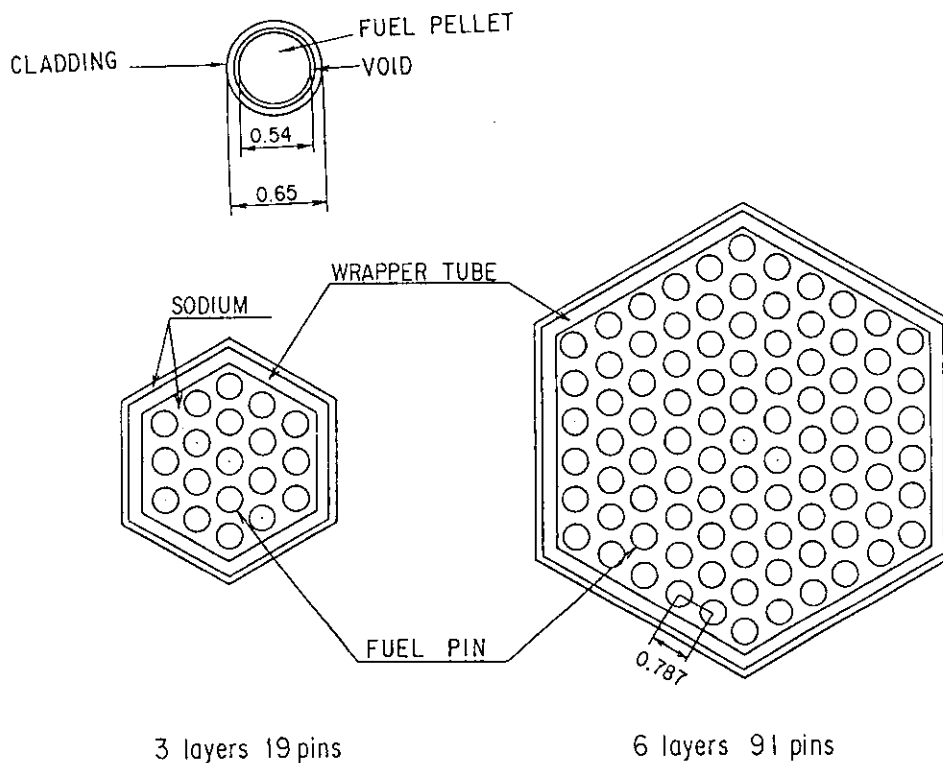


Fig. 2.2.1 Model of fuel subassembly



## 2.3 A Three-Dimensional Plotting Code for Monte Carlo Geometry

T. Mori and M. Nakagawa

Monte Carlo codes GMVP (multi-group) and MVP (continuous energy) have been developed in JAERI for vector supercomputers<sup>1),2)</sup>. These codes adopt the combinatorial geometry with multiple square and hexagonal lattices to describe geometry models. The combinatorial geometry describes a complex three-dimensional configuration by considering unions, differences and intersections of simple bodies such as right parallelepiped, arbitrary polyhedron, right circular cylinder, sphere, truncated right cone, ellipsoid, triangular prism, hexagonal prism, elliptical torus and hemispace. There is no restriction on the number of lattices, types of lattices and the number of unit cells in a lattice. A unit cell is also described by the combinatorial geometry and can include another lattice (lattice-in-lattice geometry). These capabilities considerably reduce erroneous and tedious work to prepare input data for geometry description. However, it is still difficult for a user to obtain a definite image of a complicated three-dimensional geometry model and to verify that his input data correctly describes his geometry. At the present work, a three-dimensional plotting program CGVIEW has been developed as a tool for verification and validation of three-dimensional geometry models.

The CGVIEW code can draw two types of figures from the geometry description data for both GMVP and MVP Monte Carlo codes. The first one is a bird-eye view from an arbitrary viewpoint. The second is a cross sectional view (two-dimensional slice by any plane). The program draws the former figure based on the wire frame model used in the JUNEBUG-II code<sup>3)</sup>, while the latter is based on the ray-trace method which uses the tracking routines for the Monte Carlo codes. The DISSPLA Graphics System is adopted for device independent plot capabilities. Plot resolution and subspace to be plotted can be specified by users depending on their purposes; therefore, computing time requirements are user-controlled. The user can also specify the depth of nesting lattices to be plotted. Sample outputs are shown in Figs. 2.3.1 and 2.3.2. The former figure is a bird eye view of a fuel assembly which is described by using a square lattice. Figure 2.3.2 shows cross sectional views of a critical assembly composed of two lattices and a hexagonal fuel assembly for fast reactors.

The right one of Fig. 2.3.2 is an example of error-detection. In this case, an inside of the center rod is not defined in geometry description data, and the code detects and prints out that error in the figure.

Installation and interactive use of the program on an engineering workstation are planned to significantly reduce effort in constructing and debugging a complicated three-dimensional geometry model for Monte Carlo calculations.

#### References

- 1) Nakagawa M., et al.: Nucl. Sci. Eng., 107, 58-66 (1991).
- 2) Mori T., et al.: "MVP: A Continuous Energy Monte Carlo Code for Vector Supercomputers", Proc. Int. Topical Meeting on Advances in Maths., Compu. and Reactor Physics, Vol.4, 30.4-4, Pittsburgh, May, 1991.
- 3) Emmett M.B., et al.: "JUNEBUG-II: Three-Dimensional Geometry Plotting Code", ORNL/NUREG/CSD-2/V2/R2 (1984).

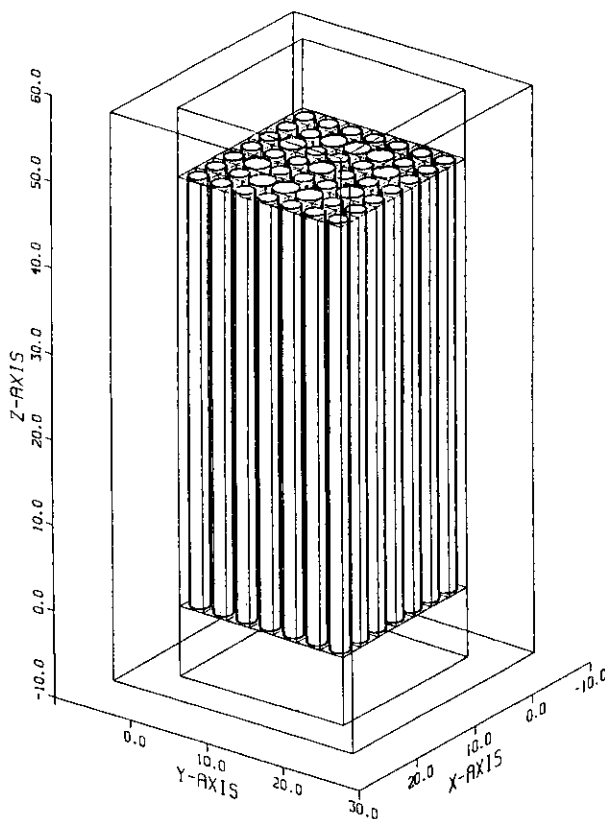
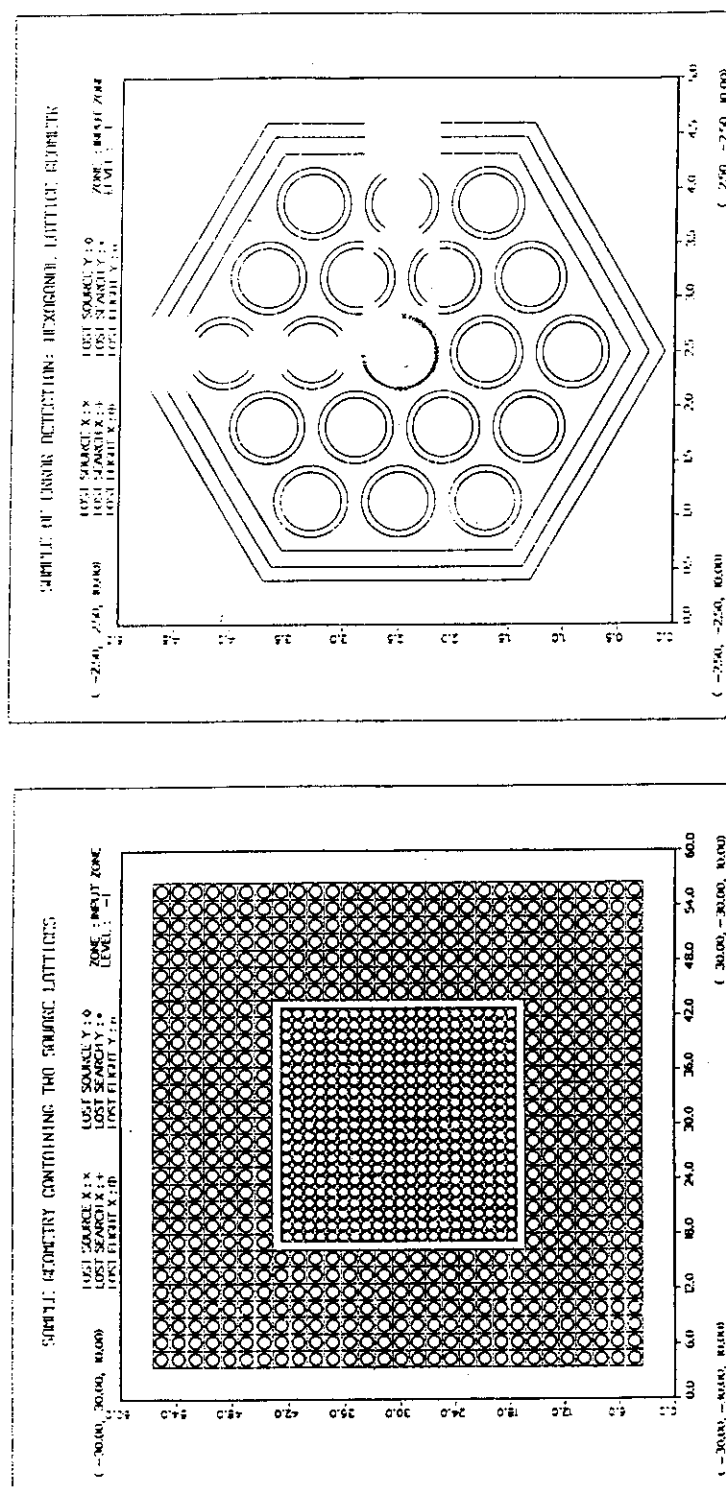


Fig. 2.3.1 Bird eye view of a fuel assembly depicted by CGVIEW



(a) Geometry containing two square lattices (b) Sample of error detection

Fig. 2.3.2 Cross sectional views drawn by CGVIEW

## 2.4 Development of Burnup Calculation Code for Boiling Water Reactor Core

Y. Moritomo<sup>\*</sup>, K. Okumura and Y. Ishiguro

A conceptual design study of HCLWRs based on a pressurized water reactor (PWR) core was performed at JAERI in these years<sup>1)</sup>. In the conceptual design study, core neutronics was analyzed by using a core burnup calculation code COREBN2 and a fuel management code HIST2<sup>2)</sup> developed at JAERI. To achieve a higher conversion ratio, the conceptual design study of HCLWR based on a boiling water reactor (BWR) core is under way<sup>3)</sup>. In order to evaluate core performances of the HCBWR core, the COREBN2 code and the HIST2 code have been improved.

Because moderator density considerably changes in the BWR core, thermal hydraulic calculations must be coupled with neutronic calculations to evaluate core performances. The functions newly installed to the codes are as follows:

- (1) Thermal hydraulics calculations: Core flow split is determined in such a way that the total static core pressure drop across each channel is the same. Using this core flow split and a power distribution, the moderator density distribution is calculated. Thermal margin is evaluated by the modified CISE correlation<sup>4)</sup>.
- (2) Interpolation scheme of macroscopic cross sections: An interpolation of tabulated cross sections by burnup, historical moderator density and temperature gives space dependent macroscopic cross sections. An instantaneous void feedback effect is represented by a quadratic formula in terms of burnup, historical and instantaneous moderator densities.
- (3) Burnup calculation under the Haling strategy: Eigenvalue and power distribution at the given end of cycle (EOC) condition are evaluated under the Haling strategy<sup>5)</sup>. An achievable incremental burnup can be evaluated under the condition of a given target eigenvalue.

Figure 2.4.1 shows the flow diagram of the program for the Haling calculation. The process of the program is summarized as follows.

At the first step, the code reads three groups of input data, that is, core operation condition, burnup history of each fuel and thermal

---

\* on leave from Energy Research Laboratory, Hitachi Ltd.

hydraulic condition.

The power distribution in the core is calculated based on a neutron diffusion method. The core neutronic and thermal hydraulic calculations are repeated until power and moderator distributions are converged (loop-1). In the eigenvalue calculation mode under the Haling strategy, the incremental burnup distribution at the EOC state is evaluated as the multiple of an operation time and a power level at each node. These steps are repeated until the power distribution is converged (loop-2). To evaluate an achievable incremental burnup, operating time is adjusted according to the difference between the eigenvalue at the EOC state evaluated above and the target eigenvalue (loop-3).

In the final step, the burnup history of each fuel is updated and stored in the history file.

The code was applied to a preliminary study of a high conversion boiling water reactor with an axially heterogeneous core using a one-dimensional model. A three dimensional analysis of the core is under way at Reactor System Laboratory.

#### References

- 1) Okumura K., et al.: "Conceptual Design Study of High Conversion Light Water Reactor", JAERI-M 90-096 (1990) (in Japanese).
- 2) Tsuchihashi K., et al.: "Revised SRAC Code System", JAERI-1302 (1986).
- 3) Morimoto Y., et al.: "Reactor Engineering Department Annual Report", JAERI-M 90-149, p.73 (1990).
- 4) Matsumoto T., et al.: "Development of Critical Power Correlation for Tight Lattice Fuel Assembly", Preprint 1987 Annu. Meeting At. Energy Soc. Japan, E-40 (1987) (in Japanese).
- 5) Haling R.K.: "Operating Strategy for Maintaining at Optimum Power Distribution Throughout Life", ANS Topical Meeting on Nuclear Performance of Power Reactor Cores, TID7672 (1963).

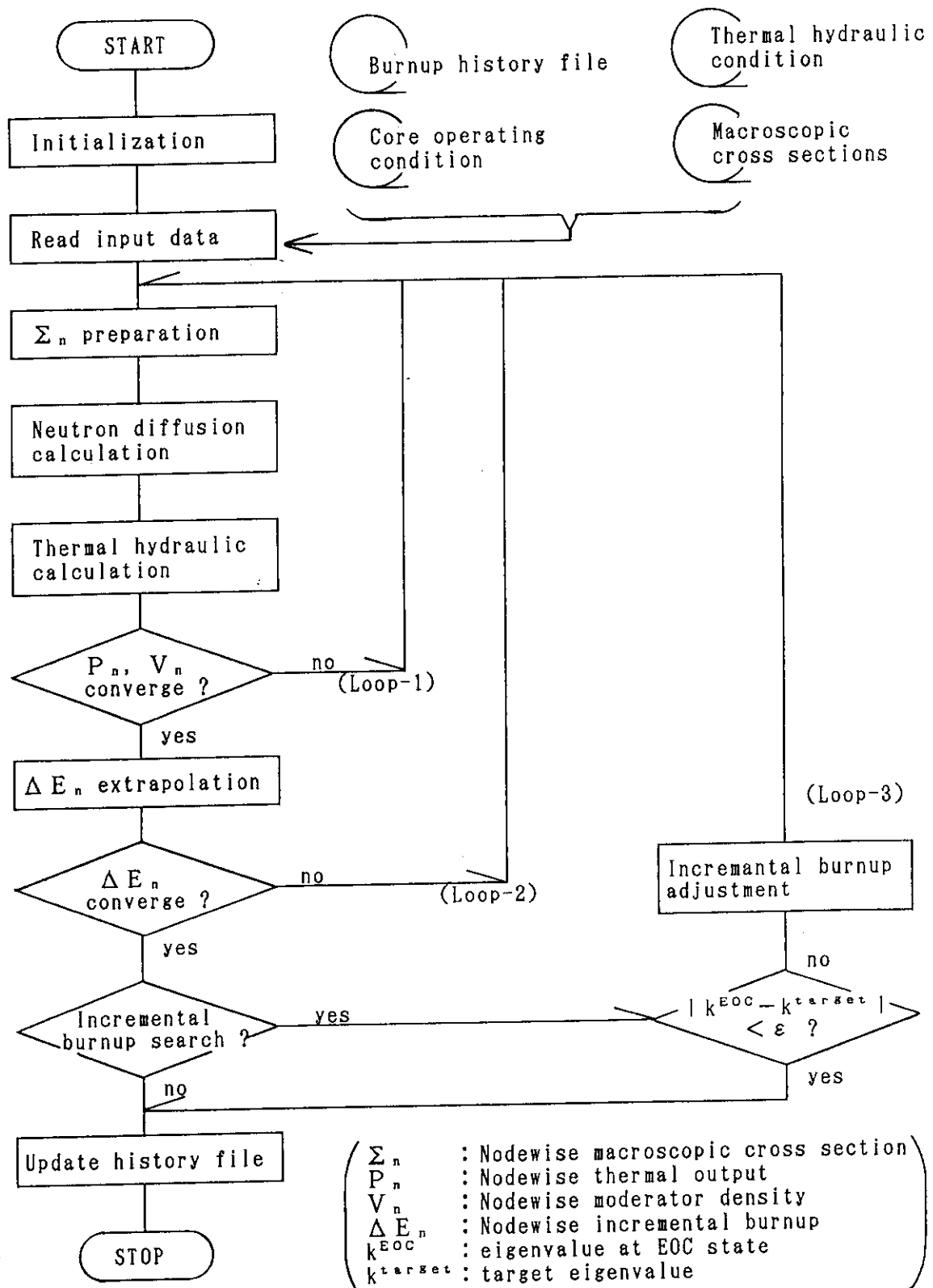


Fig. 2.4.1 Flow diagram for core burnup calculation under the Haling strategy

## 2.5 Development of Intellectual Reactor Design System IRDS

K. Tsuchihashi, M. Nakagawa, T. Mori, T. Kugo and S. Fujita\*

The development of Intellectual Reactor Design System IRDS was continued along the system design<sup>1)</sup>. The object of the system is to support feasibility study and preconceptual design of new type reactors by utilizing the latest information processing techniques in hard- and software environment. Design information on the current reactors are compiled into Design Data Base (Design DB) to provide reference and defaulted data. The knowledge and experience in design and simulation accumulated in human being will be transferred into Knowledge Base (KB) to help selection, decision and judgement. A workstation as human interface controls design process and drives DB, KB and the modular system through computer network. It serves also to visualize geometrical data and results of simulation.

Purchase of two SUN workstations during the fiscal year of 1990 brought remarkable change in our computer environment. Not only transfer of the software from the host machine into SUNs but also new programming to utilize menu and graphic display have been conducted. Using the workstation, effort was continued to develop the component technologies required in IRDS. These are construction of Design DB, extension of an input data generation tool to work on additional geometries. Programming of modules for conceptual design will be described in the following section 2.6.

Here we shall describe the progress in construction of Design DB. Functions of this DB are as follows;

1. To keep design information of the reactors currently working or under construction as reference models. (The urgent items are the data relevant to neutronics and thermal hydraulics.)
2. To accept and save a new design model under consideration.
3. To search references and choose the reactor of which design is the most similar to the new model.
4. To send the data of the new model to a simulation module if required.
5. To receive and save the data of the new model from the results of simulation.

---

\* CSK Corp.

6. To update the information through menu windows of workstation.

Note: Graphic display capability is included in the functions 3 and 4, so that structural information can be visualized on display.

To realize the above functions, Design DB must have an object oriented architecture with the following elements;

- Modularity
- Encapsulation
- Hierarchy
- Flexibility
- Inheritance

Care has been taken to realize double hierarchy because the DB has its class structure (kind of) in reactor type and also its object structure (part of) in component. An example of typing of reactors is shown in Fig. 2.5.1. And an example of object structure for a PWR is shown in Fig. 2.5.2. Flexibility in data structure is one of problems to be solved.

To realize the above architecture, the DB management system (DBMS) utilizes the data pool system<sup>2)</sup> which permits to store the data in a hierarchic structure.

The DBMS written by C-language is presently available for the functions 4 and 5 mentioned above. To confirm the performance of the DBMS, information on neutronics design for four reactors (a BWR, a PWR, a research reactor and an HCPWR) as instances was implemented in Design DB. After specifying frame of component structure and performance item, the remaining functions will be fulfilled.

Extension of a C-language module for graphic display and generation of geometry input data was made. Additional three one-dimensional geometries became available. It ran successfully on the SUN workstation. Other geometries such as RZ and XY will be shortly installed. The graphic function implemented in this module is transferred into Design DBSM so that geometrical information of reactor design can be visualized.

## References

- 1) Tsuchihashi K., et al.: "Development of Intellectual Reactor Design System: IRDS", JAERI-M 90-177 (1990) (in Japanese).
- 2) Tomiyama M., et al.: "Data Pool System", JAERI-M 8715 (1980) (in Japanese).



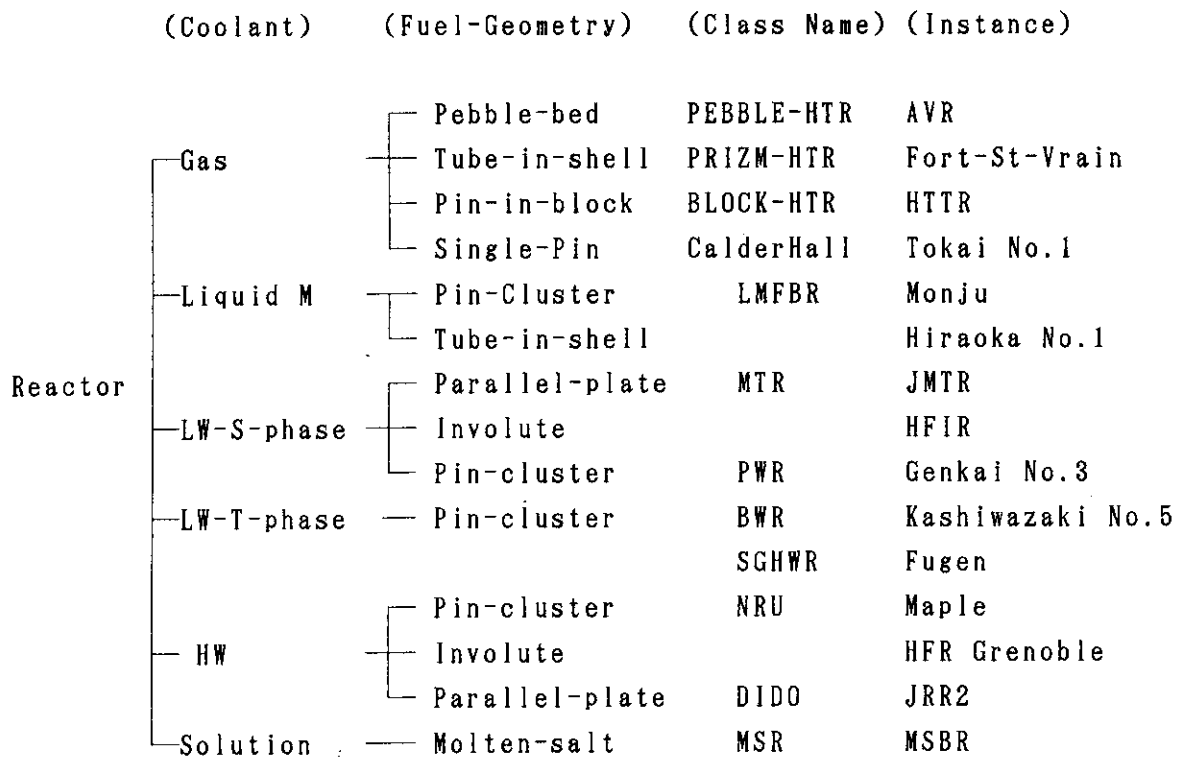


Fig. 2.5.1 An example for class structure of reactors

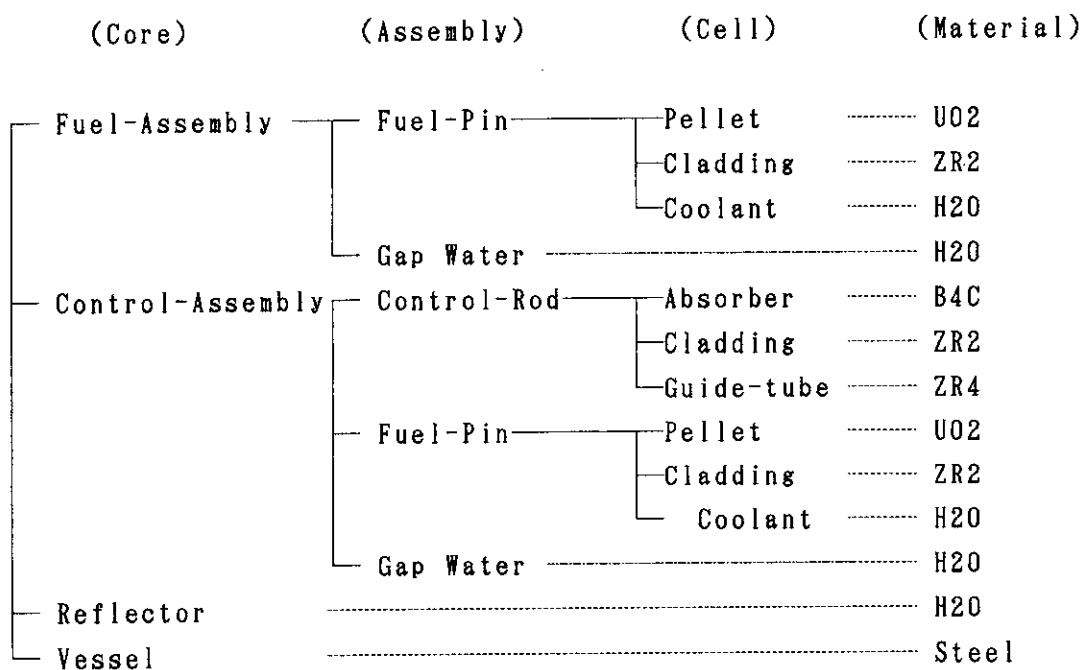


Fig. 2.5.2 An example of object structure in a PWR

## 2.6 Interactive Interface on a Workstation for Reactor Design Codes

M. Nakagawa, T. Mori, S. Fujii\* and Y. Uno\*

The intellectual reactor design system (IRDS)<sup>1)</sup> is under development to support reactor conceptual design study. The system includes the fields to cover the reactor core design, such as neutronics, thermal-hydraulics, fuel design and so on. The first version of modules for thermal-hydraulics and fuel behavior analysis has been developed and tested. The feature of this module is briefly described below.

The system has been developed on the SUN 4 workstation using SUNVIEW as a window system. To improve man-machine interface, all input and output data are interactively prepared or processed by selecting window menu with a mouse. To minimize work for input data preparation, default values are set to all parameters, which would be helpful for non-expert users. Help function provides the description on the meaning of input data and options. The interface part was written in the C programming language and the window menu is basically presented in Japanese. An example of window menu is shown in Fig. 2.6.1 where grayed parts are active. Each menu item generates the corresponding task. Figure 2.6.2 is an example of input data window. Numerical input data can be changed from a keyboard and some parameters will be selected from a pop-up menu.

Analysis codes include the modified versions of GAPCON-THERMAL-2<sup>2)</sup>, LIFE-I<sup>3)</sup> and FRAP-S3<sup>4)</sup>. These codes cover reactor types of PWR, HCLWR, a gas cooled reactor and LMFBR. Users can selectively display output results among digital values of important parameters, full output data from analysis codes and graphics. The flow of process is illustrated in Fig. 2.6.3. When an optimization option is selected, design parameters can be automatically searched to satisfy the design criteria using an expert system. This consists of inference engines and knowledge base. The former uses LISP as a programming paradigm and the latter is presented by IF-THEN type knowledge of experts. This part is still in testing stage and the number of parameters to be taken into account should be increased in future work.

---

\* Kawasaki Heavy Industries Ltd., Tokyo

## References

- 1) Tsuchihashi K., et al.: "Development of Intellectual Reactor Design System: IRDS", JAERI-M 90-177 (1990) (in Japanese).
- 2) Beyer C.E., et al.: "GAPCON-THERMAL-2", BNWL-1898 (1975).
- 3) Jankus V.Z. and Weekes R.W.: "LIFE-I", ANL-7736 (1970).
- 4) Dearien J.A., et al.: "FRAP-S2", TREE-NEUREG-1107 (1977).

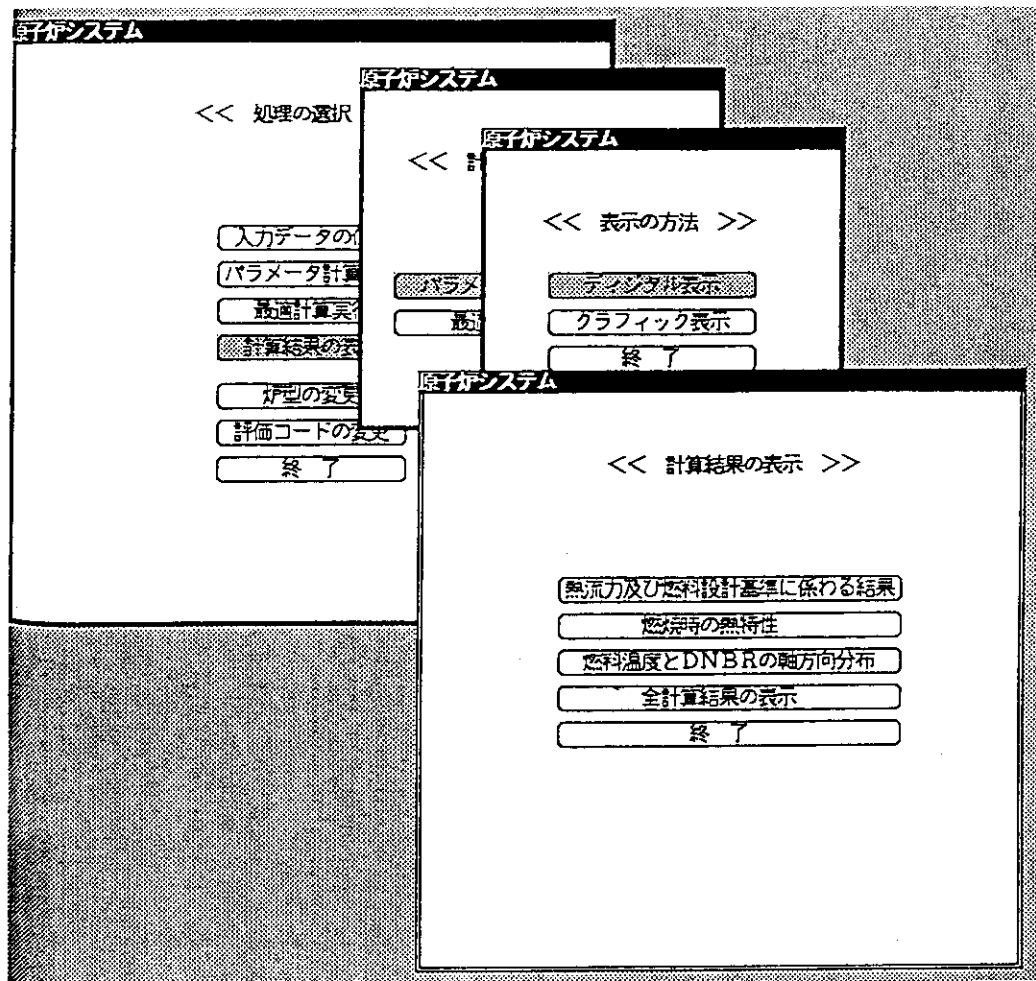


Fig. 2.6.1 An example of window menu

説明 終了

<< 熱水力設計用の入力パラメータの設定 >>

タイトル		Sample problem LWR
ピンピッチ (mm)		12.0
ピン直径 (mm)		9.5
ピン長さ (m)		2.00
平均熱出力 (kW/m)		15.0
ホットチャンネル因子の選択		1
過負荷		1.0
ホットチャンネル因子		1.50
軸方向形状因子		1.55

Fig. 2.6.2 An example of input data window

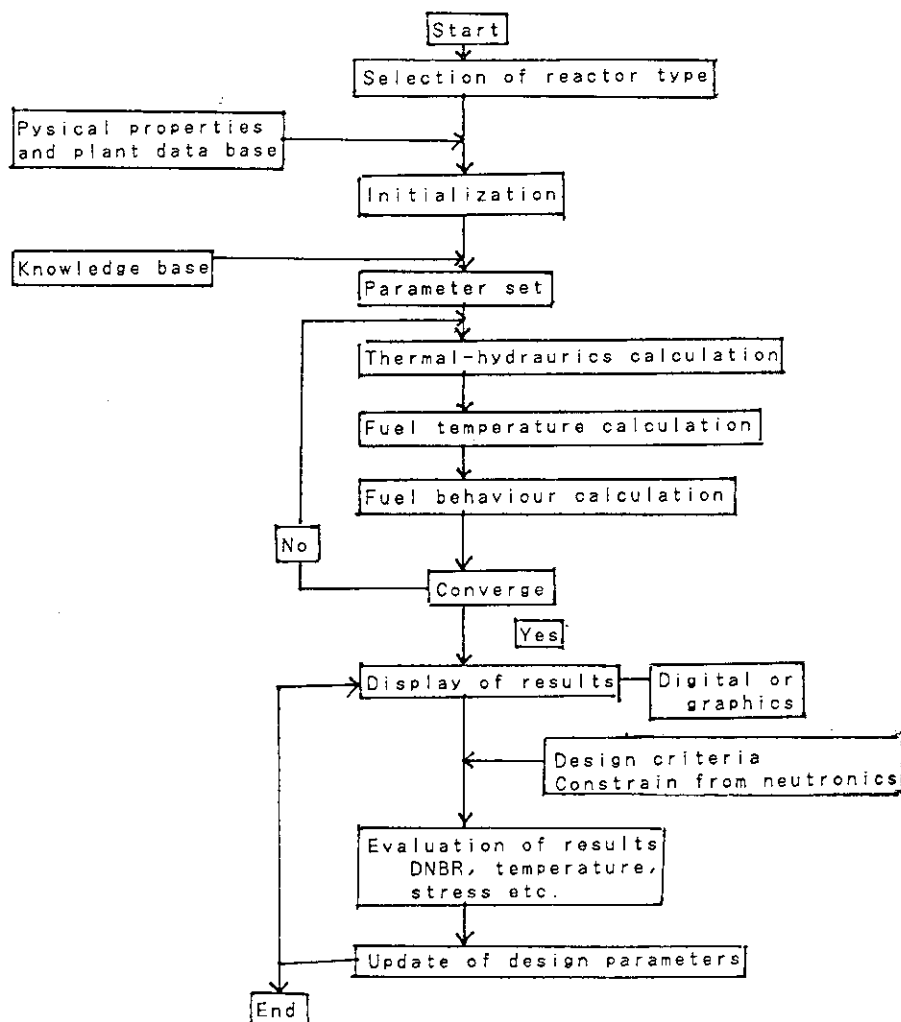


Fig. 2.6.3 Task flow of thermal-hydraulic and fuel behavior modules

## 2.7 THYDE-W: Reactor Coolant System Analysis Code

Y. Asahi

The computer code THYDE-W<sup>1)</sup> is an advanced version of THYDE-P2<sup>2)</sup>. It is applicable not only to transient analyses, but also to steady state analyses of reactor coolant system (RCS) of water reactors. Especially, THYDE-W is applicable to a large break loss-of-coolant accident (LB-LOCA), which can be considered to be the most critical for testing methods and models for plant dynamics, since thermal-hydraulic conditions in the system drastically change during the transient. Therefore, THYDE-W has intensively been applied to LOCA analyses to verify its methods and models.

There are three major problems in thermal-hydraulic analysis, which appear typically in an LB-LOCA. First of all, imbalance of mass or momentum or energy may result if improper space differencing is applied to the conservation equation. If space differencing is incorrect, mass imbalance in a LOCA analysis could be so large that a large amount of mass comparable to injected ECC water could "disappear" from the system. Secondly, even if the space differencing is correct, imbalance still could occur unless the equations thus spatially differenced are solved "exactly" by applying a non-linear implicit scheme. Thirdly, various mode transitions, e.g., coolant phase change may bring about numerical instabilities. These problems predominate especially at low pressure. This fact is the main reason why the secondary system of a PWR or the neighborhood of the turbine of a BWR, which is at low pressure already at a steady state, has not been adequately included in a transient analysis. In a LOCA analysis, in particular, to avoid numerical instability induced by condensation ("water packing") and to somehow continue a reflood calculation, it is customary either to raise the ECC water enthalpy or to neglect the time derivatives in the conservation equations. These assumptions are not only unconvincing, but also are likely to lead to erroneous conclusions.

The main features of THYDE-W are (1) the steady state adjustment, (2) the new thermal-hydraulic network model, (3) the non-linear implicit scheme for thermal-hydraulics, (4) the non-equilibrium models, (5) the automatic time step width control and (6) vectorization of the program:

(1) THYDE-W carries out steady state adjustment, which is complete in

the sense that the state obtained is the set of exact solutions to the null transient problem, i.e., the transient problem without an external disturbance. Originally, this capability was developed to obtain a well defined initial state from which a transient calculation by THYDE-W can start. From a different point of view, it provides THYDE-W with another capability, that is, what is called thermal-hydraulic design of RCSs.

- (2) A new representation of a control volume has made it possible to develop a new thermal-hydraulic network model, which well matches our physical intuitions. The model reduces the flow equations by three steps, each of which is closely related to topological features of the hydraulic network. The new model does not depend on specific forms for the conservation equations, but is quite general.
- (3) To solve the equations of a network "exactly", an iterative method which may be referred to as a non-linear implicit method is applied based on the new network model. Since a linear implicit method does not yield an "exact" solution, its applicability is questionable especially at low pressure when non-linearity of the flow equations predominates.
- (4) The non-linear implicit scheme for use in the thermal-hydraulic network requires continuity of all the parameters involved in the flow equations. Physically, this amounts to taking into consideration non-equilibrium effects arising from various mode transitions.
- (5) THYDE-W determines the time step width automatically as the calculation proceeds. The non-linear implicit method, the non-equilibrium model and the steady state adjustment are all combined to materialize the automatic time step width control of THYDE-W.

These features have enabled THYDE-W to perform a through calculation<sup>2)</sup> of LB-LOCAs without an artificial change of the method and models.

What is improved with THYDE-W as compared to THYDE-P2<sup>2)</sup> is; (1) analyses of a plural number of disjoint loops or nets are possible, (2) the control system simulation model is included, (3) the trip model is better, (4) heavy water as a coolant is allowed, (5) the effect of drift flux is accounted for in the steady state adjustment, (6) boron transport is included and (7) to obtain loop heat balance, the option of adjusting the enthalpy distribution is prepared in addition to that of adjusting heat exchanger areas.

References

- 1) Asahi Y., et al.: "THYDE-W: RCS (Reactor Coolant System) Analysis Code", JAERI-M 90-172, JAERI (1990).
- 2) Asahi Y., et al.: "THYDE-P2: RCS (Reactor Coolant System) Analysis Code", JAERI-1300, JAERI (1986).

### 3. Reactor Physics Experiment and Analysis

Activities on reactor physics experiment during the present period are mainly related to metallic fuel LMFBR and High Temperature Engineering Test Reactor (HTTR).

Benchmark physics experiments have been carried out at the FCA to investigate the nuclear characteristics of a metallic-fueled fast reactor. The experimental program consists of the two cores; a two-zone cylindrical clean core with mixed fuel of plutonium and enriched uranium (FCA XVI-1) and a partial mockup core with a central test region of plutonium fuel (FCA XVI-2). Emphases were placed on the measurement of physics parameters related to reactivity feedback and breeding performance. The experimental results were compared with the calculations based on the nuclear data file JENDL-2 and JAERI's standard calculation system for fast reactor neutronics.

Analysis has been made on the physics experiment of HCLWR core at FCA to establish "Data and Method" for the reactor physics calculation of the HCLWR or intermediate neutron energy core. Through this analysis with the nuclear data file JENDL-2, some discrepancies were found between the calculation and experiment. To explain these discrepancies and to examine the availability of the JENDL-3, the FCA-HCLWR data have been reanalyzed. Comparisons of the calculated results between JENDL-2 and JENDL-3 were made for the infinite multiplication factor, the reaction rate ratio and the sample reactivity worth.

In order to estimate the streaming effect of neutron through the holes of the control rod guide column in the HTTR core, the void reactivity worths of the control rod insertion holes of HTTR mockup control rod columns (CR block) were measured in the VHTRC-1 core by pulsed neutron source method (PNS). The experimental values were compared with the diffusion calculations with the Benoist's anisotropic diffusion coefficient as well as the conventional isotropic one for the mock up control rod column.

(Masafumi Nakano)



### 3.1 Benchmark Experiments for Metallic-Fueled LMFBR at FCA

S. Iijima, H. Oigawa, M. Bando<sup>\*</sup>, T. Nemoto, A. Ohno and T. Sakurai

The benchmark physics experiments of a metallic-fueled LMFBR are conducted on JAERI's Fast Critical Assembly (FCA) facility in order to test calculated predictions of physics parameters in a design of metallic-fueled core. Mockup cores with metallic fuel composition were built to measure the following physics parameters.

- 1) parameters related to reactivity feedback
  - Doppler reactivity worth
  - sodium void worth
  - control rod worth
  - fuel expansion and bowing reactivity worths
- 2) parameters related to breeding performance
  - reaction rate ratios.

In addition to these typical physics parameters of a metallic-fueled core the fundamental physics parameters were measured for criticality, material sample worths, reaction rate distributions.

The experiment in the FCA assembly XVI-1, which was the first core in the experimental program, was continued since October 1989 to November 1990. FCA assembly XVI-1 is a clean and cylindrical two-zone core and its core size is in a range of 100 ~ 150MWe metallic-fueled LMFBR. Because of inventory limit constrained plutonium, mixed fuel of plutonium and enriched uranium is used in the inner and outer core. Natural uranium metal plates are inserted in the fuel drawers. Plutonium and  $^{235}\text{U}$  enrichments are 10% and 5% in the inner core and 10% and 9% in the outer core. Zirconium is added at ~7 wt% in the fuel. The physics parameters related reactivity feedback were mainly measured in the assembly.

The analyses were made using the cross-section library JENDL-2 and JAERI's standard calculation system for fast reactor neutronics. The calculation system has been utilized in these ten years in the analyses of the oxide-fueled cores such as FCA assemblies and the ZPPR assemblies on the JUPITER program. On the other hand it was the first experience to examine calculation accuracy for a nuclear characteristics of a metallic-fueled core.

---

\* Hitach Ltd.

The large discrepancies between the experiment and calculation results were found on Doppler, sodium void and  $B_4C$  sample worths. Since these reactivity worths are spectrum-sensitive physics parameters, it is considered that the calculation mispredicts the neutron spectrum of the metallic-fueled core. Because the mispredictions bring uncertainty in a transient analysis of a metallic-fueled core, we investigate the calculation process and nuclear data to reduce the discrepancies.

Following the experiments of the assembly XVI-1, the experiment of assembly XVI-2 was started on November 1990. The assembly XVI-2 is a partial mockup core in which a test region fueled plutonium and natural uranium is surrounded radially by a driver region fueled enriched uranium. A breeding performance of metallic-fueled LMFBR are mainly investigated in the assembly. The reactivity feedback parameters which the calculation mispredicted their worths in assembly XVI-1 were measured in assembly XVI-2.

Table 3.1.1 Experimental program of benchmark test of metallic-fueled LMFBR at FCA

Assembly	Characteristics	Size	Typical Measurement	Period
XVI-1	two enriched zones, plutonium and enriched uranium mixed fuel	<u>diameter</u>	Doppler,	October,
		inner core	sodium void,	1989
		68.5 cm	control rod,	~
		outer core	sample worths,	November,
		90.9 cm	fuel expansion	1990
XVI-2	partial mockup test region fueled plutonium, driver region fueled enriched uranium	<u>height</u>	and bowing	
		91.4 cm	reactivity	
		<u>diameter</u>	reaction	December,
		test region	rate ratios,	1990
		68.5 cm	Doppler,	~
		driver	sodium void,	(October,)
		93.4 cm	control rod,	(1991 )
		<u>height</u>	sample worths	
		91.4 cm		

## 3.2 Reactivity Worth Measurements in Metallic-Fueled Core FCA XVI-1

S. Iijima, H. Oigawa and M. Bando\*

The fundamental physics parameters of a metallic-fueled LMFBR were measured for criticality, material sample worths and sodium void worth in FCA assembly XVI-1.

The critical state of a FCA assembly is determined very precisely (approximately  $\pm 0.0003\%$ ). For convenience in calculation modeling, reactivity was adjusted to the worth of the parked control rods and to a reference temperature of 300K. The correction factors estimated by experiments were applied to cover uncertainties not easily modeled in calculation, i.e. subcriticality caused by  $^{240}\text{Pu}$  spontaneous fission, interface gap, and presence of stainless steel structure at assembly midplane. The experimental value of  $k_{\text{eff}}$  is  $1.0038 \pm 0.0001$ .

The analyses were made using the JAERI's standard calculation system for fast reactor neutronics and JFS-3-J2 group constant set with 70 energy structure. The  $k_{\text{eff}}$  was calculated by anisotropic diffusion theory in xyz geometry. The anisotropic diffusion coefficient was derived using Benoist's formula. The transport correction, which was obtained from 25 energy groups transport and diffusion calculations in rz geometry, was applied to the result. The C/E of  $k_{\text{eff}}$  is 1.0018.

The material sample worths were measured by using two type samples of plate and cylindrical shape. The plate sample worths for following materials were measured by substitution method at the center of the assembly;

- 1) Pu(92) (principal element  $^{239}\text{Pu}$ ), EU(93) (93% enrichment), EU(20) and natural U
- 2) SUS, Zr, Mo
- 3)  $\text{B}_4\text{C}$  (20, 40, 60, 90%  $^{10}\text{B}$  enrichment).

The reactivity worths using the cylindrical samples of  $^{235}\text{U}$ ,  $^{239}\text{Pu}$  and  $^{240}\text{Pu}$  were measured by sample oscillation method.

In addition to the central reactivity worth measurements, an axial and radial distributions of Pu(92) sample worths were measured as backup data for an investigation of fuel expansion and bowing reactivity effects.

The axial distribution of sodium void worth was measured using the

---

\* Hitachi Ltd.

central 3×3 drawers (9.32cm in equivalent radius) of the test zone, applying the same method as for material sample worth. The nine unit cells -each containing 509.0g Na- were voided one by one from position 1Z to 9Z along the center axis, and the resulting change of reactivity was measured at each voiding.

The material sample worths and sodium void worth were calculated by first order perturbation method based on diffusion theory. The transport corrections were applied to the results. The typical C/E values for the reactivity worths are shown in Table 3.2.1.

Table 3.2.1 Results of reactivity worth in assembly XVI-1

	<u>Calculation/Experiment(C/E)</u>	
	Assembly XVI-1	Conventional Oxide Core
Sodium void worth	1.29	~ 1.10
B <sub>4</sub> C sample worth	0.86	~ 1.00

### 3.3 Reaction Rate Measurements in Metallic-Fueled Core FCA XVI-1

T. Sakurai, T. Nemoto, S. Iijima and K. Hayasaka

Reaction rates have been measured in FCA assembly XVI-1<sup>1)</sup> to test the reliability of calculation in a core design of metallic-fueled LMFBR. The cell-averaged reaction rate ratios at the core center together with radial and axial reaction rate distributions in the core were measured for  $^{239}\text{Pu}(\text{F}^{49})$ ,  $^{235}\text{U}(\text{F}^{25})$  and  $^{238}\text{U}(\text{F}^{28})$  fission, and for  $^{238}\text{U}$  capture ( $\text{C}^{28}$ ).

The measurements were made by using thin metallic enriched and depleted uranium foils and plutonium foils covered with aluminum. The foil activities after irradiation were determined by a high-resolution gamma-ray spectroscopy system composed of a coaxial type Ge-detector, multichannel analyzer and a 32 K byte mini-computer<sup>2)</sup>.

The fission rate ratios ( $\text{F}^{25}/\text{F}^{49}$  and  $\text{F}^{28}/\text{F}^{49}$ ) were determined from the fission product activities of  $^{143}\text{Ce}$ (293 keV),  $^{133}\text{I}$ (529 keV),  $^{97}\text{Nb}$ (658 keV) and  $^{97}\text{Zr}$ (743 keV). The capture to fission rate ratio ( $\text{C}^{28}/\text{F}^{49}$ ) was determined from these fission product activities and activity of  $^{239}\text{Np}$ (277 keV). The fission rate distributions were determined by measuring the total fission product activity above 600 keV, while the distribution of  $^{238}\text{U}$  capture rate was determined from activity of  $^{239}\text{Np}$ (106 keV and 277 keV).

The reaction rate data must be corrected for cell heterogeneity effects to derive cell-averaged reaction rates. This correction was made experimentally by means of intracell foil measurements for each reaction at typical positions in the core.

The calculations of reaction rates were made by using JFS-3-J2 cross section set<sup>3)</sup> and JAERI's standard calculation system for a nuclear characteristics of a fast reactor<sup>1)</sup>. The reference calculations were made in the X-Y-Z geometry with the 25-group anisotropic diffusion theory and transport corrections were applied to the results.

The measured cell-averaged reaction rate ratios at the core center are summarized in Table 3.3.1, together with calculated results. The calculated value agrees with the experimental value for  $\text{F}^{25}/\text{F}^{49}$ . On the other hand, the calculation overpredicts the experimental values of  $\text{F}^{28}/\text{F}^{49}$  and  $\text{C}^{28}/\text{F}^{49}$  by 5 and 6%, respectively.

The C/E values for radial and axial reaction rate distributions are

shown in Fig. 3.3.1 and Fig. 3.3.2. In these figures, the distributions of C/E values are normalized to unity at the core center. For radial distributions, the calculated values agree well with the experimental value within 3%, except two values which are shown in  $F^{28}$  and  $C^{28}$  distributions. For axial distributions, the calculated values agree well with the experimental values of  $C^{28}$  within 2%. On the other hand, the calculation underpredicts the experimental values of  $F^{49}$  and  $F^{25}$  by about 5% in the neighborhood of boundary between core and axial blanket. The C/E values of  $F^{28}$  axial distribution take almost constant values of about 0.97.

#### References

- 1) Iijima S., et al.: "Reactor Engineering Department Annual Report", JAERI-M 90-149, 46 (1990).
- 2) Koakutsu T. and Obu M.: "Data Processing Code System for Foil Experiments", JAERI-M 84-147 (1984) (in Japanese).
- 3) Takano H., et al.: "Production and Benchmark Tests of Fast Reactor Group Constants Set JFS-3-J2", JAERI-M 82-135 (1982) (in Japanese).

Table 3.3.1 Cell-averaged reaction rate ratios  
at the center of FCA XVI-1 core

	Expt.	Calc.	C/E
$F^{25}/F^{49}$	$0.933 \pm 3.1\%$	0.917	0.983
$F^{28}/F^{49}$	$0.0290 \pm 3.7\%$	0.0303	1.045
$C^{28}/F^{49}$	$0.1040 \pm 3.7\%$	0.1107	1.064

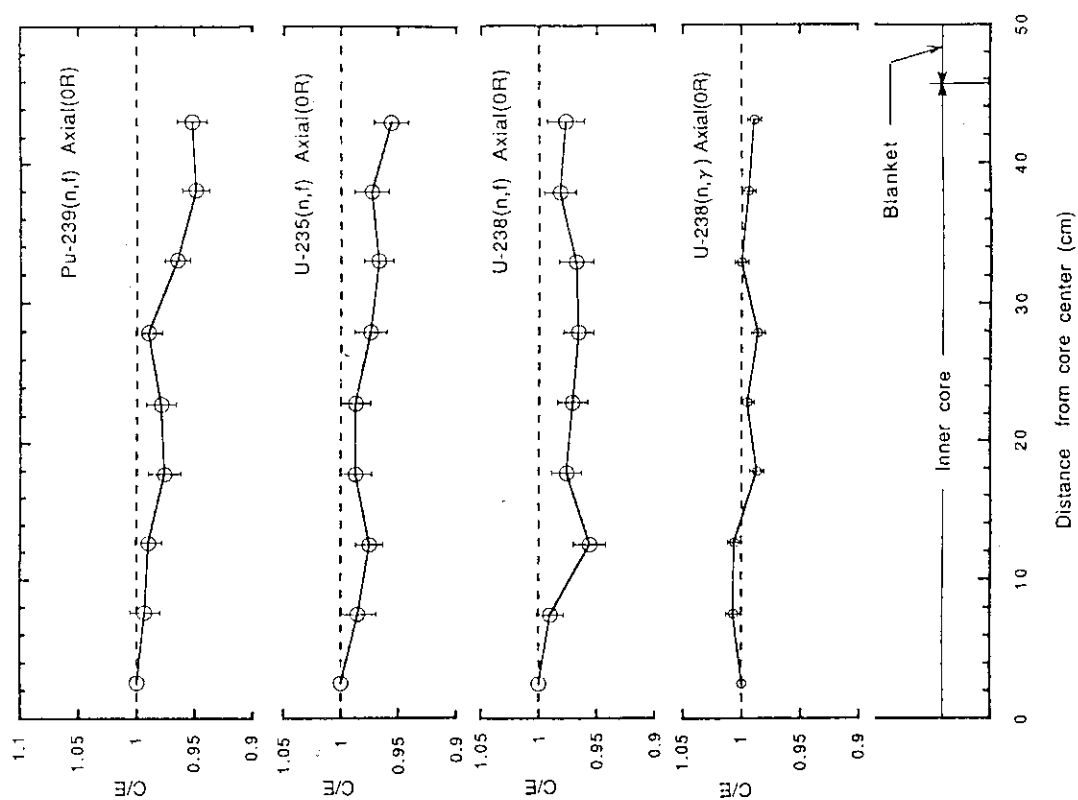


Fig. 3.3.2 C/E values of axial reaction rate distribution at OR in FCA XVI-1 core

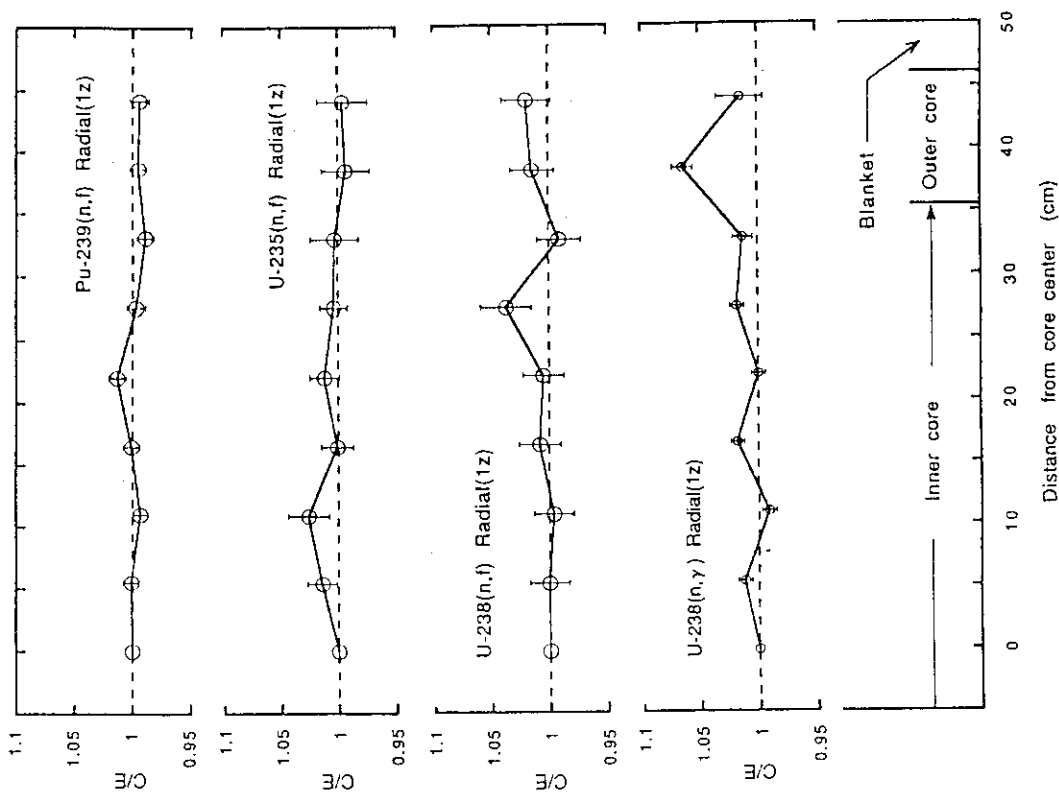


Fig. 3.3.1 C/E values of radial reaction rate distribution at lz in FCA XVI-1 core

## 3.4 Doppler Worth Measurement in Metallic-Fueled Core FCA XVI-1

H. Oigawa, K. Satoh, M. Nakano and T. Mukaiyama

Doppler effect of  $^{238}\text{U}$  is one of the most important negative feedback in fast reactors. Although Doppler reactivity worth had been measured in various oxide-fueled cores at FCA, it had not been done in metallic-fueled core which has particularly had neutron spectrum for lack of oxygen. Hence, Doppler reactivity worth of  $^{238}\text{U}$  was measured in metallic-fueled core FCA XVI-1 using the small sample oscillation technique<sup>1)</sup> to investigate the applicability of calculation method developed for oxide-fueled fast reactors to metallic-fueled ones.

Samples used in the measurement were natural uranium oxide ( $25\text{ mm}^\phi \times 150\text{ mm}^L$ , U: 605 g) and natural uranium metal ( $25\text{ mm}^\phi \times 150\text{ mm}^L$ , U: 1347 g). Reactivity change caused by the sample temperature change from  $20^\circ\text{C}$  was measured for  $300^\circ\text{C}$ ,  $550^\circ\text{C}$  and  $800^\circ\text{C}$ . The experimental results are shown in Fig. 3.4.1, where the experimental error was evaluated by the scatter of several measurements. Doppler reactivity worth increases with the sample temperature, and that of the metal sample, which contains twice of  $^{238}\text{U}$  than oxide one, is about twice larger than that of oxide.

Doppler reactivity worth was calculated based on first order perturbation theory using 70 groups diffusion calculation in two dimensional rz model. Temperature dependent effective cross sections of the sample region were generated by cell calculation code SLAROM<sup>2)</sup> and 70 groups cross section set JFS-3-J2<sup>3)</sup>, where calculational model was heterogeneous cylindrical one composed of three regions: sample, sample container and homogenized core. In this case, resonance self-shielding factors of  $^{238}\text{U}$  in the sample were determined considering only self-shielding effect of the sample itself in spite of  $^{238}\text{U}$  in the core region.

Table 3.4.1 shows the calculated and the experimental results. The calculation gives much smaller Doppler reactivity worth than the experiment, i.e., calculated to experimental (C/E) values are about 0.6, though the experimental sample worth was well predicted by the calculation. On the other hand, C/E values of Doppler reactivity worth at oxide-fueled FCA cores had been in the range of 0.85~0.99<sup>4)</sup>. The causes of the small C/E values in FCA XVI-1 core were investigated by putting the focus on following two factors: 1) Influence of neglecting Doppler effect above 40.9 keV where JFS-3-J2 has no self-shielding factor table of  $^{238}\text{U}$ . 2)



influence of  $^{238}\text{U}$  in the core region to the self-shielding effect of the sample.

The first factor is important in the hard neutron spectrum of metallic-fueled fast reactors. The contribution of high energy neutron above 40.9 keV to Doppler reactivity worth was estimated to be about ten odd percent by using ENDF/B-VI<sup>5)</sup> which has the resonance parameters of  $^{238}\text{U}$  up to 149 keV. The second factor is also considered to be important because atom density of  $^{238}\text{U}$  in metallic-fuel is larger than that in oxide one. The existence of  $^{238}\text{U}$  in the core region was estimated to make Doppler reactivity worth large at several percent, assuming that the core region was composed by the cylindrical fuel rods which have the same dimension and composition as the sample. Considering these two factors, therefore, the small C/E values become better by about 20%, but they are still 0.7~0.8. Hence, further study must be carried out for the validity of calculated neutron spectrum.

#### References

- 1) Yasuno T., et al.: "Doppler Coefficient Measurements in FCA", J. Nucl. Sci. Technol., 7, 271 (1970).
- 2) Nakagawa M. and Tsuchihashi K.: "SLAROM", JAERI-1294 (1984).
- 3) Takano H. and Ishiguro Y.: "Production and Benchmark Tests of Fast Reactor Group Constant Set JFS-3-J2", JAERI-M 82-135 (1982).
- 4) Mukaiyama T. and Okajima S.: "Neutron Spectrum Dependence of Natural  $\text{UO}_2$  Doppler Effect Measured in FCA", J. Nucl. Sci. Technol., 22, 243 (1985).
- 5) ENDF/B-VI(1990). File for  $^{238}\text{U}$ (MAT=9237) evaluated by Weston L.W., et al..

Table 3.4.1 Comparison of experimental and calculated Doppler reactivity worth in FCA XVI-1

Sample	T(°C)	Experiment( $10^{-6} \Delta K/K$ )	Calculation( $10^{-6} \Delta K/K$ )	C/E
NUO <sub>2</sub> -25 $\phi$	20	$-91.7 \pm 2.2$	-83.62	0.91
(U:605g)	20-300	$-1.96 \pm 0.20$	-1.267	0.65
	20-550	$-3.18 \pm 0.18$	-1.978	0.62
	20-800	$-4.35 \pm 0.18$	-2.490	0.57
NU-25 $\phi$	20	$-154.5 \pm 2.2$	-149.59	0.97
(U:1347g)	20-300	$-4.65 \pm 0.20$	-3.060	0.66
	20-550	$-7.42 \pm 0.21$	-4.769	0.64
	20-800	$-9.64 \pm 0.19$	-5.995	0.62

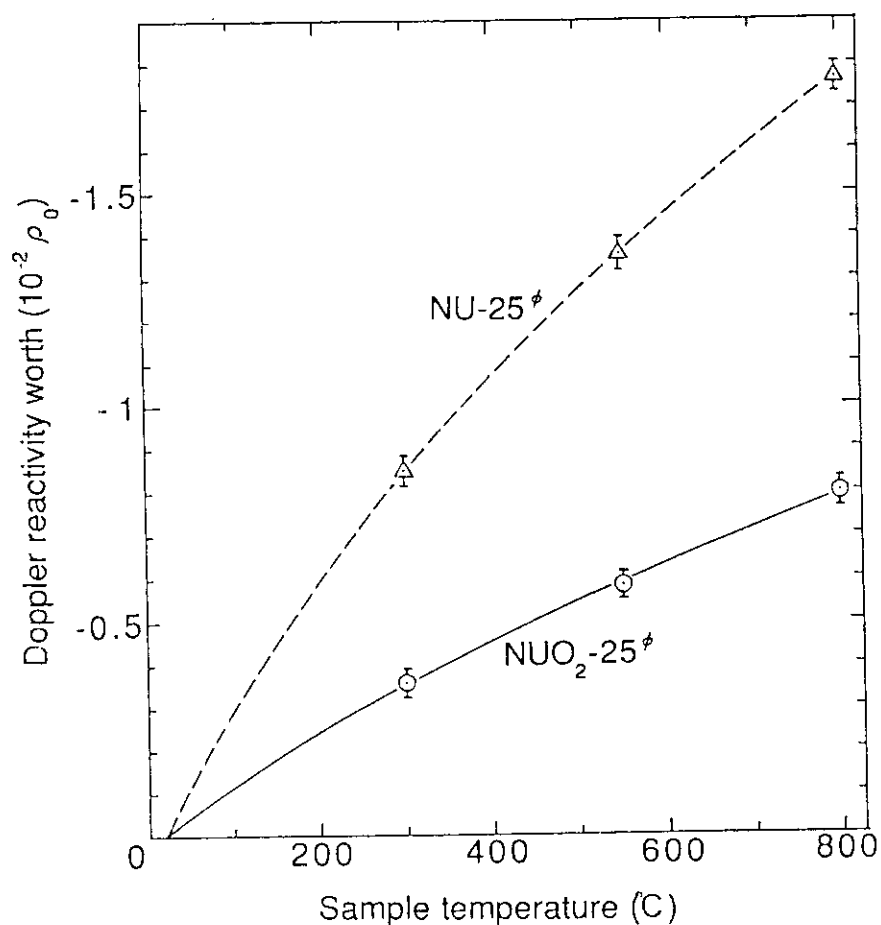


Fig. 3.4.1 Doppler reactivity worth measured in FCA XVI-1  
 $(1\rho_0 = 5.46 \times 10^{-4} \Delta K/K)$

### 3.5 Control Rod Reactivity Worth Measurement in Metallic-Fueled Core FCA XVI-1

A. Ohno, T. Osugi, M. Bando<sup>\*</sup>, H. Sodeyama and Nakano

Reactivity worth of simulated B<sub>4</sub>C control rods was measured at three different radial positions (0R, 3R and 6R) in the inner core of the metallic-fueled core FCA XVI-1 to evaluate the current analysis method. To study the dependence of the reactivity worth on <sup>10</sup>B enrichment of the control rod, measurements were also done on reactivity worth of control rods using B<sub>4</sub>C plates with different <sup>10</sup>B content (20, 40, 60 and 90%). Figure 3.5.1 shows array of B<sub>4</sub>C and sodium plates used in the simulated control rod. The control rod was loaded to the half of the core, and the rest was filled with sodium channel.

Reactivity worth of the control rod was measured by the modified source multiplication method<sup>1)</sup> and was defined as reactivity difference in substitution of the control rod by a sodium channel. Due to the insertion of the control rod into the core, a change in effective detection efficiency of each detector, placed in the core or at the core periphery, was corrected by correction factors obtained from two dimensional X-Y eigen-value and fixed source diffusion calculations.

Base calculation for reactivity worth of the control rod is three dimensional X-Y-Z and 6-group diffusion calculation with direction dependent diffusion coefficients. Effective 6-group cross sections were obtained by collapsing 70 energy-group cross section weighing with flux calculated in two dimensional RZ calculation. Effective 70-group cross section of both the control rod cell and the sodium channel cell were calculated in one dimensional super cell model of which each cell has a homogeneous fuel region of 20cm thick on either side. From diffusion calculation, reactivity worth of the control rod is calculated to make direct comparison with the measured value,

$$\Delta\rho = \frac{k(B_4C) - k(Na)}{k(Na) k(B_4C)} \cdot$$

Corrections for the transport and the energy collapsing effect were applied to the base calculations. Correction factors for transport

---

<sup>\*</sup> Hitachi Ltd.

effect are small ( $\sim 2\%$ ) at the core center (0R), while it becomes large ( $\sim 7\%$ ) at the boundary (6R) of the inner core. Correction factors for energy collapsing effect are about 3%. No dependence of  $^{10}\text{B}$  enrichment on both correction factors is found in the present calculation.

Measured and calculated results are shown in Fig. 5.3.2. The present calculation underestimates largely the measured values, and the C/E value is about 0.85. Dependence of C/E values of  $^{10}\text{B}$  enrichment is not seen in this analysis. The C/E values are almost constant for three different radial positions. This trend can be understood in Fig. 5.3.3, showing radial distributions of  $\text{B}_4\text{C}$  sample worth and adjoint flux  $\phi^*$  which is obtained as ratio of  $\text{B}_4\text{C}$  sample worth and  $^{10}\text{B}$  capture rate measured with a  $\text{BF}_3$  counter. Calculated distribution of  $\text{B}_4\text{C}$  sample worth and adjoint flux are also shown in Fig. 5.3.3. Both distributions agree well with measured ones. Further study is necessary to make clear the large discrepancy between measured and calculated control rod reactivity worths.

#### Reference

- 1) Mizoo N.: JAERI-M 7753 (1978).

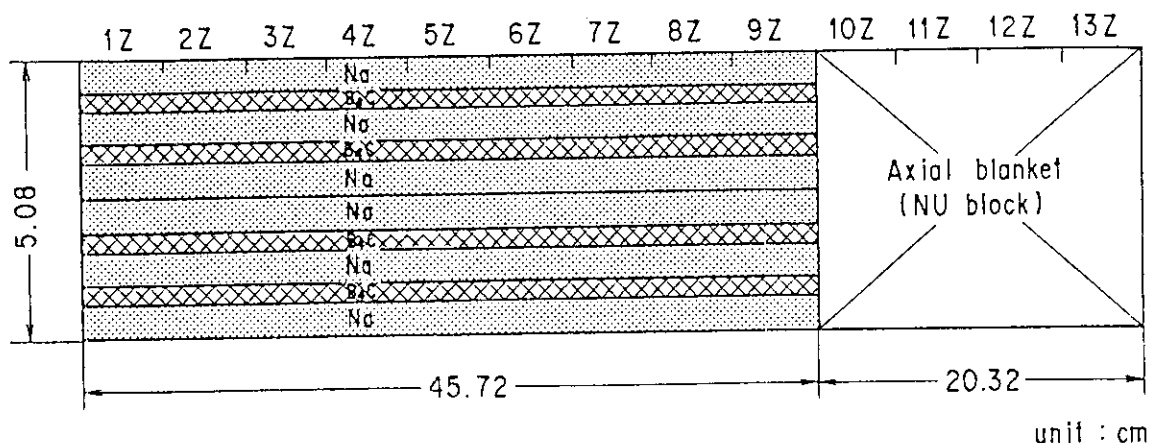


Fig. 3.5.1 Array of  $\text{B}_4\text{C}$  and sodium plate in control rod

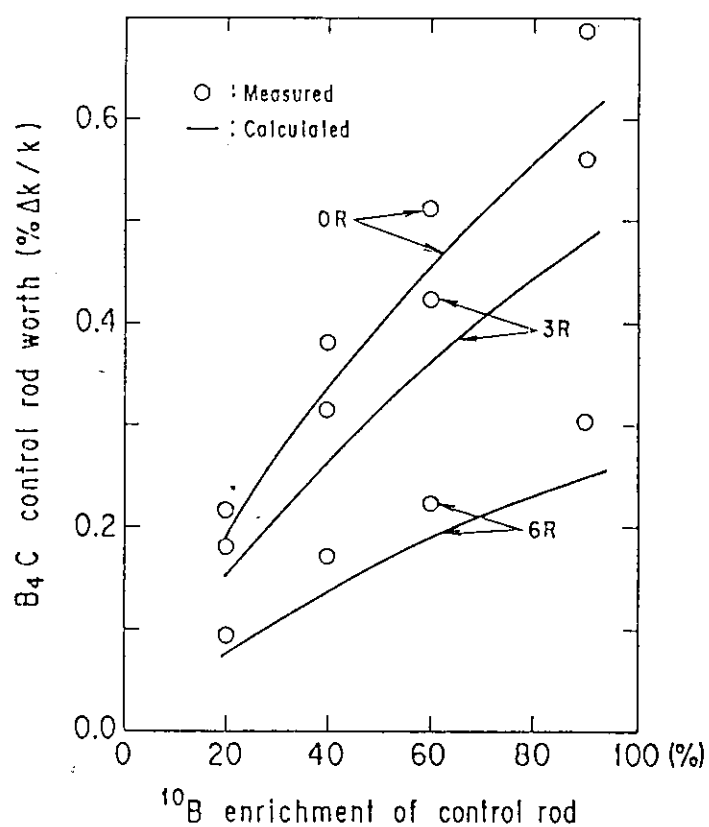


Fig. 3.5.2 Measured and calculated reactivity worth of control rod as parameter of control rod position

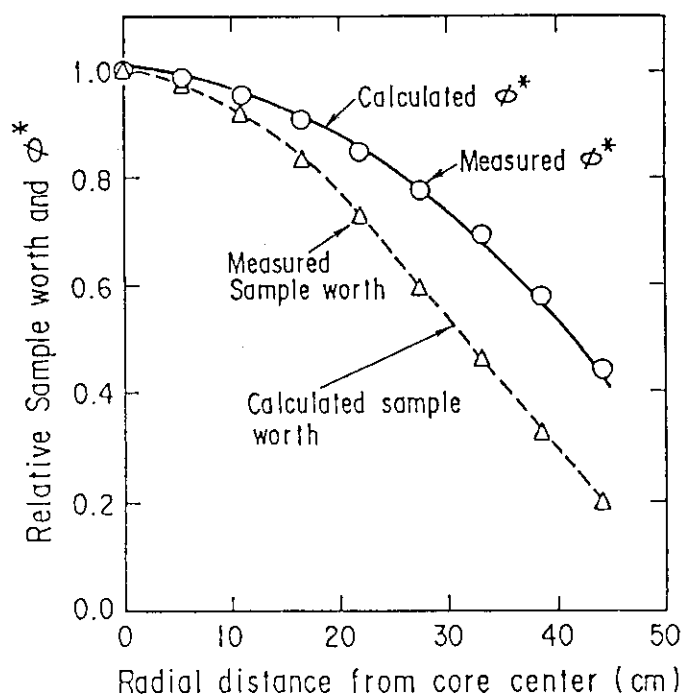


Fig. 3.5.3 Measured and calculated sample worth and adjoint flux  $\phi^*$

### 3.6 Fuel Expansion and Displacement Worth Measurement in Metallic-Fueled Core FCA XVI-1

H. Oigawa, M. Bando\* and S. Iijima

Reactivity effects caused by axial fuel expansion or radial fuel displacement due to fuel temperature rise are expected as important negative reactivity feedback in safety analysis of fast reactors. However, only a few experimental studies had been carried out for these effects. Hence, reactivity worths of fuel expansion and displacement were measured for the first time at FCA to examine the calculational accuracy.

Axial fuel expansion is supposed to be about 1% for the temperature rise of several hundreds kelvin. Since it is difficult to simulate such a little expansion in FCA, 3% and 6% expansion was simulated by inserting zirconium plates between FCA cells as shown in Fig. 3.6.1(a), and linearity between 3% and 6% expansion was investigated. Further, to investigate the expansion area dependency, the axial expansion were simulated in 1, 5, 9, and 25 drawers at the core center of FCA.

On the other hand, radial fuel displacement in power reactors is supposed to be several millimeters but to be very complicated and largely dependent upon the core design because of the interaction of individual assembly bowing, core support expansion and so on. Hence, to evaluate the position dependency of calculational accuracy, reactivity worths of 3 mm and 6 mm fuel shifting were measured at various positions of core edge: 6R, 7R and 8R, where 6R indicates the outer most position of the inner core, and 7R and 8R compose the outer core. To simulate the fuel shifting in FCA drawer, special plate arrangement with voided aluminum plates of 3 mm in thickness were prepared, and one or two aluminum plates were replaced from one side of the drawer to the other side as shown in Fig. 3.6.1(b).

The reactivity worths of axial fuel expansion and radial fuel displacement were calculated based on first order perturbation theory using 25 groups diffusion calculation in three dimensional xyz model.

The experimental and calculated results are shown in Table 3.6.1 for axial fuel expansion and Table 3.6.2 for radial fuel displacement. For axial fuel expansion, reactivity worth of 6% expansion is twice as large

---

\* Hitachi Ltd.

as that of 3%, hence the linearity between 3% and 6% expansion is achieved. The first order perturbation theory, however, gives large C/E values, which increase with extending the expansion area (1.14 - 1.27). In Table 3.6.1, the calculated results by exact perturbation theory are also shown with worth component of core and blanket region. Exact perturbation theory gives comparatively good C/E values (about 1.05), where most of the difference between two methods is caused at the blanket region. This is because the blanket region, composed of natural metal uranium block, was replaced with core material by the expansion, and neutron flux is largely changed before and after the expansion.

For radial fuel displacement, the results at 8R show that the reactivity worth is proportional to the distance of shifting. Moreover, additivity of the worth is proved by the comparison between summation of individual reactivity worths at 6, 7, 8R and reactivity worth of simultaneous shifting for 6~8R. These two factors, linearity and additivity, suggest that the first order perturbation theory is applicable to the calculation of radial fuel displacement worth in the range of displacement area measured here. However, C/E values tend to vary with the position: 1.11, 1.07 and 0.98 for 6 mm shifting at 6, 7 and 8R, respectively. This tendency is considered to be caused by misprediction of the neutron flux and adjoint flux distribution by diffusion theory. Therefore, further study using transport theory is considered necessary.

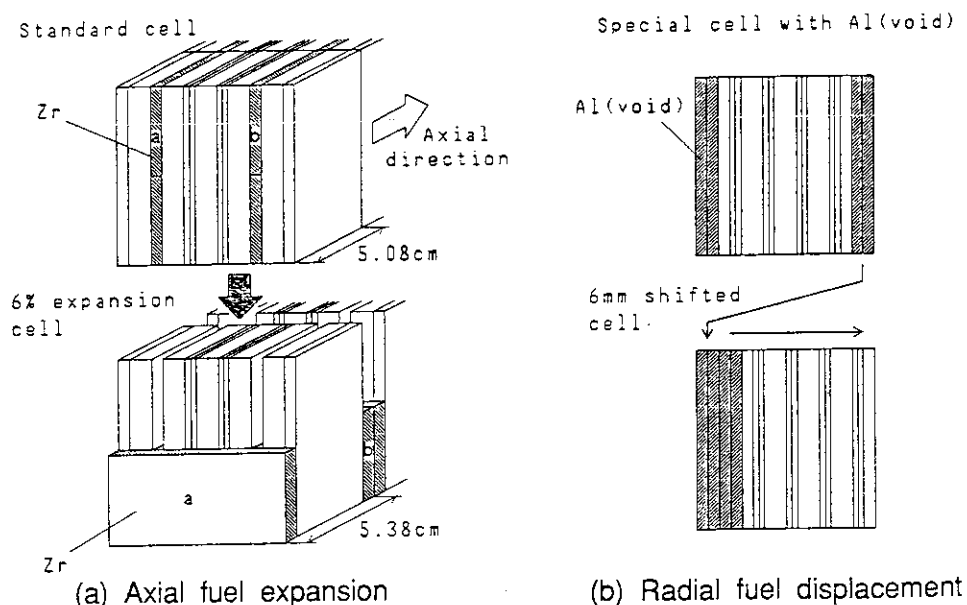


Fig. 3.6.1 Experimental method to simulate axial fuel expansion (a) and radial fuel displacement (b)

Table 3.6.1 Results of axial fuel expansion worth

Expansion percentage	No. of drawers	Experiment ( $10^{-4}\Delta K/K$ )	Calculation( $10^{-4}\Delta K/K$ )				C/E
			Method	Core	Blanket	Total	
3 %	9	$-2.41\pm 0.02$	FOP <sup>a)</sup>	-3.73	0.81	-2.93	1.21
			Exact <sup>b)</sup>	-3.72	1.11	-2.61	1.08
6 %	1	$-0.60\pm 0.02$	FOP	-0.82	0.14	-0.68	1.14
			Exact	-0.82	0.21	-0.61	1.03
	5	$-2.76\pm 0.02$	FOP	-4.07	0.70	-3.37	1.22
			Exact	-4.05	1.13	-2.93	1.06
	9	$-4.85\pm 0.02$	FOP	-7.28	1.25	-6.02	1.24
			Exact	-7.23	2.12	-5.11	1.05
	25	$-12.77\pm 0.02$	FOP	-19.50	3.27	-16.23	1.27
			Exact	-19.40	5.98	-13.42	1.05

a) First order perturbation theory    b) Exact perturbation theory

Table 3.6.2 Results of radial fuel displacement worth

Shifting distance <sup>a)</sup>	No. of drawers	Position	Experiment ( $10^{-4}\Delta K/K$ )	Calculation ( $10^{-4}\Delta K/K$ )	C/E
(A) Linearity					
6 mm	6	8R	$-1.67 \pm 0.02$	-1.63	0.98
3 mm	6	8R	$-0.79 \pm 0.02$	-0.80	1.01
-3 mm	6	8R	$0.76 \pm 0.02$	0.78	1.02
-6 mm	6	8R	$1.54 \pm 0.02$	1.53	1.00
(B) Position dependency					
6 mm	6	6R	$-1.15 \pm 0.02$	-1.27	1.11
6 mm	6	7R	$-1.40 \pm 0.02$	-1.50	1.07
6 mm	6	8R	$-1.67 \pm 0.02$	-1.63	0.98
(C) Additivity					
6 mm	18	6~8R	$-4.31 \pm 0.02$	-4.40	1.02
6 mm	summation of 6, 7, 8R		$-4.21 \pm 0.03$	-4.40	1.05

a) Minus distance indicates radially inner direction



## 3.7 Analysis on FCA-HCLWR Core Using JENDL-3

T. Osugi and M. Nagatani\*

Analysis on FCA-HCLWR core<sup>1)</sup> has been made to establish "DATA & METHOD" for the reactor physics calculation of the HCLWR or intermediate neutron energy core. Through this analysis with the Japanese Evaluated Nuclear Data Library, Version-2 (JENDL-2)<sup>2)</sup>, we found some discrepancies between the calculation and experiment. To explain these discrepancies and to examine the availability of the JENDL-3<sup>3)</sup>, the FCA-HCLWR data have been reanalyzed<sup>4)</sup>.

Comparisons of the calculated results between JENDL-2 and JENDL-3 are made for the infinite multiplication factor, the reaction rate ratio and the sample reactivity worth. Analysis was made by using the SRAC code system<sup>5)</sup> and SRACLIB-JENDL3<sup>6)</sup>.

Figure 3.7.1 shows the difference in infinite multiplication factor ( $K_{\infty}$ ) calculated by JENDL-2 and JENDL-3 as a function of atomic number ratio of hydrogen to heavy metal (H/HM). For the uranium cells (EU05 and EU06A cells), the JENDL-3 gives larger  $K_{\infty}$  values than the JENDL-2 does in the normal moderator voidage states (H/HM = 2.0 for EU05 cell and H/HM = 1.2 for EU06A cell), and smaller  $K_{\infty}$  values in higher voidage states. The  $k_{\infty}$  values calculated by JENDL-3 are larger than those by JENDL-2 for the plutonium cells (Pu08 cell). These differences increase with decreasing H/HM value (increasing moderator void ratio of the cell or hardening neutron spectrum).

The discrepancies in C/E values between uranium and plutonium cells enlarge to about 2% in the case of JENDL-3.

The JENDL-3 gives larger  $F^{28}/F^{25}$  or  $C^{28}/F^{25}$  values than the JENDL-2 does from 3.6% to 7.2% or from 0% to 1.4%, respectively, depending on the neutron spectrum as shown in Fig. 3.7.2. Differences in  $C^{28}/F^{49}$  values calculated by JENDL-2 and JENDL-3 are also shown in Fig. 3.7.2.

There are not much differences in calculated worth ratios of  $B_4C/Pu$  between JENDL-2 and JENDL-3 as shown in Fig. 3.7.3. The JENDL-3 gives larger worth ratios of  $Hf/Pu$  than the JENDL-2 does from 8% to 14% depending on the neutron spectrum. Underpredictions of  $Hf/Pu$  worth ratio by the JENDL-2 calculation are much improved in the case of JENDL-3. The

---

\* I.S.L. Inc., Tokyo

test calculation, in which the Hf cross-section of JENDL-3 are replaced with that of JENDL-2, shows that this improvement is not due to the Hf cross-section itself but due to the hard neutron spectrum of JENDL-3.

#### References

- 1) Osugi T., et al.: in Proc. of International Conference on the Physics of Reactors: Operation, Design and Computation, Marseille, France, Apr. 23-27, 1990, Vol.3, PI-93 (1990).
- 2) Nakagawa T. (Ed.): JAERI-M 84-103 (1984).
- 3) Shibata K., et al.: JAERI 1319 (1990).
- 4) Osugi T., et al.: 1990 Annual Meeting of the Atomic Energy Society of Japan, B34 (1990).
- 5) Tsuchihashi K., et al.: JAERI 1302 (1986).
- 6) Takano H., et al.: Private communication (1990).

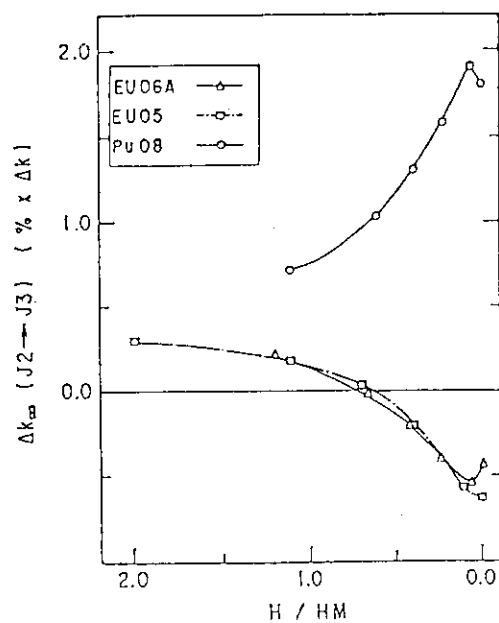


Fig. 3.7.1 Difference in infinite multiplication factors calculated by JENDL-2 and JENDL-3

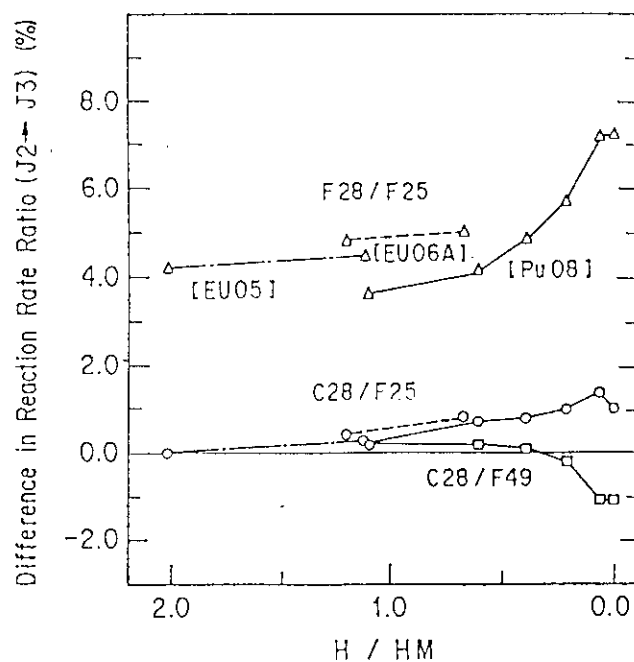


Fig. 3.7.2 Relative difference in reaction rate ratios calculated by JENDL-2 and JENDL-3

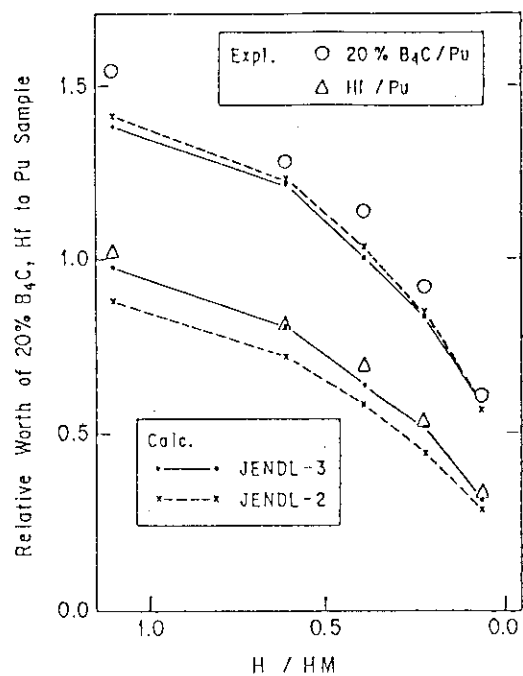


Fig. 3.7.3 Comparison between the experimental and calculated worth ratios of 20%B<sub>4</sub>C/Pu or Hf/Pu

### 3.8 Measurement of the Void Reactivity Worth of HTTR Mockup Control Rod Holes in the VHTRC-1 Core

F. Akino, M. Takeuchi, T. Ono and Y. Kaneko

In order to estimate the streaming effect of neutrons through the holes of the control rod guide column in the HTTR core, the void reactivity worths of the control rod insertion holes of HTTR mockup control rod columns (CR blocks) were measured in the VHTRC-1 core by the pulsed neutron source method (PNS).

The VHTRC-1 core<sup>1)</sup> was made by loading fuel rods, each containing 20 fuel compacts of the 4wt% enriched uranium. The core had radial and axial reflectors. The VHTRC-1 core reached criticality with 282 fuel rods at the room temperature.

The target of PNS was placed at the back-surface of the fixed half and along the core axis. Four BF<sub>3</sub> counter of 8 mm diameter were inserted into counter holes of 11 mm in diameter, made in the graphite rods. Two of the counters were placed in the fixed half and the other two in the movable half. The positions of these counters were 40 cm apart from the midplane splitting the movable and fixed half assemblies. The arrangement of PNS experiment is shown in Fig. 3.8.1.

The reference core for PNS experiment was loaded with 276 fuel rods and four BF<sub>3</sub> counters. After the measurement of prompt neutron decay constant,  $\alpha_0$ , of the reference core, the void reactivity worths of control rod insertion holes of CR blocks were measured for following voided core patterns:

- 2CV: The 2CV core was constructed from the reference core by making two void holes in the central column.
- 3CV: The 3CV core was constructed from the reference core by making three void holes in the central column.
- 2RV: The 2RV core was constructed from the reference core by making two void holes in the reflector column.
- 12RV: The 12RV core was constructed from the reference core by making 12 void holes in the reflector columns. Two void holes were located in each of 6 reflector columns.
- 18RV: The 18RV core was constructed from the reference core by making 18 void holes in the reflector columns. Three void holes were located in each of 6 reflector columns.

The arrangement of void holes in the 2CV core pattern is shown in Fig. 3.8.1. Each of void holes was made by removing the graphite rod in the control rod insertion hole in the CR block. The size of the void hole was 10.2 cm in the diameter and 240 cm long and the condition of void hole was only air at the 1-atmospheric pressure.

To determine the prompt neutron decay constant,  $\alpha$ , the raw data were fitted to an exponential function with a computer code ALPHA-D<sup>2)</sup>. The void reactivity worth was determined by the revised King-Simmon's formula ( $\rho_{RKS}$ )<sup>3)</sup> which was corrected for the change of the generation time due to the change with voided core pattern. The neutron generation time ( $\Lambda$ ) and the effective delayed neutron fraction ( $\beta_{eff}$ ) were obtained for each core pattern by using the three dimensional diffusion calculation. The measured values of the void reactivity worths of voided core patterns are listed in Table 3.8.1, together with the calculated values.

An analysis was made by using the SRAC code system<sup>4)</sup> with the ENDF/B-IV nuclear data library. The double heterogeneity of the fuel rod and the coated particles were taken into account in the cell calculation by the collision probability. On the other hand, in the case of CR block with the void holes, the collision probability method was applied to the cell calculation. The diffusion coefficient was calculated in two methods; Benoist's formula<sup>5)</sup> for considering the anisotropy of neutron diffusion in axial and radial directions, and the conventional averaged transport cross section ( $D_0 = 1/3\bar{\Sigma}_{tr}$ ).

The thermal neutrons in the energy region from 0.0 eV to 1.1254 eV were divided into 39 groups and the fast neutrons in the energy region from 1.1254 eV to 10 MeV were divided into 22 groups. Using the neutron spectra obtained by the cell calculation, the cross sections of the 61 groups were collapsed into the 24 groups (thermal: 13 groups, fast: 11 groups) for the core calculation. The group constants for the reflector region were calculated by means of the asymptotic spectrum consisting of fission,  $1/E$  and Maxwellian spectrum.

The core calculation was performed with the modified three dimensional diffusion code CITATION. A cross section of the graphite block of the hexagonal prism was subdivided into 24 triangular meshes, and in the axial direction, the half assembly of 120 cm long was divided into 15 meshes. The effective multiplication factor was calculated for each core pattern.

The calculated values predicted well the void reactivity worths when

the Benoist's anisotropic diffusion coefficients were used. But, the calculated values using the conventional diffusion coefficient ( $D_0 = 1/3\bar{\Sigma}_{tr}$ ) underestimated the experimental values by 40~50% for all core patterns.

#### References

- 1) Akino F., et al.: J. At. Energy Soc. Japan, 31, 682 (1989).
- 2) Kaneko Y., et al.: Nucl. Sci. Eng., 50, 173 (1973).
- 3) Akino F., et al.: J. Nucl. Sci. Technol., 17, 593 (1980).
- 4) Tsuchihashi K., et al.: JAERI 1302 (1987).
- 5) Benoist P.: Nucl. Sci. Eng., 34, 285 (1968).

Table 3.8.1 Void reactivity worth of HTTR mockup control rod holes in the VHTRC-1 core

Core pattern	Measured value(\$) $\rho_{RKS}$	Calculated value(\$)	
		$D_0$	D(Benoist's method)
2CV	$1.53 \pm 0.03$	0.8842	1.594
3CV	$2.33 \pm 0.04$	1.443	2.442
2RV	$0.43 \pm 0.01$	0.2002	0.4489
12RV	$2.52 \pm 0.03$	1.220	2.775
18RV	$3.34 \pm 0.03$	1.997	3.882

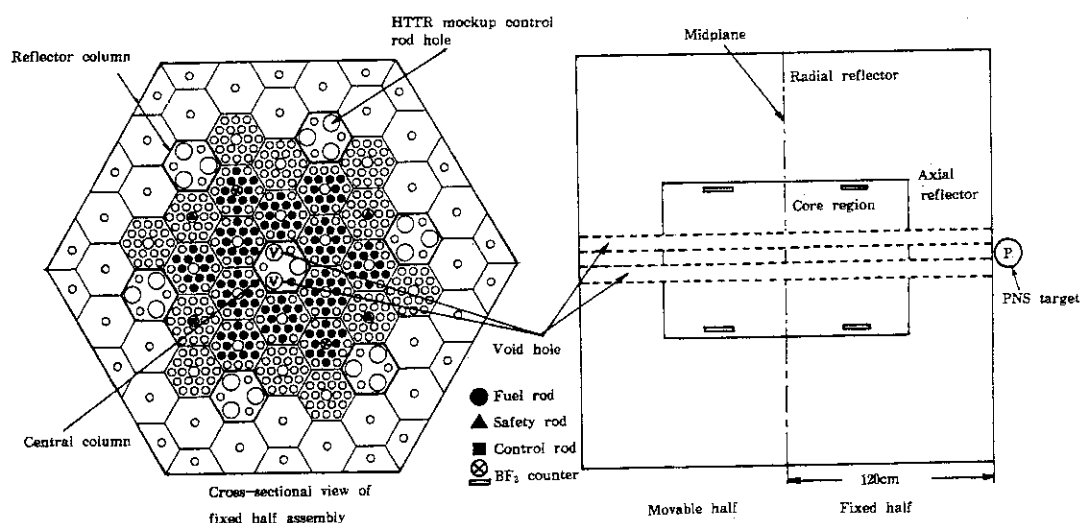


Fig. 3.8.1 Arrangement of the pulsed neutron source and detectors and the 2CV core pattern with two void holes in the central column of the VHTRC-1 core

#### 4. Advanced Reactor System Design Studies

Efforts are continued to establish new concepts of advanced reactors such as advanced fast breeder reactor (FBR), Th/U-233 fueled boiling water reactor (BWBR), high conversion light water reactor (HCLWR) and passive safe reactor. The major portion of the efforts is devoted to create advanced reactors with inherent and passive safety and to diversify the utilization form of nuclear energy resources for the future use.

A new concept of advanced FBR with instantaneous negative temperature coefficient has been proposed, and its core physics characteristics have been investigated. A sequence of parametric survey calculations have been carried out for a variety of fuel types, moderators and fissile isotopes. Based on the surveys, two types of cores have been designed, which show the instantaneous negative temperature coefficients.

A study continues to establish a concept of the Th/U-233 breeder reactor based on the present LWR technology. A BWR core with the effective  $V_m/V_f$  value of 0.25 has been considered. It can be expected that a conversion ratio of 1.0~1.1 is obtainable in such a three dimensional core with radial blanket.

Investigations have been made for reactor core performance of double flat core HCLWRs with TRU mixed fuel. A double flat core concept has a serious drawback that sharp power peakings appear at the core regions adjacent to the axial blankets. TRU loading in the axial blankets has been proposed with both objects of eliminating the power peakings and of transmuting the equivalent amount of the TRU generated in the core.

The fine structure of power distribution in a fuel assembly of tight pitch lattice is greatly affected by the insertion or withdrawal of control rods. The change of the fine structure of reaction rates caused by the control rod insertion or withdrawal has been shown to be due to that of neutron spectrum rather than of effective cross sections.

A design study on the system-integrated PWR (SPWR) has been continued aiming at general improvement of the design, implementation of better passive safety functions and examination of the applicability to a large power plant. In addition, dynamic behaviour of SPWR has been analyzed on shorter term transients. A preliminary analysis was also performed for long term transients, such as daily load following operation, using a nuclear ship engineering simulation system.

(Yukio Ishiguro)

#### 4.1 A Concept of Advanced Fast Breeder Reactor with Instantaneous Negative Temperature Coefficient

H. Takano, T. Hiraoka, K. Kaneko<sup>\*</sup> and S. Katsuragi<sup>\*</sup>

In design study of fast breeder reactor, reduction for positive sodium void reactivity coefficient is noticed as one of the most essential problems in the view point of inherent safety, especially, after the Chernobyl accident. To reduce the positive void reactivity, several ideas have been proposed: flattening pan-cake core models enhancing neutron leakage, heterogeneous core models with inner depleted uranium blanket as low importance region, etc. To design the core with nearly zero void reactivity by using these reduction methods, there is designed very flat core or large inner blanket which is not realistic model. Furthermore, there are passive safety fast reactors such as LMR proposed by ANL<sup>1)</sup>. In these reactors, negative reactivity effects such as flower-ing expansion of core supporting plate and/or extension of control rods which are caused by temperature rising are considered to overcome the positive void reactivity. However, these are significant time-delayed effect in comparison with instantaneous Doppler effect. Moreover, inherent safety fast reactors with nearly zero void reactivity coefficient are also considered. These have very small cores without blanket region to make neutron leaky. Therefore, neutron economy is very bad and a breeding ratio becomes smaller than unity.

In the present study, we propose a concept of advanced fast breeder reactor with instantaneous negative temperature coefficient of which sodium void reactivity and/or the summation in the void and Doppler reactivities becomes negative.

Doppler reactivity depends strongly on neutron spectrum shape and capture reaction rate, and on the other hand, void reactivity depend complicatedly on neutron spectrum, importance and leakage in competition among capture, fission and scattering reactions. Therefore, we performed, at first, parametric studies in which the void and Doppler reactivities are calculated for infinite cell model with zero leakage. The calculations were conducted for a lot of combinations among fuels (metallic alloy, oxygen, zirconium-hydride, carbide and nitride types), moderators

---

<sup>\*</sup> The Japan Research Institute, Ltd.



(graphite and hydrogen) and fuel materials ( $^{235}\text{U}$ , Pu,  $^{233}\text{U}$ ,  $^{232}\text{Th}$  and  $^{238}\text{U}$ ). As a result, we obtained several fuel compositions with negative void reactivity and instantaneous negative temperature reactivity as follows:

The void reactivity is negative for the case of  $^{233}\text{U}$ -Th-Zr alloy with graphite moderator in the range for graphite moderator to fuel volume ratio ( $V_m/V_f$ ) from 3 to 10. The instantaneous negative temperature reactivities are satisfied with  $^{233}\text{U}$ -Th-Zr fuel of  $V_m/V_f$  from 1 to 40 and DU-Pu-Zr fuel of  $V_m/V_f$  from 2 to 40. However, breeding ratio for these fuel compositions is about 1.

To obtain a high breeding gain, furthermore, we propose a new concept reactor which consists of two-region core: The central core region has negative void reactivity and/or instantaneous negative temperature reactivity, and the outer core region becomes high breeding composition with positive void reactivity. Moreover, an important condition is that linear heat rating in the central region is larger than that in the outer core region. This reactor can make shutdown before sodium void propagate to the whole core range. Because, when sodium flow is reduced by pump trip accident, at first, sodium are voided from the central core region with higher linear heat rating, and the effective multiplication factor ( $k_{\text{eff}}$ ) is reduced instantaneously by the negative temperature reactivity.

We have designed two kinds of cores with the instantaneous negative temperature reactivity. Table 4.1.1 shows the core performance for the reactors. One consists of metallic fuel assemblies of DU-Pu-Zr and graphite moderator in the inner core region. The outer core region is composed by standard metallic fuel assemblies of DU-Pu-Zr without the graphite moderator. In this case, the instantaneous temperature reactivity becomes negative, though the void reactivity is slightly positive. The other consists of Th- $^{233}\text{U}$ -Zr metallic fuel assemblies in the inner core region, and negative void reactivity is obtained. Very high breeding ratio of 1.5 and small burnup swing are shown for the both cores. Furthermore, the average burnup rate is about 80 GWd/t in the outer core region.

#### Reference

- 1) Wade D.C. and Chang Y.I.: Nucl. Sci. Eng., 100, 507 (1988).

Table 4.1.1 Core performance

Parameter	Pu/Pu core	Th/Pu core
Reactor power (MWt)	1800	1800
Core height(cm)	100	100
radius(cm)	164	164
Inner core radius(cm)	83	83
Axial blanket(cm)	30	30
Average linear heat rating(w/cm)	348	348
Cycle length(EFPD)	600	600
Fuel		
Inner core(IC)	DU-Pu-10%Zr	Th- <sup>233</sup> U-10%Zr
Outer core(OC)	DU-Pu-10%Zr	DU-Pu-10%Zr
Enrichment(w/o)		
IC1/IC2/OC	13.5/10.0/10.4	9.0/7.5/10.4
Moderator(IC)	graphite	graphite
Breeding ratio	1.5	1.5
Average burnup(GWd/t)		
IC1/IC2/OC	81/98/79	105/132/80
Burnup swing(%dk/k)	0.38	0.56
$\beta_{eff}$ (%dk/k)	0.42	0.41
Na-void reactivity in IC(%dk/k)	0.03	-0.08
Instantaneous temperature		
reactivity in IC (%dk/k)	-0.07	-0.21

## 4.2 Th/U-233 Fueled Boiling Water Breeder Reactor

H. Akie, Y. Ishiguro, Y. Morimoto<sup>\*</sup> and E. Doi<sup>\*\*</sup>

A study has been performed to establish a concept of the Th/U-233 breeder reactor based on the present LWR technology. A sequence of burn-up calculations, taking account of thermo-hydraulics, has been made for Th/U-233 fueled LWRs. For utilization of the Th/U-233 fuel, it is first necessary to generate the fissile material, U-233, in any other nuclear system, because U-233 is not contained in natural resources. Moreover, the conversion ratio higher than 1.0 (fuel breeding) is required for a self-sustaining fuel system.

The PWR type core was first considered<sup>1)</sup>. It was shown that the conversion ratio can be greatly enhanced by using the concept of an axially heterogeneous core, while the initial excess reactivity is fairly reduced. The volume ratio of moderator to fuel ( $V_m/V_f$ ) was selected to be 0.4, which was selected as the lower limit to use soluble boron reactivity control. Here, a core burnup calculation was made for the three-dimensional axially heterogeneous core. The average conversion ratio of 0.98 and the discharge burnup of 50 GWd/tonne were obtained for this core in the equilibrium cycle.

The result of the cell burnup parametric survey calculations shows that a higher conversion ratio than 1.0 is achievable in the lattice of  $V_m/V_f \leq 0.2$ . In such a tight lattice, however, thermo-hydraulic problems become very severe for the case of PWR type core. As a result, the BWR type core, which can have larger fuel rod clearance than PWRs with equivalent  $V_m/V_f$  value, has been considered in the next stage. The fuel lattice of an effective  $V_m/V_f$  value of 0.25 was selected from the viewpoint of excess reactivity control under the cold shutdown condition in this investigation. The result of the core burnup calculations for one dimensional models is shown in Fig. 4.2.1. This figure shows that the fuel breeding can be achieved by the use of the axially heterogeneous cores. The effect of the inner blankets is seen to decrease the excess reactivity and to increase the conversion ratio. There is a possibility to achieve the conversion ratio of 1.0~1.1 by taking account of a radial blanket. It is planned to perform a three dimensional core burnup cal-

---

\* Energy Research Lab., Hitachi Ltd.,

\*\* I.S.L. Inc.

ulation. The specifications of the core are; core height is 24 cm  $\times$  5, equivalent core diameter is 375 cm and thermal output is 900 MWt.

#### Reference

- 1) Akie H., Ishiguro Y. and Doi E.: "Core Burnup Calculation of Th/U-233 Fueled Axially Heterogeneous HCLWR", Reactor Engineering Department Annual Report (April 1, 1989 - March 31, 1990), JAERI-M 90-149 p.67, (1990).

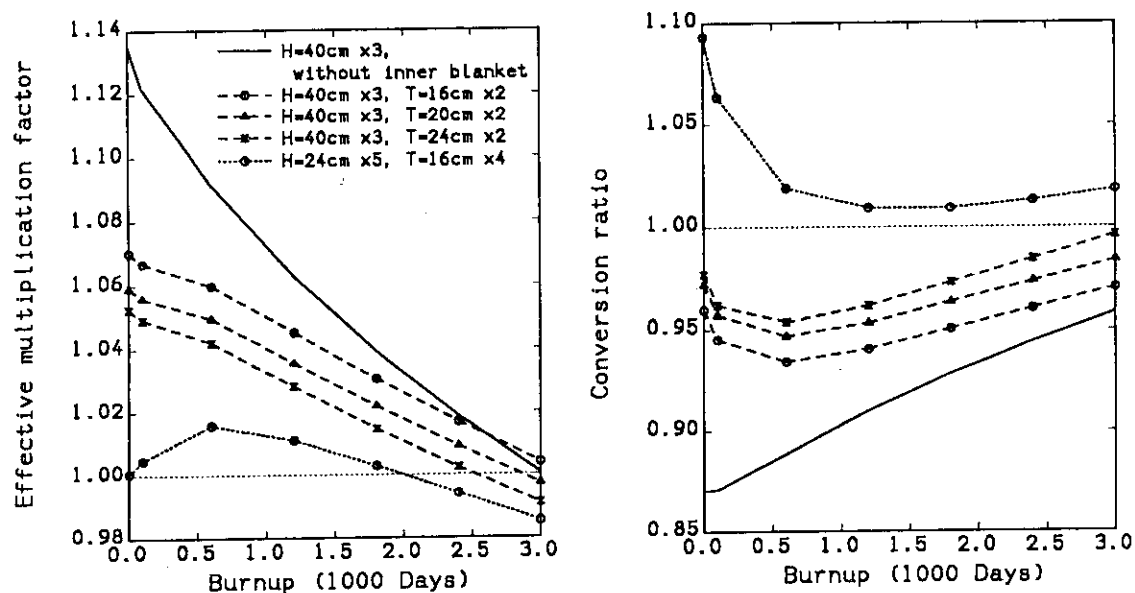


Fig. 4.2.1 Burnup characteristics of Th/U-233 fueled BWR by one dimensional core burnup calculations ( $V_m/V_f=0.25$ , H is fuel part thickness and T is inner blanket thickness)

## 4.3 Performance of Double Flat Core HCLWR with TRU Mixed Fuel

H. Akie, H. Takano and J. Saito\*

There are two concepts designed for high conversion light water reactors at JAERI<sup>1)</sup>: One uses a semi-tight fuel lattice and spectral shift rod of depleted  $\text{UO}_2$ , which changes a moderator/fuel volume ratio ( $V_m/V_f$ ) from 1.1 to 1.4 with burnup, and the other is an axially heterogeneous core of  $V_m/V_f=1.1$ , which is like a pancake with two cores of 60 cm thickness and axial inner and outer blankets of 30 cm thickness, as shown in Fig. 4.3.1. The latter is called 'double flat core', which was proposed to improve void reactivity characteristics and to increase a conversion ratio at the same time. This flat core is more suitable for TRU transmutation than the former because the positive void reactivity caused by TRU is reduced.

The double flat core has one problem that the sharp power peak appears at the fuel region adjacent to the axial blanket region. This is caused by thermal neutrons flowing from the blanket region into the fuel region. The large thermal capture cross sections of TRU nuclides, therefore, effectively suppress the power peak when TRU is mixed in the blanket fuel as shown in Fig. 4.3.1. However, it does not necessarily follow that TRU nuclides are effective for power flattening.

The results of core burnup calculations are shown in Table 4.3.1 for a one dimensional core which expresses the axial dependence of various physics quantities in the double flat core. The amount of TRU mixed in the fuel is 1% of total heavy nuclides in the core, in order to keep negative void reactivity. When TRU nuclides are mixed only in the blanket region (Cases 3 and 4), there are the following advantages over the cases that TRU is mixed in the fuel region (Cases 1 and 2):

- (1) The smaller fuel enrichment can keep the same burnup period as the Case 0; the case without TRU nuclides.
- (2) The void reactivity coefficient is more negative.

If the fuel enrichment is adjusted, the same conversion ratios are obtained for the cases 1~4. The amount of discharged TRU is almost equal to the loaded amount for all these cases. This means that the equivalent amount of TRU to that generated in the core is transmuted during burnup.

---

\* The Japan Research Institute, Ltd., Tokyo.

The TRU of 70~100kg is transmuted per 300 reactor operating days.

# Reference

- 1) Okumura K., et al.: "Conceptual Design Study of High Conversion Light Water Reactor", JAERI-M 90-096 (1990) (in Japanese).

Table 4.3.1 Core performance of double flat core HCLWR with TRU mixed fuel

	Case 0	Case 1	Case 2	Case 3	Case 4
Fraction of TRU (%)					
in inner blanket	0.0	1.0	0.0	2.33	3.5
in core	0.0	1.0	1.75	0.0	0.0
in outer blanket	0.0	1.0	0.0	2.33	1.75
Enrichment(%)	10.0	12.0	12.0<12.3>	12.0<11.2>	12.0<11.3>
Burnup(days)	1110	1090	950	1380	1340
Conversion ratio†	0.80	0.74	0.76{0.75}	0.73{0.75}	0.73{0.75}
Void coefficient* ( $\Delta k/k/\%$ void)	-8.1E-4	3.0E-5	4.6E-5	-7.4E-5	-3.3E-5
Amount of TRU (kg)					
loaded	0	1159	1159	1159	1159
discharged	313	1079	1076	1195	1184
transmuted	-	392	395	277	288
( per 300 days	-	98	99	69	72 )

< >: Adjusted enrichment to give the same burnup as Case 0

{ }: Conversion ratio for the adjusted enrichment

†: Averaged over burnup

‡: Reactivity coefficient for the void change from 0% to 90%

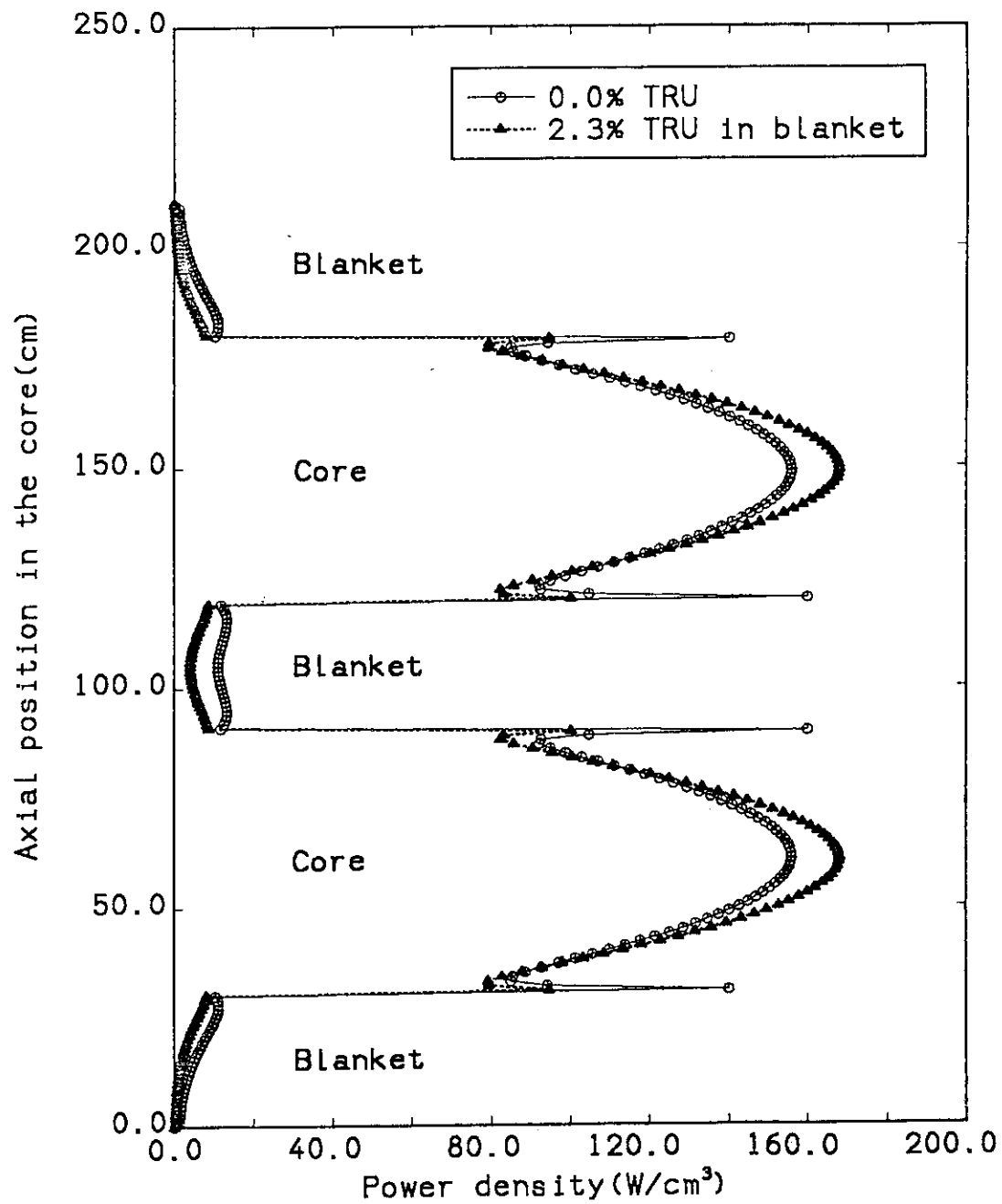


Fig. 4.3.1 Axial power distributions in the double flat core HCLWR with and without TRU in the blanket region

#### 4.4 An Analysis of Heterogeneity in the Fuel Assembly of Tight Pitch Lattice

C.S. Gil<sup>\*</sup>, K. Okumura and Y. Ishiguro

In HCLWRs, cluster type control rods with highly enriched  $B_4C$  are employed for excess reactivity control. The insertion or withdrawal of the control rod in a tight pitched lattice affects the neutron spectra and effective microscopic cross sections in the fuel rods near the control rod. In order to grasp such heterogeneity effects, the space dependent nuclide-wise reaction rates on a fine energy structure were calculated in an HCLWR fuel assembly with a continuous energy Monte Carlo code VIM.

The fuel assembly model under study is shown in Fig. 4.4.1. For simplicity, the assembly with only one control rod in the central position was assumed here. The water gap surrounding the assembly also gives the heterogeneous effects to the fuel rods near the gap. The VIM calculations were done for the following four geometries; 1) the assembly which has a  $B_4C$  rod with 93% enriched  $^{10}B$  in the central position, 2) the assembly which has a water tube as a result of withdrawal of the control rod, 3) the assembly without any special rods, that is to say, a normal MOX rod is placed in the central position, 4) infinite array of the unit hexagonal fuel cell.

Figure 4.4.2 shows the space dependence of the macroscopic fission cross section condensed to one group for each case. Strong heterogeneity can be observed in the fuel rods near the central  $B_4C$  or water rod, and also near the water gap. The neutron spectra in the fuel adjacent to the central pin are compared in Fig. 4.4.3, where remarkable differences of the neutron spectra are observed. On the other hand, such a large difference was not observed for the fine structure of effective cross sections (107 monitoring groups). That is to say, the heterogeneity effects of reaction rates caused by control rod insertion or withdrawal are almost due to the change of spectra rather than that of fine effective cross sections. This means that if a sufficiently fine energy group structure is employed in deterministic codes, HCLWR assembly calculations can be conveniently carried out with the macroscopic group constants obtained

---

\* Korea Atomic Energy Research Institute



from a simple unit fuel cell calculation ignoring the heterogeneity effects of control rods.

The assembly calculations were carried out also by using the SRAC code based on the collision probability method. The macroscopic group constants of fuel, cladding and moderator were prepared in a 107 groups-structure with a unit cell calculation. For the central  $B_4C$  rod, a super-cell model was employed to generate the group constants, where the absorber cell is surrounded by a homogenized fuel region in a cylindrical geometry.

Figure 4.4.4 shows the comparison between the SRAC and VIM results for the assembly calculations on neutron multiplication factor and power distribution. A fairly good agreement can be seen between the SRAC and VIM results. It was confirmed that the heterogeneity effects of control rods in an HCLWR fuel assembly could be successfully treated by the SRAC code with the fine energy group constants obtained in a unit cell calculation.

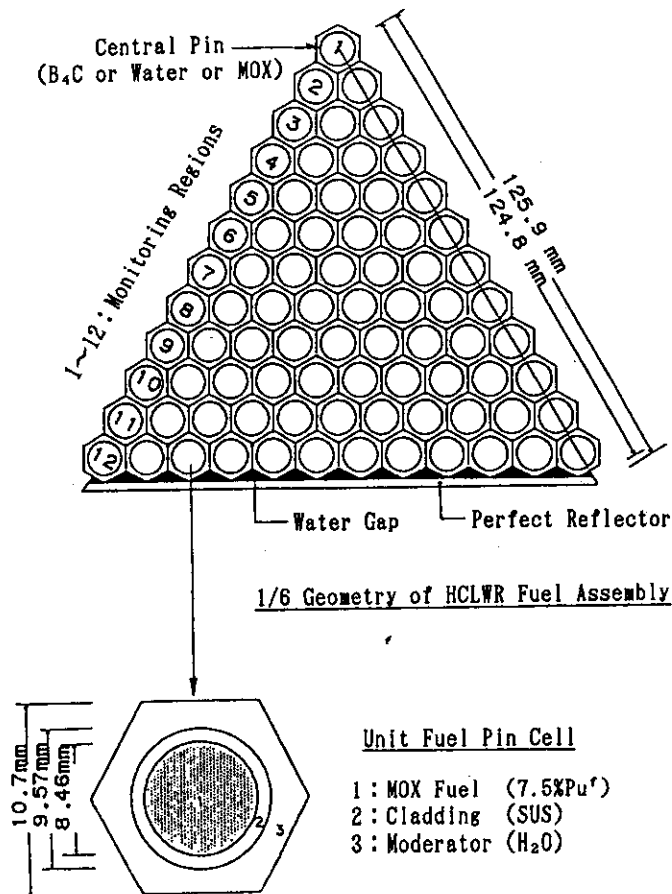


Fig. 4.4.1 HCLWR fuel assembly model

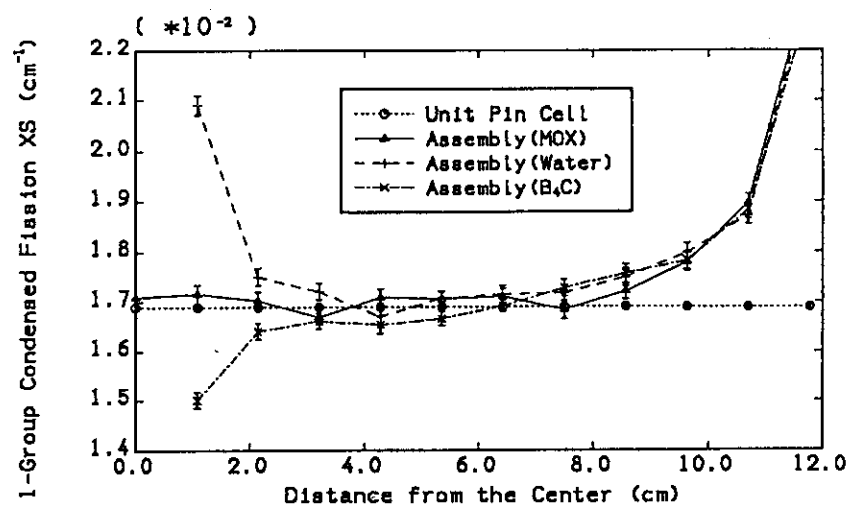


Fig. 4.4.2 Distribution of 1-group condensed fission cross section

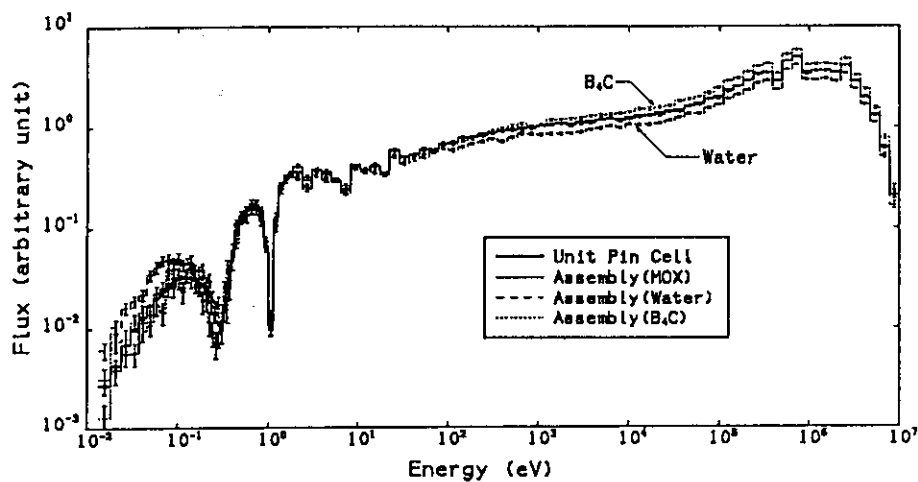


Fig. 4.4.3 Comparison of neutron spectra in monitoring region No.2

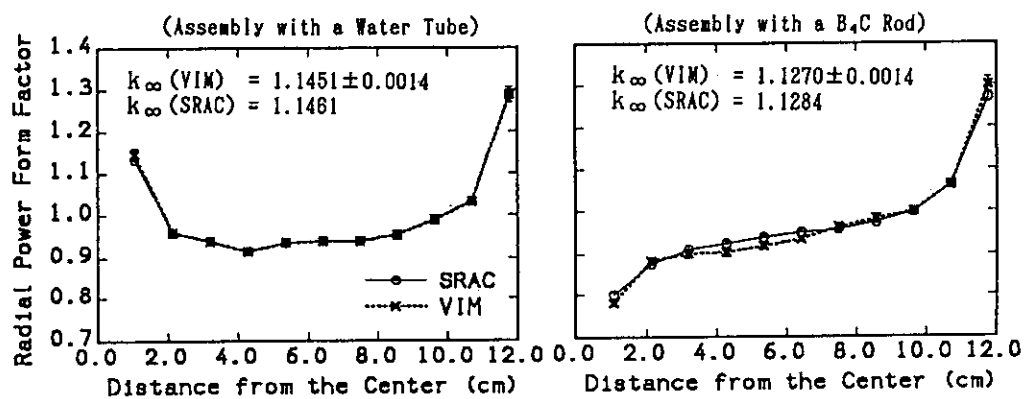


Fig. 4.4.4 SRAC and VIM results on  $k_{\infty}$  and power distribution

## 4.5 Design Study of the SPWR (System-integrated PWR)

K. Sako, J. Oda\* and M. Tougasaki\*

The SPWR is designed as a next generation power reactor realizing highly passive safety, good maintainability and economical competitiveness at the same time. Its design study has been continued in order for general improvement and implementation of better passive after heat removal system, and to examine applicability to a large power plant.

#### Reactor Concept

Table 4.5.1 and Fig. 4.5.1 show main parameters and a plan view of the SPWR with thermal power of 1100 MW, respectively.

The reactor has the following characteristics:

- (1) It is an "integrated PWR" containing a steam generator, a main circulating pump and a pressurizer in its reactor vessel. A poison tank filled with borated water is also installed in the reactor vessel for emergency reactor shutdown in place of ordinary control rod clusters. This reactor does not have any control rod and reactivity control during operation can be done by chemical shim.
- (2) Between the poison tank and primary cooling water, hydraulic pressure driven valves normally closed by delivery pressure of main circulating pump are placed at upper plate of the poison tank, while at lower part, a density lock is installed as an interface of the tank and primary coolant. In case of main circulating pump trip, the valves open passively by the gravitational force and borated water in the tank flows into the core by natural convection to shutdown the reactor.

#### Passive Safety Features

Passive safety features of this reactor can be summarized as follows;

- (1) Rapid introduction of large reactivity can not be conceivable since it has no control rod which actually gives sources of a large and rapid reactivity introduction.
- (2) Highly reliable passive shutdown system is employed.
- (3) Large scale LOCA can not happen since there is no large piping in primary cooling system. This is one of the significant advantages of an "integrated PWR". Only small scale LOCA can be conceivable and grace period before dry out of the core is long (a few hours) because of its

---

\* Ishikawajima-Harima Heavy Industries, Co. Ltd.

large amount of water inventory in the reactor vessel.

(4) The grace period can be significantly prolonged by employment of a pressure balance water injection system which is explained later.

#### Controllability

The SPWR has excellent operation characteristics without any problem in controlling nuclear reaction even though it has no control rod. Slow but large reactivity change due to fuel burn-up can be compensated by periodic change of boron concentration in the primary cooling water once in every two weeks. Reactor power level is controlled to follow rapid load changes by negative power coefficient on reactivity without controlling the boron concentration. The basic SPWR core characteristics such as a negative power coefficient is already proven since its core design is basically same as the ordinary PWR, except lower power density, which gives smaller Xe effects on reactivity.

#### Application to Large Power Plants

A single SPWR may not achieve high plant power level, limited to below about 500 MWe. This may be major disadvantage of an integrated reactor. However installing multiple reactors into a single containment vessel can realize a large power plant. Such a power plant may not constitute a complicated system, by a virtue of the fact of complete control rods absence. Figure 4.5.2 shows a 1400 MWe power plant with 4 units of 1100 MWt SPWR.

#### Concept of Passive Core Cooling System

Passive cooling system with the pressure balanced injection system as an engineering safety system for loss of coolant accidents is shown in Fig. 4.5.3.

Two types of hydraulic pressure driven valves are used in the system. During normal reactor operation those valves are closed by pump outlet pressure. When level of cooling water in the reactor vessel comes down to a certain designated level in case of LOCA, the valve A opens and decreases inner pressure of the reactor vessel and increases that of a borated water tank which is placed outside of the vessel. When the pressures of the vessel and the tank are balanced, the valve B opens leading water in the tank into the vessel by natural convection. It helps to maintain water level in the vessel for preventing the core dry out. In order to keep those valves closed during normal operation, small pumps are placed near the designated level and provide hydraulic pressure to the valves.

## References

- 1) Sako K., Takano H., Asahi H., Oda J., et al.: "Feasibility Study of SPWR as a Next Generation Power Plant", Proc. Second International Seminar on Small and Medium-Sized Reactors, Post Conf. of SMiRT, San Diego, 1989.
- 2) Advanced Reactor Assessment Team: "Conceptual Design of SPWR, a PWR with Enhanced Passive Safety", JAERI-M 89-208, 1989 (in Japanese).

Table 4.5.1 Major design parameters of SPWR

<b>REACTOR</b>	
Thermal power	1,100 MWt
Coolant inlet/outlet temp.	290/320 °C
Coolant Flow rate	23,000 t/h
Total pressure drop	0.14 MPa
Core outlet pressure	13 MPa
<b>CORE/FUEL ASSEMBLY</b>	
Equivalent core dia./height	2.99/2.4 m
<sup>235</sup> U enrichment	4.5 %
Core average power density	65 MWt/m <sup>3</sup>
No. of fuel assemblies	121
Fuel burn-up (Average)	45 GWd/t
Lattice pitch (triangle)	259 mm
No. of fuel rods	325
Rod dia./pitch(triangle)	9.5/14.0 mm
Rod average linear heat rate	14.1 kW/m
<b>STEAM GENERATOR</b>	
(Once-through helical coil type)	
Steam temp./pressure	285°C/5.3 MPa
Feed water temp./pressure	210°C/5.9 MPa
Steam flow rate	2,000 t/h
Material of tube	Incolloy 800
Tube inner/outer diameter	15/19 mm
Heat transfer area (inner, total)	8,840 m <sup>2</sup>

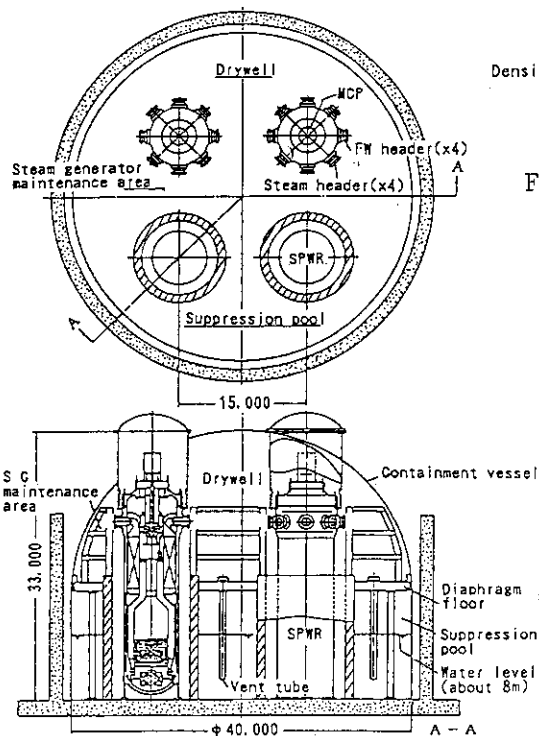


Fig. 4.5.2 Concept of 1400MWe power plant

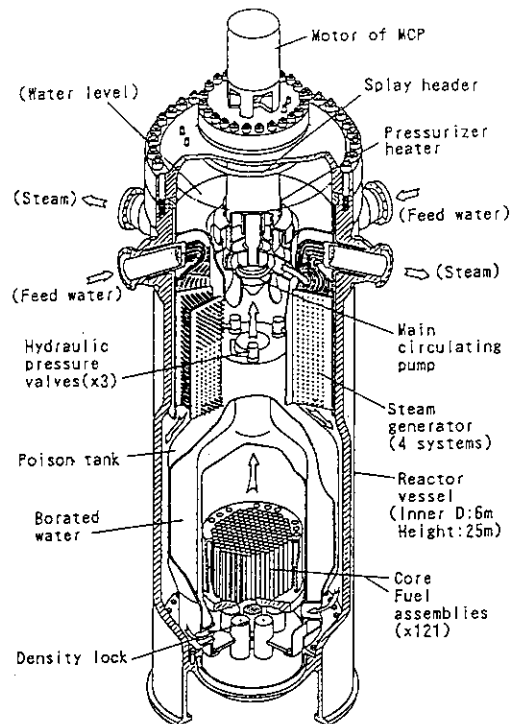


Fig. 4.5.1 Concept of SPWR

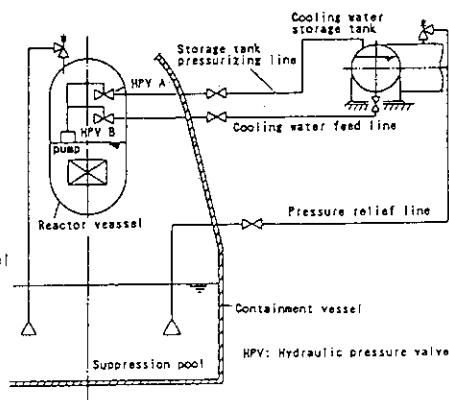


Fig. 4.5.3 Concept of passive core cooling system

## 4.6 Daily Load Following Analysis of SPWR

F. Araya, M. Akimoto, K. Hashidate<sup>\*</sup>, K. Kaneko<sup>\*\*</sup> and K. Sako

SPWR (System Integrated PWR) has been conceptually designed at JAERI<sup>1)</sup>. Behaviour of SPWR has already been analyzed on relatively short term transients, in which effects of Xe on feedback reactivity are negligible, with the transient thermal-hydraulic analysis code RETRAN<sup>2)</sup>. As the results of the analyses, it was confirmed that SPWR had excellent self-controllability in view of the short term transients.

In this study<sup>3),4)</sup>, in order to understand the characteristics of SPWR on long term transients such as daily load following operations in which Xe reactivity effects may play an important role, preliminary analyses were performed with the nuclear ship engineering simulation system (E/S) which is being developed at JAERI<sup>5)</sup>.

Although it was difficult to simulate SPWR completely because E/S was designed to model the nuclear ship "MUTSU", E/S became applicable for the present study by adjusting the most important parameters, i.e. reactor kinetics parameters to those of SPWR. Especially, a power coefficient on reactivity due to moderator temperature change and a feedback reactivity due to Xe build-up were important. Based on several checking calculations of E/S, it was found that E/S evaluated the power coefficient of moderator temperature 20% larger and the Xe reactivity 50% larger than those of SPWR.

Using E/S with the conditions described above, the load following calculations were performed. A load change was modelled by changing rotational speed of the main turbine of "MUTSU" in E/S. The most severe case in view of difficulty of start-up due to Xe build-up will be presented here, although eight cases of calculations have been performed. In this case, after the load was reduced from full load level to 50%, it was kept constant for 4 hours, and then increased to full load level. In the actual calculations, the speed of Xe build-up was accelerated 30 times faster than the real one, while the thermal-hydraulic transient was calculated in normal way. Therefore, Xe build-up for 4 hours was simulated in 8 minutes in the E/S calculations. The calculated results of

---

\* Mitsubishi Atomic Power Industries, Inc., Tokyo

\*\* The Japan Research Institute, Ltd., Tokyo

this case are shown in Fig. 4.6.1. This figure shows that the core power follows the load change without any difficulty. As shown in the figure, the maximum change in average coolant temperature during the transient was about 10°C.

Based on the preliminary analyses with E/S described above, it can be said that SPWR can follow load change excellently over the range of 50% without controlling boron concentration in primary coolant. RETRAN analyses with complete model of SPWR are currently being performed.

#### References

- 1) Advanced Reactor Assessment Team: "Conceptual Design of SPWR, a PWR with Enhanced Passive Safety", JAERI-M 89-208 (1989).
- 2) Kin E., Uchida Y., Matsui Y. and Sako K.: "Conceptual Design of SPWR, a PWR with Enhanced Passive Safety (8) Dynamic Analysis", 1990 Annual Mtg. of AESJ, D20 (1990).
- 3) Araya F., et al.: "Preliminary Analysis of Daily Load Follow Characteristics of Highly Passive Safe PWR, SPWR with Engineering Simulator for Nuclear Ship", JAERI-M 91-075 (1991).
- 4) Araya F., et al.: "Preliminary Analysis of Load Follow Characteristics of No-Control-Rod-Equipped Reactor SPWR with Engineering Simulator for Nuclear Ship", 1991 Annual Mtg. of AESJ, A53 (1991).
- 5) Itoh Y., et al.: "Development of Engineering Simulator for Nuclear Ship (1) General", 1990 Fall Mtg. of AESJ, F26 (1990).

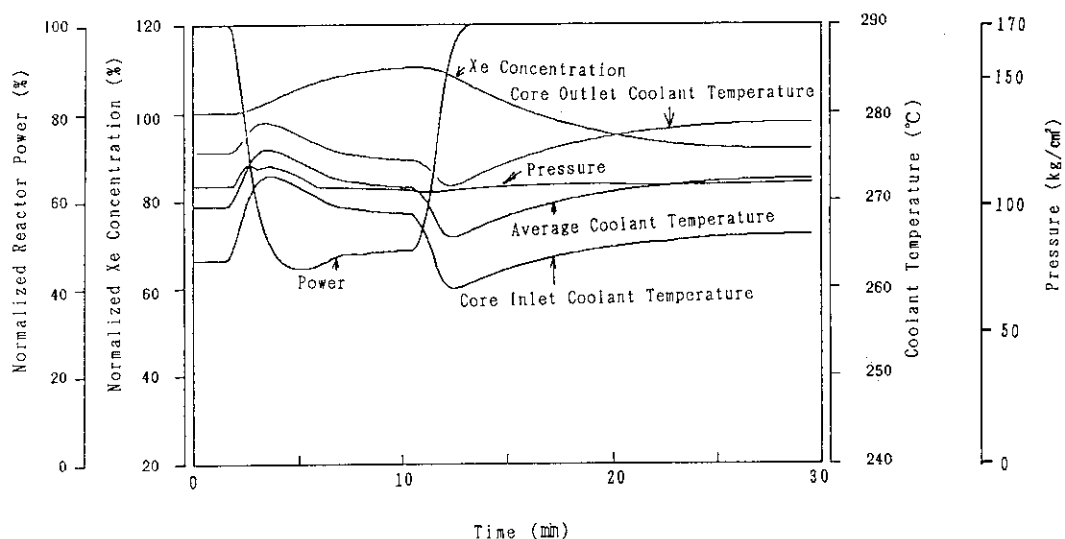


Fig. 4.6.1 Results of daily load following calculation of SPWR.  
(One minute in this figure is equivalent to 30 minutes in Xe build-up.)

## 5. Fusion Neutronics

Many efforts were devoted in the deep penetration experiment of iron assembly. Because the stainless steel is the only one choice for the structure material and inboard shield in the next fusion device such as ITER. The resonance structure of iron makes considerable complexity in the deep penetration problem. As no neutron spectrum measurement has been performed in an iron assembly for the energy less than 1 MeV, the low energy neutron spectrum has been measured in a large cylindrical iron assembly of 1 m in diameter and 0.95 m long. Two types of proton-recoil proportional counters were used in the experiment along with a newly developed data acquisition system. The experimental analysis suggested the importance of self shielding correction factor (f-table) in a group-wise calculation. Two analytical activities have been performed in the iron assemblies. One was the analysis of a time-of-light experiment on iron slabs using the SN code DOT3.5 and the Monte Carlo code MCNP. Though the f-table was used in the DOT3.5 calculation, there was some discrepancy in the energy range from 0.5 to 1 MeV between DOT3.5 and MCNP calculations. The other activity was an analysis of a benchmark problem of iron using the newly developed Monte Carlo code MVP.

A benchmark experiment has been made on a tungsten assembly. The tungsten is a candidate material for shielding in the next fusion device. The shielding power was compared experimentally with the other materials.

As the JAERI/USDOE collaborative program on fusion neutronics using FNS, an experiment has been performed on the Phase-IIIB assembly. In the assembly, a graphite armor region was placed inside of the SS304 first wall of Phase-IIIA assembly. A post-analysis of Phase-IIIA experiment was also performed by the DOT3.5 code and the Monte Carlo code MORSE-DD with the nuclear data of JENDL-3. Under the same framework, integral experiments of induced activity and decay heat were performed on various materials. As the other international collaboration, the international comparison on measuring techniques of tritium production rate is continued under the framework of NEACRP activity.

Some technical developments have been achieved at FNS. One was the development of a 40mm-dia. NE213 detector for the measurement of in-system gamma-ray spectrum. The other was a study of neutron yield characteristics of FNS rotating target in order to apply it to the FNS upgrade planning.

(Hiroshi Maekawa)



## 5.1 Measurement and Analysis of Low Energy Neutron Spectrum in a Large Cylindrical Iron Assembly Bombarded by D-T Neutrons

C. Konno, Y. Ikeda, K. Kosako, Y. Oyama, H. Maekawa, T. Nakamura  
and E.F. Bennett\*

Iron is one of the most important elements in a fusion reactor as the structural and shielding materials. Various experiments using iron assembly have been already performed. The measurements of low energy neutron spectra ( $E_n < 1$  MeV) in iron assembly, however, were scarce although the information of low energy neutron spectra is very important for the estimation of nuclear heating in a superconducting magnet.

Low energy neutron spectra in a large cylindrical iron assembly bombarded with D-T neutron were measured using a proton recoil counter (PRC) at the Fusion Neutronics Source (FNS) facility. The dimension of the iron assembly was 1 m in diameter and 0.95 m in thickness. This assembly was set at 0.2 m from the Ti-T target bombarded by deuteron beam. Measuring points were 0.19, 0.31, 0.41, 0.51, 0.61, 0.81 and 1.01 m from the Ti-T target along the central axis of the assembly. The size of PRC was 19 mm in diameter and 127 mm in effective length and it was inserted from the side of the iron assembly. To cover the energy range from a few keV to 1 MeV, two types of PRCs were used. One was filled by hydrogen gas for lower energy part and the other was filled by 50-50 mixture of hydrogen and argon gas for higher energy part. A newly developed data acquisition system<sup>1)</sup> for PRC was adopted, where high voltage varied continuously in ramped shape during acquisition. The neutron spectrum measured at 0.81 m from the Ti-T target is shown in Fig. 5.1.1 with calculated ones. The fine structures due to iron resonances around 10, 30, 100, 150, 200, 400 and 800 keV were clearly observed in this spectrum.

For the experimental analysis, the two-dimensional transport code, DOT3.5, and the continuous energy Monte Carlo code, MCNP, were adopted. The cross section sets used were FUSION-J3 (without f-table) and FSXLIB based on the JENDL-3 nuclear data library, respectively. The ratios of the calculated spectra to the measured ones (C/E) in several specific energy bins are shown in Fig. 5.1.2 and Fig. 5.1.3.

---

\* Argonne National Laboratory

The following facts were deduced for DOT3.5 calculation from Fig.

5.1.2:

- i) In the front part of the assembly, the calculation agreed with the experiment in the energy range from 500 keV to 1 MeV. However, it overestimated the experiment in the energy region below 500 keV by a factor of 2.
- ii) In the rear part of the assembly, the calculation underestimated the experiment by more than a factor of 2 in the energy range above 500 keV, particularly, more than a factor of 5 above 500 keV at 1.01 m from the neutron source. Meanwhile, the discrepancy in the spectrum below 500 keV tended to decrease.

Figure 5.1.3 clearly shows that the MCNP calculation gives a better agreement with the experiment for overall energy range in comparison with the DOT calculation. However, the agreement above 100 keV tended to become poorer as the detector position moved deeper into the assembly. Particularly, the MCNP calculation between 500 keV and 1 MeV underestimated by more than 30% at 1.01 m from the neutron source.

#### Reference

- 1) Bennett E.F.: "A Continuous Mode Data Acquisition Technique for Proton Recoil Counter Neutron Spectrometer", ANL/FPP/TM-239 (1989).

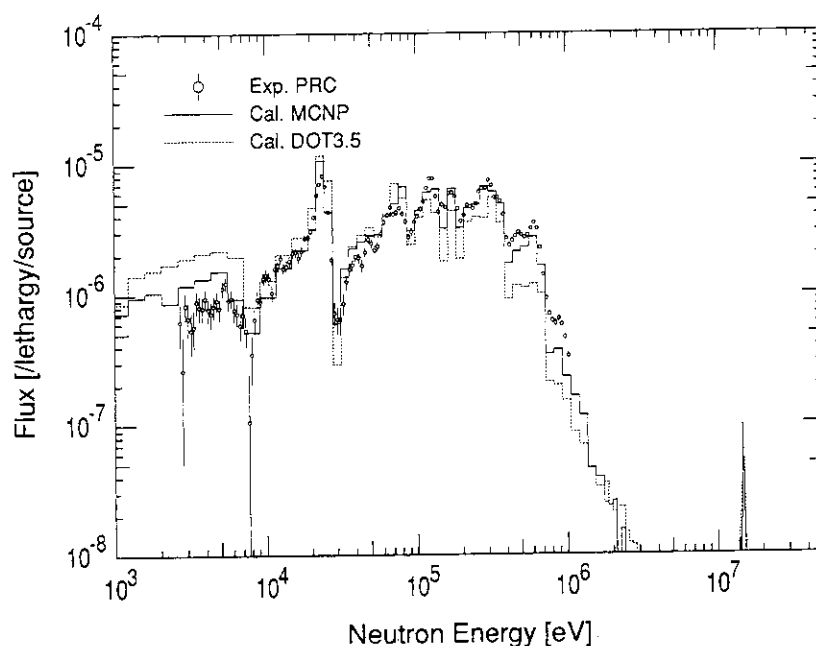


Fig. 5.1.1 Measured and calculated neutron spectrum at 0.81 m from the neutron source

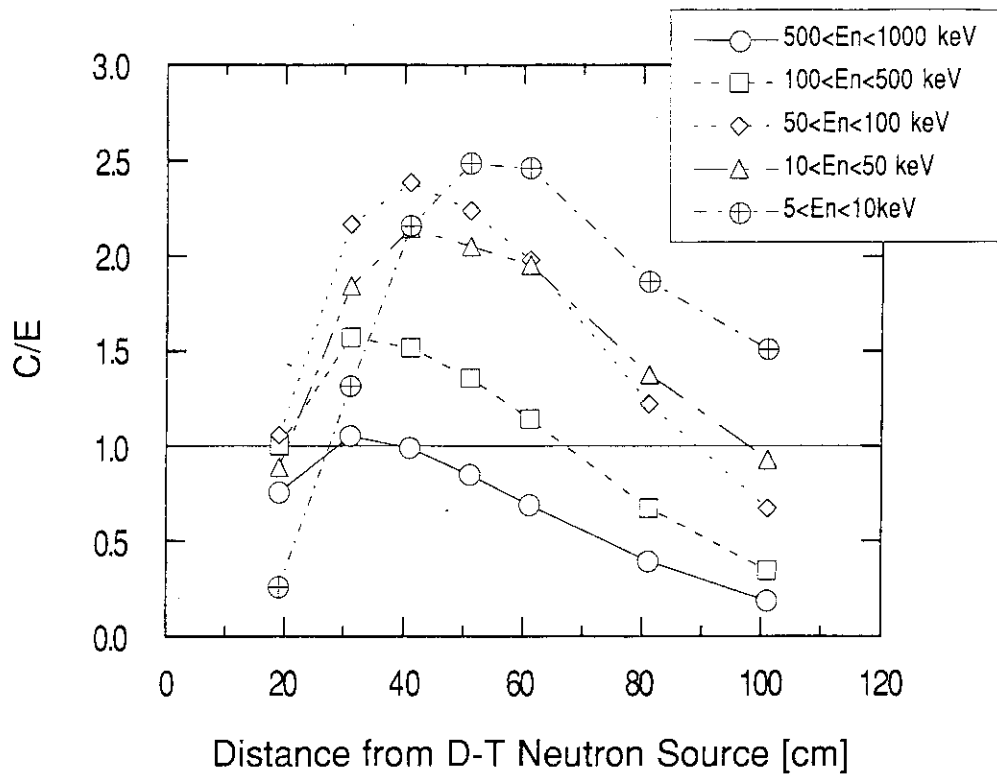


Fig. 5.1.2 Comparison between the DOT3.5 calculation and the measurement integrated in several specific energy bins

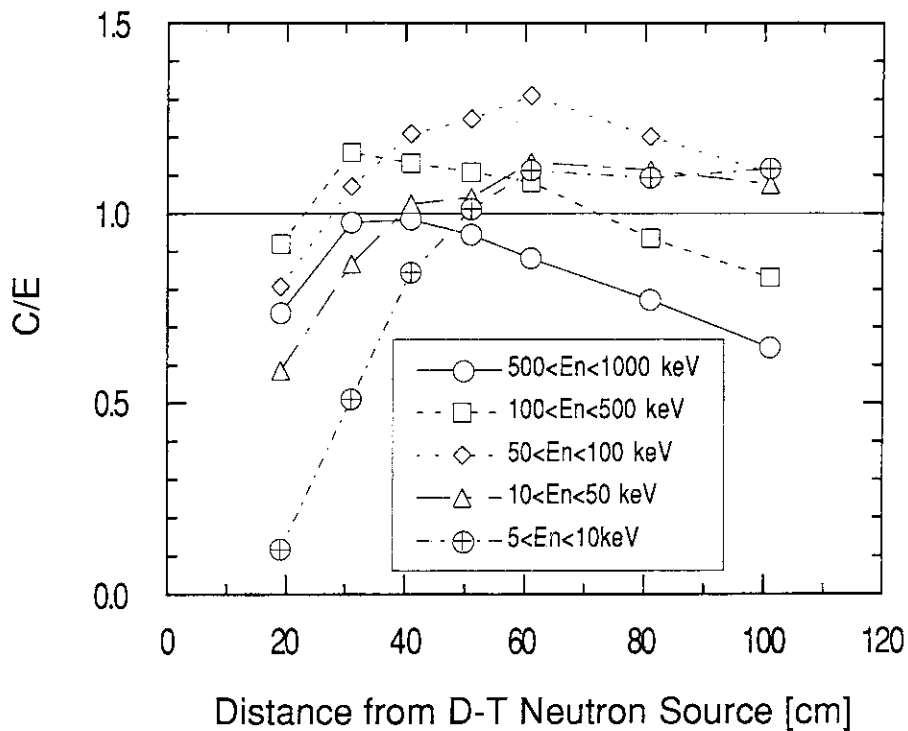


Fig. 5.1.3 Comparison between the MCNP calculation and the measurement integrated in several specific energy bins

## 5.2 Neutronics Experiment and Analysis on a Tungsten Slab Assembly Bombarded with D-T Neutrons

Y. Ikeda, K. Oishi<sup>\*</sup>, C. Konno and T. Nakamura

Tungsten (W) is one of potential candidate materials pertinent to the primary shielding and the armor of plasma facing component for the D-T fusion devices, e.g. ITER. An integral experiment has been carried out to examine adequacy of nuclear data of tungsten using the intense D-T neutron source, FNS. The dimension of W slab assembly was 320 mm in diameter and 250 mm in thickness. Nominal density of the W was 18.1 g/cm<sup>3</sup>. A 50 mm thick layer of stainless steel covered the side of the slab. The D-T neutron source was located at 200 mm distance from the surface of assembly. The reaction rate distribution as well as in-system spectrum were measured along the axis of assembly with the multiple foil activation technique and an NE213 spectrometer, respectively. In Fig. 5.2.1, measured reaction rate distributions are shown.

The neutron attenuation profile of 250 mm thick Tungsten was directly compared with those of Iron, Graphite, Beryllium and ordinary concrete, reaction rates in which had been measured previously in the same configuration of source to assembly<sup>1-4)</sup>. Figure 5.2.2 shows that the tungsten gives largest attenuation factor for the primary D-T neutron, which is given by the reaction rate  $^{90}\text{Zr}(n,2n)^{89}\text{Zr}$  with the threshold energy at 12 MeV; a factor of 2.5 to 10 higher than Fe, Be, C and concrete. A factor of 4 - 10 larger attenuation of lower energy neutrons by W was found in comparison with the materials through the reaction rate of  $^{115}\text{In}(n,n')^{115\text{m}}\text{In}$  with low threshold energy of 0.3 MeV. The most significant results were shown in the  $^{197}\text{Au}(n,\gamma)^{198}\text{Au}$  reaction rate distributions sensitive to the thermal neutrons.

The experimental analysis was performed by DOT3.5 with FUSION-J3<sup>5)</sup> based on the JENDL-3 nuclear data library. The C/E values for the high threshold reaction rates ranged between 0.94 and 1.03 through the whole region of the assembly. Although the agreement was reasonably good, the calculation tended to slightly underestimate the experiment for the reactions with threshold around 4 - 6 MeV. As shown in Fig. 5.2.3, the trend in underestimation was enhanced in the C/E for the reaction rates

---

\* Shimizu Corporation

with low threshold below 2 MeV. In particular, the large underestimation by 40% was found for the  $^{115}\text{In}(n,n')^{115\text{m}}\text{In}$  reaction. The integrated neutron spectrum obtained by the NE213 detector gave the same tendency in the reaction rate results.

These facts indicated that the calculation underestimated neutron flux below 5 MeV. This was strongly supported by the result for neutron spectrum with the NE213 detector. It was concluded that (a) the total cross section of tungsten in JENDL-3 for the 14 MeV neutron seemed adequate as long as the 250 mm thickness was concerned, (b) the elastic, inelastic and (n,2n) cross section must be underestimated in JENDL-3.

#### References

- 1) Oishi K., Ikeda Y., Maekawa H. and Nakamura T.: Nucl. Sci. and Eng. 103, (1989) 46-58.
- 2) Maekawa H., Yamaguchi S., Konno C., Oyama Y., Ikeda Y., Sekiyama K. and Kosako K.: "Benchmark Experiment and Analysis of a Beryllium Cylindrical Assembly", Fusion Technol. Vol.19 [3] Part B (1991) 1949-1954.
- 3) Maekawa H., Ikeda Y., Oyama Y., Yamaguchi S., Tsuda K., Fukumoto T., Kosako K., Yoshizawa M. and Nakamura T.: "Benchmark Experiments on a 60 cm-Thick Graphite Cylindrical Assembly", JAERI-M 88-034 (1988).
- 4) Oishi K., Ikeda Y., Konno C. and Nakamura T.: "Measurement and Analysis of Neutron Spectra in a Large Cylindrical Iron Assembly Irradiated by 14 MeV Neutrons", Proc. 7th Int. Conf. on Radiation Shielding, Bournemouth, UK, 12-16 Sep. (1988) 331-340.
- 5) K. Maki, Private communication.

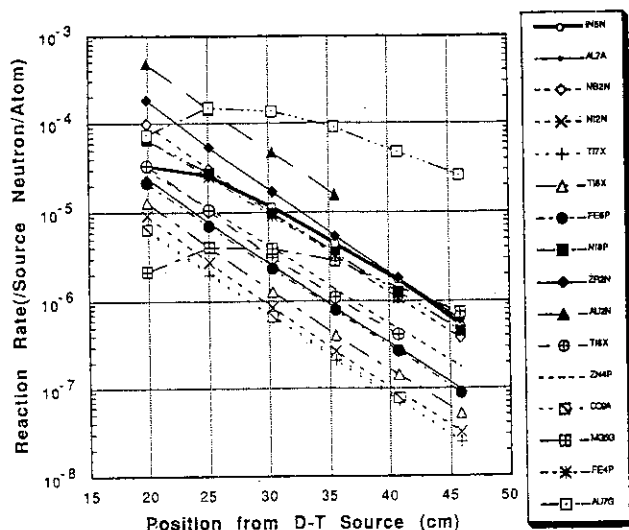


Fig. 5.2.1  
Reaction rate distributions  
in the tungsten assembly

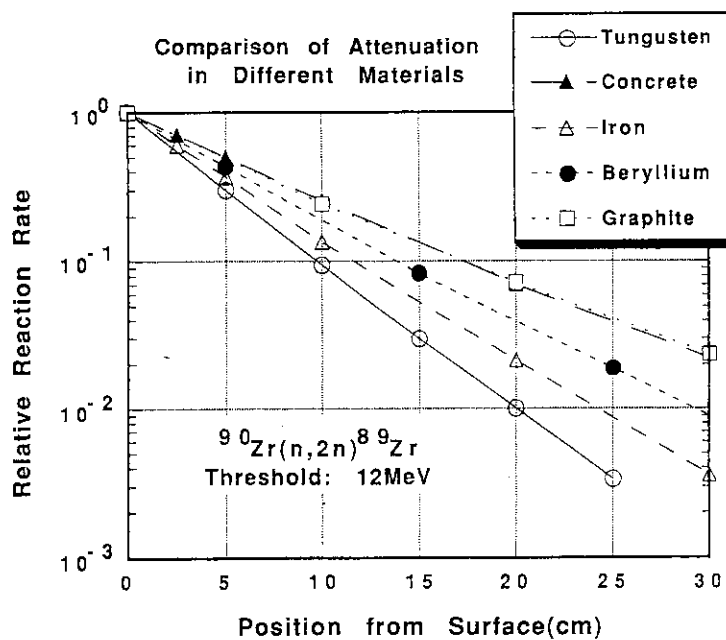


Fig. 5.2.2 The comparison of attenuation for the  $^{90}\text{Zr}(n,2n)^{89}\text{Zr}$  reaction rate in tungsten with those in concrete, beryllium, graphite and iron

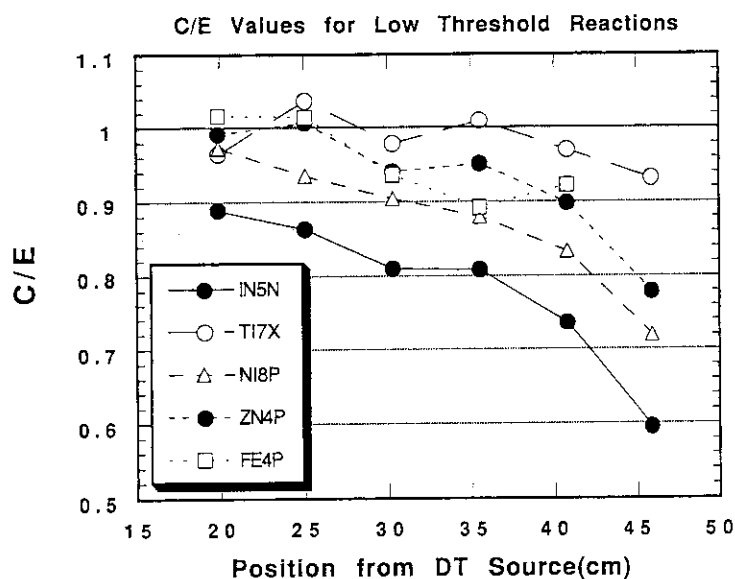


Fig. 5.2.3 The C/Es for the low threshold energy reaction rates

## 5.3 Self-Shielding Effect in Analysis of TOF Experiment on Iron Slab

Y. Oyama, K. Kosako and H. Maekawa

Shielding performance of iron for 14 MeV neutrons is very important to estimate radiation dose behind the bulk shield, e.g., the case as superconducting magnet in the ITER or FER machine. We had measured angular flux spectra leaking from the iron slabs of various thickness for 14.8 MeV incident neutrons by the time-of-flight technique.<sup>1)</sup> The experimental results were analyzed by the DOT3.5 and MCNP codes. It was pointed out from those results that the DOT3.5 results, in contrast to the MCNP, underestimated the flux in the energy range below 1 MeV with increase of the slab thickness. The reason of the underestimation in DOT3.5 calculations was considered to be due to the self-shielding effect in the multigroup cross sections with infinitely dilute density. Hence the effectiveness of self-shielding correction in the DOT calculations has been examined by analyses with self-shielding corrected cross sections<sup>2)</sup>.

The reference cross section set without self-shielding correction (infinite dilution) is FUSION-J3<sup>3)</sup> prepared for calculations in fusion neutronics with 125 groups for neutron and 40 groups for gamma-rays. Two types of the cross section sets corrected for the self-shielding effect, named JSSTD125 and JSSTD191, respectively, were obtained by reducing JSSTD295 set<sup>4)</sup> of 295 neutron groups with f-table. These sets include all expected impurities of the iron assembly and have 125 and 191 neutron groups, respectively. The JSSTD125 has the same group structure as FUSION-J3, and the JSSTD191 has the group structures of FUSION-J3 above 10 MeV and of VITAMINE-J below 10 MeV. Thus the group width of the latter set is almost a half of the JSSTD125 below 1 MeV. Both sets are based on JENDL-3. The comparison among the sets was performed for the 60 cm-thick slab case.

Figure 5.3.1 shows the comparison between the calculated results by the DOT3.5 with FUSION-J3 and the MCNP with JENDL-3. It is found that the MCNP agrees very well with the experiment, but the DOT/FUSION-J3 underestimates the flux in the range below 1 MeV. The figure also shows the results by the DOT/JSSTD125 which gives less underestimation than the DOT/FUSION-J3. However the JSSTD125 still underestimates the flux in the range of 500 keV to 1.5 MeV compared to the MCNP. The comparison between the JSSTD125 and the JSSTD191 indicates the effect of group width on the

self-shielding correction. Figure 5.3.2 shows the calculations by both sets. From the comparison it is remarked that the calculation with fine group improves much the agreement of the peak at the 80 keV, but it does not much reduce the discrepancy on the whole. Hence these suggest that the cause of the discrepancy between the DOT and the MCNP calculations in the range of 500 keV to 1 MeV includes the other reasons such as  $P_L$ - $S_N$  approximation.

#### References

- 1) Oyama Y. and Maekawa H.: "Angular Neutron Flux Spectra Leaking from Thick Iron Slabs Bombarded with D-T Neutrons", Reactor Engineering Department Annual Report, JAERI-M 90-149, pp. 98-100 (1990).
- 2) Oyama Y., Kosako K., Maekawa H.: "Self-Shielding Effect on Angular Neutron Flux Spectra Leaking from Thick Iron Slab", Proc. 2nd Specialists' Meeting on Nuclear Data for Fusion Reactors, JAERI-M 91-032 (NEANDC(J)-162/U), pp. 314-318 (1991).
- 3) Maki K., et al.: "Nuclear Group Constant Set FUSION-J3 for Fusion Reactor Nuclear Calculations Based on JENDL-3", JAERI-M 91-072 (1991) (in Japanese).
- 4) Hasegawa A.: "JENDL-295n-104G; a Common Nuclear Group Cross-Section Library Based on JENDL-3 Nuclear Data File", Proc. 2nd Specialists' Meeting on Nuclear Data for Fusion Reactors, JAERI-M 91-032 (NEANDC(J)-162/U) pp. 15-25 (1991).



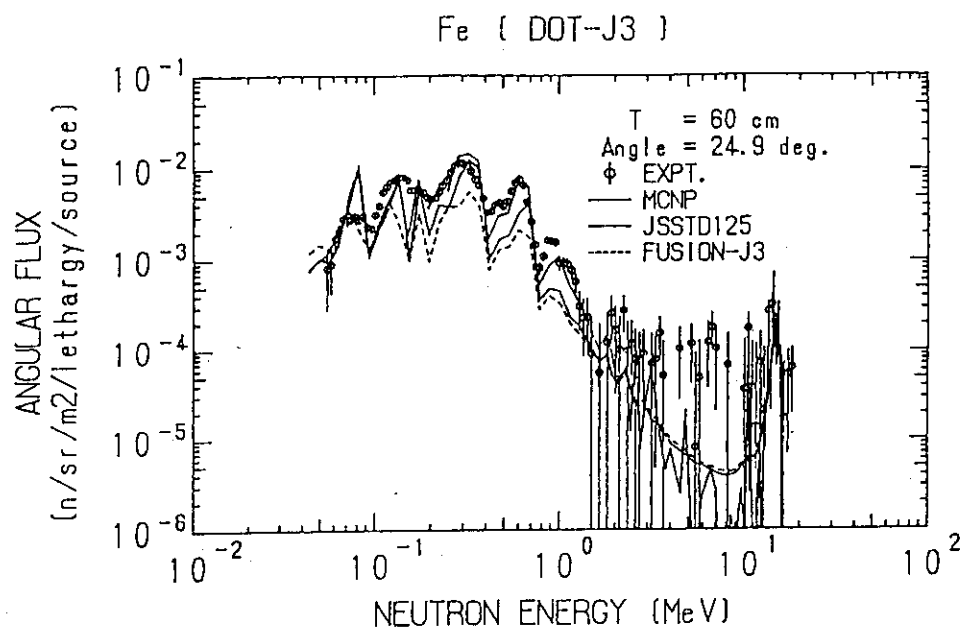


Fig. 5.3.1 Comparison among the results by the DOT3.5/FUSION-J3, DOT3.5/JSSTD125 and the MCNP for the 60 cm-thick iron assembly

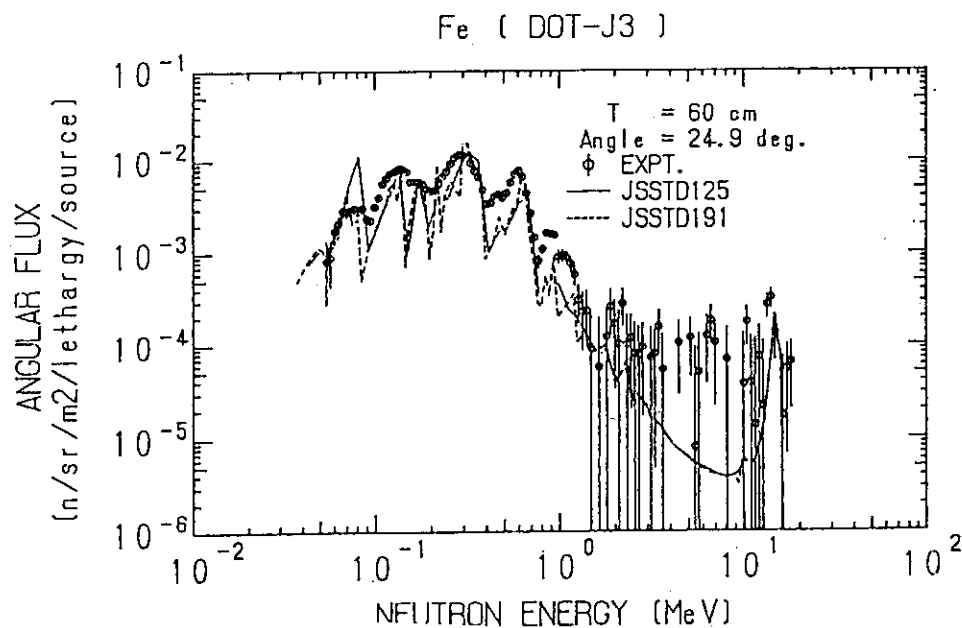


Fig. 5.3.2 Comparison between the DOT3.5 calculations with the JSSTD125 and the JSSTD191 cross section sets for the 60 cm-thick iron assembly

#### 5.4 Post-Analysis of Phase-IIIA Experiment of JAERI/USDOE Collaborative Program on Fusion Neutronics

K. Kosako and Y. Oyama

An experimental analysis has been carried out for the phase-IIIA experiment<sup>1,2)</sup> of JAERI/USDOE collaborative program on fusion neutronics. The phase-IIIA experimental configuration shown in Fig. 5.4.1 was featured by an annular blanket system and a pseudo-line D-T neutron source, which simulated a torus configuration in tokamak fusion reactor. The measured parameters were tritium production rates, activation reaction rates and neutron spectra.

In the analysis of phase-IIIA experiment, it is very important to treat accurately the angular distribution of outgoing neutron from D-T target. The angular distribution of source neutron was calculated by a Monte Carlo code MORSE-DD with a detailed model of the target assembly structure. An interval of 5 degree for the neutron emission angle was adopted. The calculated angular intensity had two large dips caused by target structure as shown in Fig. 5.4.2. The peak energy of spectrum varies from 14.9 MeV to 13.3 MeV with the angle. On the basis of these results, we modified the source generation routines of a discrete ordinate code DOT3.5 and MORSE-DD to treat the angular distribution of the pseudo-line source. Then, the calculations for the annular assembly have been performed by DOT3.5 and MORSE-DD with the multigroup cross section libraries FUSION-J3<sup>3)</sup> and DDXLIB-J3<sup>4)</sup>, both of which were based on JENDL-3. The INTERF code<sup>5)</sup> was used to retrieve the parameters, such as reaction rates, from DOT3.5 and MORSE-DD results.

There were two parts in the analysis; one was the source term without assembly, the other was with the annular blanket assembly. Figure 5.4.3 shows the ratios of calculated to measured values (C/E) of reaction rates along the line source without the annular blanket. The calculated values agreed within  $\pm 5\%$  with the measurements except  $^{58}\text{Ni}(n,p)$  and  $^{64}\text{Zn}(n,p)$  reactions. For the case with the annular blanket, the calculated values agreed within  $\pm 10\%$  for reaction rates, and the calculated spectra also agreed within  $\pm 10\%$  with the measurements by NE213 and PRC. The flat distributions of C/Es for reaction rates along the line source demonstrated the feasibility of the source angular distribution.

The calculated TPRs for lithium 6 ( $T_6$ ) in the  $\text{Li}_2\text{O}$  blanket region

agreed within  $\pm 10\%$  with the measurements as shown in Fig. 5.4.4. Those for lithium 7 ( $T_7$ ) also agreed within  $\pm 10\%$ . For most of the reaction rates, the calculation agreed within  $\pm 5\%$  with the measurement as shown in Fig. 5.4.5. While the C/E trend of reaction rate by MORSE-DD was very flat, those by DOT3.5 was slightly underestimated with depth. The difference of C/E between the both codes, however, was mostly 5%. In conclusion, the present calculation for the phase-III A system predicted the measurement with accuracy of  $\pm 10\%$ .

#### References

- 1) Oyama Y., et al.: "Reactor Engineering Department Annual Report", JAERI-M 90-149, 107 (1990).
- 2) Konno C., et al.: *ibid.*, JAERI-M 90-149, 110 (1990).
- 3) Maki K., et al.: "Nuclear Group Constant Set FUSION-J3 for Fusion Reactor Nuclear Calculations Based on JENDL-3", JAERI-M 91-072 (1991) (in Japanese).
- 4) Nakagawa M.: Private communication (1991).
- 5) Kosako K.: "INTERF: The Reaction Rates and Spectra Editing Code for Analysis of Fusion Neutronics Experiments", JAERI-M 90-199 (1990) (in Japanese).

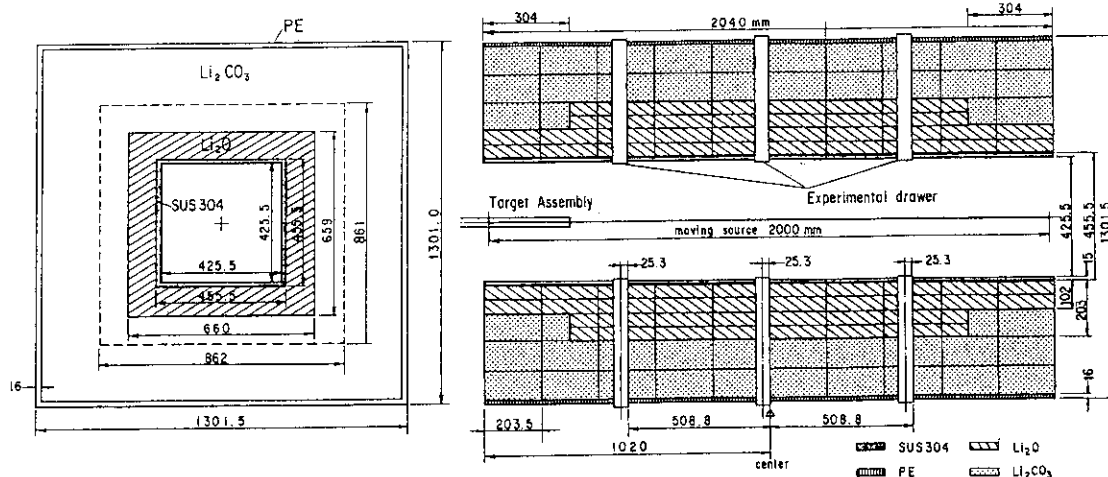


Fig. 5.4.1 Vertical and horizontal cross sectional views of the phase-III A annular blanket

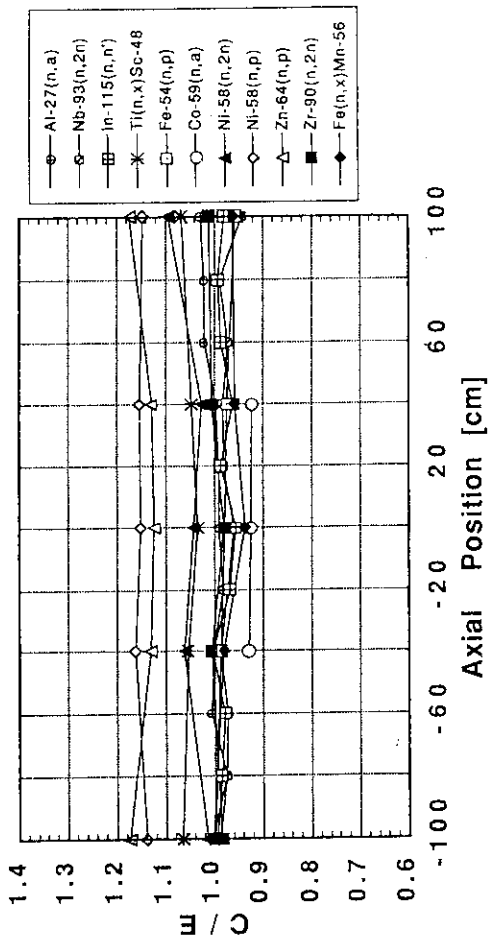


Fig. 5.4.3 C/E distributions of DOT3.5 for reaction rates along line source without blanket

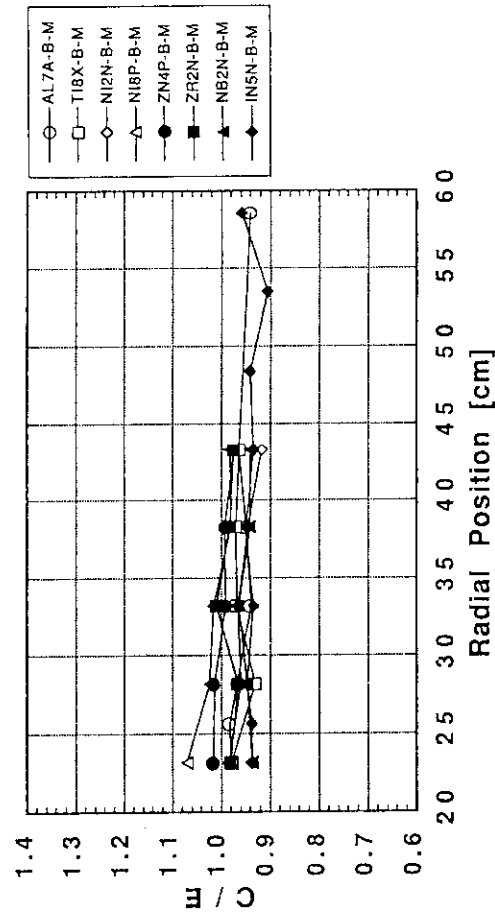


Fig. 5.4.5 C/E distributions of MORSE-DD for reaction rates in center drawer along radial direction

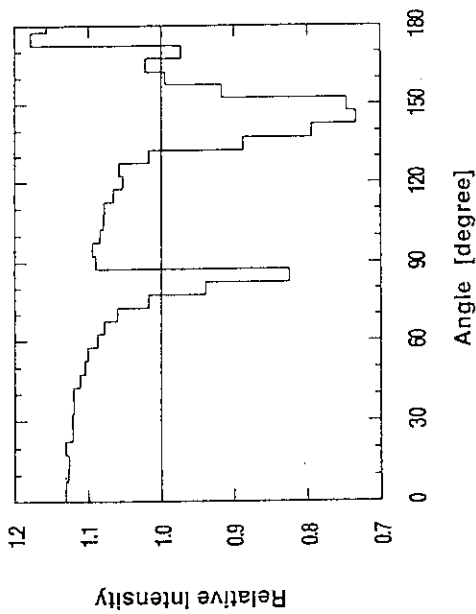


Fig. 5.4.2 Relative angular intensity of the D-T target

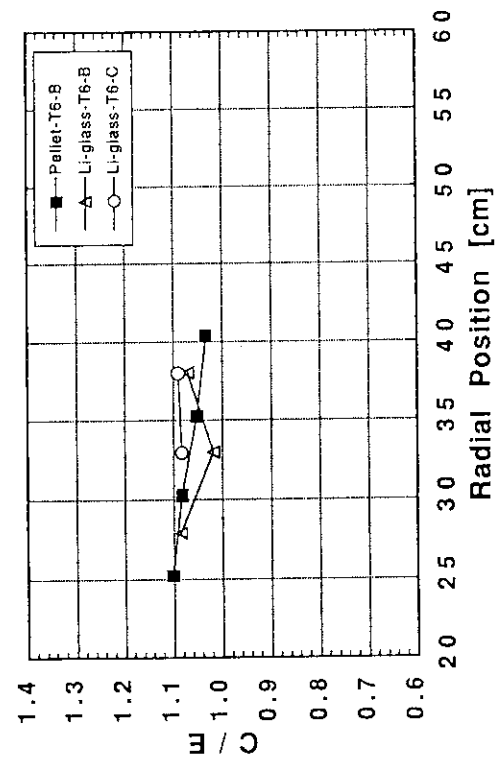


Fig. 5.4.4 C/E distributions of DOT3.5 for TRP (T<sub>6</sub>) in blanket along radial direction

## 5.5 Phase-IIIB Experimental Results of JAERI/USDOE Collaborative Program

Y. Oyama, C. Konno, Y. Ikeda, F. Maekawa, H. Maekawa, A. Kumar<sup>\*</sup> and M. Abdou<sup>\*</sup>

As the second series of Phase-III experiment in the JAERI/USDOE collaborative program on fusion neutronics, integral experiment of lithium-oxide annular blanket with graphite armor has been carried out using pseudo-line source facility<sup>1-4)</sup> at FNS. The graphite armor of 25 mm in thick was placed inside the first wall of 15 mm in thick of the Phase-IIIA assembly, i.e., the inner dimension of the cavity was 375.5 mm and the axial length was 2040 mm. In this case, the Phase-IIIA system served as a reference for the annular blanket and line source system. Figure 5.5.1 shows the configurations of liners for the cavity. The graphite armor was expected to make much reflected neutrons which are traveling along the cylindrical cavity by small-angle scattering. This feature was expected to enhance the effect of annular geometry on the neutronics parameters at the location close to the first wall. The data obtained in this experiment were compared to the previous Phase-IIIA results.

The experiment was performed in the same way as the previous experiment using three experimental channels along the radial direction. The line-source was produced in both stepwise and continuous modes. The measured parameters were tritium production rate (TPR) with NE213-indirect method, Li-glass technique and liquid scintillation counting technique of Li<sub>2</sub>O pellet, neutron spectrum with recoil proton spectrometers by NE213 and gas proportional counter, and reaction rate with several activation foils. In addition, gamma-ray spectrum and gamma-ray heating rate were measured by using a newly developed 40 mm-diameter spherical NE213 scintillator and thermo-luminescence detectors, respectively. For the on-line detectors including gas proportional counter, the detector responses from each source position in the stepwise mode were taken.

Figure 5.5.2 shows the results of TPR distribution at the central drawer measured by Li<sub>2</sub>O pellets and also compares the results with the reference case without graphite armor (Phase-IIIA). The TPR of Li-6 (T<sub>6</sub>) increased by about 20% at the front and the T<sub>7</sub> decreased by about 30% on the whole. Consequently the TPR of natural lithium increased only several

---

<sup>\*</sup> University of California, Los Angeles

% at the front. The source position profile of T6 reaction rate at the detector location obtained by Li-glass is shown in Fig. 5.5.3. Most of increase of T6 came from the nearest source position, and the source contributing to the increase of T6 at the center spread within 70 cm distance from the center. This meant that only 140 cm long region of the cavity liner along the source was important to the T6 at the central drawer.

The post-analysis of the experiment is in progress by both parties of JAERI and UCLA using DOT3.5 and MORSE-DD codes, and DOT5.1 and MCNP, respectively. The analyses on the margin for reactor design calculations will be done in the further study.

#### References

- 1) Nakamura T., et al.: "A Line D-T Neutron Source Facility for Annular Blanket Experiment: Phase III of the JAERI/USDOE Collaborative Program on Fusion Neutronics", Fusion Technol. 19, 1873 (1991).
- 2) Oyama Y., et al.: "Annular Blanket Experiment using a Line DT Neutron Source: Phase IIIA of the JAERI/USDOE Collaborative Program on Fusion Neutronics", *ibid.*, 1879 (1991).
- 3) Konno C., et al.: "Measurements of the Source Term for Annular Blanket Experiment with a Line Source: Phase IIIA of the JAERI/USDOE Collaborative Program on Fusion Neutronics", *ibid.*, 1885 (1991).
- 4) Youssef M., et al.: "Analysis for the Simulation of a Line Source by a 14 MeV Moving Point Source and Impact on Blanket Characteristics: The USDOE/JAERI Collaborative Program on Fusion Neutronics", *ibid.*, 1843 (1991).

## PHASE-III Experiment

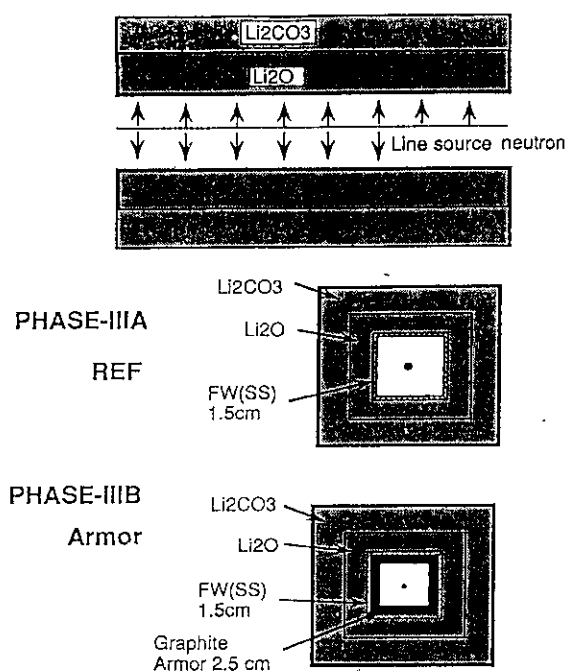


Fig. 5.5.1  
Experimental configuration of  
Phase IIIA and IIIB

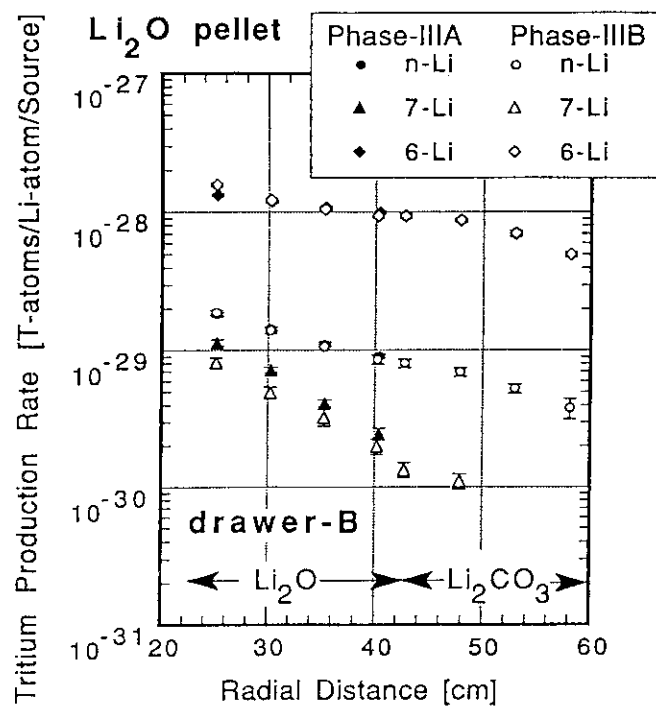


Fig. 5.5.2  
Tritium production rate distribution  
of Li at the central drawer measured  
by  $\text{Li}_2\text{O}$  pellets in comparison with  
the Phase-III A results

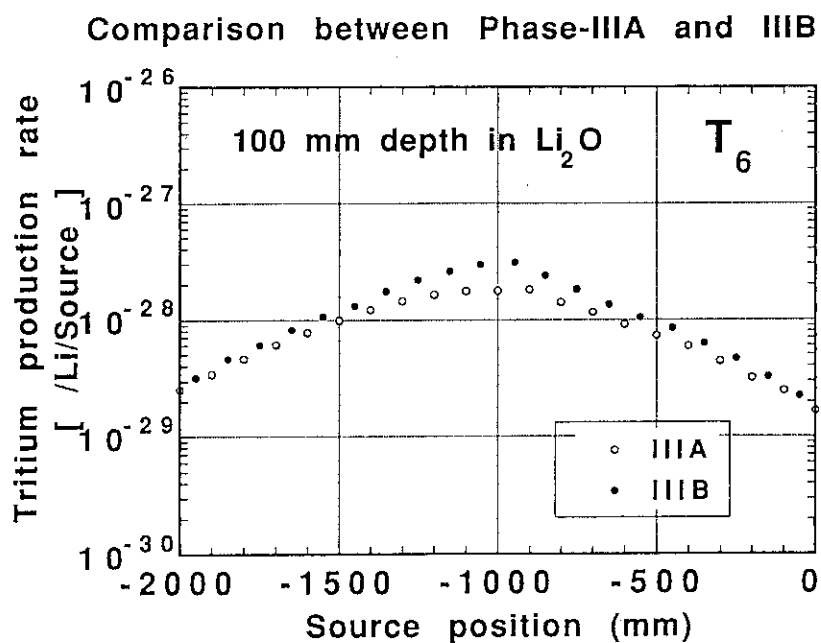


Fig. 5.5.3 Source position profile for tritium production  
rate of  $\text{Li-6}$  measured by Li-glass technique  
in comparison with the Phase-III A

## 5.6 Experimental Verification of the Current Data and Methods for Induced Radioactivity and Decay Heat Calculation in D-T Fusion Reactors

Y. Ikeda, A. Kumar<sup>\*</sup>, C. Konno, Y. Oyama, T. Nakamura, M.Z. Youssef<sup>\*</sup> and M.A. Abdou<sup>\*</sup>

From the preliminary analysis of integral experiments for induced activity<sup>1,2)</sup>, it has been clearly pointed out that there were large discrepancies between the experiment and the calculation in terms of  $\gamma$ -ray emission rates for materials of Mo, W, Mn-Cu alloy, Ti, V. In this study, the major sources of the large discrepancies were investigated in order to resolve the problems. Twenty materials of Mg, Al, Si, Ti, V, Cr, Mn-Cu alloy, Fe, Co, Ni, SS-316, Zn, Zr, Nb, Mo, Ag, Sn, Ta, W, and Pb were subjected in the present study.

The experimental analysis has been carried out by the currently available code systems of THIDA-2<sup>3)</sup>, REAC-2<sup>4)</sup> and DKR-ICF<sup>5)</sup>. Since the cross section library of THIDA-2 has been recently updated, experimental analysis has been carried out using the new version of library. In Fig. 5.6.1, C/E values for the cases (at  $\text{Li}_2\text{O}$  region in the Phase-IIC assembly, after 10 h irradiation) are plotted against the materials. One of major topics was given on the improvement of the calculation accuracy in the result of THIDA with the new cross section library (New) from that with old one (Old).

As an example for the analysis, investigation for the Vanadium case is given as follows: New version of the cross section in THIDA gave much improvement in the C/E ratios as shown in Table 5.6.1. This was mainly due to the improvement of the cross section for the  $^{51}\text{V}(n,\alpha)^{48}\text{Ti}$  being 16.2 mb which was close to the experimental data at FNS. The Old value at 14 MeV was 20% larger than the New one which was very consistent with the currently available experimental data at FNS. The overestimations in the REAC-2 and DKRICF calculations by 40% and a factor of three, respectively, were also explained by too large cross section values, 24.3 mb and 45.2 mb, respectively. It should be noted that there was no corresponding  $\gamma$ -ray peak to the activity of  $^{47}\text{Sc}$  in the measurement though calculation presented prominent lines for all calculations. The cross

---

\* University of California, Los Angeles CA 90024-1579, USA



sections of production reaction for  $^{47}\text{Sc}$  were evaluated from reaction systematic or theoretical prediction because of lack in the experimental data at 14 MeV. As long as the experimental evidence showed, the cross section must be subjected to be measured.

### Summary

The adequacy of code systems used was assured by the integral test on the reaction products for  $^{24}\text{Na}$ ,  $^{56}\text{Mn}$ ,  $^{92}\text{mNb}$ , cross section of which were assumed well evaluated with sufficient accuracy. Also, the reasonable C/E values indicated that the neutron energy spectrum above 1 MeV could be reasonable for each code. The experimental analyses for induced radioactivities in various spectra indicated inadequacy for considerable large numbers of the activation cross section data in the currently available libraries. The present study has clearly pointed out the specific reactions which gave rather poor C/Es. Thus, we could reach a reasonable solution or acceptable levels of the adequacy in the data base as long as the threshold type reactions were taken account. One serious problem associated with inadequate prediction in the products of  $(n,\gamma)$  reactions, however, was still left to be verified. However, referring that the  $^{197}\text{Au}(n,\gamma)^{198}\text{Au}$  reaction rate was systematically underestimated by 40 - 50% in the Phase-IIIC cavity through the analysis by DOT3.5 and MORSE-DD, it was concluded that the low energy neutron spectra in the Phase-IIA and IIB should be softer than those calculations. Thus, the underestimations in the codes for some products by  $(n,\gamma)$  reactions were attributable for inaccuracy in the neutron transport calculation.

We have encountered on serious improper data base associated with the decay  $\gamma$ -ray branching ratios. This would be simply because of unexpected human error in making so large data library. But it would be very important because many design calculations have been carried out giving the criticality of specific items of concern without noticing the incorrectness of the data. In this context, emphasis should be placed on the importance of the integral experiments for verifying codes and data.

### References

- 1) Ikeda Y., Kumar A., Konno C., Nakamura T. and Abdou M.A.: "Experiment on Induced Activities and Decay-Heat in Simulated D-T Neutron Fields-JAERI/USDOE Collaborative Program on Fusion Neutronics", Fusion Technol. Vol. 19, 3, PartB p.1961 (1991).

- 2) Kumar A., Ikeda Y., Abdou M.A. and Nakamura T.: "Analysis of Induced Activities Measurements Related to Decay Heat in Phase-IIC Experimental Assembly: JAERI/USDOE Collaborative Program", *ibid.*, p.1909.
- 3) Seki Y., Iida H., Kawasaki H. and Yamada K.: "THIDA-2: An Advanced Code System for Calculation of Transmutation, Activation, Decay Heat and Dose Rate", JAERI-1301 (1985).
- 4) Mann F.M.: REAC2: Status of Codes and Libraries, Fusion Technology, 15, p.449 (1989).
- 5) Henderson D.L. and Yasar O.: "DKR-ICF: A Radioactivity and Dose Rate Calculation Code Package", Vol. 1 and 2, UWFD-714 (1986).

Table 5.6.1 C/E values for vanadium cases

Case	THIDA-Old	THIDA-New	REAC-2	DKR-ICF
AS	0.88	0.78	1.06	1.35
AL	1.59	1.22	1.57	3.4
BS	1.09	1.03	1.3	1.8
BL	1.4	1.10	1.4	3.1

A: Irradiation position at 10 cm from the D-T source

B: Irradiation position at 5 cm depth in the Li<sub>2</sub>O region

S: Short irradiation (30 m) and short cooling (1 h)

L: Long irradiation (10 h) and long cooling (15 h)

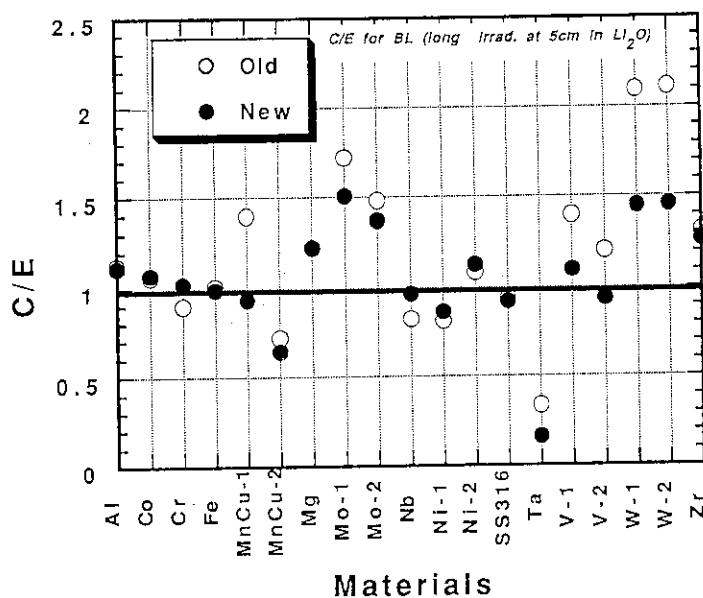


Fig. 5.6.1 The C/E values corresponding to both THIDA-Old and THIDA-New for the case of after 10 h irradiation at Li<sub>2</sub>O region in Phase-IIC assembly

## 5.7 International Comparison on Measuring Techniques of Tritium Production Rate for Fusion Neutronics Experiments

### --- Summary of Additional Questionnaire

#### and Result for ANL Samples ---

H. Maekawa

The first International Comparison on Measuring Techniques of Tritium Production Rate was done under the framework of NEACRP activity. Eight institutes and Universities from six countries applied to this comparison program. The report (NEACRP-A-1021; JAERI-memo 90-123), that was presented at the 32nd NEACRP meeting, revealed differences among the data beyond the target accuracy. To examine the causes of this discrepancies, two actions have been performed. One was the additional questionnaire for the detailed procedure of sample treatment and tritium counting. The other was the comparison of measured tritium concentrations of standard samples supplied by ANL.

### Summary of Additional Questionnaire

Three groups employed the Dierckx method to obtain a liquid scintillation sample. The rest five groups adopted quite different methods. In the case of Dierckx method, almost all tritium produced were transferred to the liquid scintillation sample except the tritium remained in gas-phase. In the cases of ANL and JAERI, most part of tritium produced was collected to make the liquid scintillation sample. While AECL sampled only about one percent of tritium produced.

---

### Contributors:

ANL/U.S.A.	K.G. Porges
AECL-CRNL/Canada	W. Workman, J.M. Miller, I.J. Hastings
IGA-EPFL/Switzerland	S. Azam, M. Schaer
ENEA/Italy	A. Moauro, P.L. Carconi
CEN Cadarache/France	P. Michailli
Univ. Tokyo/Japan	T. Iguchi, M. Nakazawa
Osaka Univ./Japan	S. Yoshida, A. Takahashi
JAERI/Japan	H. Maekawa, F. Maekawa, T. Nakamura

This report was presented at the 33rd NEACRP Meeting Oct. 15 - 19, 1990  
Paris, France.

As a dry method was adopted at ANL, it was not necessary to consider the tritium in gas-phase. CEN/Cadache and JAERI considered the tritium in gas-phase but the other five groups ignored. In the case of JAERI, the quantity of tritium in gas-phase was estimated separately using samples irradiated near the target. Because the quantity of tritium in gas-phase for a  $\text{Li}_2\text{O}$  pellet irradiated in the simulated blanket assembly was too small to measure.

Though the minimum of signal to background ratio was 1.6 and not so high, we could still measure the tritium concentration with adequate error under a long measuring time.

From the additional questionnaire, we could not deduce any concrete reason why the tritium production-rate reported was deviated so largely.

#### Summary of Present Comparison for ANL Sample

In the beginning of April 1990, JAERI sent a set of return form for the report of measured tritium concentration of the diluted ANL samples to the participants. The reports were sent back to JAERI from the participants except the University of Tokyo by the end of July, 1990. The result is shown in Table 5.7.1. From the present comparison, we can summarize as follows:

- (1) Using an appropriate tritium water standard with high accuracy for the calibration of liquid scintillation counting system, we can expect a good agreement for a blind sample among the participants.
- (2) All participants have the ability of measurement for the tritium concentration level of several Bq/g. Namely, we can measure the tritium production rate in a simulated fusion blanket under the irradiation level of  $7 \times 10^{15}$  neutrons at the target. This total neutron yield can be obtained by the D-T neutron yield rate of  $2 \times 10^{11}$  n/s and 10 hours irradiation. This irradiation level is corresponding to the last experiment at FNS.
- (3) It is important to obtain a liquid scintillation sample keeping the loss of tritium produced as low as possible without any contamination. Namely, the method and technique are essential for the chemical treatment of irradiated sample with lithium. If all participants adopt an appropriate method to extract the tritium produced from the irradiated sample and to make a good liquid scintillation sample, a good agreement is expected among the results of tritium production rate measured by the participants.

Table 5.7.1 Measured tritium concentration on April 1, 1990 for ANL samples

[ Unit : Bq/g ]

Sample ID	ANL U.S.A.	AECL/CRNL Canada	IGA/EPFL Switzerland	ENEA Italy	CEN/Cadr. France	U. Tokyo Japan	Osaka U. Japan	JAERI Japan
A 257.0±2.2*	257.3±2.7 (1.001)**	261.8±4.6 (1.019)	258.8±1.04 (1.007)	270.2±5.5 (1.051)	253.6±0.44 (0.987)	-----	270.9±0.8 (1.054)	260.0±3.3 (1.012)
B 48.54±0.42	48.42±0.40 (0.998)	49.0 ±0.9 (1.009)	51.5 ±0.52 (1.061)	50.4 ±0.5 (1.038)	48.10±0.25 (0.991)	-----	52.02±0.33 (1.072)	49.12±0.60 (1.012)
C 3.87 ±0.03	3.893±0.021 (1.006)	3.88 ±0.09 (1.003)	4.1 ±0.13 (1.059)	4.69 ±0.38 (1.212)	3.798±0.023 (0.981)	-----	4.172±0.090 (1.078)	3.898±0.057 (1.007)
Blank	0.134±0.003	0.142±0.006	(0.233cps)	0.505±0.076	0.292±0.009	-----	0.508±0.033	0.052±0.012
Background	Same as above	0.132±0.002	Same as above	0.170±0.007	Same as above	-----	0.459±0.030	0.049±0.009

\* Data are assigned by Dr. R. R. Heinrich (ANL) and corrected for decay.

\*\* Ratio to the assigned value.

## 5.8 Characteristics of a 40 mm Diameter NE213 Scintillation Counter for In-System Gamma-ray Spectrum Measurement

F. Maekawa and Y. Oyama

In the field of fusion neutronics, in-system gamma-ray spectrum provides important information about nuclear heating of the system. In-system gamma-ray spectrum measurement, however, has been scarcely performed so far. The followings are required for a detector of the in-system gamma-ray measurement. 1) Gamma-rays should be discriminated from neutrons, 2) Background gamma-rays which are generated by neutron reaction in the detector itself should be negligible, and 3) The detector must have an isotropic property. To satisfy all the requirements, we chose a 40 mm diameter spherical NE213 liquid scintillation counter which has good pulse shape discrimination, isotropic properties and small neutron capture cross sections. The counter assembled is shown in Fig. 5.8.1. A gain-stabilizing system is equipped to suppress gain fluctuation.

In our laboratory, a fourteen millimeter diameter NE213 scintillation counter has been used for a neutron spectrometer. The size of 14 mm corresponds to the range of 2.5 MeV electrons which are produced by Compton scattering with 2.7 MeV gamma-rays, resulting in losing electron energy information above 2.5 MeV. On the other hand, the size of 40 mm covers an energy range of 6 MeV electrons which are produced by pair production with 13 MeV gamma-rays. This large size, however, results in having larger perturbation and less spatial resolution in comparison with the 14 mm diameter NE213. Nevertheless this deficiency can be allowed for testing accuracy of 10 - 20%.

Linearity between electron energy and light yield up to 3.4 LU (LU:  $^{22}\text{Na}$  light unit) was examined in the same way as ref.<sup>1)</sup>. The result is shown in Fig. 5.8.2. The measured data were fitted by function of a linear form above 0.3 LU and a power form below 0.3 LU with the least squares method within 1%. To confirm the linearity for the range over 3.4 LU, light yields of recoil protons which result from neutron scattering were measured. The energy of proton ranges from 1 to 14.7 MeV, which corresponds to a light yield range from 0.2 to 7.5 LU. From comparison with V.V. Verbinski's data<sup>2)</sup> both results agreed each other within experimental error of 4%.

To unfold pulse height distribution into energy spectrum, a response matrix was calculated with a Monte Carlo code MARTHA<sup>3)</sup> modified for NE213. Not only the 40 mm diameter NE213 scintillator but also a 3 mm thick aluminum layer and a 38 mm diameter by 40 mm long aluminium cylinder were taken into account to make a precise model of the counter. The size of the response matrix was 62 energy points by 100 light yield bins, which corresponded to 0.2 to 11.5 MeV and 0.05 to 10.0 LU, respectively. The relation between light yield and electron energy as shown in Fig. 5.8.2 and measured energy resolution were taken into account in the calculation. In order to estimate the accuracy of the calculation, calculated response functions with MARTHA were compared with the measured ones and the calculated ones with another Monte Carlo code EGS<sup>4)</sup>. Results for <sup>137</sup>Cs and <sup>24</sup>Na sources are shown in Figs. 5.8.3 and 5.8.4, respectively. Though the both calculated results underestimated the measured ones below 0.3 LU, agreement among three results was very well above 0.3 LU within 5%.

To verify the overall measurement system, measurements on mono-energetic gamma-rays of calibrated standard sources (0.3 - 1.8 MeV) were carried out. Every spectrum for <sup>88</sup>Y was obtained above 0.25 MeV by the FORIST unfolding code as shown in Fig. 5.8.5. Two peaks were well reproduced, while an unexpected tail was observed below 0.6 MeV. The measurement overestimated the actual intensities of gamma-ray for all sources by 8% at maximum. This overestimation may be due to the disagreement of response function mentioned above. Achieved energy resolution (FWHM) was 16 and 21% for 2.754 MeV and 0.662 MeV gamma-rays, respectively.

#### References

- 1) Oyama Y., et al.: Nucl. Instr. and Meth., 256 (1987) 333.
- 2) Verbinski V.V., et al.: ibid., 65 (1968) 8.
- 3) Saito K. and Mori S.: "Monte Carlo Calculation of Accurate Response Functions of a NaI(Tl) detector for Gamma Rays and Analysis of Pulse Height Spectrum Formation Mechanism", JAERI-M 9471 (1981).
- 4) Nelson E.R., Hirayama H. and Rogers D.W.O.: "The EGS4 Code System", SLAC-265 (Stanford University, 1985).
- 5) Forist Spectrum Unfolding Code, Radiation Shielding Information Center, Oak Ridge National Laboratory, PSR-92 (1975).

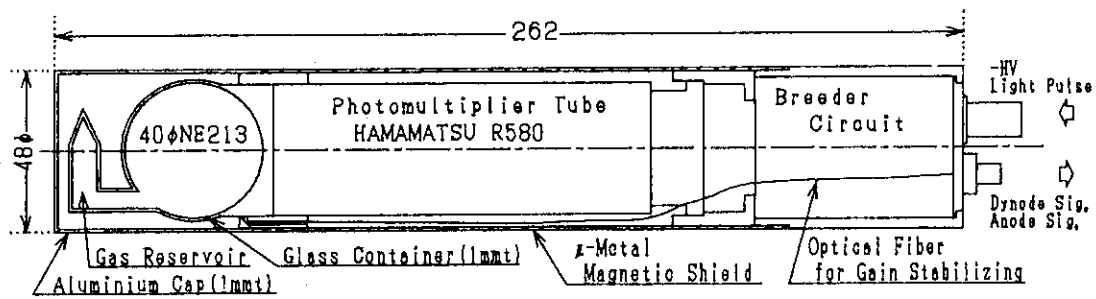


Fig. 5.8.1 Cross sectional view of 40 diameter spherical NE213 scintillation counter

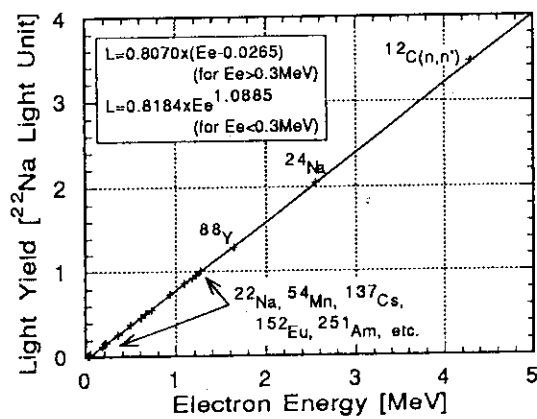


Fig. 5.8.2 Relation between Compton scattered electron energy and light yield

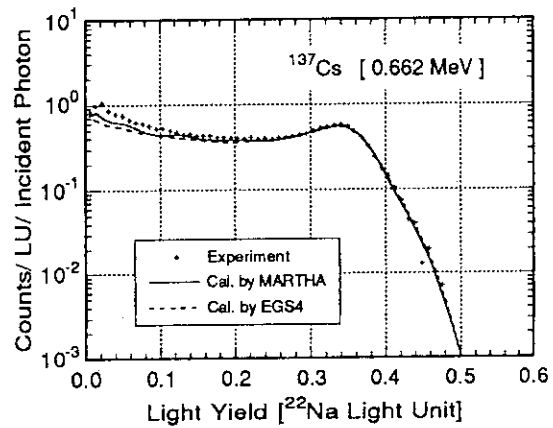


Fig. 5.8.3 The measured and calculated response functions for  $^{137}\text{Cs}$  source

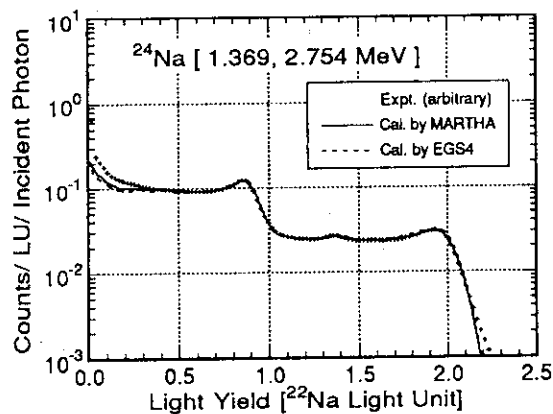


Fig. 5.8.4 The measured and calculated response functions for  $^{24}\text{Na}$  source

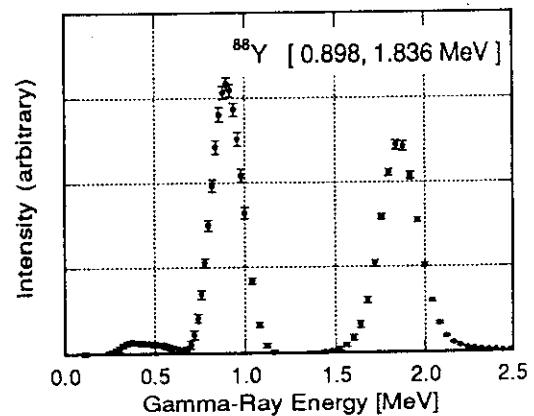


Fig. 5.8.5 Unfolded energy spectrum for  $^{88}\text{Y}$  source



## 5.9 14 MeV Neutron Generation Characteristics of FNS Rotating Target

C. Kutsukake, J. Kusano, S. Tanaka and Y. Abe

It has been proposed to upgrade the FNS accelerator in terms of increasing beam current for achieving higher intense neutron generation to meet requirement from the next fusion neutronics experiments. For the purpose, it is important to have basic data of the target performance such as the dependency of neutron generation rate on total incident beam current, incident heat flux, difference in position of beam spot on the target, and gas release from the tritiated titanium. At the FNS facility, a Rotating Target system is currently used for high intense neutron generation. In a usual operation for high intense neutron generation, the deuteron beam energy and current are 350 keV and 20 mA, respectively. The target disk has tritium amount of 24 - 35 TBq absorbed in titanium layer deposited on a copper alloy of 230 mm in diameter.

A diagnostic operation was carried out to get the neutron generation characteristics on high beam current condition. The beam current was measured by an electrometer. It was calibrated by calorimetric method to eliminate secondary electron effect. The neutron generation rate was measured by using the associated alpha particle counter method and a thorium fission counter<sup>1)</sup>. The tritium gas release to the beam duct was analyzed by a quadrupole mass analyzer. The temperature dependency of tritium gas release rate from a small piece of tritiated titanium was measured independently. A catalyzer, a cold trap and a liquid scintillation counter were used in the measurement. The small piece of the tritiated titanium was sampled during target handling work.

The present study gave results on the neutron generation characteristics as follows;

- (1) Figure 5.9.1 shows data of initial neutron generation rate and decreases of the neutron generation rate as a function of total incident deuterons. A maximum value of initial neutron generation rate was  $2 \times 10^{11}$  n/s/mA.
- (2) Figure 5.9.2 shows the relative change of neutron generation with integrated incident deuterons as a function of different position of beam spot on the target. The position is denoted by the tilt angle in percentage as shown in Fig. 5.9.2. It was observed that the neutron generation rate at inner position of the target decreased

more rapidly with integrated deuteron beam current than those at outer position. A sudden drop in neutron generation rate occurred when the beam current exceeded 20 mA. The tritium gas release rate in the beam duct increased abruptly when the beam current exceeded 20 mA. Those results indicate clearly that in the present system 20 mA is a limit of the beam current for stable neutron generation from a cooling capacity point of view.

- (3) Figure 5.9.3 shows the temperature dependency of tritium gas release rate from the small piece of the tritiated titanium. The released gas consisted of 90% of the tritium gas and 10% of the tritium moisture. All of tritium gas in titanium was released when the titanium temperature exceeded 300°C. The result of the experiment suggested the temperature of tritiated titanium area should be kept under 300°C.

In conclusion, temperature control of the target was most critical issue to design a new target system pertinent for upgrading FSN.

#### Reference

- 1) Maekawa H., et al.: "Neutron yield monitors for the fusion neutronics source (FNS)", JAERI-M 83-219 (1983).

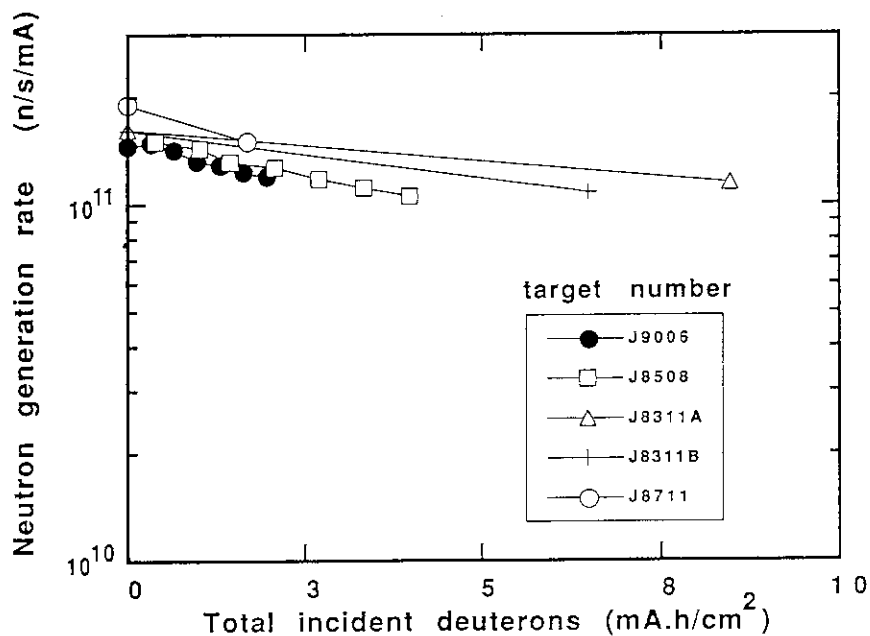


Fig. 5.9.1 Neutron generation rate of RNT

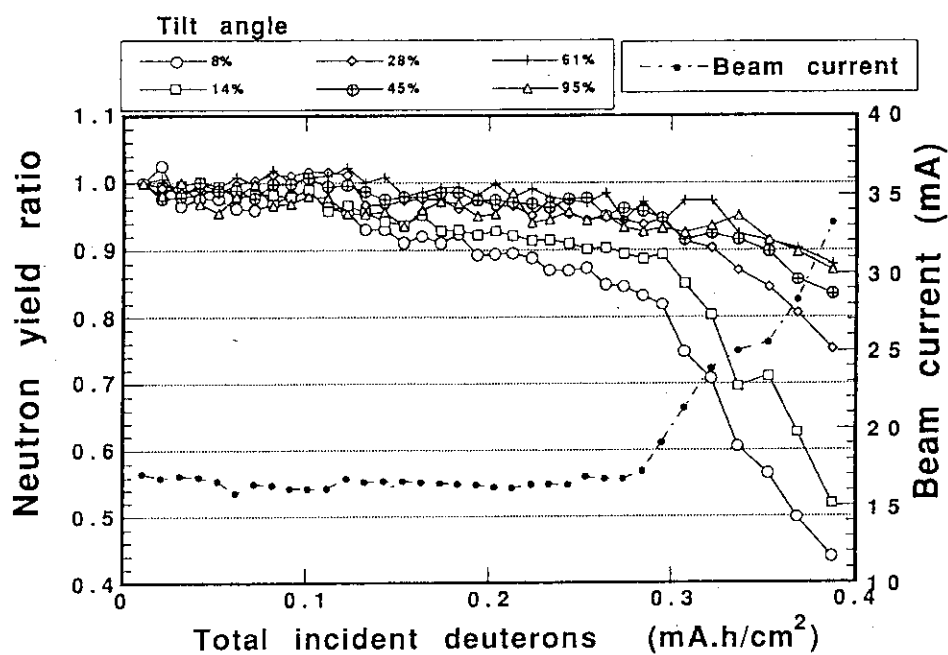


Fig. 5.9.2 Neutron yield ratio of each beam position

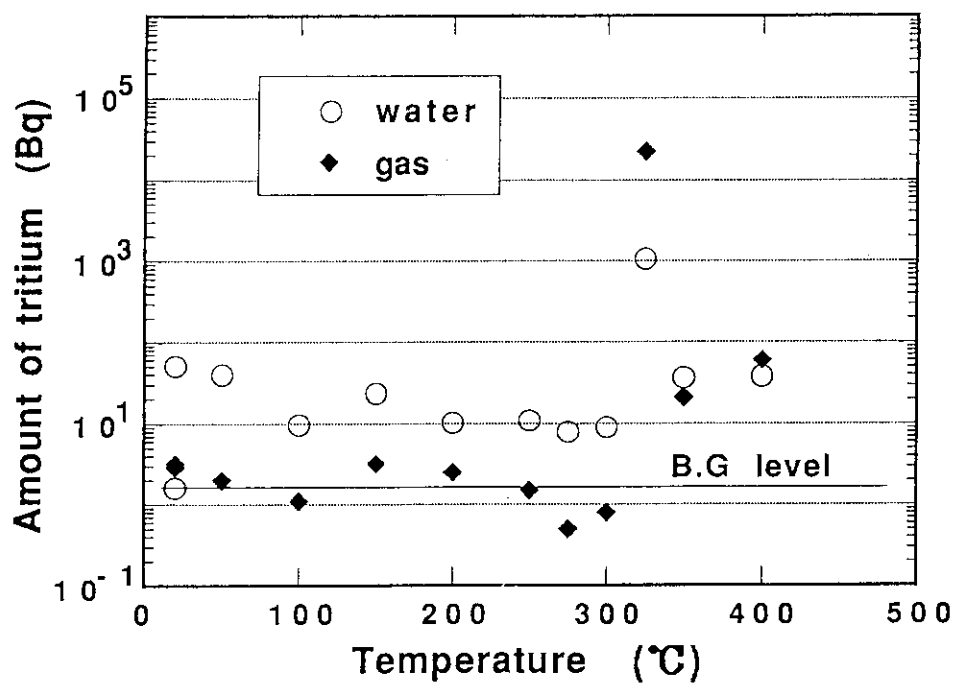


Fig. 5.9.3 Tritium gas release from Ti-T

## 5.10 Computational Benchmark for Deep Penetration of 14 MeV Neutrons in Iron

T. Mori and M. Nakagawa

Neutron transport through a shielding material containing iron is very important. Considerable complexity is introduced into a deep penetration problem by the resonance structure of iron; Streaming through cross section minima (windows) and space- and energy-dependent self-shielding effects play an important role in the calculation. This complexity indicates the need for a shielding benchmark problem to be used as a standard reference. Hendricks et al. proposed a calculational benchmark problem of a deep penetration in iron of 3 m thickness and made calculations by using a continuous energy Monte Carlo code MCNP and the ENDF/B-IV and B-V evaluated data<sup>1)</sup>. At the present work, a calculational benchmark with a domestic library JENDL-3 has been carried out by using a vectorized continuous energy Monte Carlo code MVP<sup>2)</sup>, which was developed in JAERI for vector supercomputers. The computation speed of MVP is higher by a factor of about 20 on the FACOM VP-2600 computer compared with MCNP, and can significantly improve statistical uncertainties. For comparison, a calculation with ENDF/B-IV also has been performed.

The calculation model was taken from Reference 1. An infinite slab is modelled by using perfect reflecting surfaces in three-dimensional geometry. Mono-directional mono-energetic 14 MeV neutrons enter perpendicularly on the one side of the infinite slab. As a variance reduction technique, we used only splitting and Russian roulette kill based on cell importance because of its simplicity and reliability. Two computer runs were made with each cross section library, one to optimize a calculation of the flux above 0.5 MeV, and the other to obtain the flux in the whole energy range from  $10^{-5}$  eV to 14 MeV. In the former case, the importance is increased from unity at the source by a factor of two every 10 cm in order to enhance deep penetration, while a factor of 1.3 was used in the latter case. Neutron flux spectra were evaluated in various positions by using track-length estimators of 1 cm thickness.

The attenuation of total flux in the slab is shown in Fig. 5.10.1. Both JENDL-3 and ENDF/B-IV calculations predict four-decade attenuation through 3 m penetration. No significant difference is observed, though the former calculation gives a little smaller flux beyond 0.7 m depth.

Despite that, large differences are observed in the flux spectra shown in Fig. 5.10.2. A discrepancy around a 24 keV window is caused by different total cross sections given in both libraries. However, the spatial variation of the spectrum is small below 100 keV in both results. On the other hand, it becomes considerably large in the 100 keV region. As a result of streaming through small windows, spectral jumps appear at several energies such as 1 MeV, 700, 380 keV and so on. These jumps become larger at deeper penetration. Some peaks which show a similar trend are also observed, typically at 220 keV in the JENDL-3 and at 140 keV in the ENDF/B-IV result. The largest discrepancies between the results with two libraries are of factors of 2 ~ 3 at 1 m penetration and of one order at 3 m penetration.

#### References

- 1) Hendricks, et al.: Nucl. Sci. Eng., 77, 71 (1981).
- 2) Mori T., et al.: "MVP: A Continuous Energy Monte Carlo Code for Vector Supercomputers", Proc. Int. Topical Meeting on Advances in Meths., Compu. and Reactor Physics, Vol. 4, 30.4-4, Pittsburgh, May, 1991.

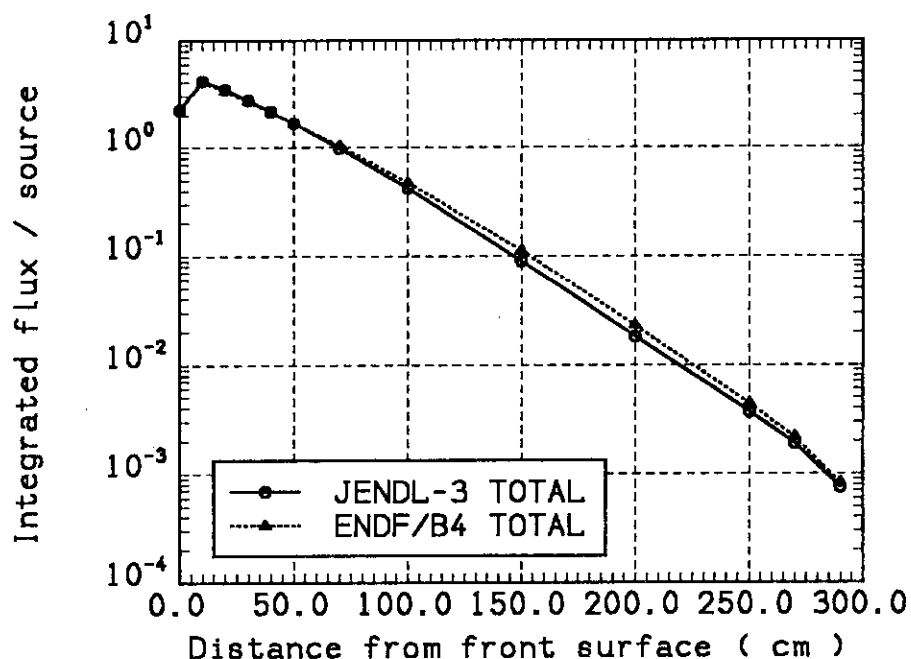


Fig. 5.10.1 Attenuation of total flux in 3 m thick iron slab

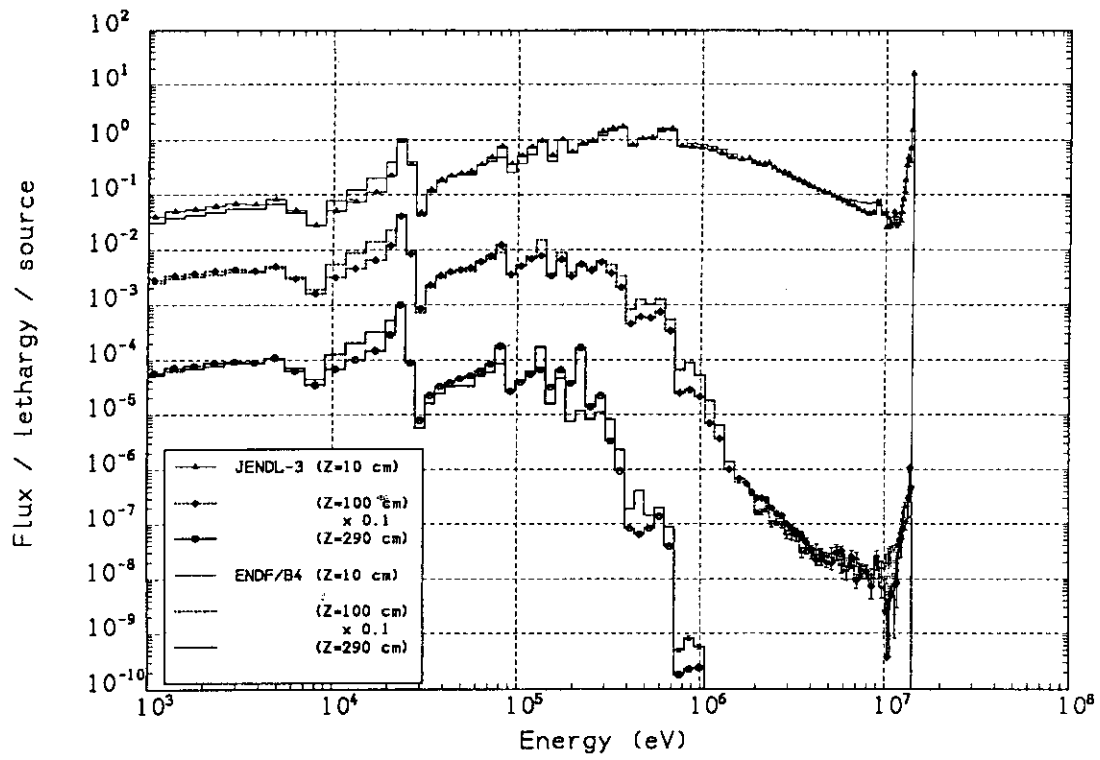


Fig. 5.10.2 Spatial variation of flux spectra in 3 m thick iron slab

## 6. Radiation Shielding

A new field of shielding research is extending to radiation physics. From 1989, experiments have been continued using synchrotron radiation (SR) at the Photon Factory in the National Laboratory for High Energy Physics. In order to investigate quantitatively the photon and electron behaviour in material, it is the first problem to measure the absolute intensity of the radiation source. To measure the absolute intensity of the SR, an excellent microcalorimeter was developed. Accuracy of the calorimeter has been confirmed by experiments to be within 1% for photons having energy of 10 to 50 keV and intensity of  $\mu\text{W}$  order.

A new project of a large scale SR facility, SPring-8, has started. Shielding design calculation for such a high energy electron accelerator is usual to be carried out with the method of point kernel from a source point, which leads naturally to an overestimation. For the ring shape source of the SPring-8, a linear source model is more reasonable. So, an empirical formula based on a point kernel method for linear source was derived, using the Gauss-Legendre numerical integration method. By assuming a line source of 8 meter in length, the dose equivalent is evaluated to be a half to that by the Jenkins' point source assumption.

Since the application of the ICRP-26 recommendation to the domestic regulation in Japan (1989), the assessment with effective dose equivalent has been obligated for radiation protection. The Shielding Laboratory has prepared the attenuation factors of neutron and secondary gamma rays dose equivalent under the contracts between the Science and Technology Agency and the JAERI. The attenuation factors have been calculated for 1 cm, 3 mm and 70  $\mu\text{m}$  doses for six kinds of important shielding materials and for neutron sources of various energy with point isotropic or perpendicular incidence.

(Tomoo Suzuki)

## 6.1 Development of a Microcalorimeter for Measuring Absolute Intensity of Synchrotron Radiations (II)

H. Nakashima, S. Tanaka, M. Yoshizawa, H. Hirayama<sup>\*</sup>, S. Ban<sup>\*</sup>,  
Y. Namito<sup>\*</sup> and N. Nariyama<sup>\*\*</sup>

A twin-type heat flow total absorption microcalorimeter was developed to measure the absolute intensity of monoenergetic SR beams above 10 keV and the feasibility study was performed in the Photon Factory in National Laboratory for High Energy Physics.<sup>1)</sup>

The experimental configuration is presented in Fig. 6.1.1. Monoenergetic photons of about  $10^8$  to  $10^{13}$  Photons/s in keV region are available at 14C beam line in the Photon Factory using a double crystal monochromator made of Si (111) or In-Sb (220). Incident beam intensity during experiments has been relatively monitored using a free air ionization chamber placed in front of the calorimeter. The photon intensity  $N$  (Photons/s) of energy  $E$  (keV) absorbed in the calorimeter is calculated from the measured heat power  $P$  ( $\mu$ W) by a following relation,

$$N = 6.242 \times 10^9 \cdot P/E. \quad (6.1.1)$$

Figure 6.1.2 is an example of the output of the calorimeter for 15 keV photons with 121.94  $\mu$ W heat power, in which a conversion factor of  $0.132 \pm 0.001$   $\mu$ V/ $\mu$ W has been given by a calibration using joule heating method from 0.9  $\mu$ W up to 1.1 mW and a background level is  $0.15 \pm 0.1$   $\mu$ W. Similar experiments have been repeated with changing photon energy, beam size, and beam absorber as summarized in Table 6.1.1. The ratio to the monitor are presented the reproducibility and the reliability within the error of  $\pm 3\%$  and the dispersion of  $2.59 \times 10^{-4}$ . No meaningful difference among the results for the Cu and Ag beam absorbers over 10 to 50 keV suggests that the energy escape with photons can be ignored in the vicinity of K-edge energies of 25.5 keV for Ag and 8.98 keV for Cu. A correction has been applied for the attenuation with air and Be between the monitor and the beam absorber, and the error in the correction restricts the application of the calorimeter to lower energy photons. It

---

\* National Laboratory for High Energy Physics

\*\* Ship Research Institute



is expected that a vacuum type calorimeter can measure the low energy photon up to 10 keV.

#### Reference

- 1) Nakashima H., et al.: to be submitted to Nucl. Instr. and Meth. A.

Table 6.1.1 Intensity of monoenergetic SR measured using the calorimeter

Energy <sup>1</sup> (keV)	Current <sup>2</sup> (mA)	Beam size <sup>3</sup> (mm <sup>2</sup> )	Calo. <sup>4</sup> (μW)	Ratio <sup>5</sup>	Date <sup>6</sup>
Cu beam absorber					
50	186	3.2x11.5	24.82	0.981	'89/ 3/ 1
	169	3.2x11.5	27.69	0.997	'89/ 3/ 1
	209	3.5x11.0	34.50	0.977	'89/ 3/ 3
30	273	4.0x10.0	40.77	1.020	'89/ 3/ 1
	183	6.0x11.5	56.81	1.009	'89/ 3/ 3
	290	6.0x15.0	63.03	1.018	'89/12/12
	280	6.0x15.0	76.68	1.032	'89/12/12
20	263	6.0x15.0	105.35	0.985	'89/12/12
	256	6.0x15.0	101.15	0.982	'89/12/12
15	246	8.0x15.4	115.67	0.997	'89/12/12
	240	8.0x15.4	109.78	0.989	'89/12/12
10	228	11.0x15.4	93.98	0.994	'89/12/12
	222	11.0x15.4	90.05	0.995	'89/12/12
Ag beam absorber					
30	338	6.0x 7.6	55.23	1.003	'91/ 2/21
	333	5.8x11.0	88.01	0.997	'91/ 2/21
20	251	9.0x 9.0	120.60	0.988	'89/12/ 6
	268	11.0x 5.5	149.63	0.992	'89/12/ 8
	262	11.0x 5.5	148.26	1.008	'89/12/ 8
	297	2.8x 9.5	88.05	1.026	'91/ 2/21
	293	2.8x 9.5	80.62	1.028	'91/ 2/21
15	283	10.5x 9.0	121.94	1.008	'89/12/ 6
	268	10.5x 9.0	93.64	0.983	'89/12/ 6
	281	7.5x 8.0	96.99	1.026	'91/ 2/21
10	208	11.0x11.0	57.03	1.004	'89/12/ 8
	206	11.0x 5.5	25.57	0.994	'89/12/ 8

$$\bar{X} = 1.001$$

$$\sigma^2 = 2.59 \times 10^{-4}$$

<sup>1</sup>Photon energy.

<sup>2</sup>Storage ring current.

<sup>3</sup>Photon beam size.

<sup>4</sup>Calorimeter output.

<sup>5</sup>Ratio of the measurements to the monitor.

<sup>6</sup>Date of Measurement.

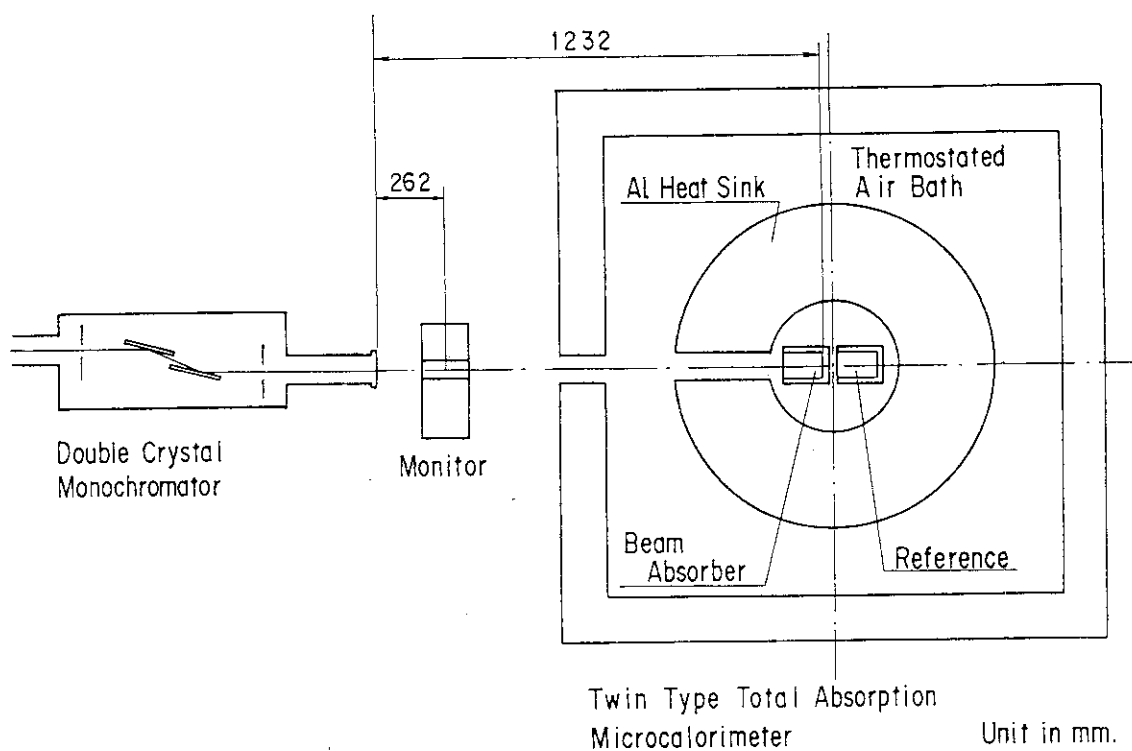


Fig. 6.1.1 Experimental configuration to measure the intensity of monoenergetic SR beams

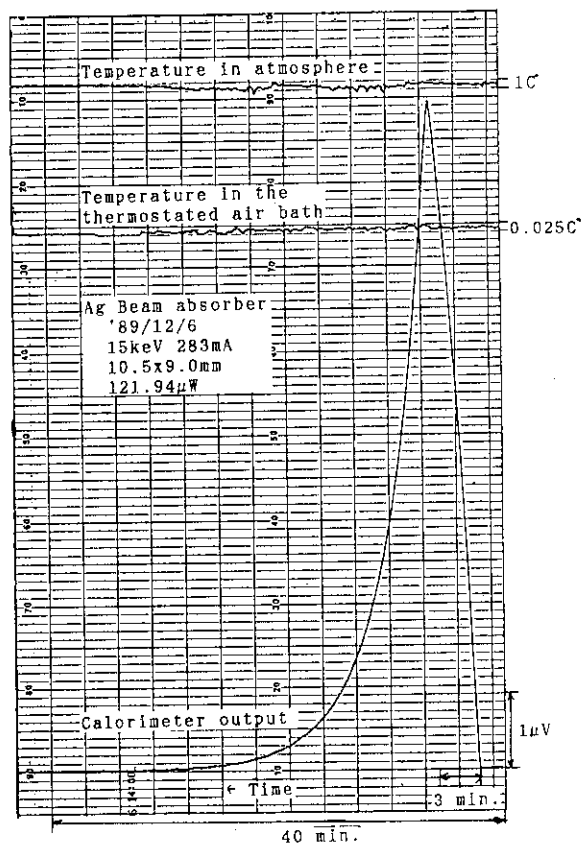


Fig. 6.1.2 Measured calorimeter output for SR beam of 15 keV

## 6.2 Bulk Shielding Calculation of High Energy Electron Accelerators with Line Source Assumptions

N. Sasamoto

In order to achieve more realistic and reasonable shielding estimates for high energy electron accelerators, I derived a formula based on a line source model by modifying the well-known Jenkins' and Swanson's formulas.<sup>1)</sup> The ratio between the dose values based on assumptions of line and point sources is given as,

$$\frac{H_{\text{line}}}{H_{\text{point}}} = \frac{a+d}{L} \cdot \frac{\int_{\theta_1}^{\theta_2} f(\theta) d\theta}{f(\theta_0)}, \quad (6.2.1)$$

where  $\theta_0 = \pi/2$  and  $f(\theta)$  represents the Jenkins' formula<sup>2)</sup> or Swanson's one<sup>3)</sup> corresponding to a point source assumption. Other parameters,  $a$ ,  $d$ ,  $L$ ,  $\theta_1$  and  $\theta_2$  are indicated in Fig. 6.2.1. Eq.(6.2.1) is integrated numerically using the Gauss-Legendre integration method.

For the configuration with  $a = 250$  cm and  $d = 200$  cm of ordinary concrete, dose equivalent ratios were calculated using Jenkins' and Swanson's formulas. Further the ratio was also calculated using the empirical formula given below.

$$\frac{H_{\text{line}}}{H_{\text{point}}} = \frac{1.9 \times \left(\frac{d}{\lambda}\right)^{-0.4} \cdot (a+d)}{L}. \quad (6.2.2)$$

In Fig. 6.2.2 are given the comparison of the calculational results. For the shielding design of SPring-8, where Jenkins' formulas are employed assuming partially line sources of 8 meter, a reduction of dose values by 30% can be expected. With increase of a line source length  $L$ , the empirical formula approaches asymptotically to Swanson's formula. This fact reveals the empirical formula is derived on the basis of Swanson's formula. For  $L < a + d$ , however, the empirical formula increases rapidly with decrease of  $L$ , leading to divergence at  $L = 0$ . Besides it is apparent that the ratio for the Swanson's formula always underestimates the one for Jenkins' formula, giving calculational results of 0.3 and 0.6 at  $L = 10$  m for the Swanson's and Jenkins' formulas, respectively. This difference is due to the fact that the Jenkins' formula takes account of  $\theta$ -dependence, while the Swanson's one does not.

## References

- 1) Sasamoto N.: "Bulk Shielding Calculation of High Energy Electron Accelerators with Line Source Assumptions", JAERI-M 90-095 (1990).
- 2) Jenkins T.M.: "Neutron and Photon Measurements Through Concrete from a 15 GeV Electron Beam on a Target - Comparison with Models and Calculations", Nucl. Instrum. Meth., 159, 265 (1979).
- 3) Swanson W.P.: "Radiological Safety Aspects of the Operation of Electron Linear Accelerators", Technical Report Series No.188, IAEA (1979).

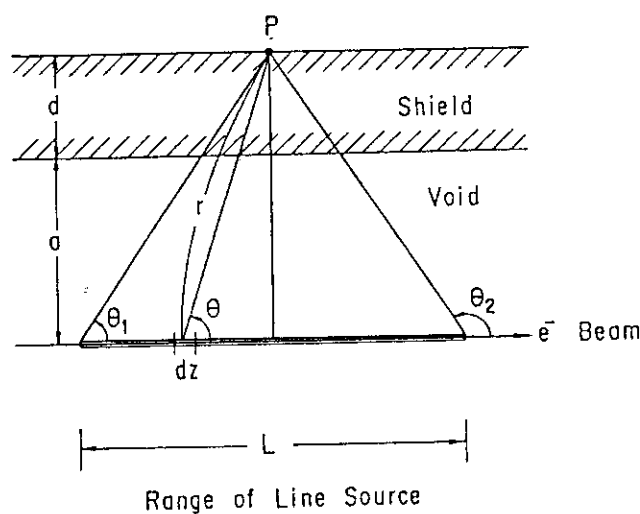


Fig. 6.2.1 Configuration of a line source model

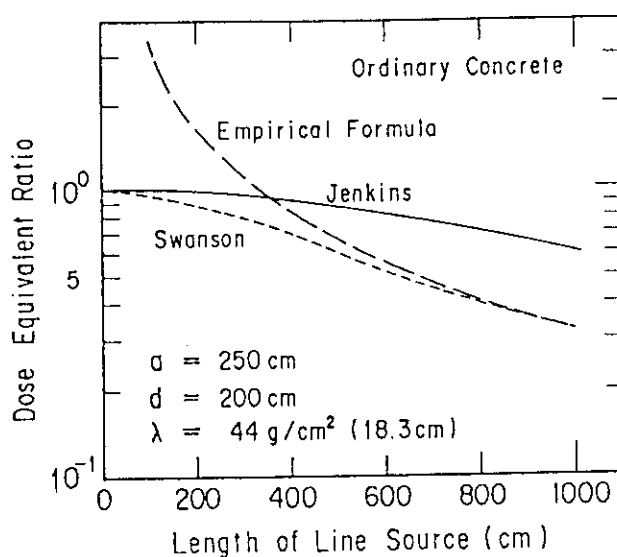


Fig. 6.2.2 Comparison of the dose equivalent ratios for ordinary concrete shield

### 6.3 Attenuation Factors of Neutron and Secondary Gamma-ray Dose Equivalents for Typical Neutron Sources in Shielding Materials

H. Kotegawa and S. Tanaka

Since the application of the ICRP recommendation (ICRP-26) to the new domestic regulation in Japan (1989), the assessments with effective dose equivalent or 1-cm, 3 mm and 70  $\mu$ m depth dose equivalents have been obligated for radiation protection, and subsequently earlier shielding data have become unavailable. Thus the following attenuation factors evaluating 1 cm, 3 mm and 70  $\mu$ m depth doses have been prepared with BERMUDA-1DN, -1DG, and ANISN-JR transport codes<sup>1-3</sup>).

- 1) Attenuation factors for  $^{252}\text{Cf}$ ,  $^{241}\text{Am-Be}$ , d-T and d-D point isotropic neutron sources in six substantial shielding materials: water, concrete, iron, lead, polyethylene and heavy concrete.
- 2) Attenuation factors for point isotropic monoenergetic neutron sources from 14 MeV to 0.01 MeV in water, concrete and iron shields.
- 3) Attenuation factors for  $^{252}\text{Cf}$ ,  $^{241}\text{Am-Be}$ , d-T and d-D normal incident neutron sources to water, concrete, and iron shields.

In Figs. 6.3.1 and 6.3.2, the attenuation factors of 1 cm dose equivalent have been demonstrated for  $^{252}\text{Cf}$  and d-T neutron sources in point isotropic and plane geometries, respectively. As shown in the figures, the attenuation in plane geometry is greater than that in point isotropic geometry, and the contribution of secondary gamma rays to the dose equivalent becomes dominant with increasing shield thickness. Therefore, the comprehensive data have been prepared including the attenuation factor of secondary gamma rays in the present work.

A calculational method of the attenuation factors for two layers has been proposed to make the shielding calculation for multilayered shields possible using the present attenuation factors. The attenuations of neutrons and secondary gamma rays from 1 MeV point isotropic neutron source in water of 42 cm radius surrounded by concrete or iron are compared in Figs. 6.3.3 and 6.3.4, in which the solid lines represent the results with ANISN-JR code and broken lines for the present analytical method using "equivalent thickness" for the first shield. Namely, the first shield is replaced by a second shield of "equivalent thickness" by which the attenuation is equal to the first one. As shown in the figures, the analytical method reproduces well the attenuation in the

water-concrete shield, while unable to reproduce the attenuation, specially the secondary gamma rays, in the water-iron shield. In the later case, the energy spectrum changes largely around the boundary, since low energy gamma rays built up in water are absorbed steeply in the iron, and a lot of capture gamma rays with the absorption of thermal neutrons are produced in the vicinity of the boundary. Contrary, the change of the energy spectrum is not significant in the water-concrete shield. As a result, we have such a conclusion that the present method is effective when the spectrum change is not large around the boundary.

#### References

- 1) Kotegawa H. and Tanaka S.: JAERI-M 90-174 (1990) (in Japanese).
- 2) Suzuki T. et al.: JAERI-M 9492 (1981), JAERI-M 84-177 (1984) (in Japanese).
- 3) Engle W.W. Jr.: CCC-82 (1968).

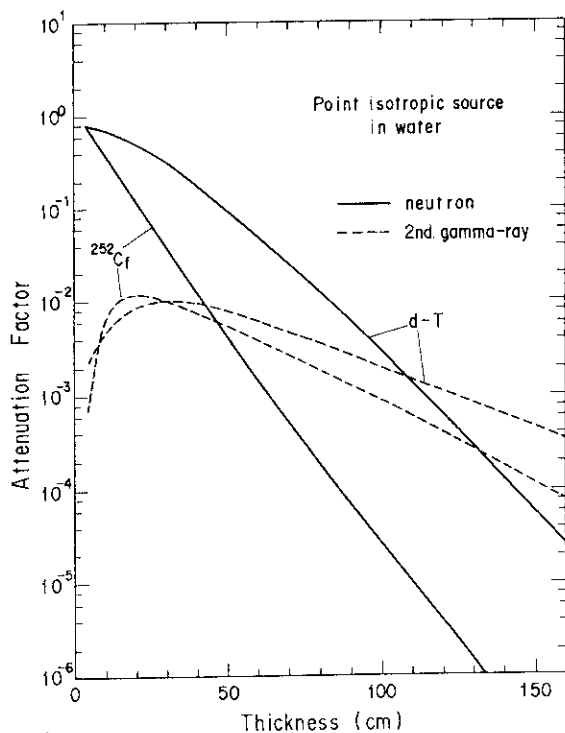


Fig. 6.3.1 Attenuation factors of 1 cm dose equivalent for  $^{252}\text{Cf}$  and d-T point isotropic neutron sources in water

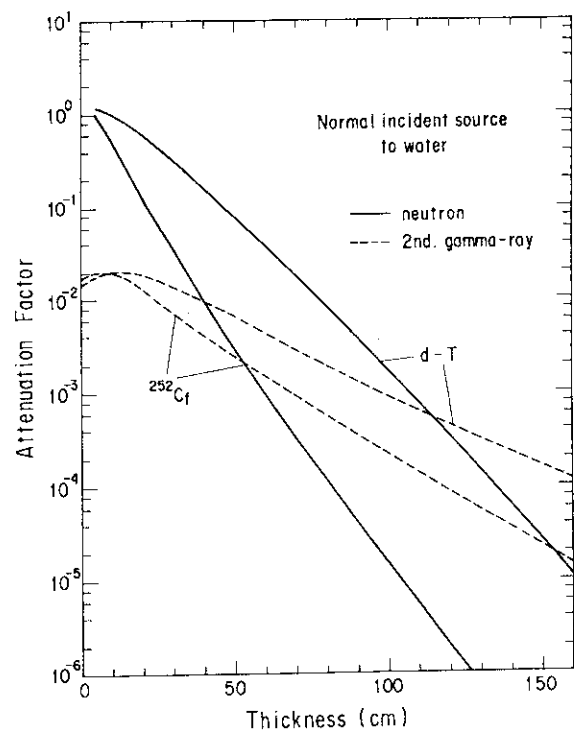


Fig. 6.3.2 Attenuation factors of 1 cm dose equivalent for  $^{252}\text{Cf}$  and d-T normal incident neutron sources to water

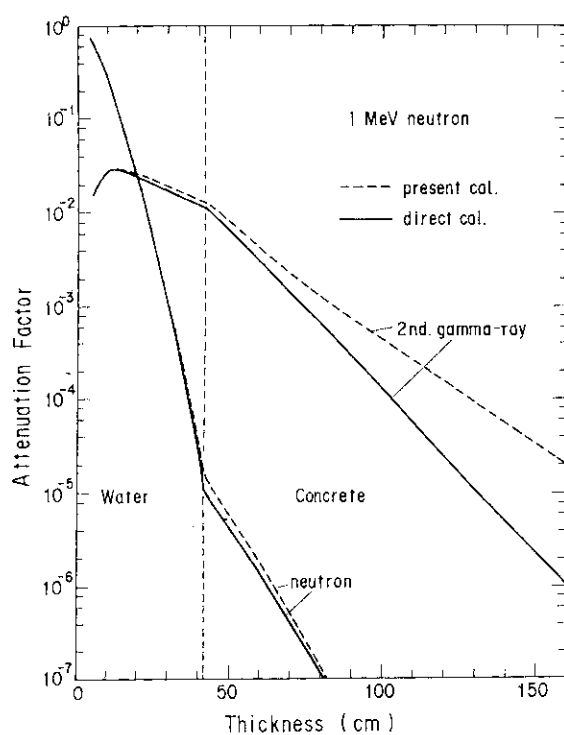


Fig. 6.3.3 Attenuation factors of 1 cm dose equivalent for 1 MeV point isotropic neutron source in a multilayer composed of water and concrete

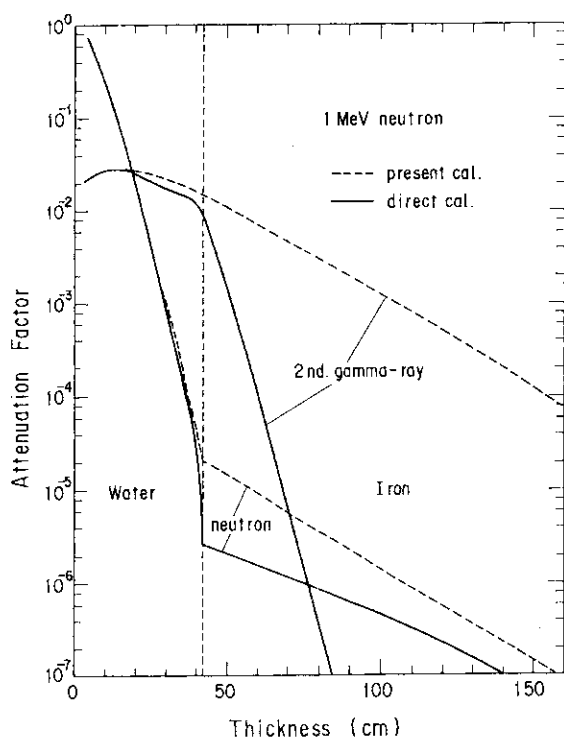


Fig. 6.3.4 Attenuation factors of 1 cm dose equivalent for 1 MeV point isotropic neutron source in a multilayer composed of water and iron

## 7. Reactor and Nuclear Instrumentation

In the field of reactor instrumentation, R & D works were performed in connection with the High Temperature Engineering Test Reactor (HTTR) project. A high-sensitive neutron detector was developed for the power range monitoring and safety channel of the HTTR. The detector was tested in the JRR-4, and good performance results have been obtained. The neutron sensitivity is about ten times larger than that of a conventional type for PWRs. As for the development of N-type thermocouples (N-TCs) for monitoring gas temperature at the HTTR core outlet, the compatibility between thermocouple elements and various sheath metals was investigated in term of EMF drifts at high temperature. As a result of the stability test for 20000 hours at 1200°C, it has been found that NTCs having a Nicrosil sheath are most stable. For fuel failure detection (FFD) in the HTTR, the development of a high-sensitive FFD system with a modified precipitator has progressed. A response function of the precipitator to various FP nuclides is introduced as a function of sampled-gas and purged-gas flow rates. By combining this with a FP-gas circulation model in the primary loop, a FFD response function is derived.

In the field of nuclear instrumentation, R & D of a non-destructive measuring technique for inspection of TRU elements in drum-sized wastes has progressed. In the works, an analytical expression, based on the theory of stochastic process, was developed for the distribution of time intervals between successive detection pulses of neutron from spontaneous fissions. The expression was evaluated through an example calculation. Also, the neutron detection efficiency was investigated through experiments with a passive system. The results of calculation with Monte Carlo programs have agreed well with experiments.

Other fundamental researches were accomplished also. The incomplete charge induction by the electrons and holes inside the dielectric plasma column is proposed as a new candidate for the residual defect in a silicon surface barrier detector. Theoretical calculations are compared with experimental values, showing a good agreement. The ultraviolet irradiation effects on a pure silica core optical fiber were investigated experimentally in term of transmission losses. A new method for directional measurement of magnetic field is proposed with applying a diamagnetic device. Its feasibility has been proved by experiments.

(Katsuyuki Ara)



## 7.1 Development of a High-Sensitive Ionization Chamber for High Temperature Gas Cooled Reactors

H. Yamagishi, H. Itoh, K. Sakasai, N. Wakayama, M. Tamura<sup>\*</sup>  
S. Fukakusa<sup>\*</sup>, H. Ieki<sup>\*</sup> and S. Yamashita<sup>\*</sup>

It is planned by JAERI to construct the High-Temperature Engineering Test Reactor (HTTR) which is a kind of high temperature gas-cooled reactor (HTGR) and has a full thermal reactor power of 30 MW. The HTTR required high sensitive neutron sensors which are installed outside the reactor vessel for power range monitoring systems and safety channels. Because the neutron flux at the outside of the reactor vessel is designed to make a low flux such as  $1.4 \times 10^{11} \text{ m}^{-2}\text{s}^{-1}$  at full reactor power. The neutron flux is 1/100 or 1/1000 less than that of conventional pressurized water reactors (PWRs). The power range detectors for the HTTR are required to permit neutron monitoring at flux levels from  $1 \times 10^5$  to  $2 \times 10^{11} \text{ m}^{-2}\text{s}^{-1}$ .

A high-sensitive ionization chamber (HSIC) of which neutron sensitivity is about 10 times higher than that of the power range detector for PWRs has been developed for nuclear instrumentations of the HTTR. The specifications of the HSIC are shown in Table 7.1.1. The HSIC is designed to detect thermal neutrons at flux levels from  $1 \times 10^8$  to  $5 \times 10^{11} \text{ m}^{-2}\text{s}^{-1}$ . An outline drawing of the HSIC is shown in Fig. 7.1.1. The outside diameter and the overall length are 100 mm and 2875 mm. The HSIC provides a 2626 mm measurement length which permits full core-height coverage of the HTTR. Mixture gas of  $^3\text{He} + 10\%\text{Ar}$  is filled at 4 atm in the chamber. The neutron and gamma sensitivities of the HSIC are  $4.6 \times 10^{-16} \text{ A} \cdot \text{m}^2\text{s}$  ( $4.6 \times 10^{-12} \text{ A/nv}$ ) and  $1.6 \times 10^{-2} \text{ A} \cdot \text{C}^{-1}\text{kg} \cdot \text{s}$  ( $1.2 \times 10^{-9} \text{ A} \cdot \text{R}^{-1}\text{h}$ ). The HSIC has three ionization chamber elements in the case and each element has a separate signal connector. Thus, the signal from each element is able to be monitored independently to obtain information for the neutron flux profile in the direction of the reactor-core axis. The signals from three elements are summed up to provide a signal proportional to the integral of the flux over the full sensitive length of the HSIC.

A neutron irradiation test was carried out in the research reactor JRR-4 in order to confirm the operating performances and the irradiation

---

<sup>\*</sup> Mitsubishi Electric Corporation

life of the HSIC. In the test, one chamber element of the HSIC was irradiated at a thermal neutron flux level of about  $1 \times 10^{14} \text{ m}^{-2}\text{s}^{-1}$  to provide accelerated neutron irradiation. The plateau curves and output linearities were measured in the flux range from about  $2 \times 10^8$  to  $5 \times 10^{11} \text{ m}^{-2}\text{s}^{-1}$  before, in the middle of and after the irradiation. The total thermal neutron fluence was  $1.6 \times 10^{20} \text{ m}^{-2}$  for the chamber element in this test. The neutron fluence is similar in the case of that the HSIC is used as a power range detector in the HTTR for about 38 years.

Figure 7.1.2 shows output plateau curves which were measured before and after the irradiation. The signal current of the HSIC showed sufficient saturation in the neutron flux range from  $2 \times 10^8$  to  $5 \times 10^{11} \text{ m}^{-2}\text{s}^{-1}$  with detector high voltage of 1000 volt. No noticeable changes of plateau curves are observed before and after the irradiation. Figure 7.1.3 shows a comparison between output linearities which were measured before, in the middle of and after the irradiation. The HSIC has good output linearities in the neutron flux range from  $2 \times 10^8$  to  $5 \times 10^{11} \text{ m}^{-2}\text{s}^{-1}$ . There is no significant difference between the output linearities in the whole irradiation period. Through this irradiation test, it was verified that the developed HSIC is a useful power range detector for the HTTR.

Table 7.1.1 Specifications of high-sensitive ionization chamber

Items	Specifications
<b>Mechanical</b> Dimensions Sensitive Length(each section) Connectors Net Weight	See Fig. 7.1.1 768mm HN Type 22 kg
<b>Materials</b> Outer Case Electrodes Insulation Neutron Sensitive Material Gas filling	Aluminum Aluminum Alumina Ceramic $^3\text{He}$ $^3\text{He}+10\%\text{Ar}$ , 4atm
<b>Typical Operation</b> Operating Voltage Thermal Neutron Flux Range Thermal Neutron Sensitivity(each section) Gamma Sensitivity(each section)	100 to 1000V <sub>dc</sub> $1 \times 10^8$ to $5 \times 10^{11} \text{ m}^{-2}\text{s}$ $1.53 \times 10^{-16} \text{ A} \cdot \text{m}^2\text{s}$ $5.3 \times 10^{-9} \text{ A} \cdot \text{C}^{-1} \text{ kg} \cdot \text{s}$

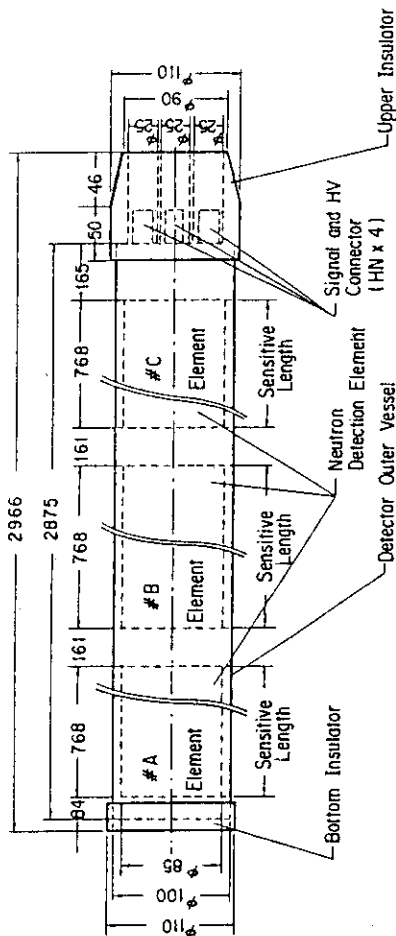


Fig. 7.1.1 Outline drawing of HSIC

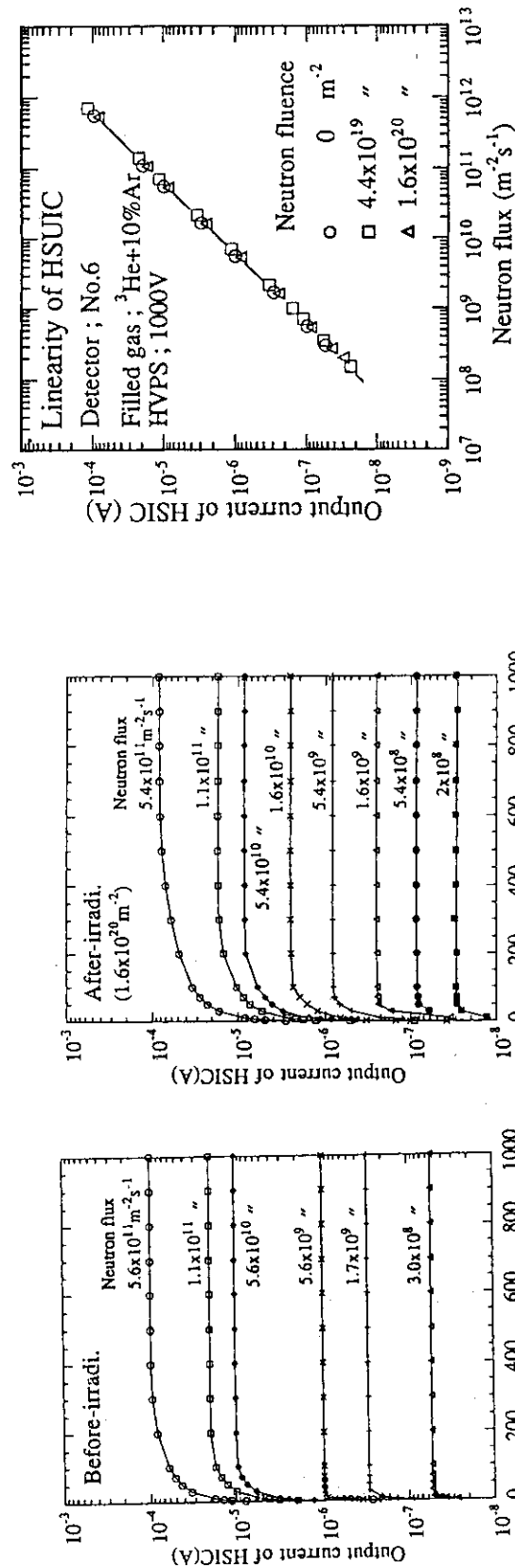


Fig. 7.1.2 Plateau curves of HSIC before and after irradiation test

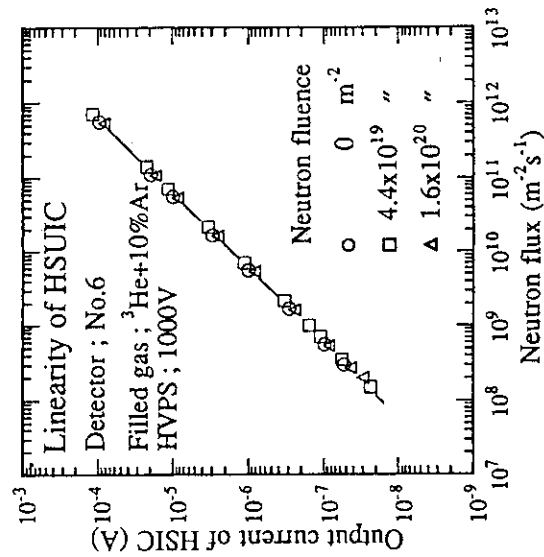


Fig. 7.1.3 Output linearities of HSIC before, in the middle of and after irradiation test

## 7.2 High-Temperature Out-Pile Tests of N-type Thermocouples

M. Yamada and K. Ara

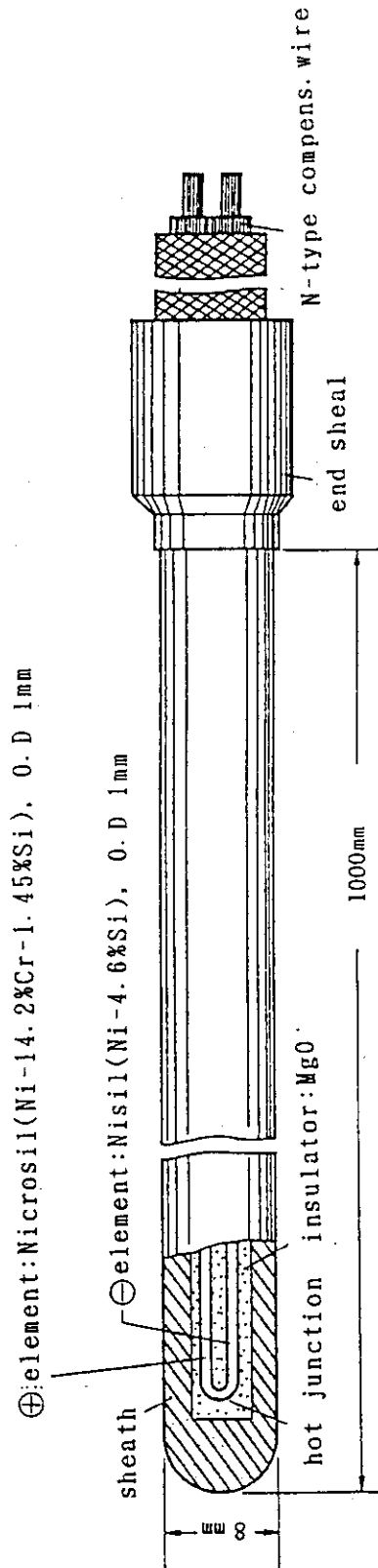
A new type of thermocouples, so-called Nicrosil-Nisil thermocouple (N-type TC), seemed to be the most suitable sensors for in-core gas-temperature measurement in the high-temperature engineering test reactor (HTTR). The actual experience on the use of N-type TCs is, however, very little so that a long-term out-pile test of them having different types of sheaths was started at high-temperature He-gas environment in 1988 and terminated in 1990.

The chemical composition of N-type TC is shown in Table 7.2.1 as compared with that of K-type. One sees differences in contents of Cr and Si: these differences make N-type more resistant to high-temperature than K-type. The electromotive force (emf) characteristic of N-type is almost the same as that of K-type.

The N-type TCs tested have sheaths with five different materials; i.e., inconel 600, incoloy 800, incoloy 825, hasteloy x and Nicrosil. The insulator is MgO in common. The structure of test sample is shown in Fig. 7.2.1. The tests were performed at the temperature of 1200°C and lasted until the total exposure time had reached 20000 hours. K-type TCs and R-type ones are also tested for comparison and as references. All sample TCs were calibrated prior to the start of the tests; and their emf's are compared with that of the reference R-type TCs. The test results are shown in Fig. 7.2.2: the N-type TCs having a Nicrosil sheath seem to be most stable.

Table 7.2.1.1 Chemical composition of N-type and K-type thermocouples

	Cr	Si	Fe	Mg	Ni	Al	Mn
Nicrosil	13.85 -14.61	1.43 -1.47	0.024 -0.1	<0.081	bal.	-	-
Nisil	<0.008	4.23 -4.88	0.054 -0.41	0.07 -0.18	bal.	-	-
Chromel	9.46	0.4	0.2	-	bal.	-	-
Alumel	-	1.2	0.1	-	bal.	2.0	1.75



sheath materials: Inconel 600, Incoloy 800, Incoloy 825, Hastelloy X, Nicrosil

Fig. 7.2.1.1 Sample thermocouple

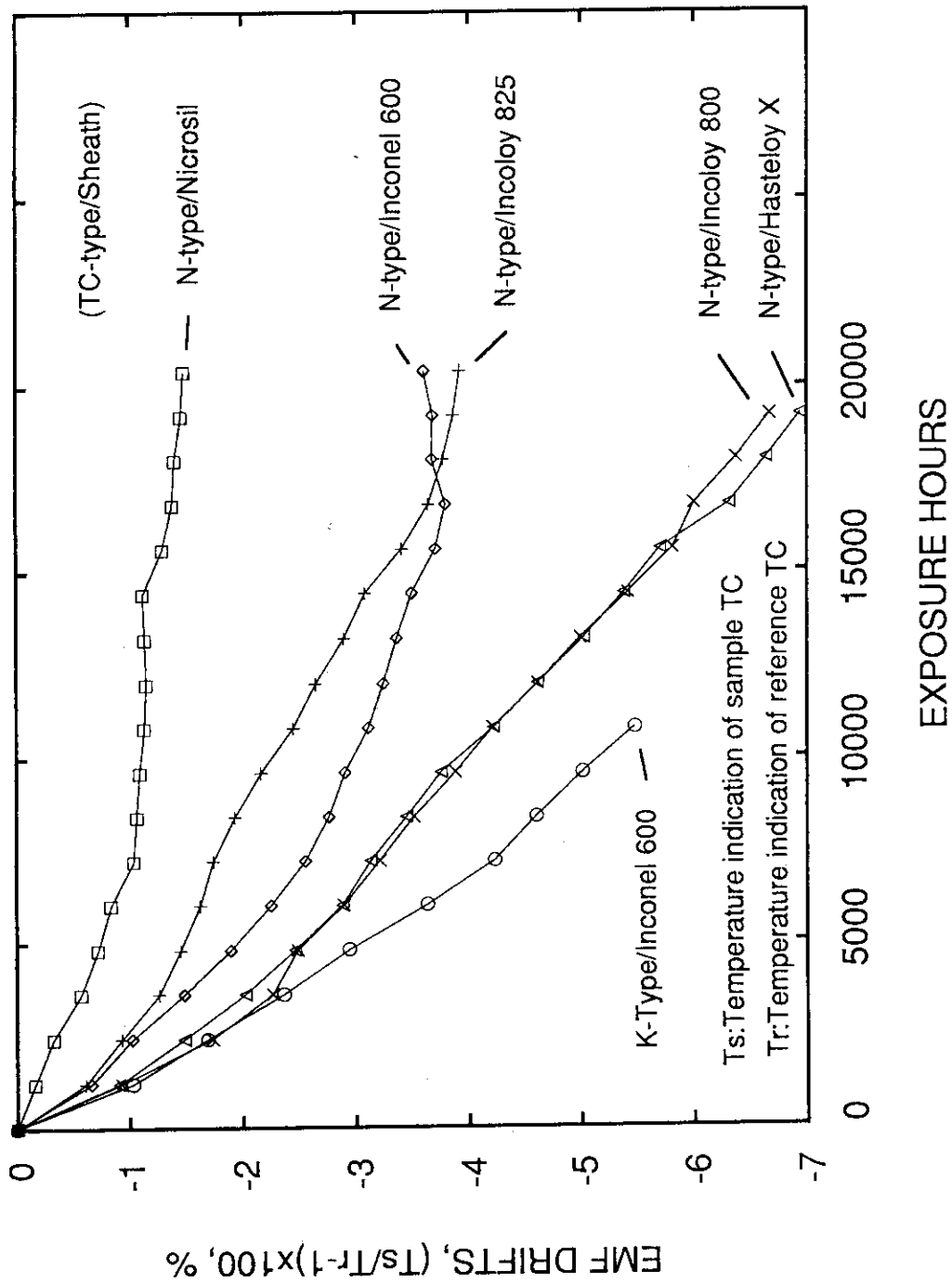


Fig. 7.2.2 EMF drifts of N-type thermocouples due to exposure to temperature of 1200, in comparison with that of K-type

### 7.3 Development of Fuel Failure Detection System for High Temperature Gas Cooled Reactor

M. Katagiri, M. Kishimoto, H. Ito, M. Fukushima, H. Ookawa  
H. Yoshida, T. Saruta, T. Kitajima and T. Tobita

A fuel failure detection (FFD) system using a wire-precipitator has been developed for a High Temperature Gas cooled Reactor (HTGR). On actual application of the FFD, it is important to inquire the response characteristics of the precipitator and the behavior of noble-gas-FPs released from coated particle fuel compacts.

In the experimental FFD system, the dependence of the precipitator counting rates on purge-gas flow-rate was measured to obtain an accurate response function of the precipitator. Under the condition of the constant flow rate of the sampling gas (132 cm<sup>3</sup>/min), the purge-gas flow-rate is changed in the range from 23 cm<sup>3</sup>/min to 100 cm<sup>3</sup>/min and the radioactivities of noble-gas-FPs were measured. The results are shown in Table 7.3.1. A response function of the precipitator is represented with considering the dilution effect and the correction of the staying time of the sampling-gas by a following function.

$$C(V_s, t_s, t_c) = \sum_{i=1}^n D_{si} V_s E_{pi} E_{bi} (1 - e^{-\lambda_{mi} t_p}) (1 - e^{-\lambda_{di} t_s}) \times \\ (v_o / (v_o + v_p)) (1 - e^{-\lambda_{di} t_c}) / \lambda_{mi} \lambda_{di} t_p t_c$$

Explanation of variables in the function is given in Table 7.3.2.

A FFD system for HTGR must distinguish between noble-gas-FPs due to intact fuels and noble-gas-FPs due to failed fuels. For this purpose, it is necessary to develop a diagnostic method using a FFD response function which estimates the noble-gas-FPs released from fuel compacts in the primary coolant system.

In the primary helium-coolant system of HTGR, the released noble-gas-FPs are circulated and the partial gas in the coolant system is purified by a purification system. It is necessary to obtain the response model of the circulated noble-gas-FPs because the FFD system uses the sampling-gas guided from the coolant system.

A gas circulation model for noble-gas-FPs in the coolant system was fabricated by using the helium gas loop OGL-1 as the model because this loop system is similar to the primary coolant system in the HTGR. The

radioactivities of noble-gas-FPs in the primary coolant system can be represented by a following function.

$$D(p,T,t) = \sum_{i=1}^n F(p(t_i), T(t_i)) e^{-\lambda(t_n-t_i)} (1-Pr)^{(n-1)}$$

Explanation of variables in the function is given in Table 7.3.3.

This function shows that the radioactivity of long-life nuclides increases according as time elapses and the radioactivity of short life nuclides reaches constant, instantly. Therefore, it is necessary to measure the radioactivity of the noble-gas-FP each nuclide for obtaining the precise fuel failure rate.

The FFD response function for HTGR consists of the gas circulation model including the state function and the response function of the precipitator. This function can be represented by the following function.

$$N(V_s, t_s, t_c, t) = \sum_{i=1}^m D_i(P, T, t) e^{-\lambda_i t_r} C_i(V_s, t_s, t_c)$$

Explanation of variables in the function is given in Table 7.3.4.

The developed FFD response function was evaluated by using the experimental system of the OGL-1. The counting rates of the precipitator were measured at the JMTR start-up and the results estimated by this function are shown in Fig. 7.3.1. The validity of this function was confirmed because both data were agreed very well.

#### Reference

- 1) Katagiri M., et al.: "Development of Fuel Failure Detection System for a High Temperature Gas Cooled Reactor (IV)", IEEE Trans. NS-37(3) pp.1400-1404 (1990).

Table 7.3.1 Dependence of precipitator counting rates on the purge-gas flow-rate and values corrected by dilution effect and the half life of nuclide

Purge-gas Flow-rate (cm <sup>3</sup> /min) Pf	Sample-gas Flow-rate (cm <sup>3</sup> /min) Sf	Dilution rate (Sf/(Pf+Sf)) Dr	Measured counting- rate (cps)	Value corrected for Dr (cps)	Value corrected for Staying time (cps)
23	132	0.850	404	474	441
36	132	0.786	386	490	446
60	132	0.688	349	507	441
80	132	0.623	321	514	432
100	132	0.569	299	527	428



Table 7.3.2 Explanation of variables in the response function of the precipitator

Variable	Content
$i$	number of noble-gas FP nuclide ( $i=1,2,3,\dots,n$ )
$C$	net counting rate of the Precipitator
$D_{si}$	concentration of the $i$ -th nuclide ( $Bq/cm^3$ )
$V_s$	volume of the Precipitator soak chamber ( $cm^3$ )
$E_p$	Precipitation efficiency of the daughter nuclide
$B_{di}$	Beta-ray detection efficiency of the Precipitator for the $i$ -th daughter nuclide precipitated on a wire
$\lambda_{mi}$	decay constant of the $i$ -th nuclide ( $sec^{-1}$ )
$\lambda_{di}$	decay constant of the daughter nuclide of the $i$ -th nuclide ( $sec^{-1}$ )
$t_p$	stay time of sampling gas in a soak chamber (sec) $t_p = V_s / (V_0 + V_p)$
$t_s$	soak time of the Precipitator (sec)
$t_c$	counting time of the Precipitator (sec)
$V_0$	flow rate of the sampling gas ( $cm^3/sec$ )
$V_p$	flow rate of the purge gas ( $cm^3/sec$ )

Table 7.3.3 Explanation of variables in the response function of the gas circulation model

Variable	Content
$D(p,T,t)$	Radioactivity of noble-gas FP
$F(p,T)$	State function
$p(t)$	Reactor power
$T(t)$	Fuel temperature
$\lambda$	Decay constant of nuclide
$Pr$	Purification rate
$t_c$	Circulation time of coolant gas
$n$	$\int_0^t (t/t_c)$
$tn$	$n \cdot t_c$
$ti$	$i \cdot t_c$

Table 7.3.4 Explanation of variables in the FFD response function

Variable	Content
$N(V_s, t_s, t_c, t)$	The precipitator counting rate
$D_i(p, T, t)$	Radioactivity
$C_i(V_s, t_s, t_c)$	Precipitator response function
$\lambda_i$	Decay constant of nuclide $i$
$tr$	travelling time between the coolant system and a precipitator
$m$	Number of nuclides

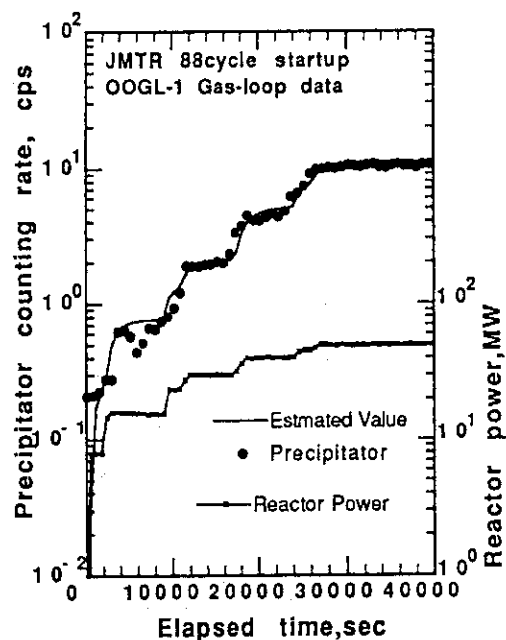


Fig. 7.3.1 Precipitator counting rates measured at the JMTR start-up and the estimation results by the FFD response function

#### 7.4 The Ultraviolet Irradiation Effects of Pure Silica Core Optical Fiber

T. Kakuta, K. Ara, N. Shamoto\* and K. Sanada\*

A large bore type step index optical fiber, which has a pure silica core and a fluorine doped silica cladding, has been fabricated and its ultraviolet (UV) irradiation effects were investigated. The large bore type optical fiber was made by a direct deposition method using  $\text{SiCl}_4$  and  $\text{SF}_6$  as a starting material. The structure of the large bore type optical fiber is shown in Table 7.4.1 and initial spectral characteristics of the fiber in Fig. 7.4.1. The core diameter of the fiber was 600  $\mu\text{m}$  and the initial transmission loss was 50 dB/km at a wavelength of 365 nm.

Measurements of the transmission loss induced by UV irradiation were conducted in-situ, while the light power was monitored through the optical fiber by use of a UV light source. The exposed fiber length was 2 m. Also the spectral transmission loss before and after UV irradiation was measured.

The decrease of the transmitted light power as a function of irradiation time is shown in Fig. 7.4.2. Although the light power is decreased by 50% after 24 hours, there is little change of the power after that.

Figure 7.4.3 shows the dependency of the induced loss spectra on a distance from the incident end. The loss near the end is greater than that far from the incident end.

From these results, it has been found that the defects in the pure silica core of the fiber are formed by the UV irradiation.

---

\* The Fujikura Ltd.

Table 7.4.1 Structure of the large bore type pure silica core optical fiber

$\Delta n$	Core		Cladding	
	diameter	material	diameter	material
1(%)	600 $\mu\text{m}$	$\text{SiO}_2$	750 $\mu\text{m}$	$\text{SiO}_2\text{-F}$

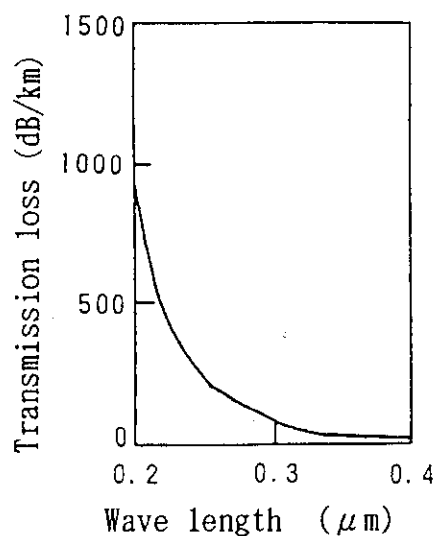


Fig. 7.4.1 Initial transmission loss spectra

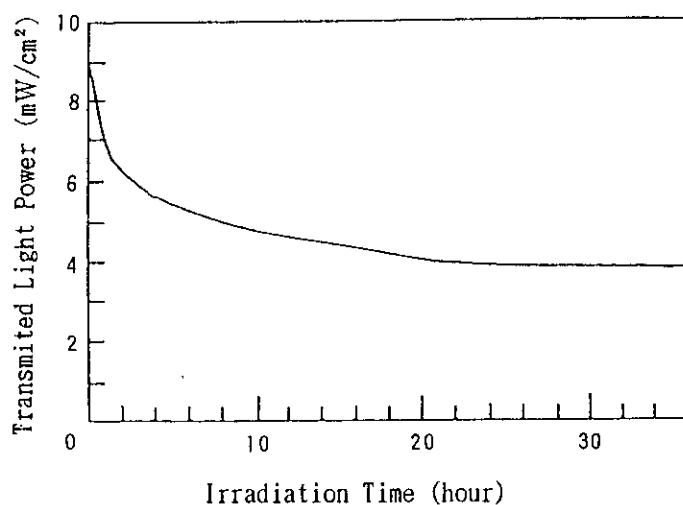


Fig. 7.4.2 Decrease of transmitted light power as a function of UV irradiation time

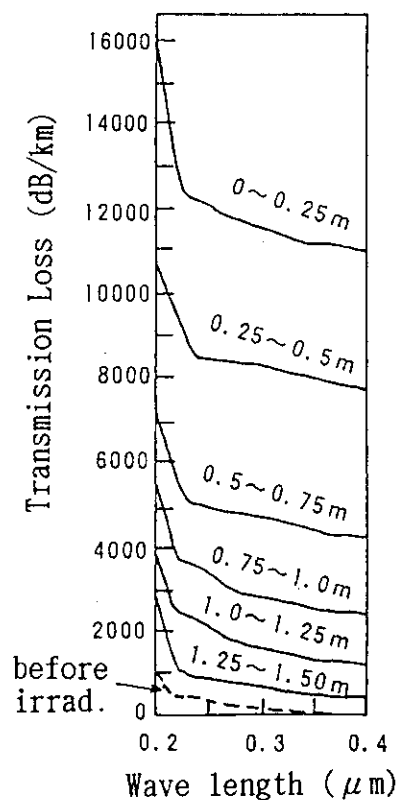


Fig. 7.4.3 Dependency of induced loss spectra on a distance from the incident end

## 7.5 New Candidate for the Residual Defect in a Silicon Surface Barrier Detector<sup>1)</sup>

I. Kanno

The pulse height defect (PHD) in a silicon surface barrier defect (SSB) has been a great interest in view of both experimental and theoretical efforts. The PHD has been considered separately as (1) energy loss in the entrance window, (2) energy loss by the nuclear stopping and (3) energy loss caused by other effects. The theme researchers have been concerned with is the third defect, called the residual defect.

The residual defect has been attributed to the recombination of electrons and holes which were created by an incident particle and formed a plasma column. Many models of recombination have been proposed with a lot of assumptions<sup>2)-4)</sup>, however, none of them have been very successful, especially in the dependences of the residual defect on applied bias voltage and on the resistivity of SSB.

This paper proposes another candidate for the residual defect. An application of the model of the charge collection process<sup>5)</sup> leads to the another origin of the residual defect rather than the recombination of the electrons and holes. A new candidate for the residual defect is the incomplete charge induction by the electrons and holes inside the dielectric plasma column.

The plasma column is assumed to have a cylindrical configuration with the homogeneous electron-hole density inside it. A pair of the free electron and hole moves the distance  $d$  in total, until they reach the positive and negative ends of the depletion layer, and induces a unit charge. The plasma column has the dielectric property at the time of erosion. The negative and positive charges are induced at the top and bottom of the dielectric plasma column. They screen the movement of carriers inside the plasma column from the positive and negative electrodes. The total distance of electrons and holes moving inside the plasma column does not contribute to induce charges on the electrodes. The effectivity induced charge quantity  $Q_c$  is obtained as,

$$Q_c = Q_0 \left( 1 - f \cdot \frac{\Delta X}{D} \right), \quad (7.5.1)$$

where  $Q_0$  is the number of electron-hole pairs created by an incident

charged particle,  $D$  the distance of electrons and holes moving until they arrive at the positive and negative electrodes,  $\Delta X$  the total distance of electron and holes moving inside the plasma column, and  $f$  the screening factor. The plasma columns formed by charged particles with various mass numbers, atomic numbers and energies have the electron-hole densities which range to some orders of magnitude. The screening of the inner movement of carriers from the electrodes is expected to change according to the carrier density of the plasma column.

Experiments were performed using the Tandem Accelerator of JAERI. Nickel ions were injected to an SSB with energies of 109.0 and 160.0 MeV. In the experiments, two SSBs were employed (ORTEC F-series, the effective area  $300 \text{ mm}^2$ ). The resistivities of the SSBs were 362 and 2100  $\Omega\text{cm}$ , respectively. Measurements were carried out at ten bias voltages up to 90 and 200 V for the SSB of 362 and 2100  $\Omega\text{cm}$ , respectively. The measured peak channels of the pulse height are shown in Fig. 7.5.1 as a function of the depletion layer thickness. The full width at half maximum of the pulse height is almost the same size as the symbols.

For the determination of the energies spent to produce electron-hole pairs  $E_0$ , the window defect  $\Delta_w$  and the nuclear stopping defect  $\Delta_n$  were calculated. The nuclear stopping defect was calculated following the method of Wilkins et al.<sup>6)</sup> The window defect and the plasma column length (range of charged particle) were calculated by the code OSCAR<sup>7)</sup>, which employed the semi-empirical formula of Ziegler et al.<sup>8)</sup> In Table 7.5.1, the window defect and the nuclear stopping defect are presented as well as the lengths of plasma columns.

The screening factors of the plasma column which were produced by nickel ions with the energies of 107.7 and 158.5 MeV were obtained as 0.21 and 0.16, respectively. The energies which should be observed by the SSBs have been calculated by Eq.(7.5.1), and are shown in Fig. 7.5.1 by solid lines. The dashed lines in Fig. 7.5.1 indicate the pulse heights which correspond to the values to  $E_0$  in Table 7.5.1.

The difference between the dashed line and the experimental points in Fig. 7.5.1 has been the residual defect. As shown in Fig. 7.5.1, the experimental result of pulse height, i.e. the residual defect is excellently reproduced by the model of incomplete charge induction. The experimental results obtained by the SSB of 2100  $\Omega\text{cm}$  resistivity look slightly lower than the theoretical curves, however, they are in the error bars which are almost the same size of the symbols.

## References

- 1) Kanno I.: J. Nucl. Sci. and Technol., 28, 87 (1991).
- 2) Finch E.C., et al.: Nucl. Instrum. and Meth., 142, 539 (1977).
- 3) Finch E.C., et al.: Nucl. Instrum. and Meth., 163, 467 (1979).
- 4) Hansen N.J.: Nucl. Instrum. and Meth., 96, 373 (1971).
- 5) Kanno I.: Rev. Sci. Instrum., 61, 129 (1990).
- 6) Wilkins B.D., et al.: Nucl. Instrum. and Meth., 92, 381 (1971).
- 7) Hata K. and Baba H.: JAERI-M 88-184 (1988).
- 8) Ziegler J.F., et al.: "The Stopping and Range of Ions in Matter", Vol. 1, Pergamon Press (1985).

Table 7.5.1 Energies deposited in SSB

$E_i$ : incident energy,  $\Delta_w$ : window defect,  $\Delta_n$ : nuclear stopping defect,  $E_0$ : energy spent to produce electron-hole pairs,  $l$ : plasma column length.

$E_i$ (MeV)	$\Delta_w$ (MeV)	$\Delta_n$ (MeV)	$E_0$ (MeV)	$l$ ( $\mu\text{m}$ )
109.0	0.4	0.9	107.7	18.0
160.0	0.4	0.9	158.5	24.5

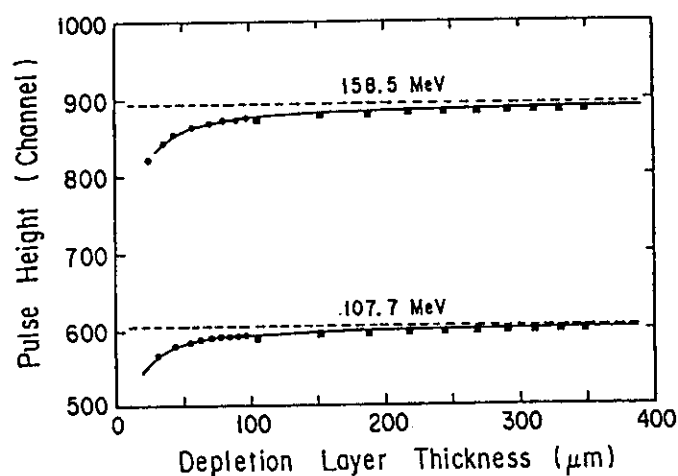


Fig. 7.5.1 Pulse heights versus depletion layer thickness for nickel ions. Experimental data were taken by SSB of 362  $\Omega\text{cm}$  (●), 2100  $\Omega\text{cm}$  (■), in resistivity.

## 7.6 An Analytical Expression for the Distribution of Time Intervals Between Successive Detection Pulses of Neutrons from Spontaneous Fissions

H. Gotoh, M. Suzuki<sup>\*</sup>, M. Haruyama and K. Teranishi<sup>\*\*</sup>

The present authors derived an analytical expression for the distribution of time intervals between successive detection pulses of neutrons emitted from spontaneous fissions and  $(\alpha, n)$  reactions of transuranic elements contained in a radioactive waste drum placed in a passive neutron detection system, basing on the theory of stochastic processes.

The distribution mentioned above is obtained through the probability  $\neg p(t)$  of non-detecting neutron pulses by the time  $t$  after detecting a pulse at the time 0. The probability is represented, under the assumption that all neutrons in the system are lost obeying an exponential distribution with a mean life  $\tau$ , as

$$\begin{aligned} \neg p(t) = & \exp\left\{-t\left[r_r\epsilon + r_f\left[1 - \sum_{v=0}^{v_{\max}} \{f_v(1-\epsilon)^v\}\right]\right]\right\} \times \\ & \times \exp\{r_r\tau\epsilon(1-e^{-t/\tau})\} \times \\ & \times \exp\left[r_f\tau \sum_{v=1}^{v_{\max}} [f_v \sum_{i=1}^v \{v C_i (1-\epsilon)^{v-i} \epsilon^i \frac{1}{i} (1-e^{-it/\tau})\}]\right] \times \\ & \times \left[\sum_{j=0}^{\infty} [Q_j \{1-\epsilon(1-e^{-t/\tau})\}^j]\right] . \quad (7.6.1) \end{aligned}$$

where the product of the first through third factors in the right side represents the probability that any neutrons emitted in the time interval  $(0, t)$  are not detected in the same interval and the fourth factor does the probability that any neutrons remaining at time 0 are not detected in the same interval. The variables  $r_r$  and  $r_f$  represent the emission rate of  $(\alpha, n)$  neutrons and the reaction rate of spontaneous fissions, respectively. The variable  $\epsilon$  is the detection efficiency of neutrons and the variable  $f_v$  ( $v=0, 1, \dots$ ), the distribution of the number of neutrons emitted in a spontaneous fission ( $\sum f_v = 1$ ). The variables  $Q_j$  ( $j=0, 1, \dots$ ) are

---

\* Present address: Tamura Electric Mfg. Co. Ltd., Tokyo

\*\* On leave from Hitachi Ibaraki Technical College, Hitachi Ltd., Hitachi City, Ibaraki-ken

the distribution of the number of neutrons remaining in the system at the time immediate after one neutron is detected ( $\sum Q_j = 1$ ). Those are represented by the unconditional distribution  $P_j$  ( $j=0,1,\dots$ ) of the number of neutrons existing in the system as

$$Q_j = \frac{j+1}{(r_r + r_f \bar{v})\tau} P_{j+1}, \quad j=0,1,2,\dots, \quad (7.6.2)$$

where 
$$\bar{v} = \sum_{v=0}^{\infty} v f_v. \quad (7.6.3)$$

The distribution  $P_j$  is given by the following recurrent relation:

$$P_j = \frac{\tau}{j} [r_r P_{j-1} + \sum_{m=0}^{\min(j-1, v_{\max}-1)} \{P_{j-m-1} (r_f \sum_{v=m+1}^{v_{\max}} f_v)\}], \quad j=1,2,\dots, \quad (7.6.4)$$

and the condition:

$$\sum_{j=0}^{\infty} P_j = 1. \quad (7.6.5)$$

Figure 7.6.1 shows an example of calculated time interval distribution for a  $^{240}\text{Pu}$  source. The parameters used for calculation, the fission rate, the  $(\alpha, n)$  reaction rate, the thermal neutron dieaway time of the system, the neutron detection efficiency, the dwell time of the analyzing instrument and the measuring time, are described in the figure. The obtained time interval was fitted with a sum of two exponential functions with different time constants. The larger time constant was  $9.187 \pm 0.026$  ms. This value is about 8.7% larger than the inverse 8.448 ms of the average counting rate for the neutrons emitted by spontaneous fissions and  $(\alpha, n)$  reactions, because a part of total count is shared to the faster component. The component with the smaller time constant is ascribed to correlated pairs in successive pulses. The time constant of this component was  $0.788 \pm 0.209$  ms. This value is smaller than the dieaway time of the system 0.930 ms nevertheless within 1 $\sigma$  uncertainty.

Figure 7.6.2 shows the time interval distribution for a  $^{252}\text{Cf}$  source to be obtained in similar measuring conditions to those of Fig. 7.6.1. The distribution is decomposed into three exponential functions with different time constants. The two faster components are ascribed to correlated pairs.



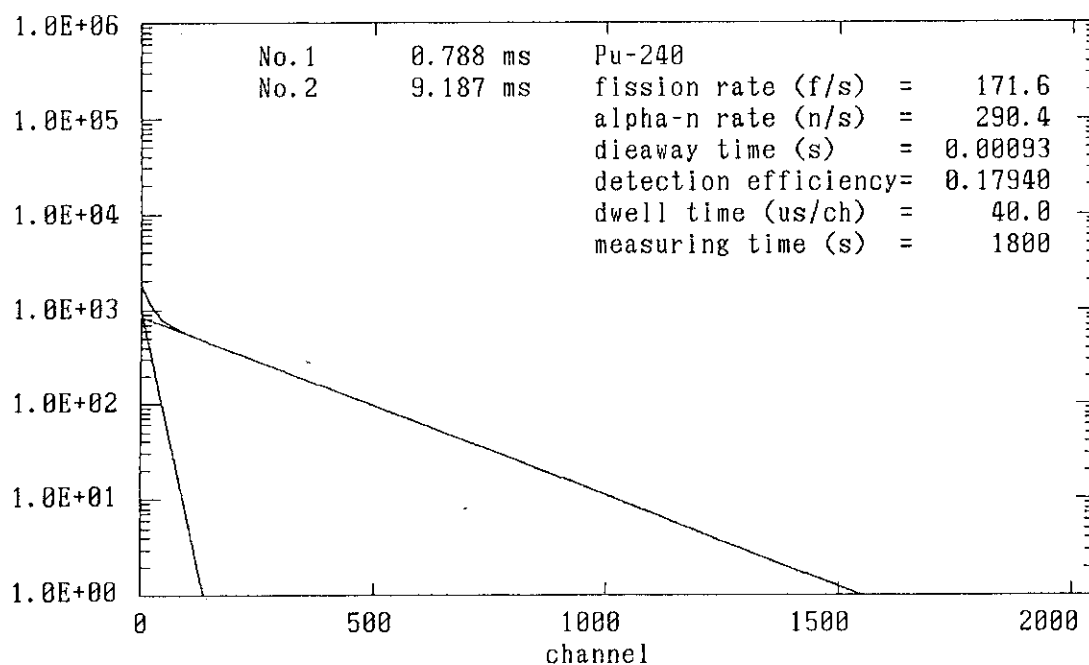


Fig. 7.6.1 A calculated distribution of time intervals between successive pulses for a highly burnt-up plutonium source

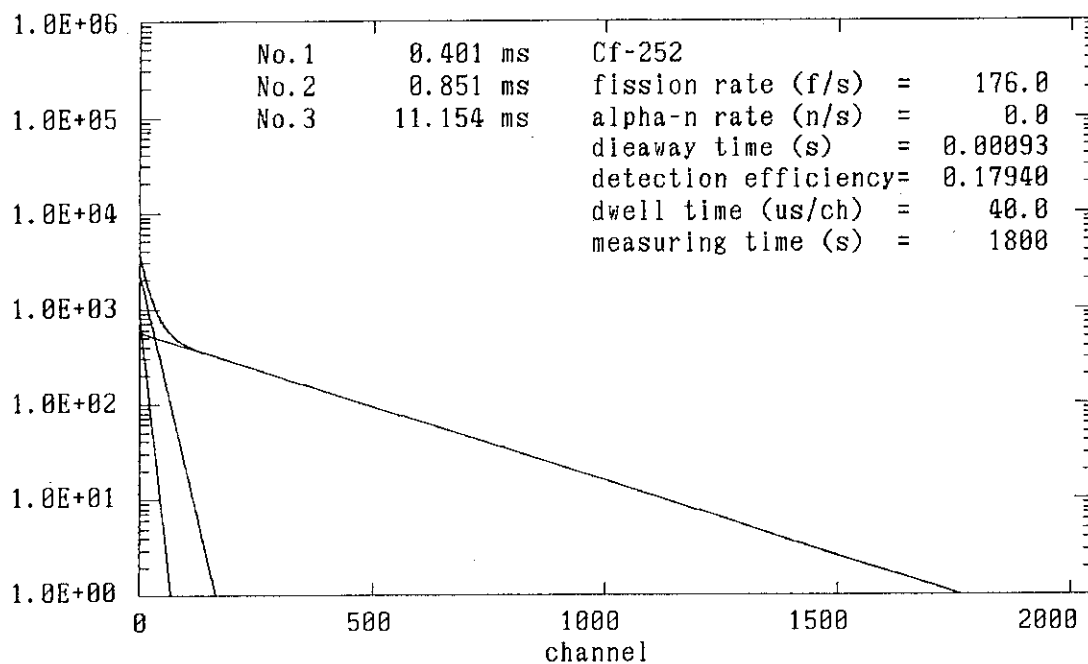


Fig. 7.6.2 A calculated distribution of time intervals between successive pulses for a  $^{252}\text{Cf}$  source

## 7.7 Detection Efficiency for Neutrons from Spontaneous Fissions and ( $\alpha$ ,n) Reactions

H. Gotoh, M. Haruyama, T. Kawamura and M. Takase

Experiments were done using a passive neutron detection system of the type of measuring all time intervals between successive neutron pulses. A  $^{252}\text{Cf}$  or a highly burnt-up plutonium sample was inserted in various positions of 200l drums containing nonradioactive matrices. Distribution data of time intervals were taken and were analyzed by fitting a sum of two or three exponential functions. The component with the largest decay time is supplied by the pairs of detection pulses in uncorrelated relation and the integrated count of the component gives the number of uncorrelated pairs recorded in the measuring time. Other component(s) are(is) supplied by pairs in a correlated relation and the (sum of) integrated count(s) of these(this) component(s) give(s) the number of correlated pairs. The sum of the uncorrelated and the correlated counts is doubtlessly equal to the total count recorded in the measuring time.

Figure 7.7.1 shows a scatter diagram of the ratio of correlated count/number of spontaneous fissions vs neutron detection efficiency obtained in the experiment. We have ninety-four data points on the highly burnt-up plutonium sample containing  $^{240}\text{Pu}$  and seventy-one on the  $^{252}\text{Cf}$  sample. We can see that those two groups draw two curves separated each other. Data points of  $^{240}\text{Pu}$  are well fitted with the prediction curve of a simple combinatorial analysis<sup>1)</sup>. Those of  $^{252}\text{Cf}$  can be fitted with a curve obtained by a more complicated calculation basing on the theory of stochastic processes<sup>2)</sup>.

The neutron emission rate of the  $^{252}\text{Cf}$  source at the time of experiment was calculated using the half-life of the isotope on the base of the certificate of that ( $\pm 0.6\%$  at the 95% confidence limit) of the National Physical Laboratory, England. The agreement between the experiment and the calculation seen in Fig. 7.7.1 means that there are no appreciable neutron emissions other than  $^{252}\text{Cf}$  fissions. The fission rate of the plutonium sample was calculated as  $171.6 \text{ s}^{-1}$  from the amount of plutonium, the isotopic composition and nuclear data. The emission rate of ( $\alpha$ ,n) neutrons of the sample was estimated as  $290.4 \text{ s}^{-1}$  from the total neutron emission rate of the sample determined by the experiment, the

fission rate and the average neutron multiplicity  $\bar{\nu}$  of  $^{240}\text{Pu}$  fission<sup>3)</sup>. No contribution of the induced fissions of  $^{239}\text{Pu}$  was ascertained by the cadmium shielding method.

Figure 7.7.2 shows the neutron detection efficiency for the  $^{252}\text{Cf}$  neutron source placed in a 200ℓ drum filled with light water. The source was moved from the center with 2 cm step along a radius at the half height of the drum. The measured data are plotted with symbol o. The efficiency was also calculated with Monte Carlo programs MNCP and MORSE. The calculated results by MCNP are plotted with symbol x. The agreement between the experiment and the calculation is excellent. The calculation method will be used satisfactorily for this kind of problems with the adopted nuclear data.

#### References

- 1) Gotoh H., et al.: JAERI-M 90-149 pp.151-153 (1990).
- 2) Gotoh H., et al.: Section 7.6 in this issue.
- 3) Norman E., et al.: BNL-NCS-35513 (1985).

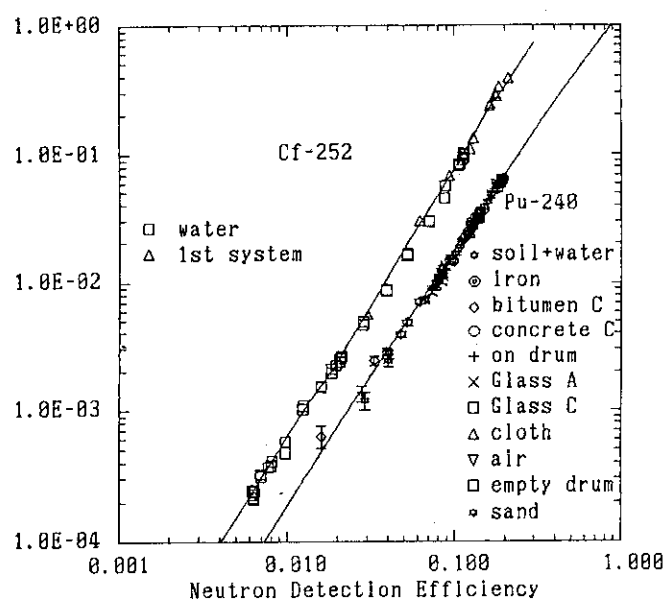


Fig. 7.7.1 A scatter diagram of the ratio of correlated count number of spontaneous fissions vs neutron detection efficiency

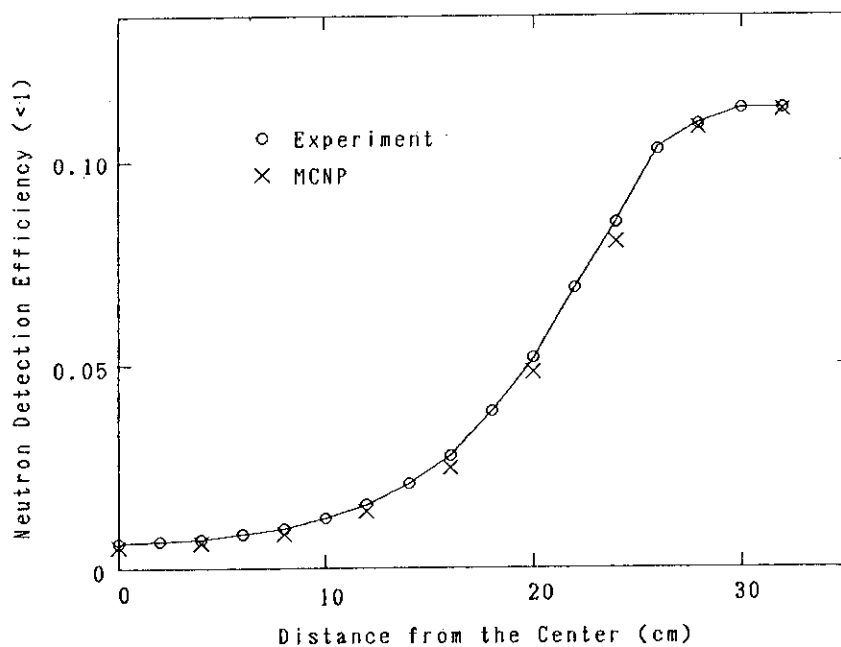


Fig. 7.7.2 Comparison of experiment and calculation of neutron detection efficiency placed in a drum filled with light water.

## 7.8 A New Method for Measurement of Magnetic Field by Utilizing Diamagnetic Materials

K. Sakasai and K. Ara

Noninvasive technique is essentially important in measuring magnetic fields produced by ionic currents associated with electrical activities of various human tissues, especially brain and heart. In order to reconstruct a source distribution of the magnetic fields from the results of magnetic field measurement outside the body, the current dipole model or the magnetic dipole model are usually introduced<sup>1),2)</sup>. The authors have introduced a new method for direct detection of current dipoles or magnetic dipoles by utilizing diamagnetic materials<sup>3),4)</sup>.

Figure 7.8.1 shows a system having diamagnetic superconducting parallel plates and a magnetic sensor. The detectable region with the system is a region being cut out by two extension planes of the two plates. In the system the sensor can detect selectively magnetic fields produced by current dipoles perpendicular to or magnetic dipoles parallel to the planes.

Figure 7.8.2 shows another system with a superconducting cylinder. The cylinder has an axial electrical insulation line (i.e.; an open slit) not to flow closed shielding currents. The detectable region is that being cut out by the extension of the cylinder. In this system the sensor can detect selectively magnetic fields produced by magnetic dipoles parallel to the extension of the axis of the cylinder.

For confirmation of the above systems, simulation experiments were carried out with high-frequency source dipoles and copper devices; good electric conductors such as copper behave as a diamagnetic material in the alternative magnetic fields with eddy currents induced on the surface of it.

Figure 7.8.3 shows a schematic diagram of an experiment with copper plates as a diamagnetic device and a pick-up coil as a magnetic sensor. In the experiment the magnetic field generated by a high-frequency current dipole is measured as an induced voltage in the pick-up coil. The result is shown in Fig. 7.8.4 as compared with that of the case without the plates. One can see that the pick-up coil can detect the dipole only when it exists in the region between the extension planes of the plates.

Figure 7.8.5 shows a schematic diagram of an experiment with a cop-

per cylinder and a pick-up coil for selective and direct detection of a high-frequency magnetic dipole. The result in Fig. 7.8.6 shows that the dipole can be detected selectively.

In conclusion, the experiments proved that the new method is very useful for selective and direct detection of sources of magnetic fields from the human body. For a next stage of the experiments, the system with superconducting devices is being prepared.

#### References

- 1) Williamson S.J. and Kaufman L.: "Biomagnetism", J. Magnetism and Magnetic Materials, 22, 129 (1981).
- 2) Ueno S. and Iramina K.: "Modeling and Source Localization of MEG Activities", Brain Topography, 3, 151 (1990).
- 3) Sakasai K. and Ara K.: "Sensing of Induced Magnetic Field from a Cross Section of Ion-beam Line by Utilizing Diamagnetic Parallel Plates and Magnetic Field Sensors", Proc. Technol. Meet. Magnetics, Paper Mag-90-177, Nov. 30 (1990).
- 4) Ara K. and Sakasai K.: "A Proposal for Measurement of Magnetic Field Produced by Human Body", *ibid.*, Paper Mag-91-100, Mar. 12 (1991).

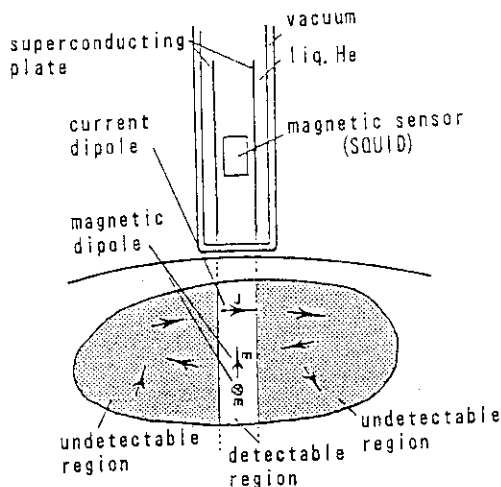


Fig. 7.8.1 Detection of dipoles with superconducting plates

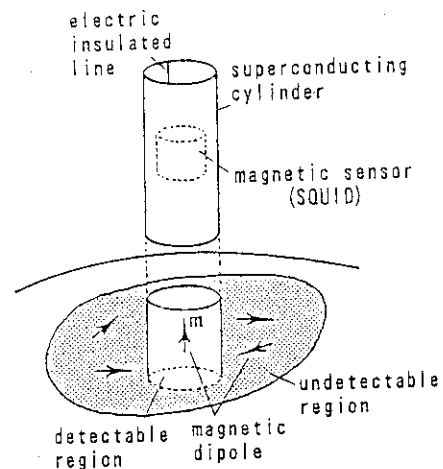


Fig. 7.8.2 Detection of dipoles with superconducting cylinder

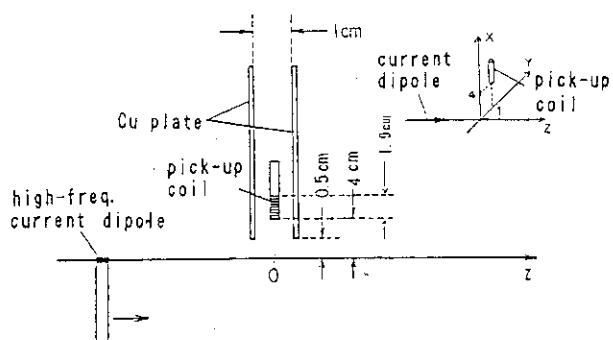


Fig. 7.8.3 Experimental scheme of detecting a high-frequency current dipole with copper plates

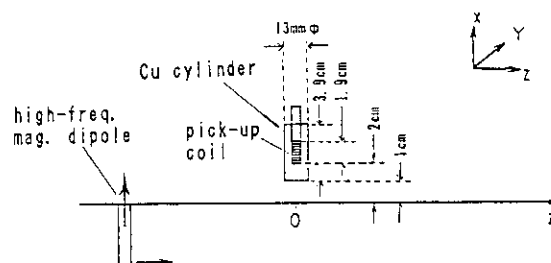


Fig. 7.8.5 Experimental scheme of detecting a high-frequency magnetic dipole with copper cylinder

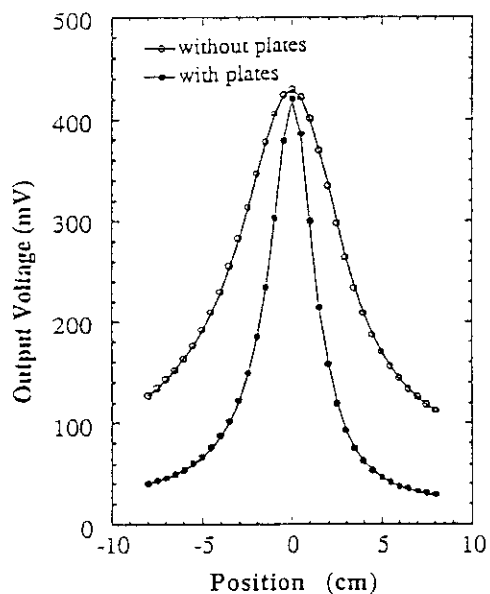


Fig. 7.8.4 Output voltage from a pick-up coil as a function of the position of the current dipole

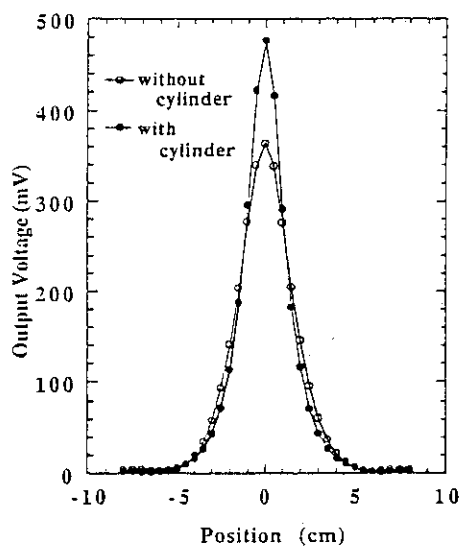


Fig. 7.8.6 Output voltage from a pick-up coil as a function of the position of the magnetic dipole

## 8. Reactor Control, Diagnosis and Robotics

In addition to the activities directly related to particular development projects, much effort has been paid for the basic studies of new analysis methods of nonlinear problems.

As one of the basic studies of advanced control methods, the Hardy-infinity control theory has been studied theoretically with the aim to apply it for control of both nuclear reactor and robotic systems. This study will be followed by an experimental study of control of a simple mechanical system.

The neural networks provide us with new possibilities for reactor diagnosis. Our experience with the networks applied to the reactor noise analysis for anomaly detection indicates that they may be better applied to complex diagnosis problems when used in combination of expert system techniques.

The noise analysis method based on the new concepts of nonlinear impulse response function and nonlinear power spectra made it possible to detect the nonlinearities which could not be detected by the conventional methods of analyses. It will open a new approach for the nonlinear noise analysis.

The benchmark analysis of sodium boiling noise signals was also made according to the IAEA Coordinated Research Program on Acoustic Signal Processing for the Detection of Sodium Boiling or Sodium/Water Reaction. A relatively simple nonlinear method of signal processing in the time domain was applied to detect the sodium boiling.

Since the reactor noise signals have been studied so far from the view point of stochastic processes, the application of chaos theory to the reactor noise analysis will also open a new approach to the problem.

The theoretical study on the manipulator inverse kinematics problems led to the development of a new analysis method which is accurate and applicable to six-link manipulators of any kind.

Experiments have been performed using pseudo-random binary signals (PRBS) in the first experimental navigation of the nuclear powered ship Mutsu to determine her dynamic characteristics. The data are being analyzed using various noise analysis methods to identify the plant dynamics.

(Yoshikuni Shinohara)



## 8.1 Dynamic Identification Experiment of "Mutsu" Reactor by Using Pseudo Random Binary Signal

J. Shimazaki, K. Nabeshima, K. Hayashi and Y. Shinohara

An experiment of "Mutsu" dynamic identification was carried out in the first experimental navigation from February 25 to March 11, 1991. A series of Pseudo Random Binary Signal (PRBS) were adopted<sup>1)</sup> for use in the experiment because it permits only small perturbation to the reactor and is capable of giving a wide-range of frequency characteristics.

The problem in the experiment was how to input the binary signals to the reactor since PRBS had to be applied by manual operation in "Mutsu" reactor. Therefore special equipment was prepared for operator support which shows the PRBS sequence on a small CRT display, remaining seconds for subsequent manipulation, directions of control rod movement (up or down) and melodic sound for time count. In practice, the operators manipulated the control rod or turbine valve watching the information supplied from the equipment in cooperation with the chief person monitoring the reactor responses.

The experiment consisted of two kinds of operation: control rod movement for reactivity perturbation and main turbine valve operation for load-changing perturbation. The PRBS signals and reactor operation conditions were as follows: reactivity disturbance (power level 70%, reactivity change 36 pcm (5.2 cent), PRBS minimum time step 5 sec, period 635 sec, 2 cycles); load disturbance (power level 65%, load change 10%, PRBS minimum time step 10 sec, period 630 sec, 3 cycles).

The measurement data in the reactivity disturbance are shown in Fig. 8.1.1 and also the power spectra of four neutron detector signals in Fig. 8.1.2. These show that the input signals manually operated were large enough to excite the reactor plant variables and that frequency characteristics below about 0.1 Hz are able to analyze using the measurement data obtained. Analyses in more detail are now going on for evaluation of the stability and load following characteristics of "Mutsu" reactor and for preparation of the next experiment dynamic identification to be carried out under different conditions of sea wave as well as ship and reactor operations.

## Reference

- 1) Nabeshima K., et al.: "Reactor Eng. Dep. Annual Report", JAERI-M 90-149, 168 (1990).

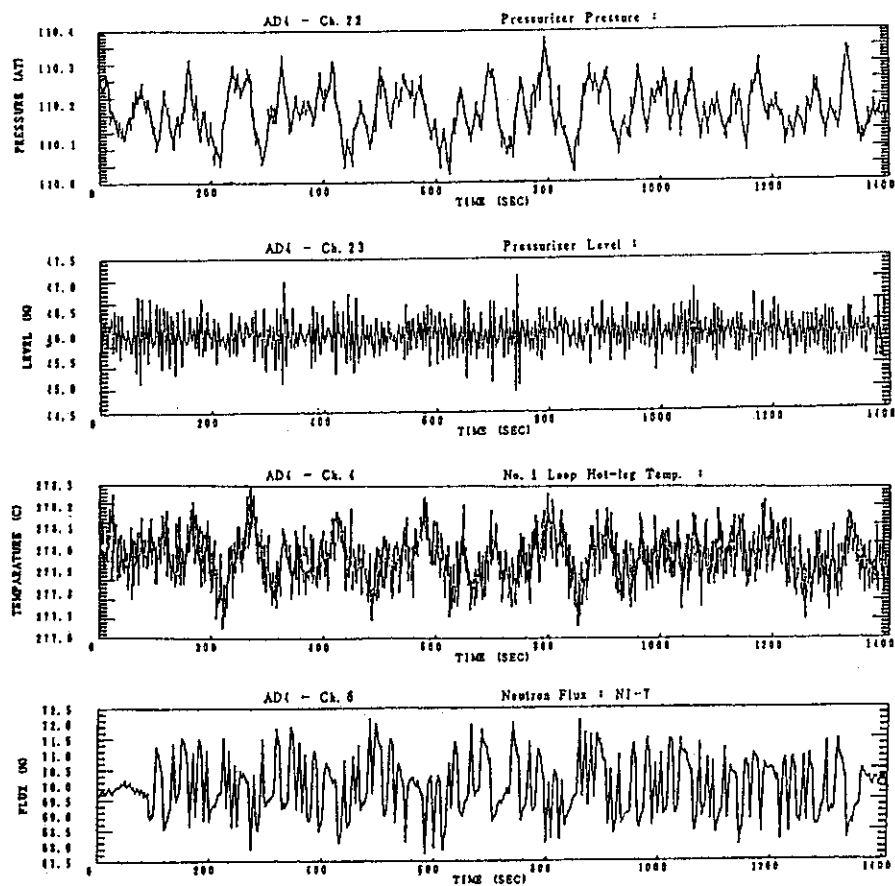


Fig. 8.1.1 Measured data in dynamics identification experiment

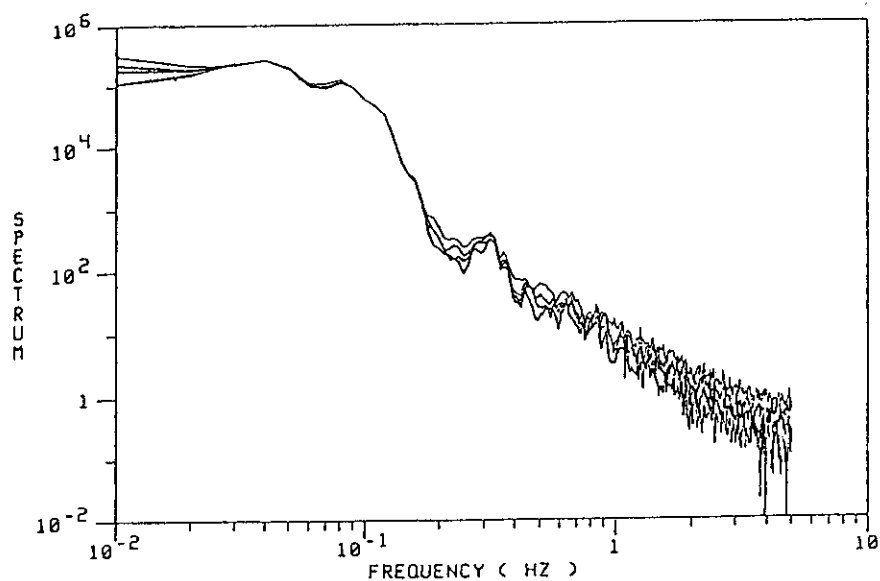


Fig. 8.1.2 Spectra of neutron flux

## 8.2 Application of Layered Neural Networks to Anomaly Diagnosis

K. Nabeshima, J. Shimazaki, K. Suzuki, K. Hayashi and Y. Shinohara

The applicability of the neural networks is studied with the aim to develop a practical method of signal processing for sodium boiling detection. The layered neural networks with the error back propagation scheme for training of network were applied to the acoustic noise signals obtained in a sodium boiling experiment.

Layered neural networks have the simplest structure without feedback connections between layers. The networks used have three or four layers, and 14 or 28 input units. The sigmoidal logistic function representing continuous and nonlinear activation is selected as the activation function.

The data for the input units are 7 statistical values of pressure-sensor signal (P2) located at the center of reactor and sonic-sensor (W1) at the edge. The 7 statistical values are the average, standard deviation, skewness, kurtosis, range, maximum deviation and minimum deviation, which are calculated for 640 data sampled over a time interval of 2 msec with a sampling frequency of 320 KHz. The data from the output units indicate boiling or non-boiling.

Here, the data in only non-boiling and boiling state were used. 703 sections corresponding to 1.4 second in each state are continuous, but only data between non-boiling and boiling state is discrete. The data in the first 100 sections in each state are used for training. The data in the remaining sections are used for testing.

The case-1 neural network involves 14 units at the input layer, 9 units at the intermediate layer (hidden units) and 2 units at the output layer. After 10,000 presentations, the squares of the errors between the actual and desired output values cannot be reduced, shown in Table 8.2.1. But it is clear that the maximum deviation and standard deviation are most important among 7 statistical values.

The case-2 neural network has 28 input units, the same 14 statistical values as in case-1, and 7 time-sequential data of standard deviation for P2 and W1, which are most influential in case-1. In this case, the convergence was reached after 10,000 presentations of training patterns. This neural network showed a good performance in detecting sodium boiling in test data, as shown in Fig. 8.2.1.

The structure of the case-3 network is similar to that of case-1.

The input data are the time-sequential maximum deviation and standard deviation for the W1 signal. The case-4 network has two hidden layers consisting of 16 and 6 unit, respectively. The input data are the same as in case-3. The error in the testing region is smaller than that in case-3. But the learning time is longer than the three-layered network.

It is concluded that the more the input data have informative characteristics, the easier the learning becomes for the neural networks. There remains the problem of optimization of the number of layers and hidden unit.

Table 8.2.1 Sum-squared error of neural networks

network	learning region		testing region		total
	non-boiling	boiling	non-boiling	boiling	
Case 1	1.3	1.1	72.1	130.7	202.8
Case 2	$6.9 \times 10^{-3}$	$7.9 \times 10^{-3}$	24.7	51.5	76.2
Case 3	$8.0 \times 10^{-4}$	1.0	35.0	104.0	139.0
Case 4	$9.5 \times 10^{-3}$	2.0	25.6	98.4	124.0

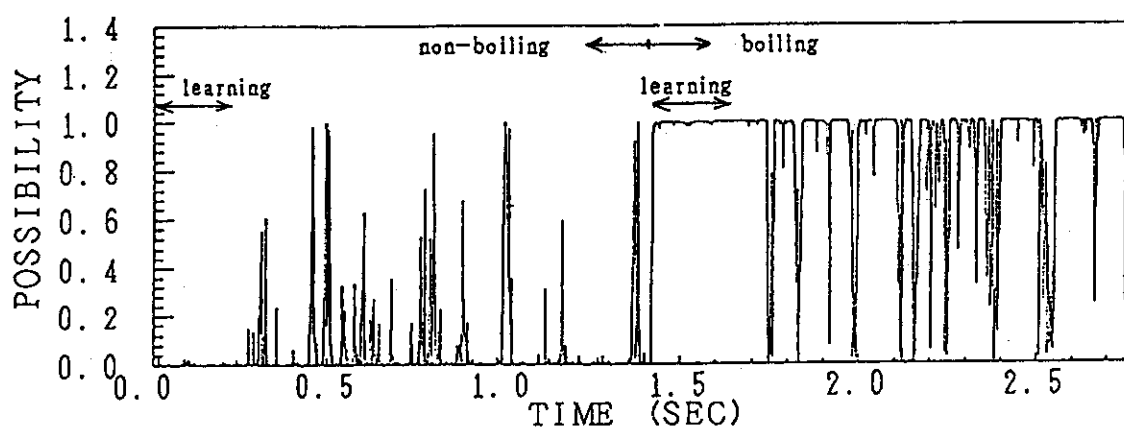


Fig. 8.2.1 Possibility of boiling by case-2 network

## 8.3 Study of a Modeling Method for Nonlinear Reactor Noise

K. Hayashi, Y. Shinohara and H. Konno<sup>\*</sup>

A layered modeling method based on the group method of data handling (GMDH) has been studied for nonlinear reactor noise analysis<sup>1)</sup>.

For practical application to noise analysis of a system, direct use of the model expression and coefficients of the layered model is difficult because a general rule relating the layered model to the physical model of the system is little known. In the present study, we propose a new analysis method using the layered model with a view to reactor noise analysis.

From the obtained complete description  $f(\cdot)$  of the layered model, an overall nonlinear impulse response function, instead of each function, can be calculated recursively according to the equation

$$h_t = f(h_{t-m1}, h_{t-m2}, \dots, h_{t-mk}), \quad t=1, \dots, T \quad (8.3.1)$$

with initial conditions  $h_0=+1, 0$  or  $-1$  and  $h_{-t}=0$ . This function can describe the nonlinear characteristics with single time-lag and, therefore, can be treated easily.

Furthermore, assuming a Gaussian white noise as the system driving source, a power spectrum of  $x_t$  can also be calculated as follows;

$$S_f = |h_f|^2 \sigma^2 \Delta t \quad (8.3.2)$$

where  $h_f$  is the frequency response function obtained from the single Fourier transform of the nonlinear impulse response function,  $\sigma^2$  the residual covariance of the layered model and  $\Delta t$  a sampling time interval.

The new analysis method for the layered model was tested using a typical nonlinear reactor noise data generated from the simple phenomenological nonlinear BWR dynamics model<sup>2)</sup>.

Figure 8.3.1 shows the positive and negative nonlinear impulse response functions estimated for the layered model together with the linear impulse function for the UAR model. The linear impulse response also

---

<sup>\*</sup> Institute of Materials Science, University of Tsukuba,  
Tsukuba-shi, Ibaraki-ken, 305 Japan

shows an oscillation in which the amplitude increases initially and then damps slowly. On the other hand, both nonlinear impulse responses show clear damping oscillations.

Figure 8.3.2 shows the positive and negative nonlinear power spectra estimated for the layered model together with the UAR spectrum. The significant peak at 0.4 Hz of the reactor characteristics frequency of oscillation in the BWR simulation model appears in each spectrum.

On the other hand, the second harmonic of the fundamental frequency is not found in the UAR spectrum, which shows a broad hump at 0.8 Hz, but it is found in both nonlinear power spectra as a slight peak and dip at the same frequency. This fact indicates that the neutron noise signal has already a slight nonlinearity and that the nonlinear power spectrum estimated with the layered model can describe such a slight peak component. It is difficult to find such a slight peak using conventional spectral analysis methods because a number of sample data are required for statistical averaging which picks up the slight peak components masked by other noise components. Therefore, nonlinear power spectrum estimated from the nonlinear model is very useful for detecting nonlinear effects.

#### References

- 1) Hayashi K., et al.: "Layered Model Based on GMDH for Reactor Noise Signals", JAERI-M 89-175 (1989) (in Japanese).
- 2) March-Leuba J., et al.: "Nonlinear Dynamics and Stability of Boiling Water Reactors: Part 1 - Qualitative Analysis", Nucl. Sci. Eng. 93, pp.111-123 (1986).

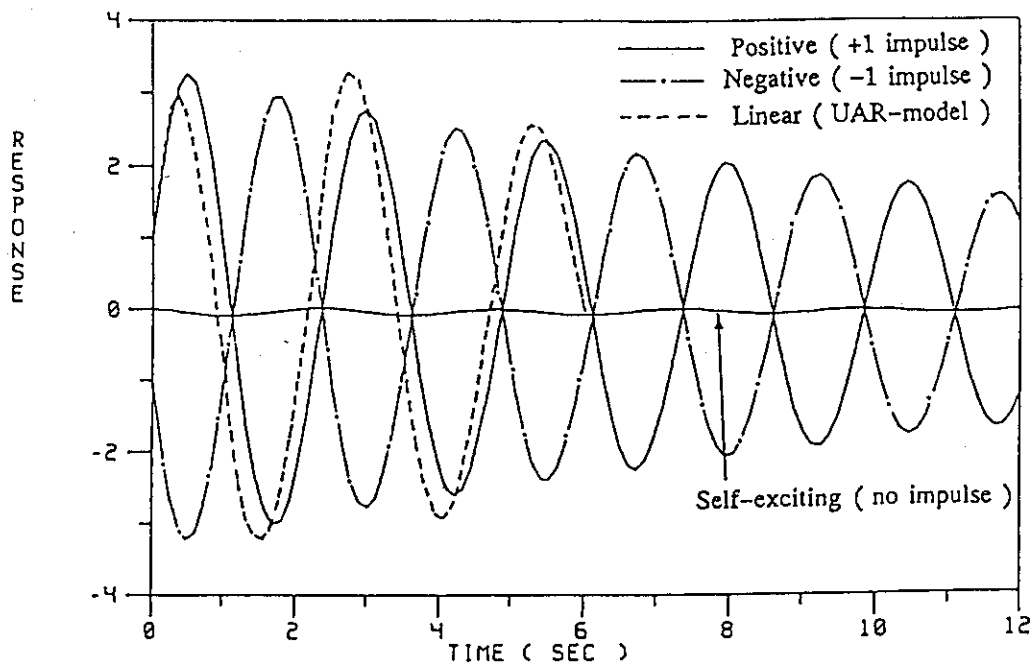


Fig. 8.3.1 Nonlinear impulse response functions

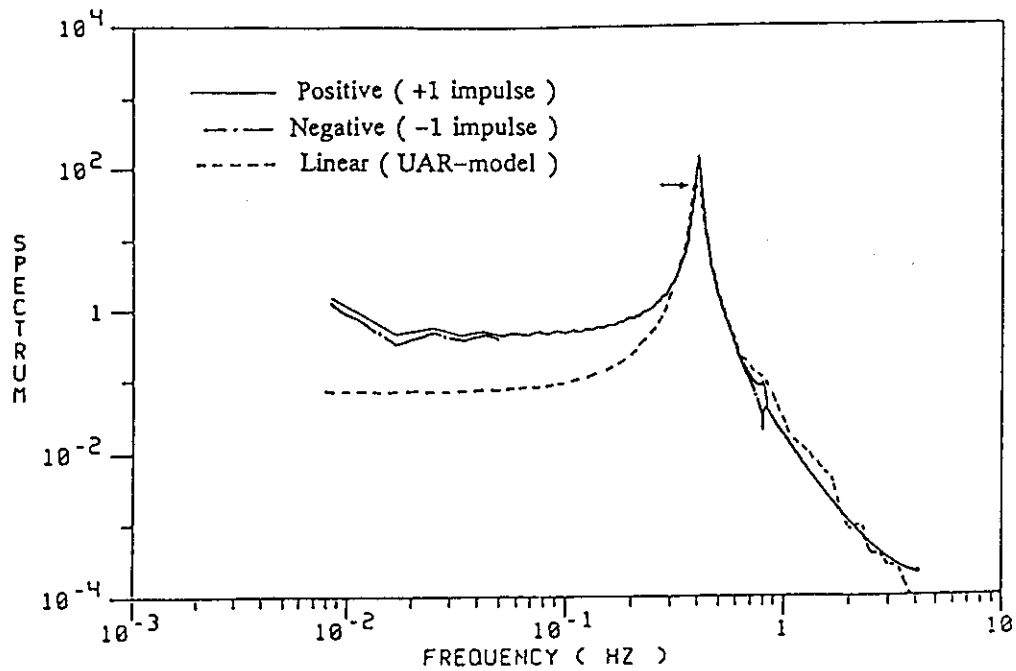


Fig. 8.3.2 Nonlinear power spectra

## 8.4 Search for Chaotic Character of Reactor Noise Signals

T. Suzudo and K. Hayashi

In order to develop a monitoring and diagnosing system for nonlinear reactor noise, the possibility of the application of chaos theory to reactor noise analysis has been examined. For this purpose two basic quantities of a dynamic system (especially for a nonlinear dynamic system), correlation dimension  $D$  and the largest Lyapunov exponent  $\lambda_1$  have been searched for from the reactor noise of NSRR.

The power of the NSRR was observed to oscillate unexpectedly at a stationary high-power-level when operated in an automatic control-mode<sup>1),2)</sup>. Some of typical neutron-flux noise with different gains of the control-rod drive system are shown in Fig. 8.4.1. Some of them are oscillating, the others are not oscillating but fluctuating. We believe that the oscillations are caused by certain nonlinear properties in the automatic control-rod drive system.

In order to apply the chaos theory it is necessary to reconstruct the system trajectory in a multi-dimensional phase space from one-dimensional reactor noise data. The embedding method<sup>3)</sup> was used for this purpose, and two typical reconstructed trajectories are shown in Fig. 8.4.2.

To evaluate  $D$ , the method proposed by Grassberger et al.<sup>4)</sup> is adopted. For the oscillating data,  $D$  is evaluated as 1.26. The result suggests that one periodic mode is excited and the deviation of  $D=1.26$  from the number of the excited mode, 1, may be generated by the influence of the stochastic noise. For the fluctuating noise it is impossible to evaluate the finite value of  $D$  which suggests none of the oscillating-modes is excited and the result shows the influence only of the stochastic noise whose correlation dimension is positively infinite.

The sensitive dependence of the trajectory on initial conditions is a very important feature of chaotic system. The exponential growth rate of the deviation with increasing time caused by the error in the initial condition is called the largest Lyapunov exponent  $\lambda_1$ . One can classify the system by the quantity, i.e., a chaotic system has a positive  $\lambda_1$ . The method proposed by Sato S. et al.<sup>5)</sup> was adopted; this method is so far believed to be the most accurate one where one traces the exponential growth rate of two trajectories from the two very close points, and  $\lambda_1$



is measured as an ensemble average of the rate. We tried to measure the quantity for the oscillating data. It is known that the continuous-time chaotic system has at least  $D > 2$ , so the oscillating data is considered not to be chaotic. As a result we found it difficult to identify the proper value of  $\lambda_1$ , because the exponential rate with increasing time is waving like shown in Fig. 8.4.3.

In conclusion the correlation dimension  $D$  seems to be a useful quantity to measure the number of the excited oscillating mode. It is expected that the correlation dimension  $D$  is worth monitoring to check the anomalous oscillation. The largest Lyapunov exponent  $\lambda_1$  may be useful quantity in the absence of the stochastic noise, but it is too difficult to be determined in the presence of the stochastic noise. This quantity should be used not for a practical monitoring but for a simulation studies.

#### References

- 1) Hayashi K., et al.: JAERI-M 84-056 (1984) (in Japanese).
- 2) Hayashi K., et al.: JAERI-M 84-137 (1984) (in Japanese).
- 3) Takens F.: Lecture Note in Mathematics, 898, 336 (1981).
- 4) Grassberger P., et al.: Physica, 9D, 189 (1983).
- 5) Sato S., et al.: Progress of Theoretical Physics, 77-1, 1 (1987).

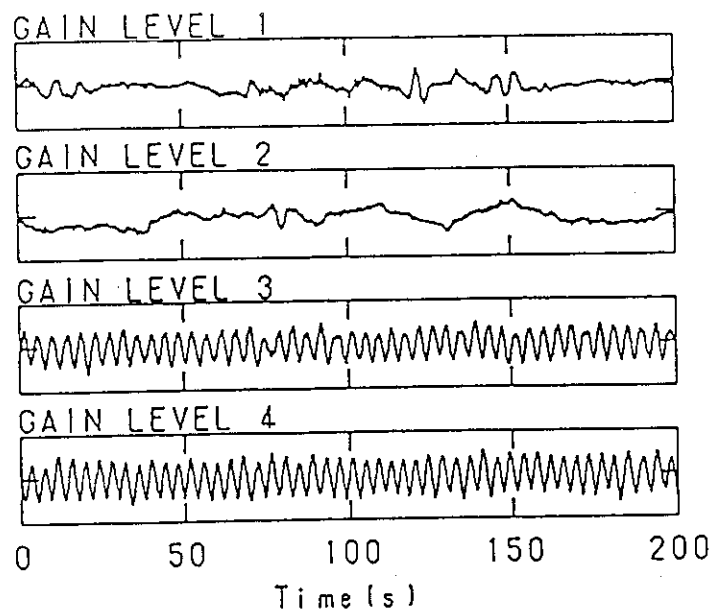


Fig. 8.4.1 Neutron-flux noise of NSRR

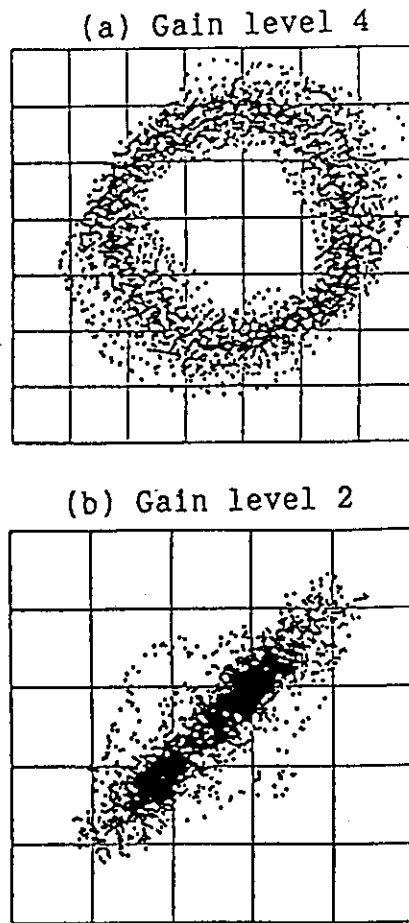


Fig. 8.4.2 Reconstructed trajectory  
( $d=2$ ,  $t_d=0.625$  sec)  
 $d$ : Embedding dimension  
 $t_d$ : Delay time for embedding

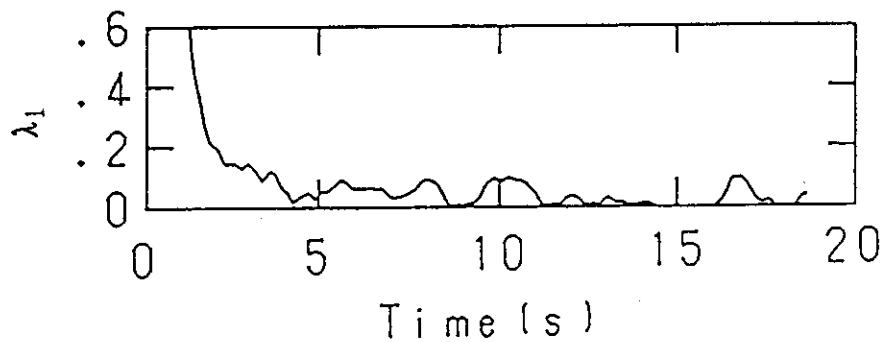


Fig. 8.4.3  $\lambda_1$  of oscillating data ( $d=20$ ,  $t_d=0.0625$  sec)  
 $d$ : Embedding dimension  
 $t_d$ : Delay time for embedding

## 8.5 Detection of Sodium Boiling by Means of Acoustic Noise Analysis

Y. Shinohara, K. Watanabe, K. Hayashi and K. Nabeshima

A benchmark test of signal processing for sodium boiling detection has been performed using a relatively simple nonlinear signal processing method for analyzing boiling acoustic noise. In the test were used ten sets of acoustic noise signals which were synthesized using the experimental data obtained at the out-of-pile sodium loop KNS of KfK, Germany to produce different signal-to-noise ratios. Among these ten sets of test data, only seven sets contained the boiling signals with signal-to-noise ratios from -3 dB to -21 dB in 3 dB steps.

The method was developed on the basis of the following conditions about the acoustic signals which contain both boiling and background acoustic noise:

- 1) The dominant components in the power spectra of the acoustic noise signals corresponding to sodium boiling lie in a high frequency region practically above 30 kHz. The signal-to-noise ratio may be much improved by extracting these components from the background noise by using a high-pass filter.
- 2) The peak amplitudes of boiling noise signals are generally larger than those of the background noise. The noise-to-signal ratio may therefore be further improved by means of some simple nonlinear transformation such as squaring of the filtered signals to enhance the impulsive nature of the boiling noise.

In the present analysis, the original noise signal is first filtered by a high-pass filter with 48 kHz cut-off frequency and then squared. The squared signal is again filtered by another high-pass filter with 80 kHz cut-off frequency and squared again. The resultant signal is integrated over a time interval of 0.5 msec to obtain the feature signal which is used for detecting the boiling.

From this test, the sodium boiling signals with the signal-to-noise ratio down to -12 dB could be detected with 100% reliability (i.e. with zero probability of spurious trip and zero probability of missing boiling). For the signals with the signal-to-noise ratio of -15 dB, boiling could not be detected by the present method. To investigate more effective method of detection, applicability of artificial neural networks is now being studied.

8.6 On a Study of Robust Control Based on  $H^\infty$  Control Theory

K. Suzuki, J. Shimazaki and Y. Shinohara

This study focuses on a mathematical background of  $H^\infty$  control theory. To begin with the outline of  $H^\infty$  control theory is explained by looking at two simple examples of control problems: robust stabilization and wideband disturbance attenuation.

Hilbert space and Banach space are studied in special detail. Then some basic concepts of Hankel operators on Hilbert space are used to prove Nehari's theorem which provides a very powerful tool to find the distance from an  $L^\infty$ -matrix  $R$  to  $H^\infty$  space. Finally, the basic factorization theorem concerning spectral factorization, inner-outer factorization and  $J$ -spectral factorization is proved, which is used in the matrix-valued model-matching problems.

Next we studied mathematical formulations of the standard problems, a model-matching problem, a tracking problem and a robust stabilization problem (See Fig. 8.6.1). The fact is found that the standard problems can be transformed to the model-matching problem through the procedure which is to parametrize all controllers  $K(s)$  stabilizing a plant  $G(s)$  in terms of the coprime factorization over  $RH^\infty$  space.

Then the model-matching problem is one of the most important theme in the  $H^\infty$ -control theory. For the model-matching problem we showed a sufficient condition for an optimal solution to exist and the fact that the infimal error of model-matching to the optimal solution is equal to the norm of the Hankel operator. This can be used to construct a design algorithm of the optimal controller in the  $H^\infty$ -norm sense.

We also discussed the problem of attenuating effect of a disturbance on the output of minimum phase system, the characteristics of sensitivity function of non-minimum phase system and the problem of attenuating the effect of a disturbance on the control signal (the problem to achieve feedback stability by a controller with most limited control energy).

## References

- 1) Suzuki K., et al.:  $H^\infty$  Control Theory (I) - Mathematical Background - (1990).
- 2) Suzuki K., et al.:  $H^\infty$  Control Theory (II) - Standard Problems and

Robust Stabilization - (1990).

- 3) Suzuki K., et al.: H Control Theory (III) - Model Matching Problem and Performance Bounds - (1990).

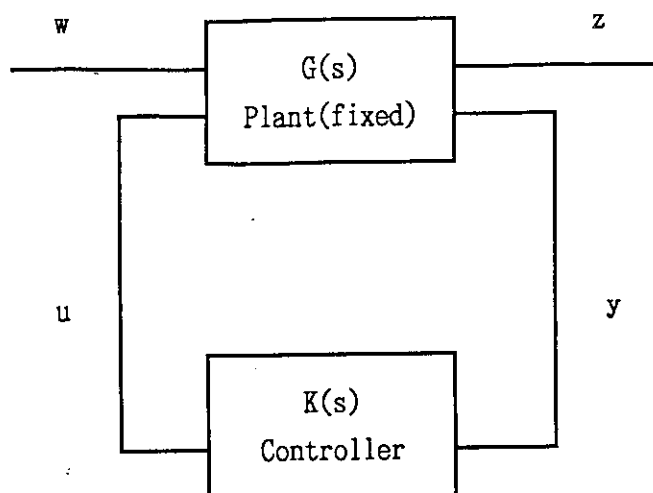


Fig. 8.6.1 Block diagram of the standard problem of  $H^\infty$ -control theory  
 $w(s)$ : exogenous input  
 $u(s)$ : control signal  
 $z(s)$ : output to be controlled  
 $y(s)$ : measured output

## 8.7 Development of Telerobotic Systems for Reactor Dismantlement

Y. Shinohara, H. Usui and Y. Fujii

The program of development of advanced robotic remote handling, or telerobotic, systems for reactor dismantlement has been terminated with accomplishment of all the tasks assigned to the system development group. The main objective of this program was to develop basal technologies of functionally flexible telerobotic systems applicable to various remote handling tasks to be performed in high radiation and unstructured environments during reactor dismantling work such as cutting structural components of complex form located in a narrow space. For this purpose, an advanced system named JARM-25 was developed and used for dismantling radioactive reactor internals of an experimental boiling water power reactor.

The system was constructed on the basis of the experience gained from the design and test of precedent prototype light-duty and heavy-duty systems which were constructed as the cold test facilities for technology development. The total system was designed as a relatively compact transportable system consisting of a multi-functional telerobotic manipulator with a load capacity of 25 daN, a chain-driven transporter and a computer-assisted monitoring and control system. The manipulator is amphibious, i.e. it can be used both in the air and in the water. It is driven electrically and has four modes of operation, i.e. manual push-button, bilateral master-slave, teach-and-playback and programmed control.

Preceding to the application of the telerobotic system to actual dismantling operation, a mockup test of underwater plasma arc cutting of reactor internals was performed to check its performance in a realistic environment using actual-size test pieces of reactor internals. The system was then applied to dismantling a part of the actual radioactive reactor internals of the JPDR, an experimental boiling water power reactor. Successful application of the system has demonstrated the validity and usefulness of such a telerobotic system in dismantling highly radioactive part of reactor.

The slave part of the system used in radioactive environment could be decontaminated completely, therefore the total system was used again to perform various tests for further technology development such as manipulator control with motion constraint.

## 8.8 Kinematic Analysis of Robot Manipulator Using Optimization Technique

S. Sasaki

The kinematic analysis of manipulators consists of two subproblems - the so-called direct and inverse kinematics. The former is to determine the position and orientation of the manipulator hand in regard to a reference coordinate system, which can be straightforwardly formulated in a general form using the coordinate transformation matrix and vector algebra. On the other hand, the latter involves finding the required joint variables given the position and orientation of the hand with respect to the reference coordinate system. It appears quite difficult to solve this problem numerically as well as analytically due to complicated nonlinear equations including trigonometric functions, except for manipulators having special joint structures. From a practical standpoint, the Newton method has been widely used by means of linearization of the kinematic equations with six joint variables. However, since this method has the serious numerical problems such as the singularity of inverse Jacobian matrix, so far we have proposed several different methods to determine the feasible solutions without touching directly that problem. In this presentation, we consider another approach for solving the inverse kinematics of six-link manipulators, in which expressions related to the hand position are replaced with an objective function of the position errors as a typical mathematical programming problem. As the key point, it is needed to depart from the usual idea of dealing with all given joint variables at one time and to pay attention to only three of them, while the remaining three variables are regarded as dependent on the first three. Then, the solutions will be obtained by transforming the original problem into an optimization problem of minimizing the objective function, which is based on the Euclidean norm of the above three joint variables.

The results of computer simulation showed that the numerical solutions are sufficiently reliable in numerical comparisons with the traditional method. In particular, correction of step width at each iteration process made a great contribution to avoid numerical instability and to extend the application ranges of the algorithm. Theoretically, the proposed approach is applicable to all types of six-link manipulators with the articulated joints.

## 9. Heat Transfer and Fluid Dynamics

There are three major fields of research involved in this chapter. The first one is related to thermo-hydrodynamic studies on reflooding behavior during the large break loss-of-coolant accident (LBLOCA) in pressurized water reactors (PWRs). A lot of reflooding experiments were conducted with the large scale Cylindrical Core Test Facility (CCTF) and Slab Core Test Facility (SCTF) of JAERI as a part of the international 2D/3D program. Investigation of reflooding behavior for the combined-injection type emergency core cooling system (ECCS) has been continued, analyzing SCTF test results. A long-term core cooling after the core quench and a flow pattern in the cold leg during the ECC water injection have also been investigated. The research in this field has been performed over ten years and is now at the last stage.

The second field is related to a code development for analyses of reactor transients including accidents. A best-estimate three dimensional two-phase flow code REFLA/TRAC has been developed at JAERI based on the TRAC codes in the USA. Many models in the codes such as TRAC-PF1 and TRAC-BF1 have been investigated and improved to be implemented in the REFLA/TRAC. An interfacial friction model and a numerical treatment of the convection term have been improved. For the assessment purpose of the models, a compact driver program MINI-TRAC has recently been developed and is expected to be effectively utilized. An assessment calculation for the slug flow and the annular flow in a horizontal tube has been performed with the MINI-TRAC.

The third one is related to thermo-hydrodynamic studies on a high conversion pressurized water reactor (HCPWR) development. A double-flat-core type HCPWR was proposed by JAERI and feasibility studies on it have been performed for a couple of years. Safety evaluation for it with the REFLA/TRAC code has been continued. A reactivity initiated accident is a new item analyzed. Characteristics of the critical heat flux (CHF) for the tight lattice core have also been investigated. Experiments with a newly constructed high pressure loop, whose maximum pressure is 16 MPa, was initiated and will be continued for a couple of years.

(Yoshio Murao)



### 9.1 Investigation on Long-Term Core Cooling Behaviors after Reflood Phase of PWR LBLOCA

T. Iguchi, T. Okubo, T. Iwamura, H. Akimoto, A. Ohnuki, Y. Abe and Y. Murao

According to the present design of PWRs, water from emergency core cooling system (ECC water) is injected into the primary loops to cool down the core during the reflood phase of a large-cold-leg-break loss-of-coolant accident and to keep the core cooled for long term (Long term core cooling). Previous tests with Cylindrical Core Test Facility (CCTF) indicated that ECC water cooled the core effectively during the reflood phase without the core exceeding the maximum temperature allowed in the licensing. However, long term core cooling behavior, especially with primary system response, had not been investigated yet in previous experimental works. Therefore, the present CCTF tests had been performed.

Evaluation on the present CCTF tests were focused on:

- Primary system response until 1 day after scram; Decay heat generated in the core decreases with time. Hence, it is very low on 1 day after scram in comparison with that at the reflood initiation. System response under low decay heat is one of concerns of the present CCTF tests.
- Primary system response after switching of ECC water injection point; In typical PWRs, ECC water is injected into cold legs during reflood phase. However, about 1 day after scram, ECC water injection point is switched to both hot legs and cold legs. Effect of this switching of ECC water injection point on thermal hydraulic system response is the other concern.
- Long term core cooling; Core must be kept cooled for long term. CCTF will show the core cooling behavior affected by the system response, as in PWRs. Whether core can be kept cooled is another concern in terms of reactor safety.

CCTF tests indicated for primary system response until 1 day after scram as follows; Basically, thermal hydraulic response in the primary system was the same as that just after whole core quenching. Namely, a part of ECC water injected into the cold legs entered the core via the downcomer. The remainder flowed out through the cold leg break point. Water cooled the core and steam was generated. The core and the upper

plenum were filled with two-phase flow. Steam and entrained water flowed through loops and discharged through break point.

Other behaviors observed were as follows;

- (1) Short period fluid oscillation (Period=about a few seconds) occurred around cold legs, accompanied with low decay heat level due to condensation at ECC injection points. This type of fluid oscillation had been observed in the previous CCTF tests simulating the reflood phase<sup>1)</sup>.
- (2) ECC water flowed reversally and filled the cross over legs because of low steam flow rate through loops. Resultantly, "loop seal" occurred.
- (3) Loop seal occurrence was earlier under "BE" condition, i.e. high ECC water injection condition, than under "EM" condition. Under loop seal, fluid oscillation with long period (Period=about 100 seconds) occurred, resulting in ① mass movement between the core and the downcomer and ② fluid temperature oscillation in the core. This type of fluid oscillation had been observed in some previous CCTF tests, eg. "BE" simulation test<sup>1)</sup>. Reason of the oscillation is analyzed in the reference<sup>1)</sup>.
- (4) Core was kept cooled even under fluid oscillation with short and long periods. Loop seal did not indicate adversal effect on core cooling.

CCTF tests indicated for primary system response after switching of ECC water injection point as follows; Important effect of switching of ECC water injection point on primary system response was the changing of the water flow direction in the core. Before the switching the water flowed from the bottom to the top like in reflood phase, while after the switching the water flowed from the top to the bottom. Water injected into the hot legs flowed down the core, and flowed up in the downcomer. Finally, water flowed out through the cold leg break point. Steam was completely condensed by the water injected into the hot legs, and then the core and the upper plenum were filled with water only. All cross over legs in intact loops were filled with water, i.e. "Loop seal".

The purpose of the switching of ECC water injection point is to suppress the boiling in the core. CCTF tests indicated that the upper plenum was filled entirely with the subcooled water after the switching. Therefore, it was considered that there was no boiling in the upper plenum. On the other hand, in the core the saturation temperature was

detected locally. Hence, the local boiling might occur in the core. However, from the measured differential pressure between the top and the bottom of the core, the amount of steam in the core was considered to be small or almost null. Thus, the boiling in the core was considered to be suppressed.

Through the present CCTF tests, it was confirmed that the core was cooled for long term.

#### Reference

- 1) Okabe K., et al.: Private communication.

## 9.2 Investigation on Flow Pattern in Cold Leg during PWR Reflood Phase by Using CCTF Data

T. Iguchi, H. Akimoto, T. Iwamura, T. Okubo, A. Ohnuki, Y. Abe,  
M. Okazaki and Y. Murao

During reflood phase of a PWR large-break loss-of-coolant accident, subcooled water is injected into horizontal cold leg pipings, where the water contacts the flowing steam. It is well known that the significantly strong condensation occurs due to the direct contact between water and steam, and that fluid oscillation occurs resultantly. This oscillatory behavior instabilizes the calculation in reactor safety analysis with the present existing codes. To stabilize the calculation and to apply to PWR accident analysis, it is necessary to understand the behavior phenomenologically especially in large radius pipe. Accordingly, by using data obtained with Cylindrical Core Test Facility (CCTF), which had a large radius horizontal pipe, fluid oscillation phenomena had been investigated. In addition, major factors influencing the oscillation phenomena and the effect of pipe diameter had been investigated.

Figure 9.2.1 shows the CCTF cold leg, which was used in the present tests. The inner diameter was 155 mm, which was about 1/5 of PWR cold legs. Steam and water were injected from the points shown in the figure and flowed out to the downcomer. In the downcomer, steam and water were separated. Water was accumulated in the downcomer, while steam flowed out through another piping attached to the downcomer. Steam and water flow rates were adjusted to simulate PWR situation. Downcomer water level and pressure were also controlled. Cold leg piping was made of transparent material, so that the flow pattern could be observed.

According to previous small scale experiments, fluid oscillatory behavior is mainly depend on the ratio ( $R_T$ ) of injected steam flow rate  $m_g$  (kg/s) and the condensibility of injected subcooled water  $m_{cmax}$  (kg/s) ( $= m_{ECC} \Delta h_{ECC} / h_{fg}$ ;  $m_{ECC}$  = Water injection rate (kg/s),  $\Delta h_{ECC}$  = Subcool enthalpy of injected water (kJ/kg),  $h_{fg}$  = Latent heat (kJ/kg)), i.e.  $R_T = m_g / m_{cmax}$ . As shown in Fig. 9.2.2, fluid behavior was oscillatory in small scale experiments when  $R_T < 0.84$ .

In the same figure, present data are also shown. Data can be classified into two regions as follows;

(1)  $m_{cmax} > 4.5 \text{ kg/s}$ 

This condition is simulating accumulator injection condition in PWRs. In such high ECC water injection rate,  $R_T$  is below about 0.2, when steam injection rate is the value expected in PWRs ( $m_g \approx 1 \text{ kg/s}$ ). Therefore, steam was completely condensed and water plug was formed in cold leg. The water plug oscillated violently upstream and downstream around the water injection point (upstream in most case). Period of the oscillation was depend on steam flow rate. It was usually about 2 seconds. This behavior was nearly the same as small scale experiment result.

(2)  $m_{cmax} < 1 \text{ kg/s}$ 

This condition is simulating low pressure coolant injection condition in PWRs. In this ECC water injection rate, the condensibility is comparable with steam injection rate. In small scale experiment result, fluid behavior was stable at  $R_T > 0.84$ , while it was oscillatory at  $R_T < 0.84$ . On the other hand, the observed fluid behavior in CCTF tests was always stable.

The reason of stable fluid flow at  $R_T > 0.84$  was explained by the small scale experiment that, since condensibility of injected water is not large enough to condense all injected steam, steam remains and no water plug is formed. In CCTF tests, remaining steam was observed under this boundary conditions. Same behavior as in small scale experiments stabilized the fluid behavior at  $R_T > 0.84$ .

At  $R_T < 0.84$ , oscillatory fluid behavior was observed in small scale experiments. This was explained that, since condensibility of injected water is large enough to condense all injected steam, water plug is formed and then flow oscillation occurs. However, in CCTF tests, stable flow was observed. According to the observation in CCTF tests, injected water piled up at the bottom of cold leg piping and steam flowed through at the upper part of the horizontal cold leg piping. Thus, stratified flow was established downstream at the water injection point and no water plug was formed. This difference was considered due to the different pipe diameter. In large pipe, stratified flow can be easily established.

CCTF results described above were obtained by controlling the water level in the downcomer not to block the exit of the cold leg (Low downcomer water level). However, in PWRs such control is not conducted. Therefore, the flow pattern under high water level in the downcomer was

additionally investigated in CCTF tests. Results indicated that the flow pattern was oscillatory even under  $m_{cmax} < 1 \text{ kg/s}$  and  $R_T < 0.84$ , when the water level in the downcomer blocked the exit of the cold leg.

In summary, it was found that fluid oscillatory behavior was depend on  $R_T$ , pipe diameter and water level in the downcomer. In large radius pipe, flow was stabilized due to stratification of water and steam. Even in such stable case, flow became unstable when water blocked the exit of the pipe.

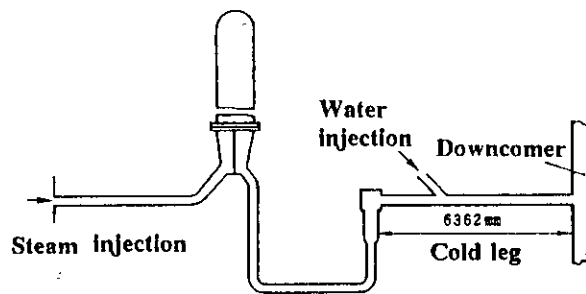


Fig. 9.2.1 Test facility

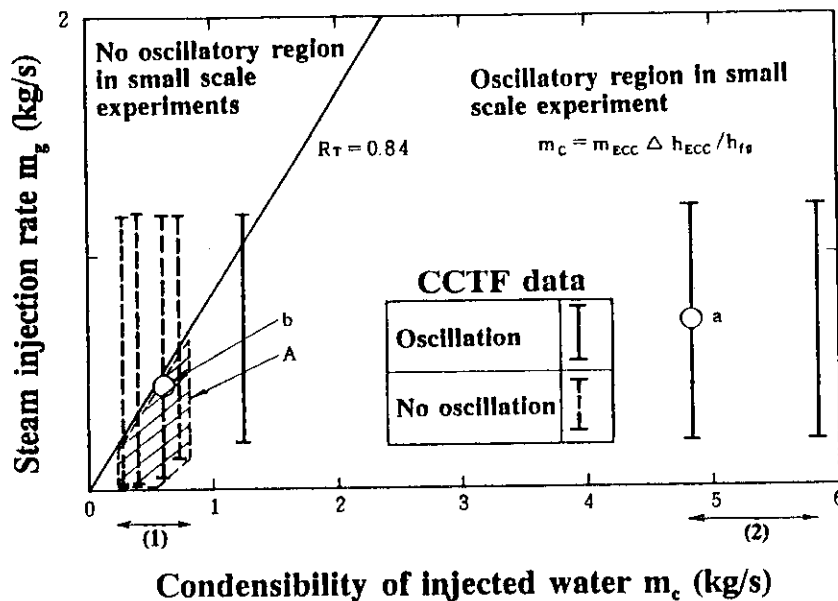


Fig. 9.2.2 Flow pattern map under low water level in downcomer

- (1) Water injection rate corresponding to Accumulator injection in PWRs.
- (2) Water injection rate corresponding to low pressure coolant injection in PWRs.

### 9.3 Refill Behavior in the Simulated PWR under Combined ECC Injection Mode

M. Okazaki, T. Iguchi, T. Iwamura, H. Akimoto, T. Okubo, A. Ohnuki, Y. Abe, H. Adachi\* and Y. Murao

The test S3-21 was performed with SCTF in order to confirm that the water falling-down behavior from the upper plenum to the top part of the core was continuous in spite of the intense steam upflow resulted by the evaporation of the water even under the conditions of the low pressure, the high core power, the high initial clad temperature, and the hot ECC water. The test conditions were selected to give the more intense steam upflow than those of the previous SCTF tests, as follows: the low containment pressure (0.2 MPa), the high core power (initially 9.4 MW), the high initial clad temperature (maximum 850°C), and the hot ECC water (110°C).

The test result of S3-21 is compared with that of S3-18 (Hot ECC water test):

Major experimental conditions for both tests are as follows.

	S3-18 (Run 722)	S3-21 (Run 725)
Initial core power (MW)	7.5	9.4
Initial clad temperature (°C)	700	850
ECC water temperature injected to upper plenum (°C)	110	35 (for first 15 seconds after blowdown) 110
Containment pressure (MPa)	0.3	0.2

Through the comparison the following results are observed.

- (1) Higher initial peak clad temperature and core power delayed the turnaround time and increased the maximum turnaround temperature (Fig. 9.3.1)
- (2) Start of lower plenum refilling after blowdown was earlier even in the higher initial peak clad temperature and higher core power than

in test S3-18. This is because ECC water temperature injected at upper plenum was selected at 35°C during first 15 seconds in this test (Fig. 9.3.2)

- (3) Oscillatory water downflow did not occur in the region of water down-flow during core reflooding, even in the condition of high core power and high clad temperature, and stable water downflow continued until the end of core reflooding.

Through the evaluation of the test result, the following conclusions were obtained.

- (1) The qualitative behavior before the lower plenum refilling were similar to the previous SCTF test results.
- (2) Water head difference between in downcomer and in lower plenum which initiates the lower plenum refilling is measured as about 4.1 mH<sub>2</sub>O in S3-21 test (Fig. 9.3.3). This corresponds approximately to the difference between  $\Delta P_{HL}$  and  $\Delta P_{CL}$  as shown in Fig. 9.3.4. The water head in the downcomer, which is necessary to initiate the lower plenum refilling, is higher as  $\Delta P_{HL}$  is higher.
- (3) However, some quantitative differences from the previous SCTF test results were observed. During the reflood phase, the void fraction in the core was higher, the heat transfer coefficient was lower, and hence the clad temperature continued the increasing for a while after the reflood initiation due to higher core power and the lower pressure in the present test than in the previous SCTF tests. And, the rising speed of the core collapsed water was smaller and the core collapsed water level itself was lower in the present test than in referenced previous SCTF test S3-18 performed under the low core power and the high containmmnet pressure.
- (4) The steam flow rate through the broken hot leg before the lower plenum refilling could not sufficiently be explained by the estimated steam flow rate due to i) the volume expansion of the steam in the primary system, ii) the flushing of the water in both the pressure vessel and the steam/water separator, and iii) the evaporation by the heat release of the core. There possibly exist other causes for steam generation like the heat release of the structure in the pressure vessel.



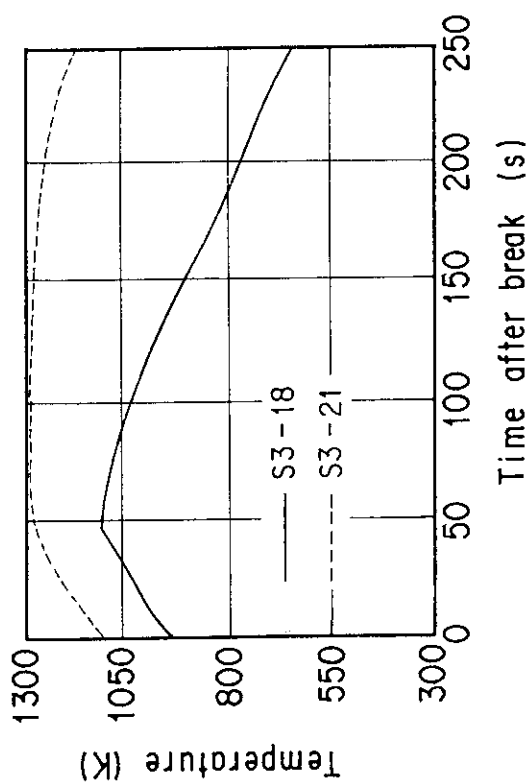


Fig. 9.3.1 Clad temperature

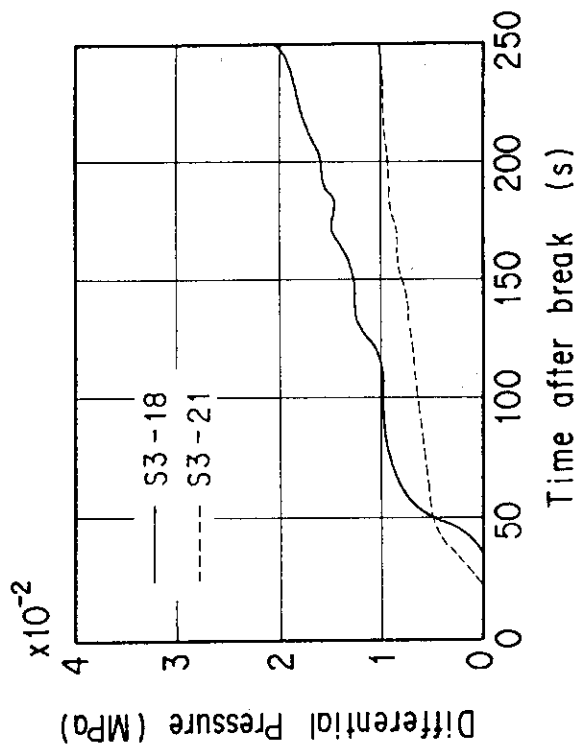


Fig. 9.3.2 Differential pressure across the core

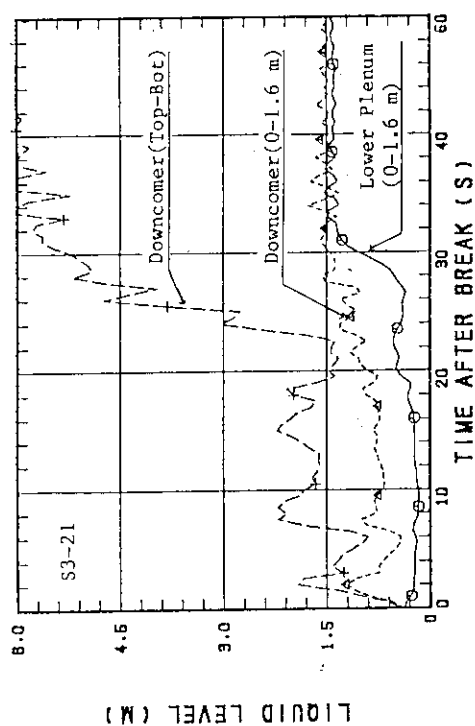


Fig. 9.3.3 Liquid level in pressure vessel

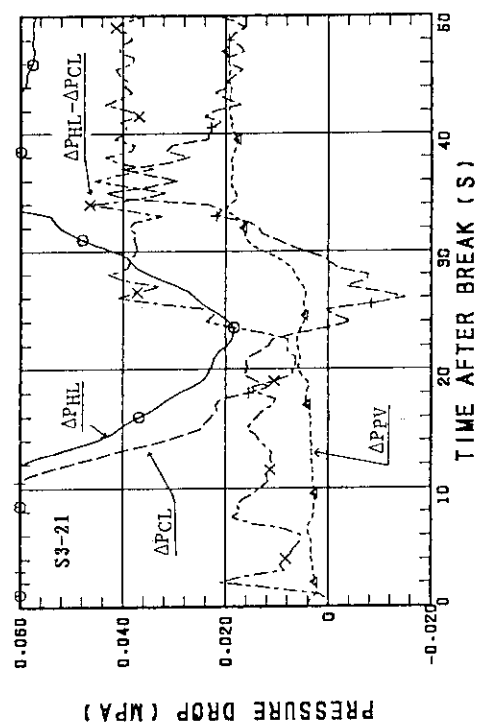


Fig. 9.3.4 Pressure drop in loops

#### 9.4 Investigation of Water Break-through and Core Cooling Behaviors under Intermittent ECC Water Delivery to Upper Plenum during Reflood Phase in PWRs with Combined-Injection type ECCS

T. Okubo, T. Iguchi, T. Iwamura, H. Akimoto, A. Ohnuki, Y. Abe,  
I. Sakaki\*, H. Adachi\*\* and Y. Murao

During the reflood phase of the loss-of-coolant accident (LOCA) in a Pressurized Water Reactor (PWR) with the combined-injection type Emergency Core Cooling System (ECCS), the ECC water injected into the hot legs is considered to be delivered to the upper plenum. Although this water delivery was expected to be steady, there are some information<sup>1),2)</sup> which show that ECC water delivery to the upper plenum is not steady but intermittent due to steam condensation in the hot legs.

Based on these information, a test (Test S3-20)<sup>3)</sup> was conducted with the Slab Core Test Facility (SCTF) Core-III in order to investigate the water break-through and core cooling behaviors under the intermittent ECC water delivery to the upper plenum during the reflood phase. In this test, subcooled ECC water was injected intermittently just above the upper core support plate above Bundles 7 and 8 of the core. The average injection rate was set to be the same as that in SCTF Test S3-13<sup>4)</sup>, which was conducted under an Evaluation Model condition with continuous ECC water injection. ECC water injection rates in both the tests are compared in Fig. 9.4.1.

Figure 9.4.2 shows fluid temperatures just below the tie plate holes. When the temperature is subcooled, it suggests the water break-through at the location. Based on these data, it has been found that the break-through occurred intermittently immediately corresponding to the intermittent ECC water injection (above Bundles 7 and 8). When the break-through occurred, there observed different thermo-hydrodynamic behaviors between the break-through region and the non-break-through region. This is the same core thermo-hydrodynamic behaviors as observed in the previous tests<sup>4)</sup> simulating the combined-injection type ECCS.

Figure 9.4.3 shows a comparison of the core total differential pressure between Tests S3-20 and S3-13. During the periods when ECC water

---

\* Toshiba, Ltd., Kawasaki

\*\* Yamagata University, Yonezawa

injection was nearly zero in Test S3-20, the data decreased and then recovered when the injection increased. The reason of the decrease in the core differential pressure is considered to be the increase in the intact loop differential pressure (i.e. the steam binding) due to the decrease in the steam condensation by the ECC water in the upper plenum.

This oscillatory core differential pressure behavior resulted in the oscillatory core cooling behavior as observed in Fig. 9.4.4. Although the core cooling behavior was oscillatory, it has been found that the core cooling is nearly identical to that for the continuous injection case.

#### References

- 1) Weiss P.A. and Hertlein R.J.: "UPTF First Integral Test with Combined ECC Injection", NUREG/CP-0091, Vol. 4 (1988).
- 2) Cappiello M.W.: Private communication.
- 3) Okubo T., et al.: "Evaluation Report on SCTF Core-III Test S3-20", JAERI-M 90-080 (1990).
- 4) Iguchi T., et al.: "Evaluation Report on SCTF Core-III Test S3-13", To be published as a JAERI-M report.

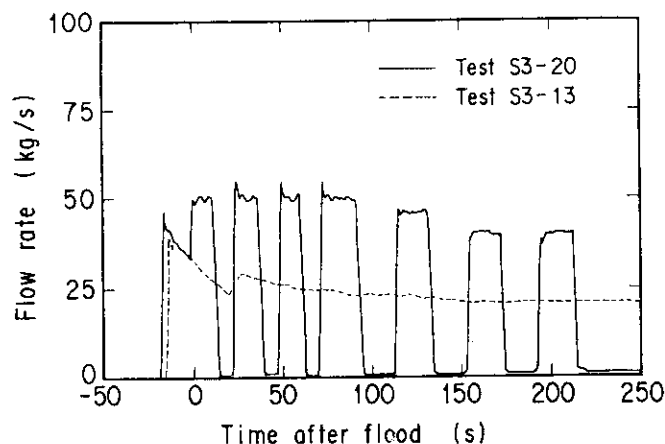


Fig. 9.4.1 Comparison of ECC water injection rate into upper plenum between Tests S3-20 and S3-13

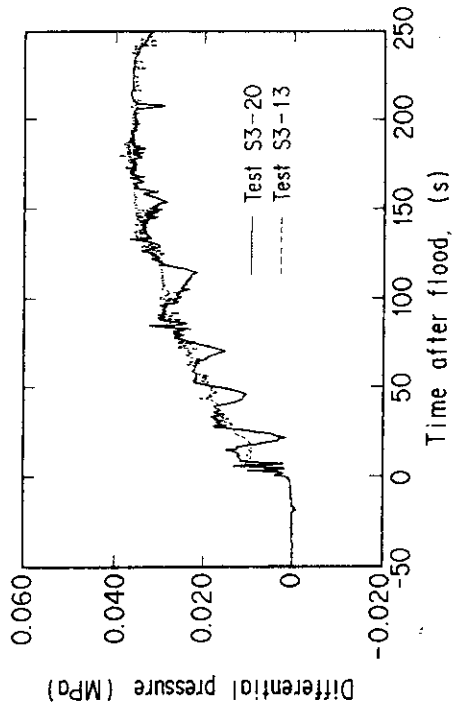


Fig. 9.4.3 Comparison of core total differential pressure between Tests S3-20 and S3-13

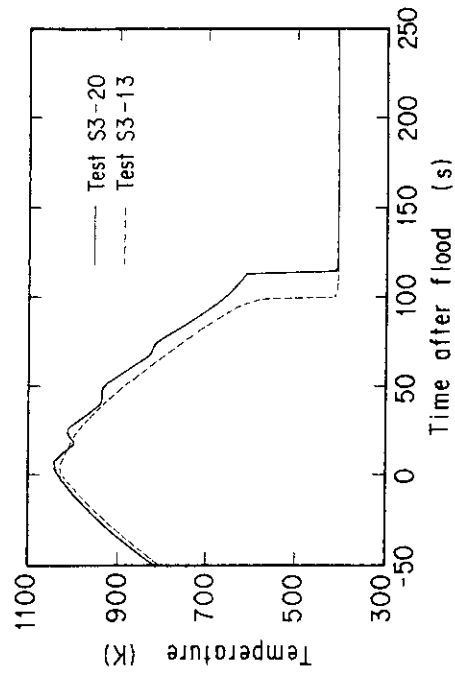


Fig. 9.4.4 Comparison of rod surface temperature at 1.905 m elevation in Bundle 2 between Tests S3-20 and S3-13

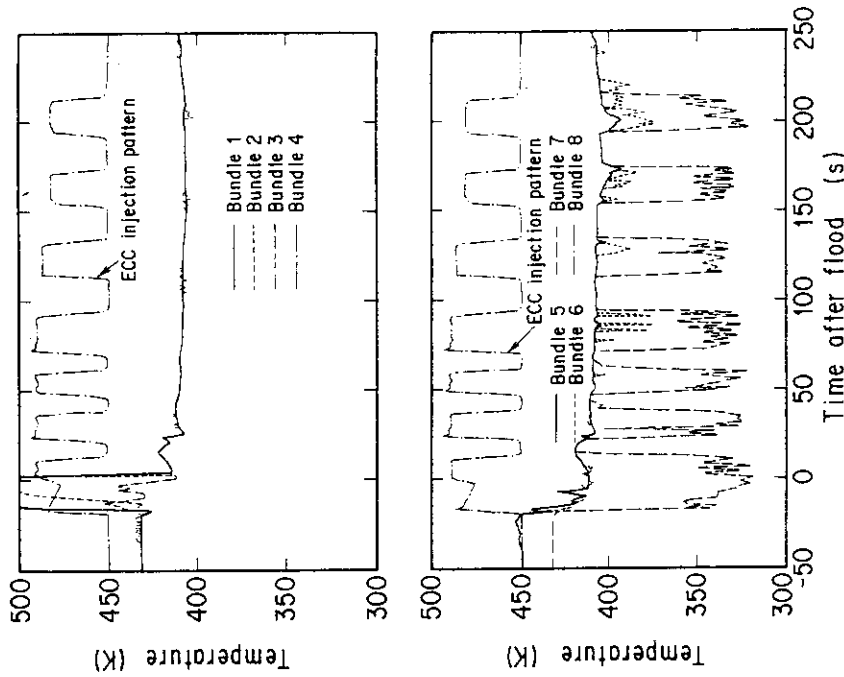


Fig. 9.4.2 Fluid temperatures just below tie plate holes

## 9.5 Analysis of SCTF/CCTF Counterpart Test Results

T. Okubo, M. Sobajima, T. Iwamura, A. Ohnuki, Y. Abe, H. Adachi<sup>\*</sup>  
and Y. Murao

Slab Core Test Facility (SCTF) and Cylindrical Core Test Facility (CCTF) are large scale experimental facilities of JAERI for the investigation of reflooding behavior during a postulated loss-of-coolant accident (LOCA) in PWRs. Although the flow area scaling ratios of both facilities to a 1,000 MWe class PWR are the same and 1/21.4, there are some differences in the design. Most important one is considered that the SCTF has the same core width as the radius of the reference PWR while the CCTF has a 1/4.5 times shorter core radius. Then, a few SCTF/CCTF counterpart tests were conducted<sup>1),2)</sup> in order to investigate the difference in core reflooding behavior between in the SCTF and CCTF tests as well as the effect of core radial length on core two-dimensional thermohydrodynamic behavior.

Figure 9.5.1 shows a comparison of core total differential pressure between SCTF Test S2-14<sup>1)</sup> and CCTF Test C2-6<sup>3)</sup> conducted under the similar conditions with flat radial power distribution. A significant difference in increasing rate of the data is observed between 100 and 300 s and this was the major difference between in the two tests. The reason for this difference was considered to be the difference in core flow area between the facilities. That is, the effective core flow area of the SCTF is 1.24 ~ 1.35 times larger due to its excess flow area between rod bundles and vessel wall. Figure 9.5.2 shows calculational results with REFLA-1DS code<sup>4)</sup> performed to see the effect of core flow area on the core total differential pressure under the conditions for Test S2-14. This shows that the larger core flow area results in the larger increasing rate in the core differential pressure. The average increasing rate between 100 and 300 s was about 22 Pa/s in Test S2-14, whereas about 20 Pa/s in the calculation for 1.4 times larger core flow area case. Therefore, the larger effective core flow area in the SCTF is judged to be the main reason for the different characteristic observed between the SCTF and CCTF tests.

In order to investigate the effect of core radial length on core

---

<sup>\*</sup> Yamagata University, Yonezawa

two-dimensional thermo-hydrodynamic behavior, results from SCTF Test S2-18<sup>2)</sup> and CCTF Test C2-5<sup>5)</sup> were also analyzed. These tests were conducted under the same slant radial power distribution of 1.36 : 1.20 : 0.76 (see Table 9.5.1). Core two-dimensional thermo-hydrodynamic behavior was remarkable in these tests, whereas it was not remarkable in the flat radial power distribution tests mentioned above. Figure 9.5.3 shows ratios of heat transfer coefficient for the slant radial power distribution tests to that for the flat radial power distribution tests. The figure shows that heat transfer enhancement or degradation in radial direction is more in the SCTF (i.e. in the longer radius core) even under the same radial power distribution as in the CCTF.

#### References

- 1) Iwamura T., et al.: "Two-dimensional Thermal-hydraulic Behavior in Core in SCTF Core-II Forced Feed Reflood Tests", JAERI-M 86-195 (1987).
- 2) Okubo T., et al.: "Analysis of SCTF/CCTF Counterpart Test Results", JAERI-M 90-083 (1990).
- 3) Akimoto H., et al.: "Evaluation Report on CCTF Core-II Reflood Test C2-6 (Run 64)", JAERI-M 85-027 (1985).
- 4) Murao Y., et al.: "REFLA-1D/MODE3: A Computer Code for Reflood Thermo-hydrodynamic Analysis during PWR-LOCA", JAERI-M 84-243 (1985).
- 5) Iguchi T., et al.: "Evaluation Report on CCTF Core-II Reflood Test C2-5 (Run 63)", To be published as a JAERI-M report.

Table 9.5.1 Core radial power distribution of Tests S2-18 and C2-5

Test S2-18		Test C2-5	
<u>Bundle No.</u>	<u>Power ratio</u>	<u>Bundle No.</u>	<u>Power ratio</u>
1	1.36	1 ~ 16	0.76
2 ~ 4	1.20	17 ~ 28	1.20
5 ~ 8	0.76	29 ~ 32	1.36

Note: Core average power corresponds to power ratio of 1.00

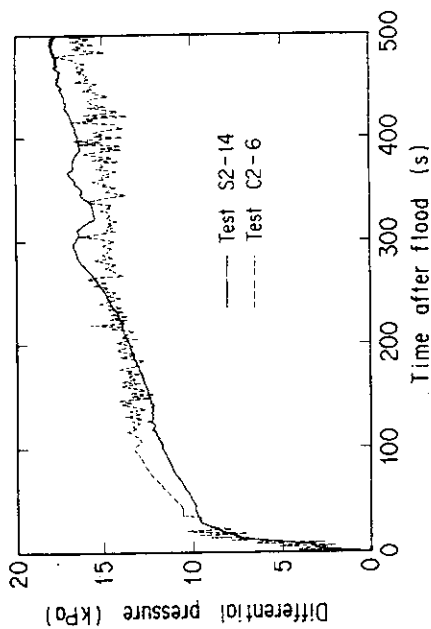


Fig. 9.5.1.1 Comparison of core total differential pressure between Tests S2-14 and C2-6

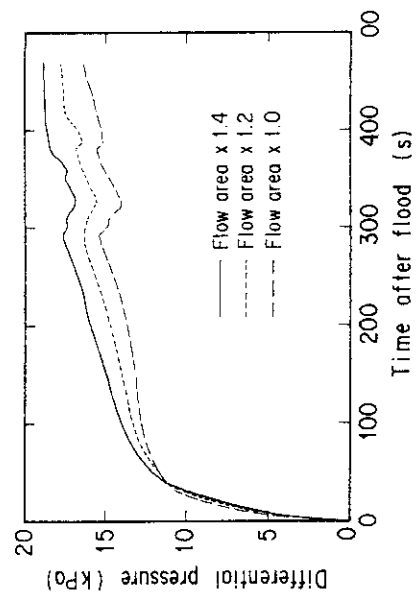


Fig. 9.5.2 Comparison of calculated core differential pressure for three core flow area under same core boundary conditions

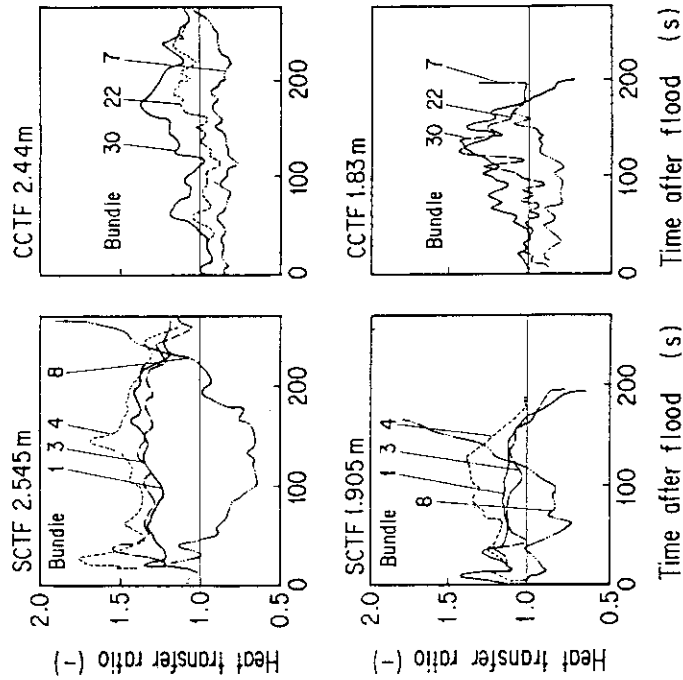


Fig. 9.5.3 Comparison of heat transfer ratios of slant core radial power distribution test to flat radial power distribution test between SCTF and CCTF

## 9.6 Development of a Driver Program for Assessment of Constitutive Equations for Two Fluid Model Code: MINI-TRAC

H. Akimoto, Y. Abe, A. Ohnuki and Y. Murao

Recent days, two-fluid model for two phase flow is used in many codes for safety analyses of light water reactors<sup>1)-3)</sup> to provide advanced prediction. It is necessary for two-fluid model calculation to be given particular coefficients such as friction factors and heat transfer coefficients to close basic equation system. Those coefficients are calculated with physical relationships called constitutive equations which model the two phase flow. The accuracy of the two fluid model code is strongly dependent on the accuracy of those constitutive equations.

It is very important to assess the accuracy of each constitutive equation for wide range of conditions. However, assessment studies for each constitutive equation are not performed sufficiently at present, because most of the two-fluid model code are very big and need large main frame computer to be run.

MINI-TRAC code, a driver program for assessment of constitutive equations of two fluid model, has been developed to perform assessment and improvement of constitutive equations of two fluid model widely and efficiently. The MINI-TRAC code uses one-dimensional conservation equations for mass, momentum and energy based on the two-fluid model. The code can work on a personal computer because it can be operated with core memory size less than 640 KB. The MINI-TRAC code includes constitutive equations of TRAC-PF1/MOD1 code, TRAC-BF1 code and RELAP5/MOD2 code. The code is modulated so that one can easily change constitutive equations to perform a test calculation.

Figures 9.6.1 and 9.6.2 show the comparisons of calculated system pressure and void fraction for the Edwards' pipe blowdown test<sup>4)</sup> between TRAC-PF1 and MINI-TRAC. MINI-TRAC results agree excellently with TRAC-PF1. Although the MINI-TRAC code is much simpler than the TRAC-PF1 code, MINI-TRAC code is expected to give the same results as the TRAC-PF1 code for the one-dimensional calculations.

The MINI-TRAC code mitigates the restriction for the assessment of the constitutive equations caused by the hardware limit. This fact implies that assessment and development of constitutive equations can be performed by more researchers and more efficiently. It is expected that



the reliability of the code based on the two-fluid model shall be increased as a result of assessmental and developmental studies with the MINI-TRAC code.

#### References

- 1) Liles D.R., et al.: TRAC-PF1/MOD1; An Advanced Best-Estimated Computer Program for Pressurized Water Reactor Thermal-Hydraulic Analysis, NUREG/CR-3858, LA-10157-MS (1986).
- 2) Weaber W.L., et al.: TRAC-BF1 Manual, Extension to TRAC-BD1/MOD1, NUREG/CR-4391, EGG-2417 (1986).
- 3) Ransom V.H., et al.: RELAP5/MOD2 Code Manual, NUREG/CE-4312, EGG-2396 (1985).
- 4) Edwards A.R. and O'Brien T.P.: Studies of Phenomena connected with the Depressurization of Water Reactors, J. Br. Nucl. Energy Soc., 9 (1970).

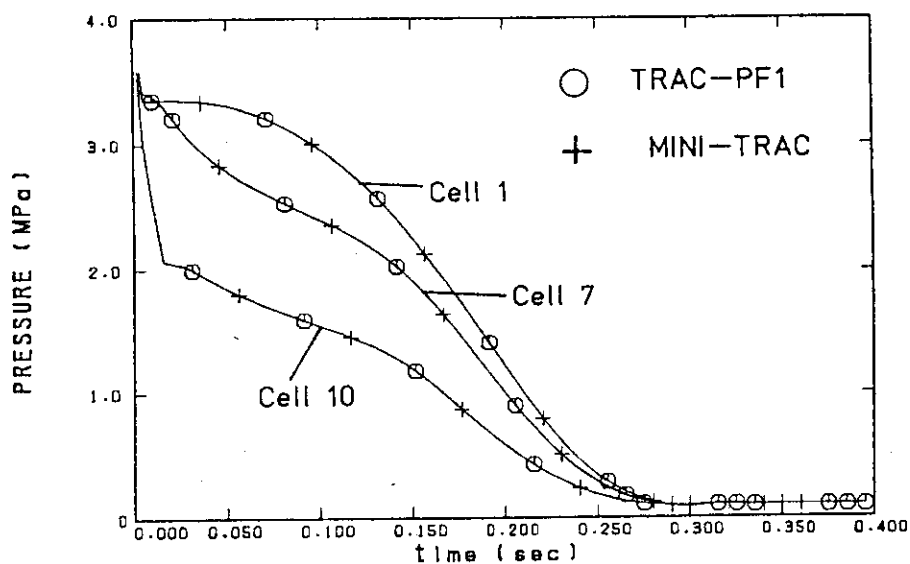


Fig. 9.6.1 Comparison of system pressure between calculated results by TRAC-PF1 and MINI-TRAC

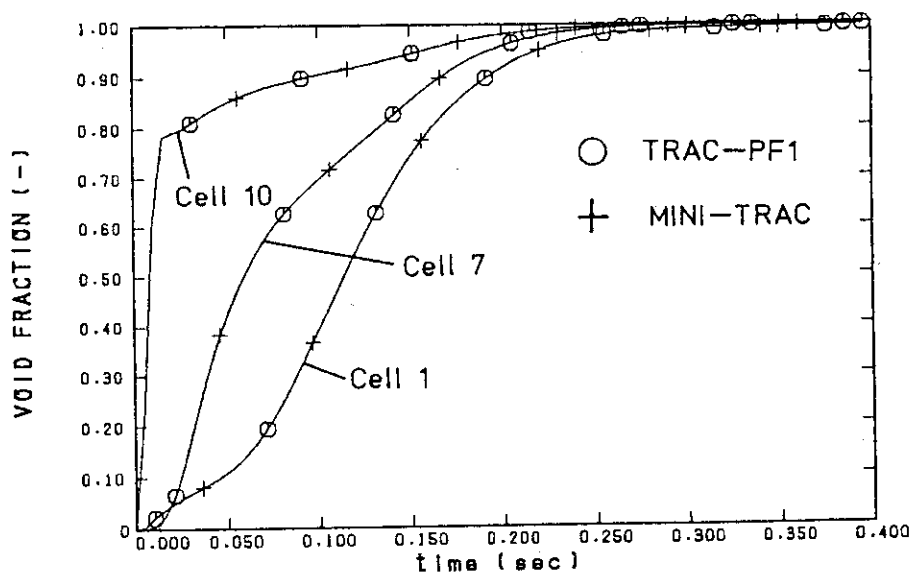


Fig. 9.6.2 Comparison of system pressure between calculated results by TRAC-PF1 and MINI-TRAC

## 9.7 A Study of Interfacial Friction Model for Upward Flow in Vertical Pipe at Low Mass Velocity

H. Akimoto, A. Ohnuki, Y. Abe and Y. Murao

To understand the basic predictive capability of the TRAC-PF1<sup>1)</sup> and TRAC-BF1<sup>2)</sup> interfacial friction models, an assessment study was performed for the upward flow in vertical pipes at low mass velocity. The assessment calculations were performed using void fraction data from tests<sup>3)-8)</sup> of which major conditions are summarized in Table 9.7.1. Test ranges of these tests are also shown in Fig. 9.7.1. The assessment calculations cover relatively wide range of pipe diameter, pressure and fluid velocities in bubbly/slug flow regime.

The void fractions were calculated using momentum balance relations at steady state with subroutines picked up from the TRAC-PF1 and TRAC-BF1 codes to save computational time. It was confirmed that the calculated results by the momentum relations agreed with the results by the original codes excellently. Through comparisons with measured data, it was found that both the TRAC-PF1 and TRAC-BF1 models can predict overall trend of void fraction. However, the TRAC-PF1 model tended to overestimate the void fraction in bubbly flow regime and underestimate the void fraction in slug flow regime quantitatively. The TRAC-BF1 model predicted the void fraction fairly good quantitatively except the region where liquid velocity is low.

Although the mechanistic model of the TRAC-PF1 code is attractive, it is considered that the TRAC-PF1 model for the bubbly/slug flow regime is not practical at present because the model requires detail information of flow that was not measured under wide range of conditions. On the other hand, wide range of data are available for the TRAC-BF1 model because the interfacial friction model of the TRAC-BF1 code was developed based on the drift flux correlation. Additionally, the TRAC-BF1 model can easily include the effect of the phase drift caused by ununiform distribution of gas and liquid phases in a flow section, which is important in the bubbly/slug flow regime. Therefore the TRAC-BF1 model was selected as the basis of the further improvement of the interfacial friction model in the bubbly/slug flow regime.

In the TRAC-BF1 model, the accuracy of the void fraction prediction is highly dependent on the drift flux correlation used to develop equiv-

alent interfacial friction correlation at steady state. To improve the accuracy of the void fraction prediction in bubbly/slug flow regime, an assessment was performed for the void fraction correlations through comparisons with test data. As a result of the assessment, the drift flux correlation by Kataoka and Ishii was selected as the basis of the new interfacial friction model in bubbly/slug flow regime.

The modified model was assessed for the tests shown in Table 9.7.1. Figure 9.7.2 shows an example of comparisons between calculated and measured results. The accuracy of the prediction of the void fraction in bubbly/slug flow regime at steady state is improved by the interfacial friction model based on the Kataoka-Ishii correlation. The accuracy of the prediction of void fractions was also improved for the other tests in Table 9.7.1.

#### References

- 1) Los Alamos National Laboratory: NUREG/CR-3858 LA-10157-MS, July 1986.
- 2) Weaver W.L., et al.: NUREG/CR-4391 EGG-2417, August 1986.
- 3) Sudo Y. and Murao Y.: JAERI-M 7490, February 1977.
- 4) Currier F., et al.: ANCP-63021, July 1963.
- 5) Smitsaert G.E.: ANL-6755, July 1963.
- 6) Hughes T.A.: B&W Report No. 5435, February 1958.
- 7) Petrick M.: ANL-6581, July 1962.
- 8) Agostini A., et al.: CISE-R-291, December 1969.

Table 9.7.1 Major conditions of tests used in assessment calculations

Test name	Fluid	Diameter (m)	Pressure (MPa)	$j_l$ (m/s)	$j_g$ (m/s)
Sudo	A/W	0.022-0.096	0.1	0	0-1.5
Currier	S/W	0.46	4.1-13.8	0	0-1.2
Smitsaert	A/W	0.07	0.1	0-0.305	0-11.0
Hughes	S/W	0.168	8.2-16.5	0-0.45	0-0.51
Petrick	A/W	0.083-0.139	0.1	0.45-0.84	0.15-2.1
Petrick	S/W	0.076	4.1-10.3	0.6 -1.2	0.3-2.3
CISE	S/W	0.00916	2.9- 4.9	0.1 -4.4	0-58

Note) A/W :Air-Water, S/W :Steam-Water  
 $j_l$ :Superficial liquid velocity,  $j_g$ :Superficial gas velocity

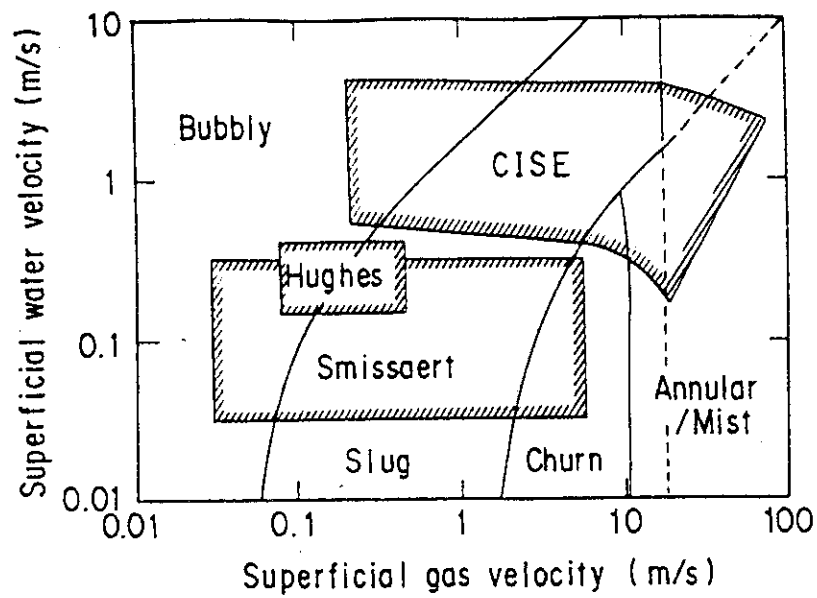


Fig. 9.7.1 Test range of superficial gas and water velocities used in assessment calculations

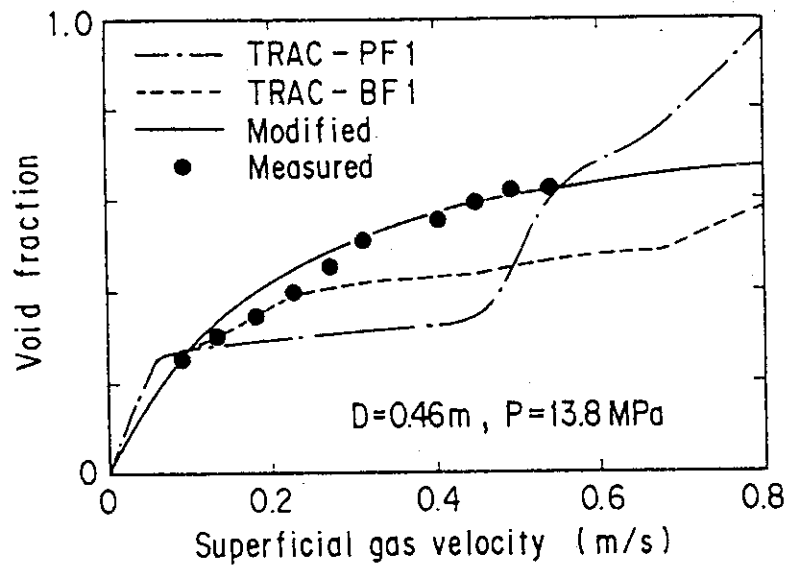


Fig. 9.7.2 Assessment results for Currier's test

## 9.8 Assessment of Model in Two-Fluid Model Code for Slug Flow and Annular Flow in Horizontal Tube with MINI-TRAC Code

A. Ohnuki, H. Akimoto, Y. Abe and Y. Murao

In recent years, postulated accidents in a LWR are being analyzed by several best-estimate codes (TRAC-PF1, RELAP5 etc.) to provide advanced predictive analyses for licensing issues<sup>1)</sup>. These codes model thermal-hydraulic behaviors based on a two-fluid model with flow-regime-dependent constitutive equation treatment. Because the accuracy of the prediction is strongly dependent on the constitutive equations such as wall and interfacial friction models, it is important to assess the validity of the constitutive equation with experimental results. In this study, the validity of horizontal flow models in TRAC-PF1/MOD1<sup>2)</sup> and RELAP5/MOD2<sup>3)</sup> codes is assessed for slug and annular flow regimes because the validity of the model for those regimes has not been studied as far as the authors understand.

MINI-TRAC code<sup>4)</sup> with the constitutive equations in each code was used in the assessment. Figure 9.8.1 shows the calculational noding and conditions for two experiments<sup>5),6)</sup> referred to in this study. The experiment by Ruder et al. was conducted only under the slug flow.  $U_l$  and  $U_g$  in this figure are superficial liquid velocity and gas velocity, respectively. The assessment was performed by the comparison between the flow pattern and void fraction in the calculation and those in the experiment.

Figure 9.8.2 shows the comparison between the calculated flow pattern and the flow pattern map by Mandhane or Baker. Since the flow pattern in the experiments is reported to almost correspond to the map by Mandhane or Baker, the calculated flow pattern can be considered to agree well with the experimental results.

Figure 9.8.3 shows the comparison of void fraction  $\alpha$ . The models in both codes predict well the data under the slug flow in the small scale flow path by Chisholm et al.. However, the models in both codes underestimate the void fraction under the slug flow in the relatively large scale flow path by Ruder et al. and overestimate that under the annular flow in the small scale flow path.

The following remarks can be summarized from this assessment:

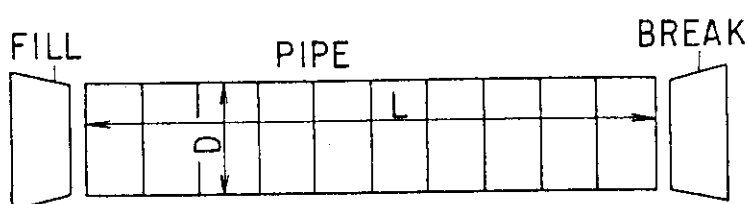
- (1) Both horizontal flow models in TRAC-PF1/MOD1 and RELAP5/MOD2 codes

predicted well the flow pattern under slug and annular flows.

- (2) Although the calculated void fraction by both models agreed well with the data under slug flow in the small scale flow path, the effect of flow path scale on the void fraction was not predicted.
- (3) Both models overestimated the void fraction under annular flow.

#### References

- 1) Ross D.F., et al.: Compendium of ECCS Research for Realistic LOCA Analysis, NUREG-1230 (1988).
- 2) Liles D.R., et al.: TRAC-PF1/MOD1: An Advanced Best-Estimate Computer Program for Pressurized Water Reactor Thermal-Hydraulic Analysis, NUREG/CR-3858, LA-10157-MS (1986).
- 3) Ransom V.H., et al.: RELAP5/MOD2 Code Manual, NUREG/CR-4312, EGG-2396 (1985).
- 4) Akimoto H., et al.: MINI-TRAC Code: A Driver Program for Assessment of Constitutive Equations of Two-Fluid Model, JAERI-M91-086 (1991) (in Japanese).
- 5) Chisholm D. and Laird A.D.K.: Two-Phase Flow in Rough Tubes, Trans. ASME, 80-2 (1958).
- 6) Ruder Z., et al.: Necessary Conditions for the Existence of Stable Slugs, Int. J. Multiphase Flow, 15[2] (1989).



	Chisholm et al.	Ruder et al.
L (m)	6.9	24.6
D (m)	0.0254	0.0953
Number of cell	10	20
$U_l$ (m/s)	0.4 - 2.0	0.5 - 0.95
$U_g$ (m/s)	0.2 - 60.0	1.0 - 5.0

Fig. 9.8.1 Calculational noding and conditions

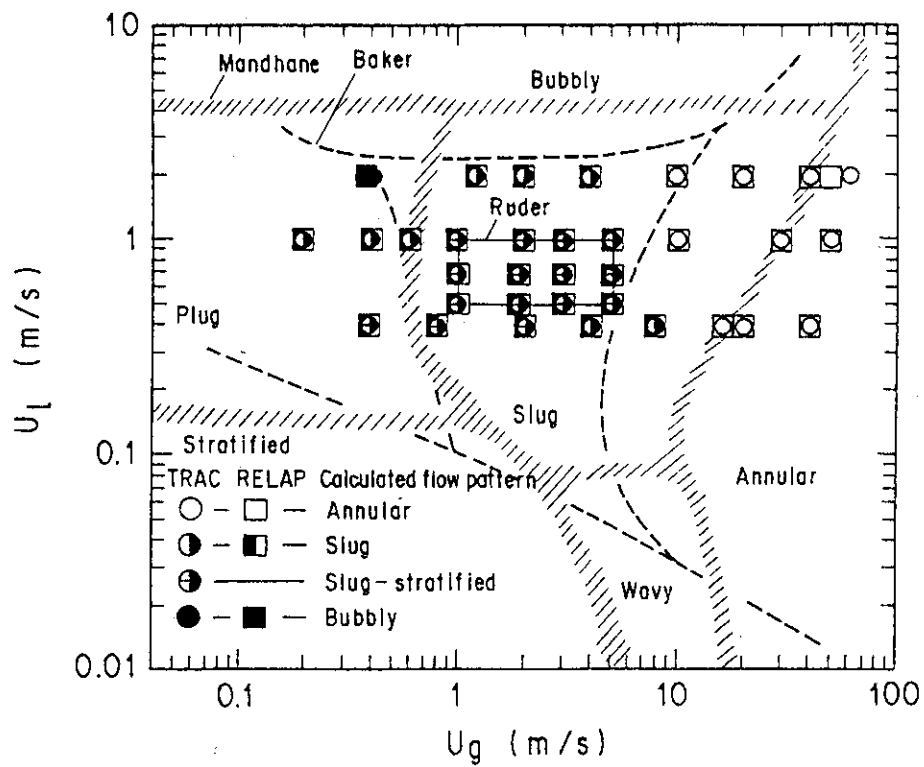


Fig. 9.8.2 Comparison of flow pattern

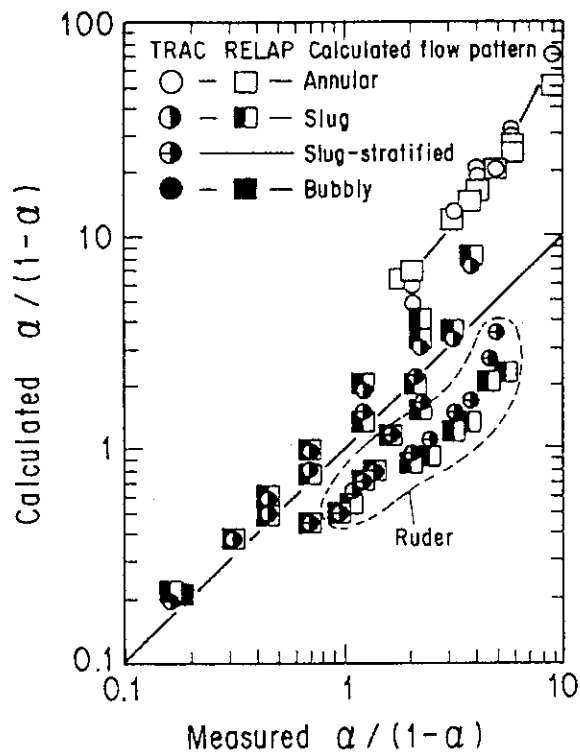


Fig. 9.8.3 Comparison of void fraction



## 9.9 Improvement of Numerical Treatment of Convection Term in TRAC-PF1 Code at Transition from Single Phase Flow to Two Phase Flow

Y. Abe, H. Akimoto, A. Ohnuki and Y. Murao

TRAC-PF1 code is one of the most typical two-fluid model codes which are used for safety analysis of light water reactors<sup>1)</sup>. TRAC-PF1 has two distinctive features as two-fluid model code. One is to adopt non-conservative form of momentum equations. The other is to continue to solve the same set of basic equations for both phase even in single phase flow as in two phase flow. These features make numerical solution procedure simple and make it easy to get stable numerical solution. However, these features sometimes cause particular deficiencies.

Figure 9.9.1 shows the system pressure calculated with TRAC-PF1 and the core outlet pressure measured in the reflood experiment. During reflood phase of PWR LOCA, liquid phase and gas phase are separated and a solid liquid level is established. In TRAC-PF1 calculation, pressure oscillation is calculated after coolant water injection starts as shown in Fig. 9.9.1. But this pressure oscillation is not observed in the experiment<sup>2)</sup>. The pressure oscillation is judged to be caused not by physical reason but by some numerical reason. Since the pressure oscillation decreases predictability of the code, it is important to mitigate the pressure oscillation caused by such a numerical problem.

Figure 9.9.2 shows schematic diagram of numerical situation calculated by TRAC-PF1. Two major problems are pointed out. That is, (1) negative liquid velocity is numerically calculated in physically gas single phase flow above the liquid level and (2) pressure starts to increase when water level passes through cell edges and the negative liquid velocity changes positive. These results suggest the pressure oscillation is caused by change of the liquid velocity in gas single phase flow. The most effective term for pressure fluctuation by velocity change is convection term in the momentum equation. It is supposed that the reason why change of liquid velocity in gas single phase flow affects pressure is the problem in the treatment of the convection term in the momentum equation of TRAC-PF1 code.

This is very common problem in two-fluid model codes which adopt momentum equations of non-conservative form and which continue to solve the same set of basic equations for both phase even in single phase flow

as in two phase flow. It is clarified that any special treatment is needed when flow changes from single phase flow to two phase flow.

A correction factor is introduced into the equations of motion in TRAC-PF1. The correction factor makes the convection term in a phase very small when the phase does not physically exist. Assessment result with modified TRAC-PF1 is shown in Fig. 9.9.3. As seen in Fig. 9.9.3, the unreasonable pressure oscillation shown in Fig. 9.9.1 disappears and moderate pressure transient corresponding to the experiment is calculated. This result confirms the effectiveness of this numerical modification applied to the convection term.

#### References

- 1) Los Alamos National Laboratory: TRAC-PF1/MOD1; An Advanced Best Estimate Computer Program for Pressurized Water Reactor Thermal-Hydraulic Analysis, NUREG/CR-3858, LA-10157-MS, July 1986.
- 2) Murao Y., et al.: Multi-Dimensional Thermal-Hydraulics in Pressure Vessel during Reflood Phase of a PWR-LOCA, NURETH-4, October 1989, pp.54-59.

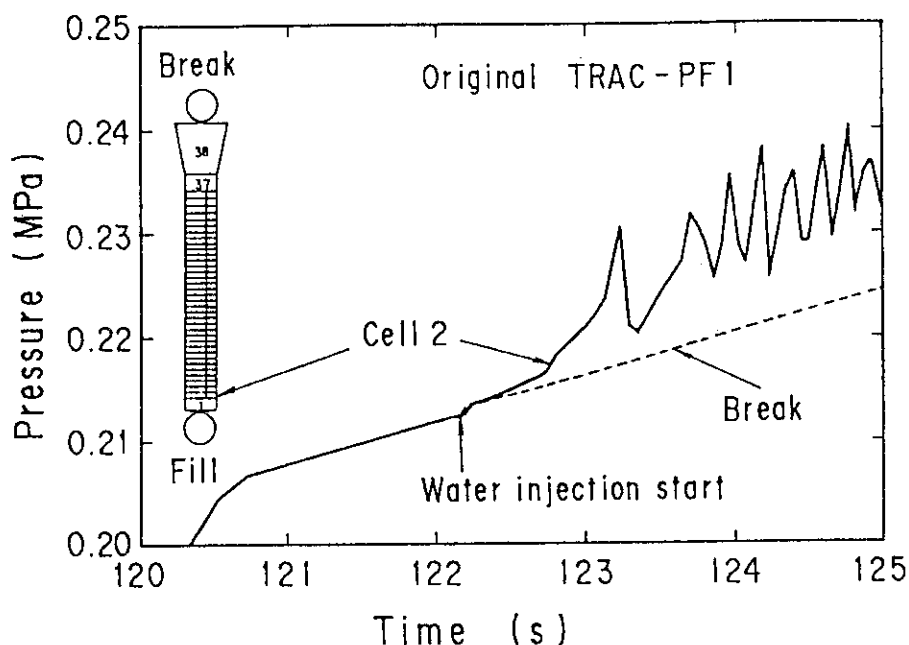


Fig. 9.9.1 Calculated results of system pressure with original TRAC-PF1

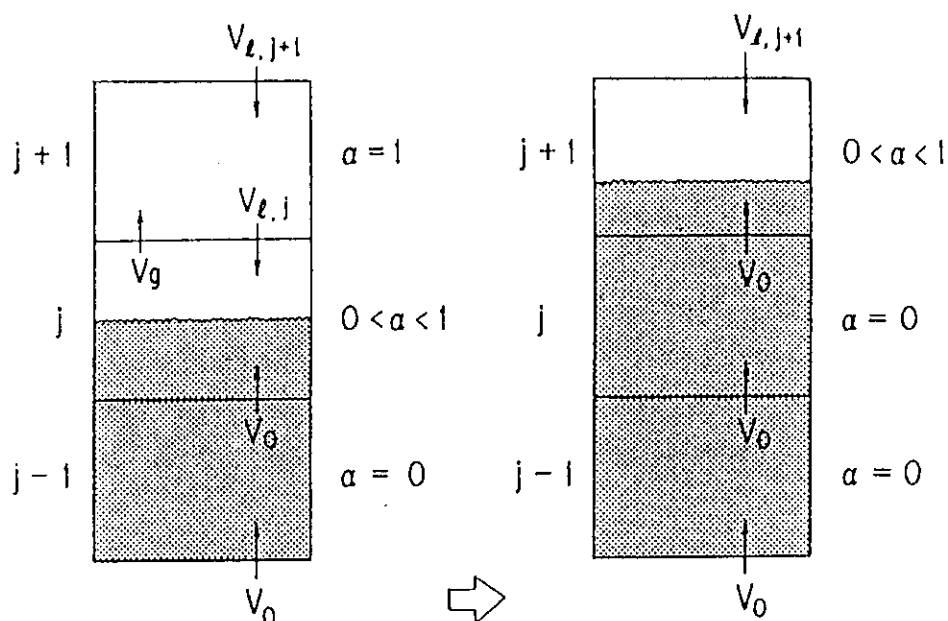


Fig. 9.9.2 Schematic diagram of numerical situation when water level pass through numerical cell edge

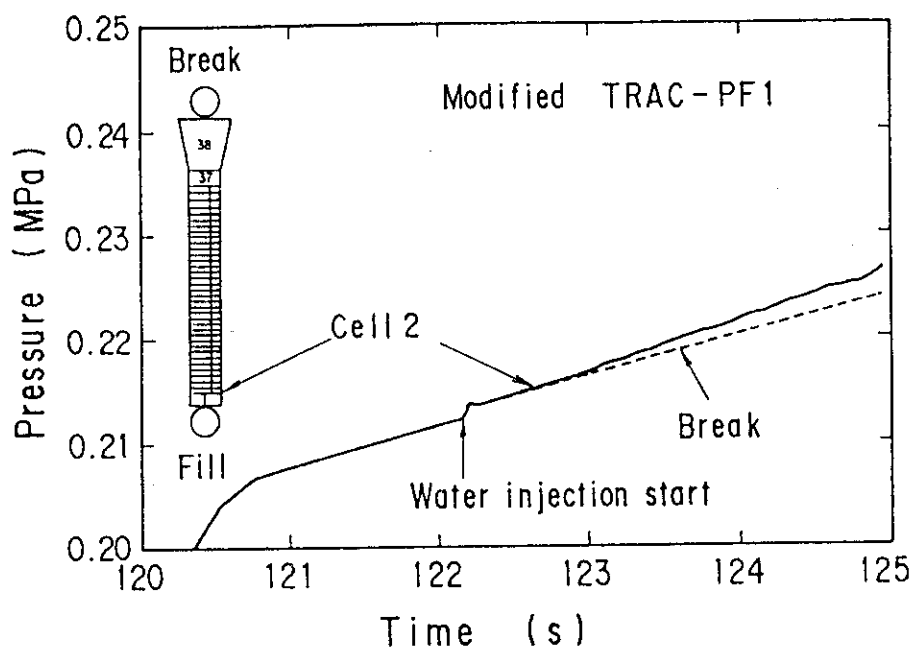


Fig. 9.9.3 Calculated result of system pressure with modified TRAC-PF1

## 9.10 Effect of Rod Pitch on Critical Heat Flux

T. Iwamura, H. Watanabe, T. Okubo, F. Araya and Y. Murao

Prediction of critical heat flux (CHF) is one of the most important safety concerns in a high conversion light water reactor (HCLWR) because the smaller gap width between fuel rods may reduce the CHF. CHF experiments have been performed with transient boiling test facility for various test sections<sup>1)</sup>. The test results were used to develop an evaluation method of DNBR (Departure from Nucleate Boiling Ratio) for a double-flat-core type HCLWR which was proposed by JAERI<sup>2)</sup>. As a part of the experimental program, effects of pitch-to-diameter ratio (P/D) on CHF characteristics were investigated in 1990.

In the experiments, three test sections (C, E and F) were used. The test section consists of 7 simulated fuel rods arranged in a triangular lattice. The simulated fuel rod was a stainless steel tube and uniformly heated electrically with direct current. The heated rod bundles were placed in a ceramic flow shroud for electrical insulation. The heat flux of the center rod was about 20% higher than the average heat flux so as to force the first CHF detection at the center rod which was surrounded by other heater rods. The rod bundles were supported by grid type spacers. The rod diameter and heated length were 9.5 and 500 mm, respectively. The rod pitches for test sections C, E and F were 10.7 mm (P/D: 1.126), 13.5 mm (P/D: 1.421) and 12.6 mm (P/D: 1.326), respectively. The rod pitches of 12.6 mm (Test section F) and 13.5 mm (Test section E) were determined to give the same gap width (3.1 mm) and the same hydraulic equivalent diameter (11.7 mm) as the current  $17 \times 17$  PWR fuel assembly, respectively. The experimental conditions are listed in Table 9.10.1.

The measured CHF's are plotted against the inlet mass velocities in Fig. 9.10.1. It should be noted that for test sections E and F, CHF data could not be obtained at mass velocities higher than  $1300 \text{ kg/m}^2\text{s}$  due to a limit of heating power capacity. As shown in Fig. 9.10.1, the CHF decreases with decreasing the P/D under the same mass velocity and inlet temperature conditions. Since the smaller P/D implies the smaller hydraulic equivalent diameter, the above-mentioned trend is consistent with the well known fact that the CHF decreases with decreasing the hydraulic equivalent diameter under the same mass velocity and inlet enthalpy conditions as pointed out by Tong<sup>3)</sup>.

Using bundle average flow conditions, CHF was calculated with KfK correlation<sup>4)</sup> which was developed for HCLWR fuel configuration and found to be well agreed with previous CHF data obtained at JAERI<sup>1)</sup>. The ratios of calculated CHF to measured CHF (CHFR) are plotted against the inlet mass velocities in Fig. 9.10.2. For all of the three test sections, the KfK correlation significantly over-predicts the CHF at lower mass velocities while slightly under-predicts at higher mass velocities. The result indicates that the KfK correlation cannot be applied to the mass velocities lower than  $1000 \text{ kg/m}^2\text{s}$ . It is also suggested from Fig. 9.10.2 that the CHFR increases with decreasing the P/D. However, the effect of P/D on the predictive capability of the KfK correlation tends to diminish as increasing the mass velocity.

Due to the lack of CHF data at high mass velocities for test sections E and F, the effect of P/D on predictive capability of KfK correlation at the HCLWR mass velocity condition (higher than  $2000 \text{ kg/m}^2\text{s}$ ) has not been clarified. Also the maximum pressure of 4 MPa is not adequate to simulate the HCLWR operating condition of 16 MPa. Therefore, further CHF experiments are planned under more realistic conditions using a high pressure loop.

#### References

- 1) Iwamura T., et al.: "Evaluation of DNBR under Operational and Accident Conditions for Double-Flat-Core Type HCLWR", J. Nucl. Sci. Technol., 28(1), 45 (1991).
- 2) Iwamura T., et al.: "Thermal Hydraulic Feasibility Study of a Double-Flat-Core Type High Conversion Light Water Reactor", ASME Winter Meeting, Dallas, Nov. 25-30 (1990).
- 3) Tong L.S.: "Boiling Heat Transfer and Two-phase Flow", Robert E. Krieger Publishing Company, 181 (1975).
- 4) Dalle Donne M., et al.: "Critical Heat Flux Correlation for Triangular Arrays of Rod Bundles with Tight Lattices, Including the Spiral Spacer Effect", Nucl. Technol. 71, 111 (1985).

Table 9.10.1 Test conditions

Test section	C	E	F
Pressure (MPa)	1.08 - 3.93	3.88	1.08 - 3.88
Inlet subcooling (kJ/kg)	53 - 477	41 - 215	69 - 337
Mass velocity (kg/m <sup>2</sup> s)	462 - 3090	200 - 952	326 - 1510
Exit quality	0.082 - 0.260	0.174 - 0.533	0.092 - 0.308
CHF (MW/m <sup>2</sup> )	0.742 - 2.90	1.66 - 3.69	1.79 - 3.68

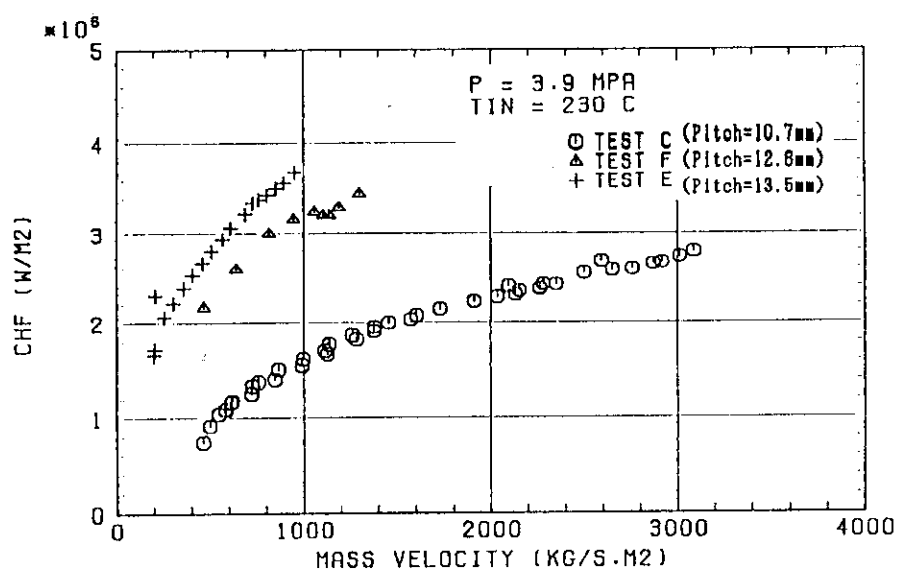


Fig. 9.10.1 Effect of rod pitch on CHF vs. mass velocity

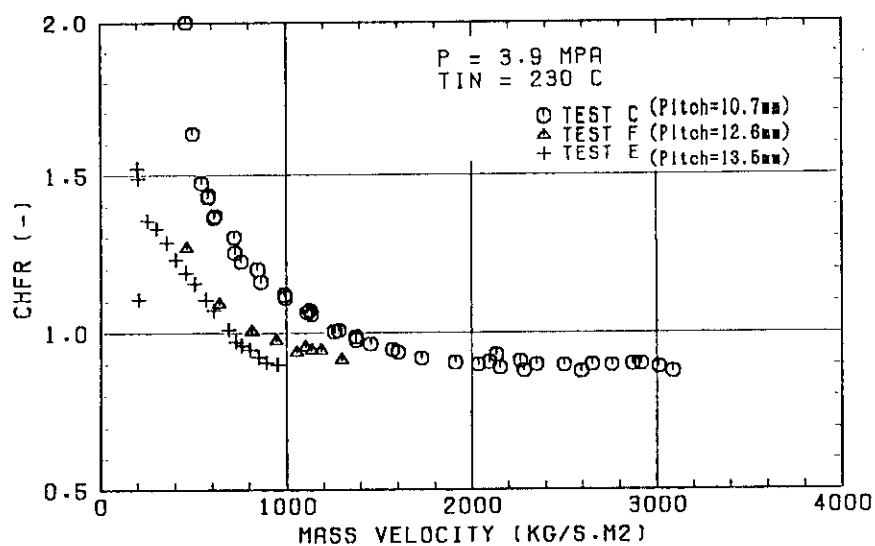


Fig. 9.10.2 Effect of rod pitch on calculated-to-measured CHF ratio (KFK CHF correlation)

## 9.11 Effect of Axial Power Distribution on Critical Heat Flux of HCPWR

T. Iwamura, H. Watanabe, T. Okubo, F. Araya and Y. Murao

Effect of axial power distribution on critical heat flux (CHF) under HCPWR condition has been investigated with a high pressure water loop. Figure 9.11.1 shows the schematic diagram of the test facility. The loop consists of test section, pressure control tank with heater and spray system, air-cooler, circulation pump, flow meters and pre-heater tank. The test section consists of 7 simulated fuel rods arranged in a triangular lattice with pitch to diameter ratio of 1.23. The simulated fuel rod is an electric heater which consists of a boron nitride (BN) core, a Ni-Cr heating element, a BN insulator and a NCF600 cladding. Several C-A thermocouples are embedded inside the cladding to detect the onset of CHF. The diameter and heated length of heater rod are 9.5 mm and 600 mm, respectively. The heating power of the center rod is about 17% higher than the peripheral rods to ensure the first CHF detection at the center rod. The rod bundle is supported by grid type spacers. Figure 9.11.2 shows the axial power profile which simulates the calculated axial power distribution of the upper half core of a double-flat-core type HCPWR<sup>1)</sup>. The experimental conditions are: pressures 8.1 - 15.8 MPa, mass velocities 470 - 2290 kg/m<sup>2</sup>s, and average exit qualities 0.0 - 0.44.

COBRA-IV-I subchannel analysis code<sup>2)</sup> was used to calculate local flow parameters such as mass velocity and enthalpy in a hot channel where the first DNB (Departure from Nucleate Boiling) was detected. Using the calculated local flow parameters, CHF's were calculated with several CHF correlations. Table 9.11.1 shows the average and standard deviation of the calculated to measured CHF ratios. The axial heat flux parameter (Y-factor) proposed by Bowring<sup>3)</sup> was used in the CHF correlations except EPRI-B&W correlation<sup>4)</sup> to take into account of the effect of axial power distribution on the CHF. As noted from Table 9.11.11, the KfK correlation<sup>5)</sup> gives the best agreement with the data followed by the WSC-2 correlation<sup>3)</sup>. Therefore, the validity of the CHF evaluation method used in the thermal-hydraulic feasibility study of the double-flat-core HCPWR<sup>6)</sup> has been confirmed.

The present CHF correlations are based on an empirical fitting rather than fundamental observations of the DNB phenomenon. In order to obtain a more general predictive method, several mechanistic CHF models

have been proposed. The experimental data are compared with existing CHF mechanistic models in Table 9.11.2. The first two models are based on a near-wall bubble crowding mechanism in which turbulent interchange between the bubbly layer and core region is assumed to be the limiting mechanism for the onset of CHF. The other three models are based on the dryout mechanism of a thin liquid layer (sublayer) beneath an intermittent vapor blanket due to a Helmholtz instability at the sublayer-vapor interface. As shown in Table 9.11.2, the Weisman-Pei model<sup>7)</sup> gives relatively good agreement with the experiments. However, it should be noted that there exists large differences in the magnitudes of physical quantities such as void fraction, quality, bubble diameter or sublayer thickness obtained in the course of calculations. Therefore, more detailed observation is necessary to clarify the CHF mechanism and establish a reliable mechanistic model.

#### References

- 1) Iwamura T., et al.: "Evaluation of DNBR under Operational and Accident Conditions for Double-Flat-Core Type HCLWR", J. Nucl. Sci. Technol., 28(1), 45 (1991).
- 2) Wheeler C.L., et al.: "COBRA-IV-I: An Interim Version of COBRA for Thermal-Hydraulic Analysis of Rod Bundle Nuclear Fuel Elements and Cores", BNWL-1962 (1976).
- 3) Bowring R.W.: "WSC-2: A Subchannel Dryout Correlation for Water-Cooled Clusters over the Pressure Range 3.4-15.9 MPa (500-2300 psia)", AEEW-R983 (1979).
- 4) Uotinen V.O., et al.: "Technical Feasibility of a Pressurized Water Reactor Design with a Low-Water-Volume-Fraction Lattice", EPRI-NP-1833 (1981).
- 5) Dalle Donne M., et al.: "Critical Heat Flux Correlation for Triangular Arrays of Rod Bundles with Tight Lattices, Including the Spiral Spacer Effect", Nuclear Technology, 71, 111 (1985).
- 6) Heat Transfer and Fluid Flow Laboratory: "Thermal-Hydraulic Study of a High Conversion Light Water Reactor", JAERI-M 91-055 (1991) (in Japanese).
- 7) Weisman J. and Pei B.S.: "Prediction of Critical Heat Flux in Flow Boiling at Low Quality", Int. J. Heat Mass Transver Vol. 26, No. 10, 1463 (1983).



Table 9.11.1 Comparison with CHF correlations

CHF correlation	(CHF)cal./ (CHF)meas.	
	Average	Standard deviation
WSC-2	1.101	0.054
KfK	0.957	0.049
EPRI-B&W	0.626	0.030
EPRI-Columbia	0.641	0.064

Table 9.11.2 Comparison with CHF models

CHF model	(CHF)cal./ (CHF)meas.	
	Average	Standard deviation
Weisman-Pei	1.056	0.084
Chang-Lee	1.254	0.209
Lee-Mudawwar	1.381	0.138
Lin-Lee-Pei	1.166	0.162
Katto	1.328	0.184

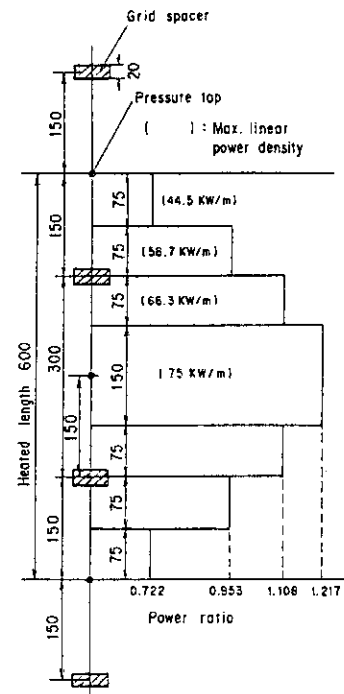


Fig. 9.11.2 Axial power distribution

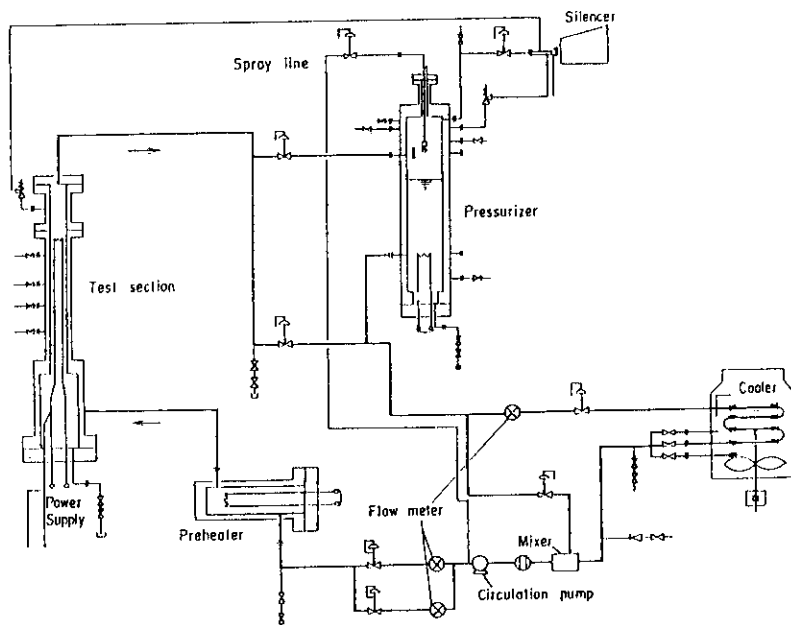


Fig. 9.11.1 High pressure water loop

## 9.12 Safety Evaluation of Reactivity Initiated Accidents for Double-Flat-Core Type HCLWR

F. Araya, T. Iwamura, T. Okubo, H. Akimoto and Y. Murao

A conceptual design of a double-flat-core type high conversion light water reactor (HCLWR) has been developed at JAERI to improve fuel utilization. In order to confirm thermal-hydraulic feasibility of the present design, a series of safety analyses<sup>1)</sup> were performed on five major events such as large and small break LOCAs, with the best estimate code REFLA/TRAC<sup>2)</sup>. Based on the results derived from the calculations, it was confirmed that the present design was feasible against the events analysed.

As a part of the safety analyses, control rod cluster ejection accidents have been analyzed with REFLA/TRAC as the most severe reactivity initiated accident. The calculations were performed according to the licensing analysis on current PWRs. The input data used in the present calculations were produced based on the data used in the previous calculations<sup>1)</sup> and the neutronic design calculations. From the viewpoint of the reactivity change during a plant operation, calculations were performed on the following four conditions; zero power (ZERO) and full power (FULL) levels at the beginning of cycle (BOC) and the end of cycle (EOC), respectively. The point reactor kinetics model was used to evaluate power transients in all calculations. The inserted reactivities were set to be 0.233 and 0.247%  $\Delta K/K$  for the BOC and EOC conditions, respectively at both power levels, based on the neutronic design calculations. The reactivity insertion duration was assumed to be 0.1 seconds in all cases.

The calculated power transients of all cases are plotted on Fig.

9.12.1. The core power increases from the initiation of accident according to insertion of reactivity and decreases after reaching the peak value due to negative fuel temperature reactivity feedback. The highest core power is experienced in the (ZERO, EOC) case. The decrease in core power at around 1.4 seconds in each case is caused by reactor scram.

Figure 9.12.2 shows average pellet temperatures in all cases. It is shown that the highest average pellet temperature 1495 K is calculated in the (FULL, EOC) case. The corresponding fuel enthalpy is evaluated to be 97 cal/g·UO<sub>2</sub>. That is, the fuel enthalpies in all cases are significantly lower than the safety limitation on fuel enthalpy under a reactivity initiated accident condition (230 cal/g·UO<sub>2</sub>).

Figure 9.12.3 shows lower plenum pressure behaviours in all cases. The highest peak pressure 16.65 MPa is calculated in the (ZERO, EOC) case and is lower than the limitation on pressure boundary (20.6 MPa). This shows that the integrity of pressure boundary is not violated.

As described above, the calculated results show that the present design is considered to be feasible from a viewpoint of safety analysis of control rod cluster ejection accident. It can be said that the large safety margin of the present design is originated from characteristics of the HCLWR, which has smaller excess reactivity, more number of control rod cluster, smaller maximum linear heat generation rate and larger liquid mass in pressure vessel than current PWRs.

#### References

- 1) Heat Transfer and Fluid Flow Lab.: Thermal-Hydraulic Study of a High Conversion Light Water Reactor, JAERI-M 91-055 (1991).
- 2) Akimoto H., et al.: Assessment of J-TRAC Code with CCTF/SCTF Test Data, Presented at Sixteenth Water Reactor Safety Information Meeting, Gaithersburg, MD (1986).

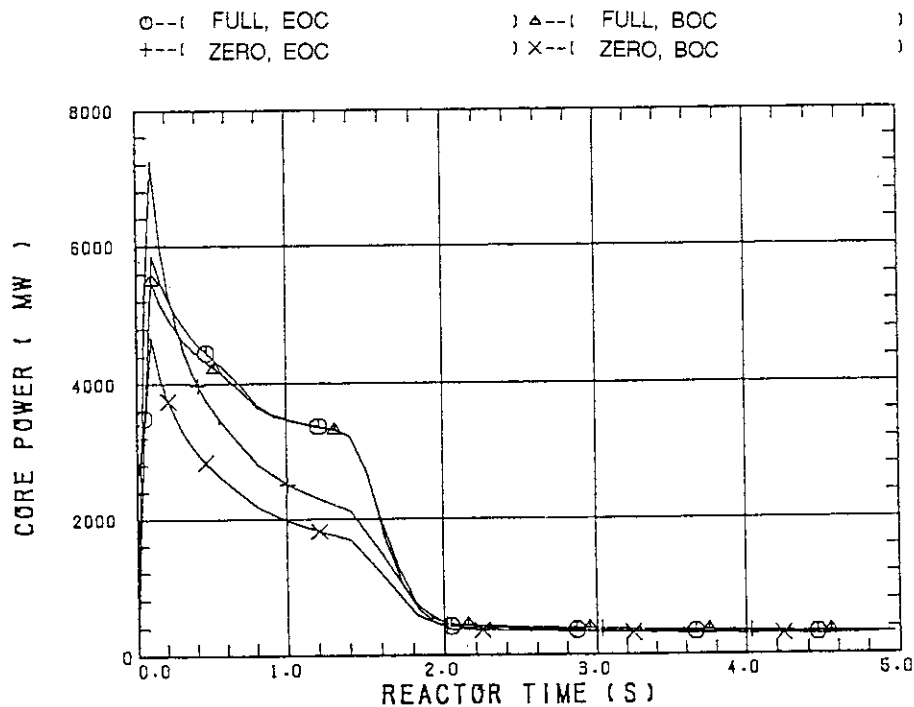


Fig. 9.12.1 Calculated reactor power transients

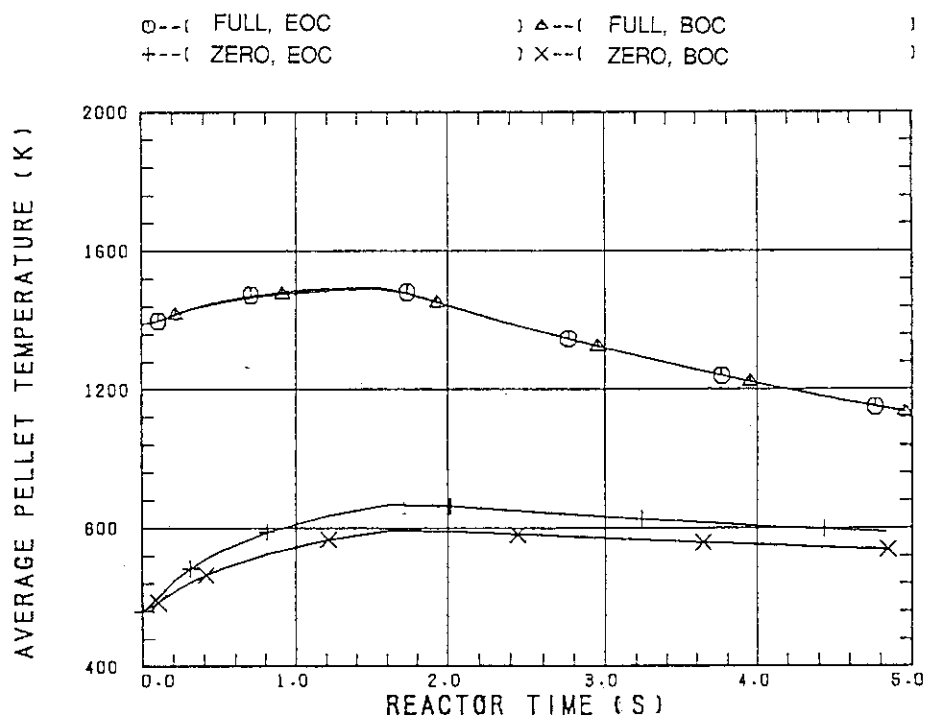


Fig. 9.12.2 Calculated average pellet temperature transients

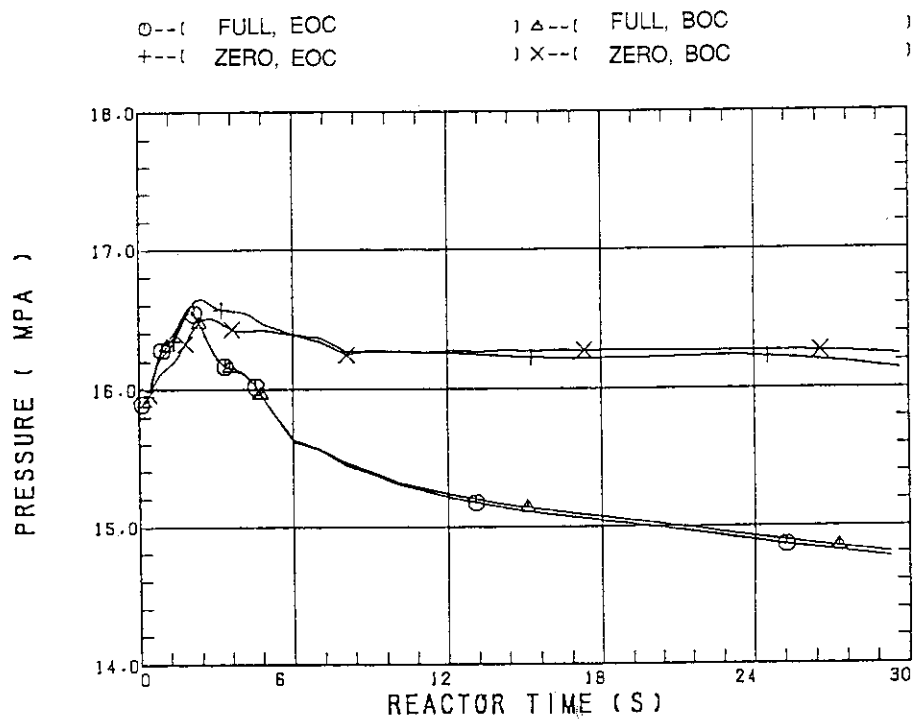


Fig. 9.12.3 Calculated upper plenum pressure transients

### 9.13 Discussion on Differences between Calculated Results with 1-D and 3-D Models on 0.5% Small Break LOCA at Vessel Bottom of Double-Flat-Core Type HCLWR

F. Araya, T. Iwamura, T. Okubo, H. Akimoto and Y. Murao

Analyses with 1-dimensional (1-D) and 3-dimensional (3-D) models<sup>1)</sup> of the REFLA/TRAC code<sup>2)</sup> have already been performed on 0.5% small break loss of coolant accident (LOCA) at vessel bottom of a double-flat-core type high conversion light water reactor (HCLWR) conceptually designed by JAERI. Large difference between results of the 1-D and 3-D analyses was already found<sup>3)</sup>. In the present study, in order to clear the causes of the differences, an additional 1-D calculation was performed with revised input data in which noding schemes was changed at the lower plenum, downcomer and upper plenum, considering actual plant configuration. Then the causes of the differences were surveyed by comparing the calculated results each other.

Figure 9.13.1 shows calculated peak cladding temperature in revised 1-D calculation together with old 1-D and 3-D cases. As shown in the figure, core uncover times in both 1-D cases are almost the same. This means that overall thermal-hydraulic behaviour in the revised 1-D case is basically the same as the old 1-D case. Therefore, the differences between old 1-D and 3-D cases have not been resolved even in the revised 1-D case. Namely, the beginning times of core uncover in both 1-D cases were more than 1500 seconds earlier than that in the 3-D case. Based on detailed survey of the calculated results of all cases, it was found that the differences were caused by local flow conditions calculated in 3-D case as described below. As shown in Fig. 9.13.2, in 3-D case, circulation flows were calculated inside the core and the downcomer in addition to flow paths between the core and the bypass. Therefore, since the circulation flows mixed the cold ECCS water with hot water in the core, relatively hot water reached the break locations at vessel bottom. On the other hand, in both 1-D cases, the flow path between the core and the bypass and circulation flows could not be modelled inside the core and the downcomer. Therefore, the cold ECCS water reached the break location. Based on the above description, it was found that the differences of circulation flow conditions caused the different break flow rates between 1-D and 3-D cases. As a result of this, the differences of clad-

ding temperature behaviour were caused.

In the calculation described above, local flow conditions, which could not be calculated by the 1-D model, caused large differences in results between 1-D and 3-D analyses. Based on the present study, it is suggested that validity of the calculated results with 1-D model be confirmed by 3-D analysis, especially in analyses of transients which are well known.

#### References

- 1) Hiraga F., et al.: "Small Break LOCA Analysis of Double-Flat-Core HCLWR", JAERI-M 90-085 (1990).
- 2) Akimoto H., et al.: "Assessment of J-TRAC Code with CCTF/SCTF Test Data", Presented at Sixteenth Water Reactor Safety Information Meeting, Gaithersburg, MD (1986).
- 3) Hiraga F.: Private Communication.

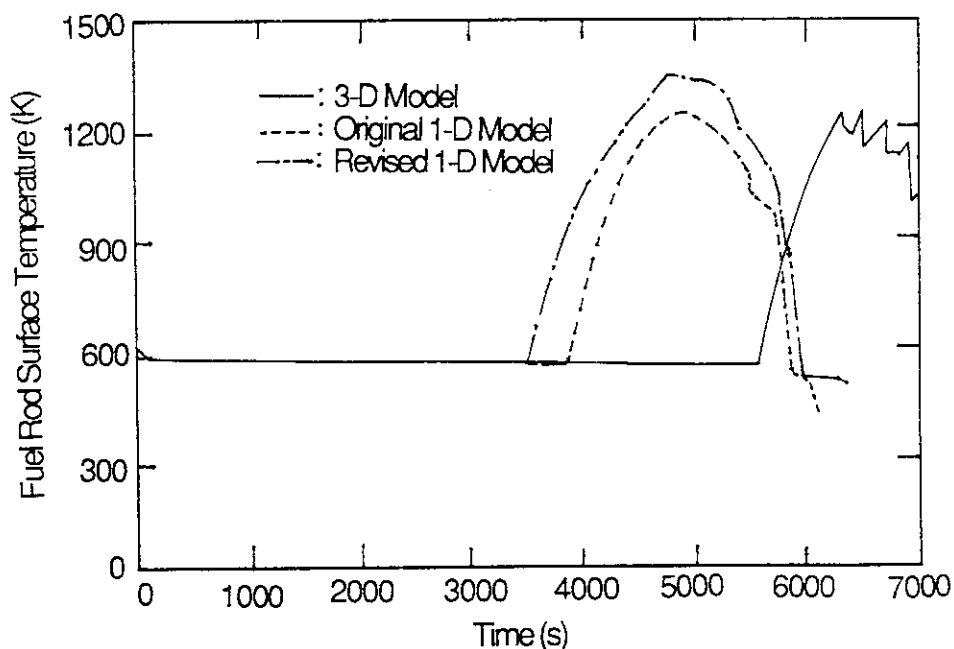


Fig. 9.13.1 Calculated peak cladding temperatures in all cases

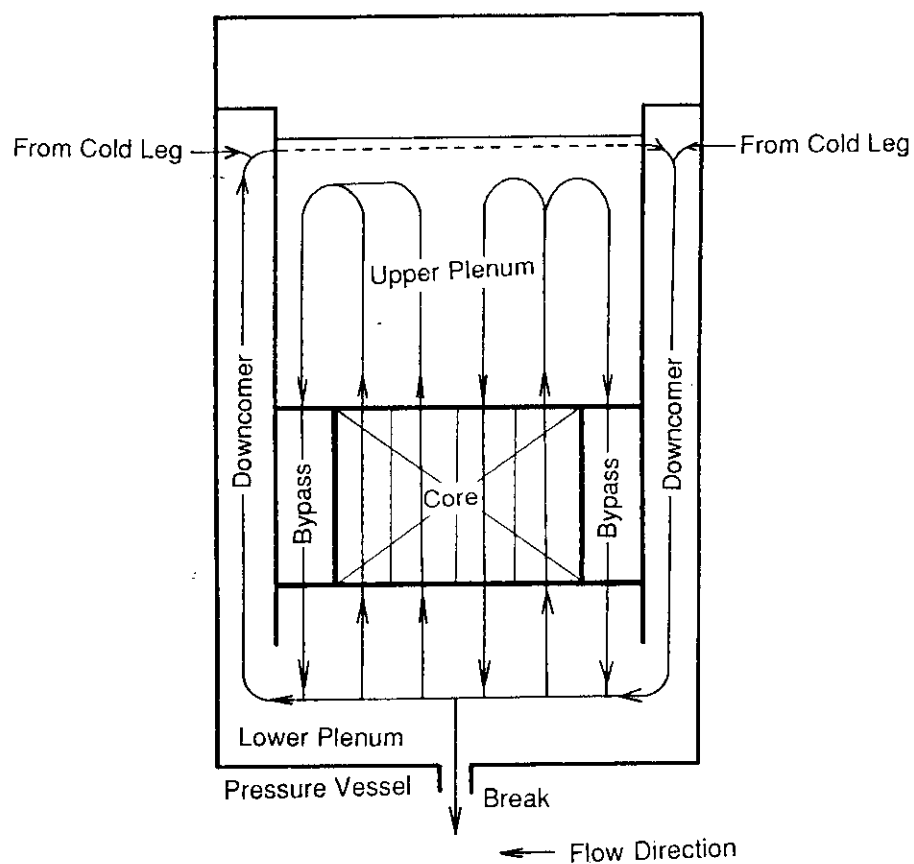


Fig. 9.13.2 Circulation flow paths calculated in 3-D case

## 10. Nuclear Energy Systems Analysis and Assessment

Annual research activities on nuclear energy systems analysis and assessment are reviewed in the following three research subjects: 1) Development of analytical method and data base for energy environment systems analysis, 2) strategy analysis of nuclear power and process heat utilization, and 3) nuclear heat technology assessment.

As for research item 1), the integrated E<sub>3</sub> Model System, which has accumulated a variety of application experiences since its development, has been utilized in the analyses such as on greenhouse gas emissions reduction of the IEA/ETSAP (Energy Technology Systems Analysis Project) -Annex IV research subject, on the role of HCLWR in long-term fuel cycle, etc.. The model system installs now the PC-MARKAL and MUSS and also OMNI PC/ASM, a software package for compilation of programs written in the OMNI language. For further enhancement of model capability, especially, to environmental consequence analysis, efforts are now being made in model development on energy-environment risk analysis and in data base development.

As for research item 2), two different kinds of work have been done, i.e. 1) a preliminary analysis of CO<sub>2</sub> emission reduction in Japanese energy system by the MARKAL model and 2) an analysis of HCLWR installation role in long-term Japanese fuel cycle system by the JALTES model. The former analysis is conducted under the IEA/ETSAP, and in the time horizon covering 45 years from 1985 the potential of CO<sub>2</sub> emission reduction has been analyzed along such emission reduction strategies as conservation, fuel switching, technology substitution, etc.. The analyses show us one important point that the government target of CO<sub>2</sub> emission reduction can be technologically feasible if GDP growth and CO<sub>2</sub> emission reduction strategy are taken appropriately. Further analysis including other greenhouse gases is necessary in the next step.

As for research item 3), a cycle simulation study on the UT-3 thermochemical hydrogen production process is made. Simulation results indicate us the necessity of setting an alternative gas flow through the reactors whether the reaction is hydrolysis or bromination if steady state composition profile of CaBr<sub>2</sub> must be maintained. From a comparative study on synthetic fuel production, we obtained a fact that hydrogen from thermochemical reaction rather than from methane steam reforming is more advantageous to reduce CO<sub>2</sub> emission when SNG and/or methanol production is processed from coal with hydrogen reforming. (Shigeru Yasukawa)



## 10.1 Development of Integrated Energy-Economy-Environment Model System

O. Sato, Y. Shimoyamada, H. Shiraki and S. Yasukawa

The Integrated Energy-Economy-Environment Model System<sup>1),2)</sup> has been developed so far in order to provide analytical tools for the studies on the role of nuclear energy and relevant technologies in the long-term evolution of energy, economy, and environment systems in Japan. It has been already applied to various studies, e.g. the study on the role of future technology options for reducing oil imports, the energy-environment study for reducing SO<sub>x</sub> and NO<sub>x</sub> emissions, and for reducing greenhouse gas emissions under the IEA/ETSAP (Energy Technology Systems Analysis Project), the study on effective utilization of plutonium and the role of new reactor types, and others.

The system consists of four model blocks for generating long-term energy-economy scenarios, for analyzing structurally energy and/or economy systems, for analyzing in detail nuclear reactor and fuel cycle systems, and for cost-benefit-risk assessment of energy technologies. Basic models in the first three blocks are already in the stage of application, and effort is now directed to the improvement and extension of these models and the development of models and data bases in the fourth block. Followings are major recent progresses in such development.

The MARKAL model<sup>3)</sup> has been originally developed and utilized on the mainframe computers. However, with a rapid progress in performances of personal computers (PC), it can now be practically used also on PCs. At the same time, the Brookhaven National Laboratory has developed the MARKAL Users Support System (MUSS)<sup>4)</sup> which supports users of MARKAL in preparing input data, executing optimization, and producing tables and figures of results. In order to operate PC-MARKAL and MUSS, a high-performance PC with i80486 CPU and 4MB main memory has been installed in our laboratory together with OMNI PC/ASM, a software package to compile and execute the PC-MARKAL program written in the OMNI language<sup>5)</sup>.

The current practice of energy-environment systems analysis has focused mainly on evaluating amounts of emissions of major air pollutants such as SO<sub>x</sub>, NO<sub>x</sub>, or greenhouse gases including CO<sub>2</sub>. Besides a broad range of global effects to be given by greenhouse gases, quantitative evaluation of environmental consequences by energy production and utilization is very important for the purpose of discussing implications of

reducing emissions from energy systems. Current scientific knowledges have been investigated recently on possible impacts to humans and plants given by SO<sub>x</sub> and NO<sub>x</sub> in the ambient air. Based on this information, quantitative relationships between dose and response have been summarized and damage functions have been estimated. These damage functions are to be incorporated into the model for energy-environment risk analysis.

Development of reliable data bases and an efficient system for utilizing them is an essential task for carrying out systems analysis. Strong effort has been made so far for collecting and compiling characteristic data of energy technologies and emission control technologies for SO<sub>x</sub> and NO<sub>x</sub>. In the context of the global warming study, fundamental principles and characteristics of various technology options for CO<sub>2</sub> recovery, disposal, and recycle have been investigated recently. Also, costs and potential effects of energy conservation technologies mainly in the industry sector have been investigated. The data has provided realistic estimates on the possible reduction of future energy consumption in the study for reducing CO<sub>2</sub> emissions under the IEA/ETSAP.

In parallel with the development of technology data bases described above, effort is also directed to utilize efficiently energy-economy statistical data. The EDMC energy data bank of the Institute of Energy Economics and the energy-economy data bank CERTAIN of the CRC Research Institute provide on-line data service on the contractual basis. The PC system in our laboratory is now connected to these data banks using a public telephone line.

#### References

- 1) Yasukawa S., et al.: "Development of Integrated Models for Energy-Economy Systems Analysis at JAERI", JAERI-M 84-139 (1984).
- 2) Yasukawa S., et al.: "Progress in Integrated Energy-Economy-Environment Model System Development", JAERI-M 87-188 (1987).
- 3) Fishbone L.G., et al.: "User's Guide for MARKAL (BNL-KFA Version 2.0)", BNL/USA and KFA/Germany (internal memo) (1982).
- 4) Goldstein G.A.: "PC-MARKAL and the MARKAL User's Support System (MUSS) - User Documentation", Brookhaven National Laboratory, USA (internal memo) (1990).
- 5) Haverly Systems Inc.: "OMNI Modeling and Data Management System - Reference Manual", Haverly Systems Inc. (1987).

## 10.2 Preliminary Analysis on CO<sub>2</sub> Emission Reduction in Japanese Energy System by MARKAL Model

S. Yasukawa, O. Sato, M. Konta, Y. Shimoyamada, T. Kajiyama,  
H. Shiraki and Y. Tadokoro

The Energy Technology Systems Analysis Project (ETSAP) of the International Energy Agency of the Organization for Economic Co-operation and Development is carrying out the systems analysis on greenhouse gas (GHG) emissions reduction as its Annex IV programme. The objective of this programme is to study CO<sub>2</sub> emission reduction potential through investigating long-term energy utilization and associated technology introduction.

In relation to this programme, we have conducted a CO<sub>2</sub> emission reduction analysis by application of the MARKAL model. The time horizon in the study is 45 years from 1985 to 2030, and the reference energy system (RES) covers total energy system of Japan, i.e. industrial, residential and commercial, transportation, and conversion and distribution sector. In this RES included are 39 different kinds of conversion technology, 82 kinds of process technology, and 197 demand device technologies. Energy carriers of 109 kinds connect them.

The analysis was made by using scenario method, and for this purpose three scenario descriptors, i.e. population, GDP growth, and import fuel price are introduced. Two different scenarios were generated using those descriptors, i.e. a vigorous scenario represented by high GDP growth with low fuel price and a restrained scenario with low GDP growth and high fuel price. Introduction timing technologically possible of energy technology and its capacity bound are partly served as exogeneously given constraints.

The energy system is optimized by linear programming method where objective function is selected from those of discounted system cost, accumulated CO<sub>2</sub> emission, accumulated imported oil, and linear combination of those quantities. For CO<sub>2</sub> emission control, such strategies as energy conservation, fuel switching, technology substitution, recycle of carbonaceous materials, and CO<sub>2</sub> storage and disposal are included in the analysis.

Historical trend of energy conservation is built in GDP growth as well as in useful energy demand projection beforehand. Other energy conservation efforts such as rational use of heat and power, efficiency

improvement, and recycle use are treated technologically. Here, combined heat and power (CHP) and fuel cell are the representative technologies for rational use of heat and power. Efficiency improvements are taken into account in various energy technologies such as electric power plant, industrial heat use process, residential and commercial heat use devices, and transportation system. Recycling activities for iron scrap, reclaimed aluminium, cullet, waste paper, industrial wastes and municipal solid wastes, waste lubricants are included in the analysis, and municipal waste heat recovery is also taken into account.

Analytical results indicate us several interesting points: 1) CO<sub>2</sub> emission is possibly stabilized till 2000 at the 1990 emission level in terms of emission per capita. If GDP growth and CO<sub>2</sub> emission strategy are properly taken, and furthermore reduction can be anticipated beyond 2000 through efforts on making energy conservation, fuel switching, substitution of fossil fuel technology by nuclear and renewable, as shown in Fig. 10.2.1. 2) Primary energy supply declines to more intensive use of nuclear and renewable energy and increases the share of natural gas in fossil fuel supply. 3) Final energy demand increases electricity and direct heat use and is switching more intensively from solid fossil fuel to liquid and gaseous fuels. 4) About two thirds of electricity is supplied by nuclear power in 2030 and off peak electricity generated by base load power increases its role through the use of electric car and hydrogen production, etc.. 5) Conservation has advantages not only in primary energy saving but also in environmental emission reduction. Relative importance of conservation activities is in the order of efficiency improvement, rational use of heat and power, and recycle use.

From technological view points, we can say that efficiency improvement of enduse technologies should be accelerated and rational use of heat and power through intensive use of combined heat and power system and co-production system would be increased. Extended use of heat pump will be popularized for heat recovery, and fuel cell will gain relatively larger role. Concerning automotive fuel, it will be switching from fossil to synthetic fuel and electricity. Advanced fossil fuel reforming and refinery technologies using nuclear energy and fossil fuel symbiotically would become competitive technology for this purpose. For further CO<sub>2</sub> emission reduction, CO<sub>2</sub> storage and disposal as well as flue gas recycle use by IES technology need to be evaluated technologically.

## Reference

- 1) Yasukawa S., et al.: "Preliminary Analysis on CO<sub>2</sub> Emission Reduction in Japan by MARKAL Model", Distribution paper for participants to Joint ETSAP/IIASA Meeting held at the IIASA in Laxenburg, Austria on May 21-22 (1991).

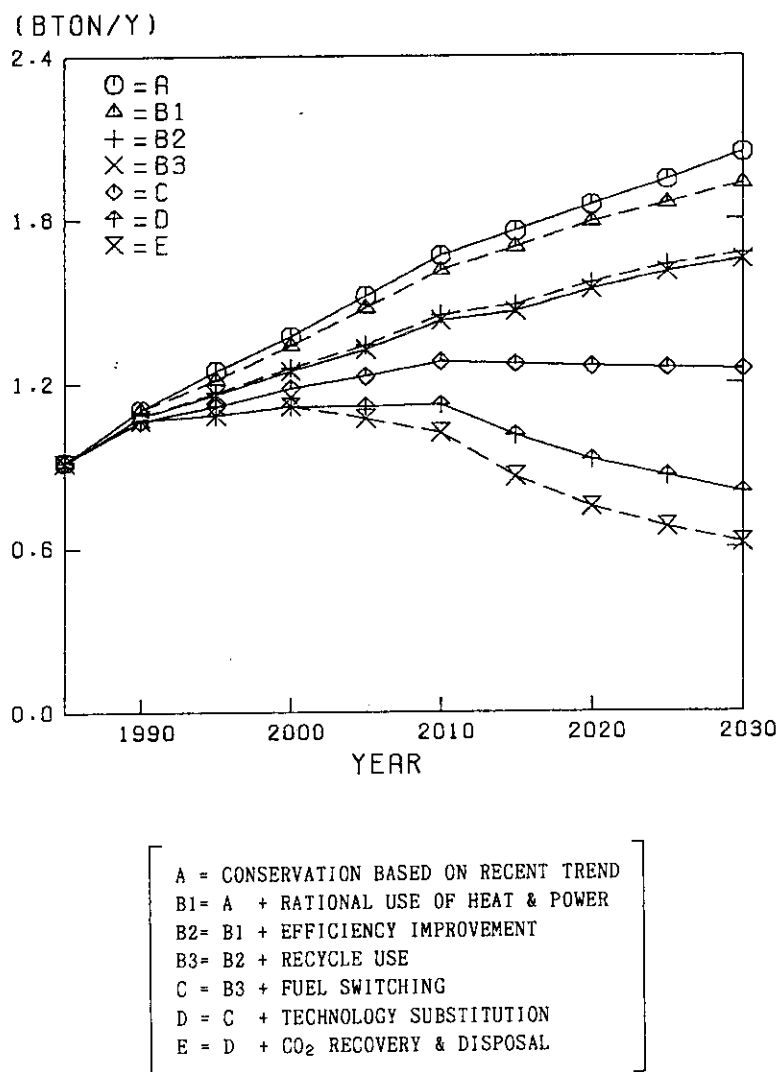


Fig. 10.2.1 CO<sub>2</sub> emission reduction by each strategy

### 10.3 An Analysis on the Role of HCLWR from the Viewpoint of Long-Term Fuel Cycle

O. Sato, Y. Shimoyamada and S. Yasukawa

Possible roles of high conversion light water reactors (HCLWR) in future power reactor and fuel cycle systems in Japan have been analyzed for the time horizon 1970 to 2100 with particular emphasis on reducing natural uranium consumption through effective utilization of plutonium<sup>1)</sup>. The linear programming optimization model of long-term nuclear fuel cycle systems JALTES-II<sup>2)</sup> has been employed for the analysis.

Total nuclear power capacity is assumed to increase to 50.5 GWe in 2000, 72.5 GWe in 2010, 107 GWe in 2030, and 177 GWe in 2100 with an annual increment 1 GWe during 2030 and 2100. In addition to this reference case, an alternative case is considered where total capacity increases to 140 GWe in 2044 and remains at this level thereafter.

Reactor types considered are LWR, FBR, and HCLWR. Modest burnup around 33 Gwd/t is assumed for the fuel of LWR. No external constraint is given to its capacity. In a special case advanced light water reactors (A-LWR) with higher burnup is used in replacement of LWR. FBR employs MOX fuels with a breeding ratio 1.2 and a core burnup 150 GWD/t. It is assumed to be available from 2030, or alternatively from 2050, with a maximum introduction rate 1 GWe/year during the initial five years.

Two types of HCLWR has been examined; HCPWR with rather low fissile plutonium inventory and a modest conversion ratio and HCBWR with large fissile plutonium inventory and a higher conversion ratio. In a replacement core of HCBWR, the amount of plutonium discharged is even a little larger than that charged. HCLWR is assumed to be available from 2000 without external constraint on its capacity.

Natural uranium consumption in each analytical case is compared in Fig. 10.3.1. In the case where only A-LWR is employed, the cumulative consumption up to 2100 amounts to 2.17 Mton (uranium metal). If HCLWR is used in combination with LWR, it decreases to 1.55 Mton. HCPWR reduces natural uranium a little more than HCBWR.

When FBR is available from 2030 or 2050 in combination with LWR, the cumulative consumption of natural uranium becomes 0.87 or 1.25 Mton, respectively. These amounts can be further reduced by introducing HCLWR, i.e. by 0.06 or 0.17 Mton in the case of HCPWR and by 0.11 or 0.23 ton

in the case of HCBWR, respectively. Despite the large initial plutonium requirements, HCBWR saves more natural uranium than HCPWR because of its much higher conversion ratio. In the case where FBR is available from 2050, the cumulative capacity of HCPWR or HCBWR introduced is 43 GWe or 45 GWe with the starting year 2008 or 2001, respectively.

If total nuclear capacity is kept at 140 GWe after 2044, the possible saving of natural uranium by HCLWR becomes larger. In the case of LWR + FBR (available from 2050), the cumulative consumption of natural uranium is 1.31 Mton, a bit larger than above because FBR can be installed only as replacement for retired LWR. When HCPWR or HCBWR is introduced here, the consumption is reduced by 0.24 or 0.26 Mton, respectively.

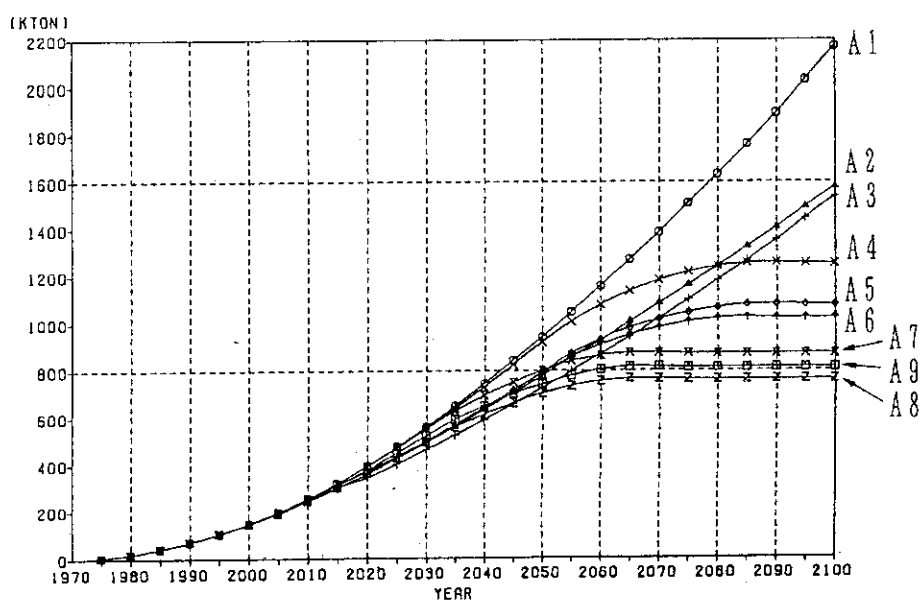
The amount of fissile plutonium stock outside reactors is shown in Fig. 10.3.2 for the above cases. This figure indicates that still large amount of plutonium is left unused even when FBR is introduced from 2030. Such plutonium can be effectively used by HCLWR. Particularly when HCBWR is introduced, the plutonium stock is kept at the almost zero level.

Demand for separative work can be also reduced by the introduction of HCLWR. With the combination of LWR and FBR (from 2050), the peak annual demand reaches 14.7 ktonSWU. When HCPWR or HCBWR is introduced here, the demand is reduced by 8% or 25%, respectively. On the other hand, total requirements for both fuel fabrication and spent fuel reprocessing increase a little when HCLWR is introduced in the LWR-FBR system because of relatively low specific power of HCLWR.

Summarizing the results, it has been confirmed that HCLWR is effective in reducing the consumption of natural uranium particularly when the commercialization of FBR is delayed. Among two types of HCLWR examined, HCBWR saves more natural uranium than HCPWR when total nuclear capacity grows steadily to the future. If growth of nuclear capacity is stagnant, larger savings are expected with less difference between the effects by both types of HCLWR.

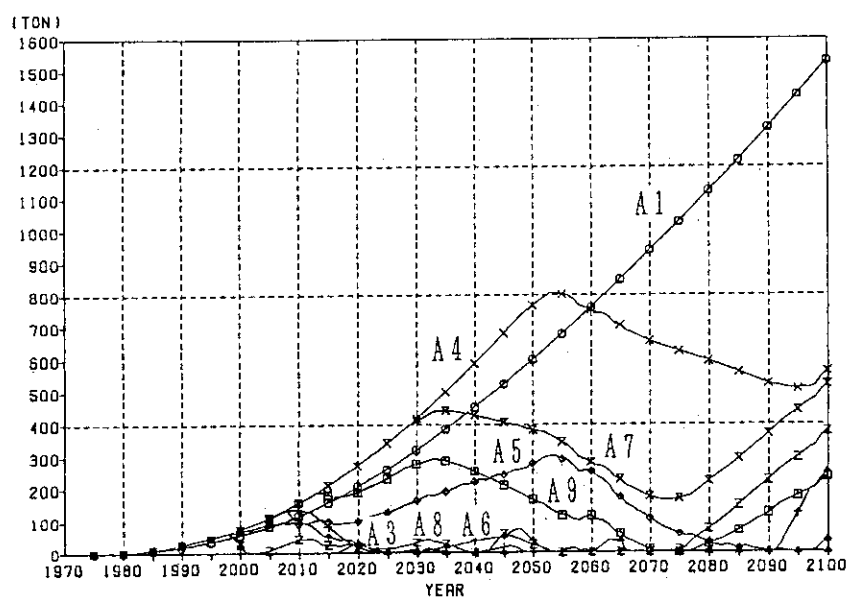
#### References

- 1) Sato O. and Yasukawa S.: "JALTES-III: A System Analysis Model for Long-Term Strategy on Nuclear Power Development", JAERI-M 85-129 (1985).
- 2) Nuclear Energy Technology Assessment Laboratory: "Effect of High Conversion Light Water Reactors on Long-Term Nuclear Fuel Cycle", Final Report on Conceptual Study of High Conversion Light Water Reactors in JAERI pp.66-83 (1991) (in Japanese).



A-1 : A-LWR	A-6 : LWR + HCBWR + FBR(2050)
A-2 : LWR + HCBWR	A-7 : LWR + FBR(2030)
A-3 : LWR + HCPWR	A-8 : LWR + HCBWR + FBR(2030)
A-4 : LWR + FBR(2050)	A-9 : LWR + HCPWR + FBR(2030)
A-5 : LWR + HCPWR + FBR(2050)	

Fig. 10.3.1 Cumulative consumption of natural uranium



(refer to the above for definition of cases)

Fig. 10.3.2 Stock of fissile plutonium outside reactors



## 10.4 A Study on Broad Economic Impact of Nuclear Power

S. Yasukawa, O. Sato and S. Yamazaki<sup>\*</sup>

A survey study of "Broad Economic Impacts of Nuclear Power" is now proceeding under the Nuclear Development Committee of the Nuclear Energy Agency in the Organization for Economic Co-operation and Development. In relation to this study, an analysis of induced production effects by nuclear power generation was made by the input-output method.

The analysis is made for the calendar year 1985, utilizing the nuclear industry statistics compiled by Japan Atomic Industrial Forum<sup>1)</sup> and the input-output tables<sup>2)</sup>. In the I/O analysis, we disaggregate only electric utility sector into two subsectors, i.e. a nuclear related sector and a non-nuclear related sector. Other industry sectors are treated with no separation.

Utilizing the I/O matrix A which includes the nuclear related sector and the I/O matrix A' which excludes the nuclear related sector, we can evaluate induced production effect as follows: the effect of induced production, which is brought by the investment on nuclear power plant, in the industrial sector is derived by multiplying  $(I-A)^{-1}$  by the quantity of the fixed capital formation of the nuclear related sector. While the induced production effect, which is brought by the production activities of the nuclear related sector, to the industries is derived by multiplying  $(I-A')^{-1}$  by the input vector of the nuclear related sector.

The analyses indicate us the facts that an induced production of the electric utility investment, 1137 billion yen, on nuclear power plant, reach to 2946 billion yen, which is 2.95 times larger than the original investment as shown in Table 10.4.1. Such industries as machinery, iron and steel, construction, and transportation contribute largely to the induced production. The induced production effect by the production activities of nuclear power plant was also analyzed in the same way, and we find its yield rate being 1.98, which is much larger than 1.12 in the case of transportation machinery sector as an example. Those industries as electric machinery, construction, finance and insurance, services are large contributors.

---

\* CRC Research Institute, Inc.

## References

- 1) Japan Atomic Industrial Forum: Survey Report on Nuclear Industry (1986).
- 2) Statistics Bureau, Management and Coordination Agency of Japan: 1985 Input-Output Table (1989).

Table 10.4.1 Production induced by nuclear investment  
of electric utility

Industry	Nuclear Investment (billion yen)	Production Induced in Each Industry	
		Amount (billion yen)	Coefficient*
Agri., Fishery & Forestry	0.	14.0	0.0123
Mining	0.	63.2	0.0556
Food	0.	12.1	0.0106
Textile	0.	11.8	0.0104
Pulp and Paper	0.	54.0	0.0475
Chemical Products	0.	70.5	0.0620
Oil and Coal Products	0.	57.4	0.0505
Cement and Ceramics	0.	44.3	0.0390
Iron and Steel	4.7	179.8	0.1582
Non-Ferrous Metals	1.9	84.6	0.0744
Metal Products	1.2	59.5	0.0523
General Machinery	29.4	83.8	0.0737
Electric Machinery	424.3	647.6	0.5697
Transport Machinery	403.2	655.6	0.5768
Precision Instruments	1.	3.4	0.0030
Other Manufacturing	0.	92.6	0.0814
Construction	270.7	281.9	0.2480
Electricity(Nuclear)	0.	13.0	0.0114
Electricity(Non-Nuclear)	0.	36.3	0.0320
Gas and Heat	0.	3.0	0.0026
Water and Waste	0.	7.5	0.0066
Wholesale and Retail	0.	104.2	0.0917
Finance and Insurance	0.	72.2	0.0635
Real Estate	0.	21.7	0.0191
Transportation	0.6	103.7	0.0912
Communication	0.	13.8	0.0121
Public Services	0.	1.7	0.0015
Education and Research	0.	40.7	0.0358
Services	0.	74.2	0.0653
Stationery	0.	4.7	0.0041
Unclassified	0.	33.2	0.0292
Total	1136.8	2946.0	2.5915

\* Production Induced in Each Industry/Total Nuclear Investment

## 10.5 CO<sub>2</sub> Emission Coefficient of Nuclear Power and Process Heat Utilization

S. Yasukawa, Y. Tadokoro and T. Kajiyama

Carbon dioxide emission coefficient of nuclear power and that for the utilization of nuclear process heat are important quantities for evaluation of long-term nuclear role in greenhouse gas emission reduction. To estimate those, we selected a 1000 MWe light water reactor and associated fuel cycle processes as a reference of nuclear power, and a 1000 MWt very high temperature reactor and associated heat utilization system as a reference of high temperature process heat utilization<sup>1)</sup>.

Emission coefficient consists generally of two parts, i.e. a part of direct CO<sub>2</sub> emission and a part of indirect CO<sub>2</sub> emission. The former part is the emission from direct fossil fuel combustion, while the latter is the emission from indirect processes such as material production, fabrication of system components, construction of facilities, transportation of various kinds of goods, etc. For direct part, if we know the quantity of fuel consumption, we can calculate the emission coefficient of this part directly. As for indirect part, we need information not only of fuel consumption but also on value added process because especially in fabrication process capital goods are used generally for multiple purposes. Such information can be obtained from I/O analysis.

Comparison of CO<sub>2</sub> emission coefficient of nuclear power and fossil fuel fired electric is shown in Table 10.5.1. The emission coefficient of nuclear power is only a few percent of that of coal steam power. If fossil fuel share in the electric sector declines further, the emission coefficient of nuclear power can be further lower because three fourths of CO<sub>2</sub> emission come from electric utilization. Especially, enrichment process takes a large share of total emission.

Another example of CO<sub>2</sub> emission analysis is shown in Table 10.5.2. Here, we do not include an emission of indirect processes. SNG and methanol are produced from coal in two ways, i.e. the first one by use of non-nuclear heat and the second one by nuclear heat, and for the latter both steam reforming and thermochemical hydrogen production process are compared. Analytical results show us that in any case of analyses, nuclear heat use through thermochemical process emits less CO<sub>2</sub> than other processes.

## Reference

- 1) Yasukawa S., et al.: "HTGR's Role on CO<sub>2</sub> Reduction", Distribution paper for JITA's meeting on CO<sub>2</sub> problem, November 7 (1990).

Table 10.5.1 Comparison of CO<sub>2</sub> emissions of fossil fuels fired electric and nuclear power

ITEMS	COAL FIRED	OIL FIRED	GAS FIRED	NUCL. POWER
CO <sub>2</sub> EMISSION (kg/kWh)	1.078	0.874	0.605	0.034

Table 10.5.2(a) CO<sub>2</sub> emissions per unit of SNG production from coal

HEAT SOURCE	ITEMS H <sub>2</sub> PROD. PROCESS	CONSUMED ENERGY (Mcal/kg)	CO <sub>2</sub> EMISSION COEFFICIENT				
			PRODUCTION		COMBUSTION	TOTAL	
			(kg/Mcal)	(t <sub>CO<sub>2</sub></sub> /t <sub>CH<sub>4</sub></sub> )	(t <sub>CO<sub>2</sub></sub> /t <sub>CH<sub>4</sub></sub> )	(t <sub>CO<sub>2</sub></sub> /t <sub>CH<sub>4</sub></sub> )	(kg/Mcal)
NON-NUCL. HEAT	STEAM REFORMING	21.1	0.192	4.05	2.75	6.80	0.512
NUCLEAR HEAT	STEAM REFORMING	21.6	0.134	2.90	2.75	5.65	0.426
	THERMOCHEM. H <sub>2</sub> PROD. UT-3 PROCESS	29.4	0.	0.	2.75	2.75	0.207
COAL COMBUSTION		—	—	—	2.83 (t <sub>CO<sub>2</sub></sub> /t <sub>COAL</sub> )	2.83 (t <sub>CO<sub>2</sub></sub> /t <sub>COAL</sub> )	0.434

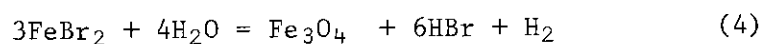
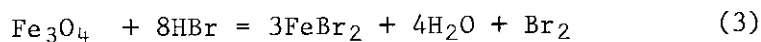
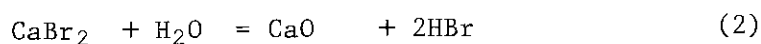
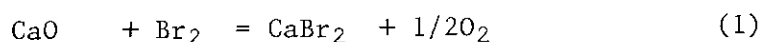
Table 10.5.2(b) CO<sub>2</sub> emissions per unit of METHANOL production from coal

HEAT SOURCE	ITEMS SYNGAS PROD. PROCESS	CONSUMED ENERGY (Mcal/kg)	CO <sub>2</sub> EMISSION COEFFICIENT				
			PRODUCTION		COMBUSTION	TOTAL	
			(kg/Mcal)	(t <sub>CO<sub>2</sub></sub> /t <sub>CH<sub>3</sub>OH</sub> )	(t <sub>CO<sub>2</sub></sub> /t <sub>CH<sub>3</sub>OH</sub> )	(t <sub>CO<sub>2</sub></sub> /t <sub>CH<sub>3</sub>OH</sub> )	(kg/Mcal)
NON-NUCL. HEAT	STEAM REFORMING	11.9	0.184	2.18	1.38	3.56	0.656
NUCLEAR HEAT	STEAM REFORMING	12.3	0.097	1.19	1.38	2.57	0.473
	STEAM REFORMING THERMOCHEM. H <sub>2</sub> PROD. UT-3 PROCESS	14.1	0.	0.	1.38	1.38	0.254
COAL COMBUSTION		—	—	—	2.83 (t <sub>CO<sub>2</sub></sub> /t <sub>COAL</sub> )	2.83 (t <sub>CO<sub>2</sub></sub> /t <sub>COAL</sub> )	0.434

## 10.6 Study on Cycle Simulation of the UT-3 Thermochemical Hydrogen Production Process

Y. Tadokoro and T. Kajiyama

The technical feasibility study has been carried out on the UT-3 thermochemical hydrogen production process of an industrial scale by utilizing a simulation model of the UT-3 reaction cycle<sup>1)</sup>. This process is a cycle of the following four reactions to form chemical decomposition of water.



In the UT-3 cycle, all the four different reactions must proceed at the same rate in fixed bed reactors so that no excess or shortage of reactants may occur. The control of the reaction rate requires adjustments of temperature, pressure and gas flow rate as well as the structural condition of the solid reactants which do not move during the reaction.

The most appropriate process scheme for constant heat source such as nuclear energy is different from that for time-variant heat source such as solar energy source. In this study the preliminary simulation analysis has been made on the UT-3 reaction cycle in order to obtain appropriate process scheme when applying nuclear energy as its heat source.

Figure 10.6.1 shows the composition profile of solid reactants at each cycle of a Ca-reactor, consisting of Ca compounds, with gas supply from the same direction. Figure 10.6.2 shows the results when the direction of the gas supply is alternated in each cycle. It is found that the steady composition profile of  $\text{CaBr}_2$  can be maintained by changing the direction of gas supply from top-to-bottom to bottom-to-top of the fixed bed reactor and vice versa in the alternation of hydrolysis and bromination. The simulation indicates that the direction of the gas flow through the reactions must be alternated depending upon whether the reaction is hydrolysis or bromination.

## Reference

- 1) Tadokoro Y., Kajiyama T., et al.: "Cycle Simulation of the 'UT-3' Thermochemical Hydrogen Production Process", 8th World Hydrogen Energy Conference, Honolulu and Waikoloa, Hawaii, USA, July 22-27 (1990).

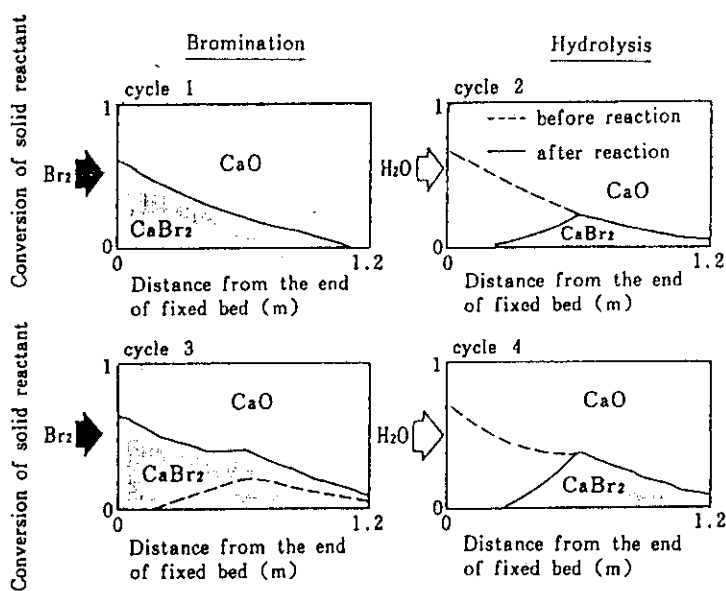


Fig. 10.6.1 Calculated result of cycle simulation for Ca-reactor in the case of gas supply from same direction

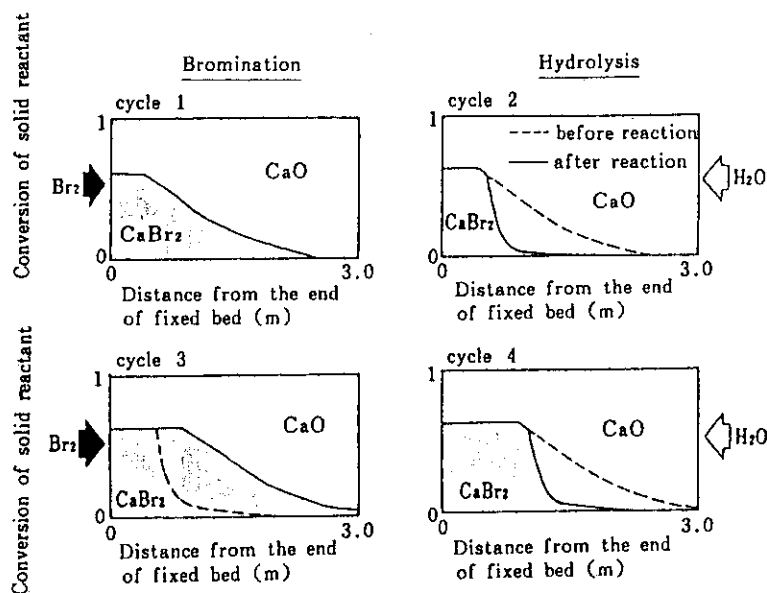


Fig. 10.6.2 Calculated result of cycle simulation for Ca-reactor in the case of gas supply from alternate direction

## 11. Development of Proton Linear Accelerator and Transmutation Target System

The accelerator-driven nuclear transmutation system has been proposed for the OMEGA project (Options Making Extra Gains of Actinides and Fission Products). The conceptual design study for the system has been continued to achieve higher transmutation rate and examine the technical feasibility. In the current concept, the estimated annual transmutation rate is about 250 kg, which corresponds to the actinide production rate in about 10 units of 3000 MWt LWR.

The conceptual study on the molten salt core has been also started as one of the other attractive options for the accelerator-driven transmutation system. The further study will be carried out in more detail.

The development of the SPCHAIN code system has been made to analyze the time evolution behavior of spallation products during irradiation and cooling time. The differential equations for the process were formulated by adding the spallation reaction terms to the burnup equation of the reactor fuel.

Integral experiments with a lead bulk have been performed to investigate the transport process of the particles produced by spallation reaction. The experiments have been carried out in the beam dump room of the 500 MeV booster proton synchrotron facility of National Laboratory for High Energy Physics (KEK).

The high intensity proton accelerator (ETA: Engineering Test Accelerator) with an energy of 1.5 GeV and a current of 10 mA has been proposed to perform various engineering tests for the transmutation system. As the first step development, the design studies and some R&D works of the Basic Technology Accelerator (BTA) have been carried out for the low energy mock-up test of the ETA.

As a study on multicusp type ECR ion source, source plasma production has been measured by 2.45 GHz microwave. By injecting 2 kW microwave, a hydrogen plasma of density of  $1.7 \times 10^{11} \text{ cm}^{-3}$  was produced at a pressure of 0.1 Pa. For the design of the RFQ and DTL, extensive analyses were carried out to optimize the beam optics and mechanical structure. Heat dissipation in the structure was considered to be the most important technical issue and evaluated by an electromagnetic field analysis and a heat calculation code.

(Motoharu Mizumoto)

### 11.1 A Progress in the High Intensity Proton Linear Accelerator Development

M. Mizumoto, K. Hasegawa, H. Yokobori, H. Mino, H. Tanaka<sup>\*</sup>,  
Y. Okumura and Y. Kaneko

The accelerator-based nuclear transmutation system has been studied as one of the options for the OMEGA project (Options Making Extra Gains of Actinides and Fission Products). The high intensity proton linear accelerator (ETA: Engineering Test Accelerator) with an energy of 1.5 GeV and a current of 10 mA has been proposed to perform various engineering tests for the transmutation system such as plant test, large-scale integral test, material test and nuclear data experiment<sup>1),2)</sup>.

Such a high intensity proton accelerator requires several technological developments. In particular, the average beam current of 10 mA is nearly 10 - 50 times larger than that for the existing proton accelerators. A study of low energy portion of the accelerator structure is considered to be essential, because the beam quality is determined mainly by this low energy part.

The design study of the Basic Technology Accelerator (BTA) has been carried out as a first step for the development of the high intensity proton accelerator. The mock-up test for the low energy portion of the ETA is planned to be made by this BTA with a beam energy of 10 MeV and a current of 10 mA. Simultaneously, various basic accelerator technologies will be accumulated from the course of design, construction and operation of the BTA.

Main items for the R&D works consist of high current ion source, radio frequency quadrupole (RFQ), drift tube linac (DTL) and RF power source as shown in Fig. 11.1.1. In the conceptual design study of the system, main aims are to obtain good beam quality (low emittance) and high beam transmission efficiency.

The specification of the BTA is given in Table 11.1.1. The peak beam current is chosen to be 100 mA with a duty factor of 10% resulting in average current of 10 mA. The goal of the transverse beam emittance at the output of the DTL is set at  $0.5 \pi \text{ cm.mrad}$ . After many discussions, the operating RF frequency for the RFQ and DTL was finally decided to be

---

\* Nissin Electric Co. Ltd.



200 MHz due to two main reasons; availability of the 200 MHz high power RF sources and heat removal problem in the higher frequency structure, say, 270 MHz or 300 MHz, although it may be expected that the higher frequency structure can accelerate high intensity proton beam current with low emittance from the advanced beam dynamics theory.

The several computer codes for the accelerator design study have been prepared; SUPERFISH for electromagnetic field, CURLI and RFQUIK for RFQ design, PARMTEQ and PARMILA for beam dynamics and TRACE-3D for beam transport calculation<sup>3)</sup>. The code for three dimensional heat dissipation calculation in the accelerating structure is also being prepared and preliminary results have been obtained. The design calculations for RFQ and DTL have been progressed during 1990 as described in the separated contributions in this annual report<sup>4)</sup>. The R&D works on the high intensity ion source have been carried out in collaboration with the group of NBI Heating Laboratory<sup>5)</sup>.

The layout of the BTA building has been investigated by considering the space required for the accelerator structures, RF power source, beam transport system and beam dump facility as well as the safety aspects and utilities such as radiation shielding, electricity, water consumption, air conditioning system in cooperation with the Departments of Construction and Health Physics.

#### References

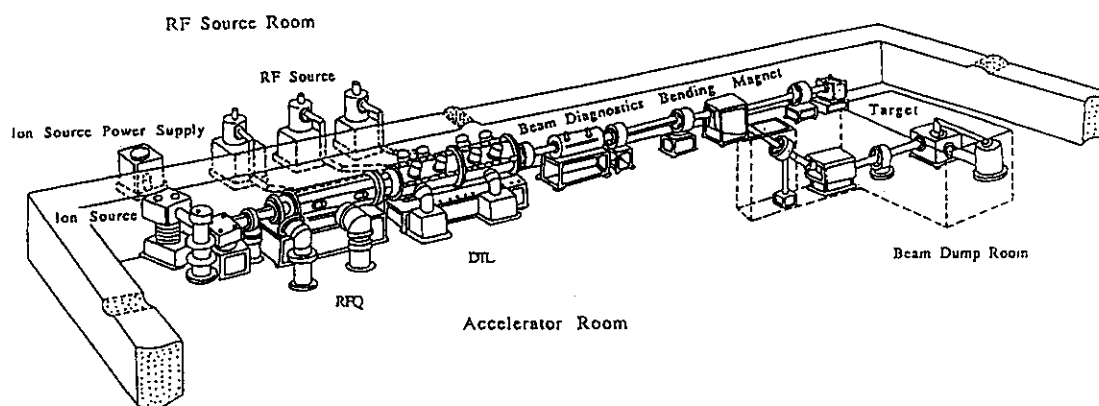
- 1) Kaneko Y.: Proc. of the 2nd International Symp. on Advanced Nuclear Energy Research - Evolution by Accelerator -, Mito p.25 (1990).
- 2) Mizumoto M., et al.: *ibid*, p.219.
- 3) Los Alamos Accelerator Code Group: Computer Codes for Particles Accelerator Design and Analysis, LA-UR-90-1766 (1990).
- 4) Hasegawa K., et al. and Yokobori H., et al.: Reactor Engineering Department Annual Report (April 1, 1990 - March 31, 1991) (1991).
- 5) Okumura Y., et al.: *ibid*. (1991).

Table 11.1.1 Basic specification of BTA

Accelerated particle	proton
Operation mode	pulse
Duty factor	10 %
Output Energy	10 MeV
Average beam current	10 mA
Peak beam current	100 mA

## Target specification of BTA

Normalized emittance	$0.5 \pi \text{ cm.mrad}$
Energy resolution	1 %



Basic Technology Accelerator ( BTA )

Fig. 11.1.1 Conceptual layout of the Basic Technology Accelerator

## 11.2 Study on a High Brightness Ion Source for the Basic Technology Accelerator

Y. Okumura, K. Hasegawa, H. Tanaka\* and H. Yokobori

For the Basic Technology Accelerator, it is necessary to develop a high brightness ion source that is capable of producing a high current proton beam with a low beam emittance and a high duty cycle. Basic specifications proposed for the ion source are listed in Table 11.2.1. Although high current ion sources have been developed for heating of thermonuclear fusion devices, some of the specifications are beyond the performances achieved in the present source<sup>1)</sup>. Especially, required emittance and beam size are very small in spite of the large beam current. Steady-state operation of the source also requires further development to make the life time of the source longer.

Figure 11.2.1 shows a conceptual design of the ion source. The source is basically a multicusp ion source; hydrogen ions are produced in a magnetically confined plasma chamber and extracted with a four electrode extractor or a two-stage extraction system. An example of the ion beam trajectory in the extractor is shown in Fig. 11.2.2 together with an emittance diagram. The ions are extracted and accelerated up to 100 keV by the potential applied to the first and the second electrodes. A negative potential of 5 kV is applied to the third electrode to repel backstream electrons from the beam plasma downstream. The two-stage extraction system is adopted to obtain a highly convergent ion beam by electrostatic lens effect in the second electrode. The calculated beam emittance is as low as 0.15 mm.mrad (90%), although thermal velocity of the produced ions is not taken into account in the present calculation.

The hydrogen ion beam contains not only  $H^+$  ions (protons) but also molecular ions such as  $H_2^+$  and  $H_3^+$ . Higher proton yield is preferable for the accelerator application. To enhance the proton yield, the ion confinement in the plasma chamber is improved by a strong magnetic field and a large plasma volume so that the produced molecular ions are confined for enough time to dissociate to the protons. We expect the proton yield of 90% in the present design.

Although the source plasma is produced by arc discharge in a conven-

---

\* Nissin Electric Co. Ltd.

tional multicusp ion source, plasma production by RF is desirable for making the life time longer. For this purpose, we have tried to generate the source plasma by 2.45 GHz microwave<sup>2)</sup>. The microwave was injected in a multicusp plasma chamber, whose dimensions are 200 mm in inner diameter and 270 mm in length. By injecting 2 kW microwave, a hydrogen plasma of a density of  $1.6 \times 10^{11} \text{ cm}^{-3}$  was produced at a pressure of 0.1 Pa. This density is more than twice that of the cutoff condition for the 2.45 GHz microwave, indicating that there is a possibility to produce high density plasma in a field free region of the multicusp plasma chamber. Spatial profiles of the ion saturation current and the plasma parameters were uniform over the central region of 120 mm in diameter.

#### References

- 1) Okumura Y.: Proc. 2nd International Symp. on Advanced Nuclear Energy Research, Jan. 24-26, 1990, Mito, 441 (1990).
- 2) Tanaka H., Hasegawa K., Okumura Y. and Yokohori H.: Proc. 14th Symp. on Ion Sources and Ion-Assisted Technology, June 3-5, 1991, Tokyo, 35 (1991).

Table 11.2.1 Basic specifications of the ion source

Energy	100 keV
Current	120 mA
Duty Factor	CW
Emittance	0.5 $\pi$ mm.mrad (100% normalized)
Proton Ratio	> 90 %
Impurity	< 1 %
Current Density	240 mA/cm <sup>2</sup>
Extraction Aperture	8 mm in diameter

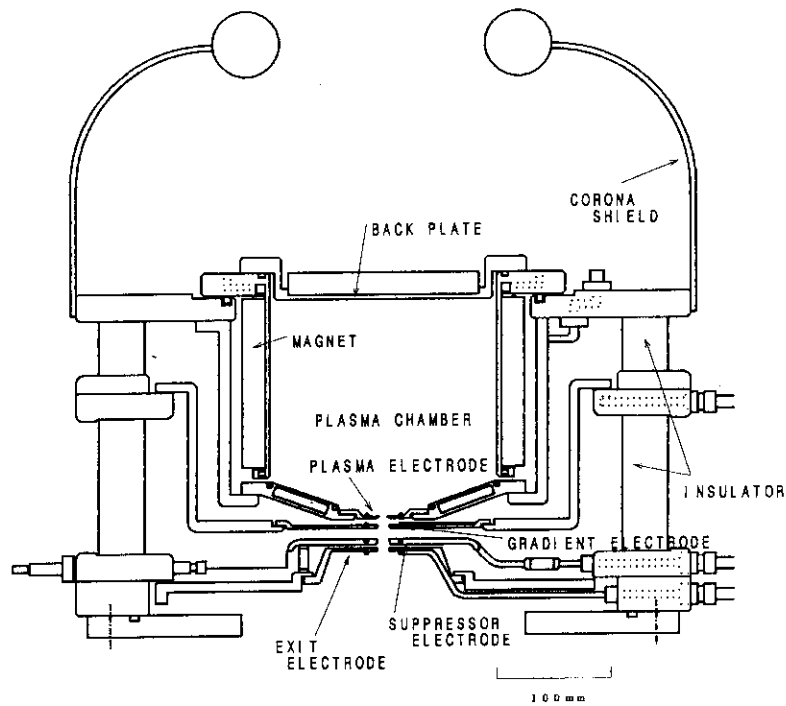
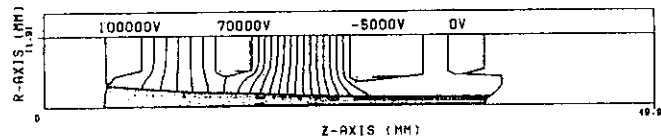


Fig. 11.2.1 A conceptual design of the BTA multicusp ion source

\*KASOKUKI-YOU I.S. VRCC=100KV GRM=0.7 H+ 240.0MA/CM2 (AA01)

CURRENT DENSITY	=	2.4000E+02 (MA/CM2)
TOTAL CURRENT	=	9.7886E-02 (A)
PERVEANCE	=	3.0954E-09 (A/V**1.5)
MINIMUM POTENTIAL	=	-2.4557E+03 (V) AT Z = 3.0034E-02 (M)
DIVERGENCE (RMS)	=	3.0405E-01 (DEG)
ELECTRON TEMPERATURE	=	0.0 (EV)
ION TEMPERATURE	=	0.0 (EV)



EMITTANCE DIAGRAM

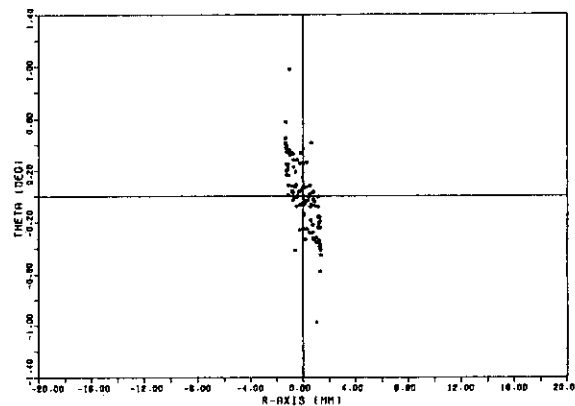


Fig. 11.2.2 An example of the ion trajectory in two-stage extraction system, where the beam energy is 100 keV and the current is 120 mA. Emittance diagram at the exit of the source is also shown.

### 11.3 Design Study on a Radio Frequency Quadrupole for the Basic Technology Accelerator

K. Hasegawa, M. Mizumoto, H. Yokobori, H. Mino and Y. Kaneko

A radio frequency quadrupole (RFQ) linear accelerator is one of the important structures for the low velocity intense proton accelerator. This structure can accept a DC beam, bunch it with high capture efficiency, and accelerate it to a velocity suitable for injection into a drift tube linac (DTL). The design study on the RFQ for the Basic Technology Accelerator (BTA)<sup>1)</sup> has been carried out.

Table 11.3.1 shows the parameters of the RFQ for the BTA. An operating frequency is 201.25 MHz and the RFQ resonator is a four-vane type. Proton beam from the ion source with an energy of 0.1 MeV is accepted and accelerated up to 2 MeV. Average output beam current is 10 mA and duty factor is 10%. The peak surface electric field of 26.5 MV/m (1.8 times Kilpatrick breakdown field<sup>2)</sup>) is chosen, which corresponds to the intervane voltage of 0.113 MV.

For the design of the RFQ, several computer codes are used such as CURLI, RFQUIK, PARMTEQ and SUPERFISH. The undesired effects of the space-charge forces cause degradation of the emittance of the beam. These effects usually occur at the low-velocity end of the linac, where beam is bunched and the focusing is weakest<sup>3)</sup>. The CURLI code was used to calculate the current limit of this section in the RFQ. The beam current of 200 mA was chosen for the design calculation, because the necessary peak current is 100 mA with the safety factor of 2. If the ion species, the initial and final energies, the frequency and the intervane voltage are specified, the RFQ design is determined by the RFQUIK<sup>4)</sup> which gives the three independent values  $a(z)$ ,  $m(z)$  and  $\phi(z)$ , where  $z$  is the axial distance along the accelerator, radius parameter  $a$ , radius modulation parameter  $m$  and synchronous phase  $\phi$ , respectively. The obtained RFQ parameters as a function of cell length are shown in Fig.

11.3.1. The output emittance and transmission efficiency are predicted from the PARMTEQ (Phase And Radial Motion in Transverse Electric Quadrupoles), which simulates the performance of the RFQ including the space-charge effects. Iterative design procedure from RFQUIK to PARMTEQ was taken to obtain the satisfactory results of the output emittance and transmission efficiency.

The SUPERFISH was used to calculate the resonant frequencies in the RF cavity. Using the post processor of the SUPERFISH, various results related to the electromagnetic field are obtained such as a quality factor (Q) of the RF cavity, lines of electric force, field strength and RF wall loss power as can be seen in Fig. 11.3.2. The frequency shifts of the cavity due to the alignment or fabrication errors and due to the thermal displacement under the operation were also estimated by the SUPERFISH.

Since the average beam current of 10 mA is relatively high in comparison with other existing accelerators, heat removal problem is an important issue for the mechanical structure design of the RFQ. Temperature distributions and thermal stresses of the vane and RF cavity are also studied by the 3 dimensional heat calculation code of NASTRAN.

#### References

- 1) Mizumoto M., et al.: "A Progress in the High Intensity Proton Linear Accelerator Development", Reactor Engineering Department Annual Report 11-1 (1991).
- 2) Kilpatrick W.D.: Rev. Sci. Instr. 28 p.824 (1957).
- 3) Wangler T.P.: "Brightness Limits in Linear Ion Accelerators", LA-UR-86-3491 (1986).
- 4) Crandall K.R., Stokes R.H. and Wangler T.P.: "RF Quadrupole Beam Dynamics Design Studies", Proc. of Linear Accelerator Conference 1979, p.205 (1979).

Table 11.3.1 Parameters of the RFQ for the BTA

Frequency	201.25 MHz	Transmission	95 %
Energy	0.1 ~ 2 MeV		
Beam Current	110 mA	Cavity Diameter	35.1 cm
Duty Factor	10 %	Quality Factor (Q)	~13000
Vane Voltage	0.113 MV ( $1.8E_k$ )	Wall Loss Power	462 kW
Synchronous Phase	-90° ~ -35°	Beam Power	209 kW
Vane Length	333.7 cm		
Number of Cell	180		

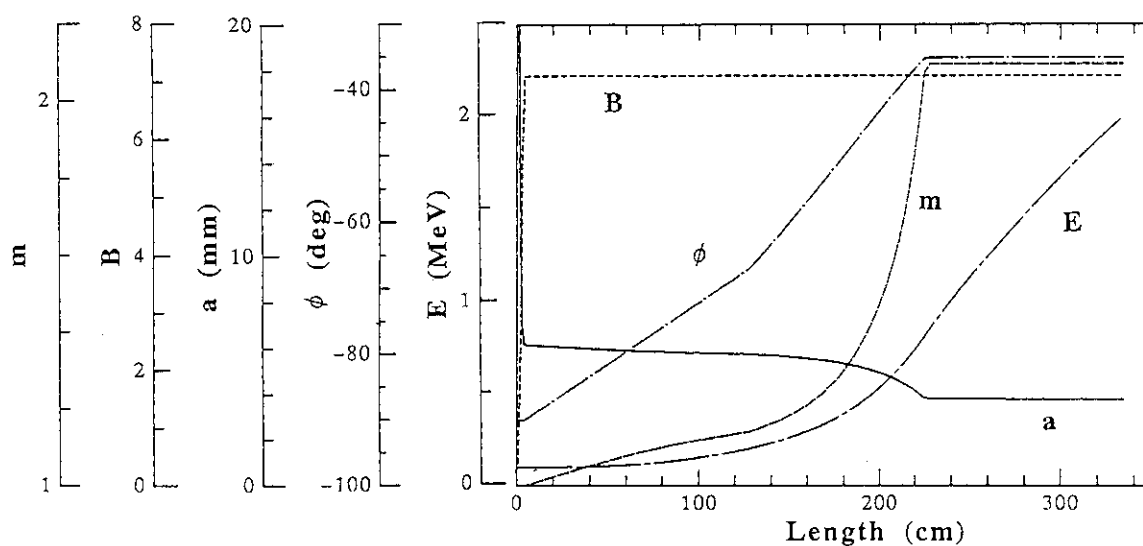


Fig. 11.3.1 Design parameters of the RFQ  
 $\phi$ : Synchronous phase     $m$ : Modulation Factor  
 $E$ : Proton Energy         $B$ : Focusing Force Factor  
 $a$ : Bore Radius

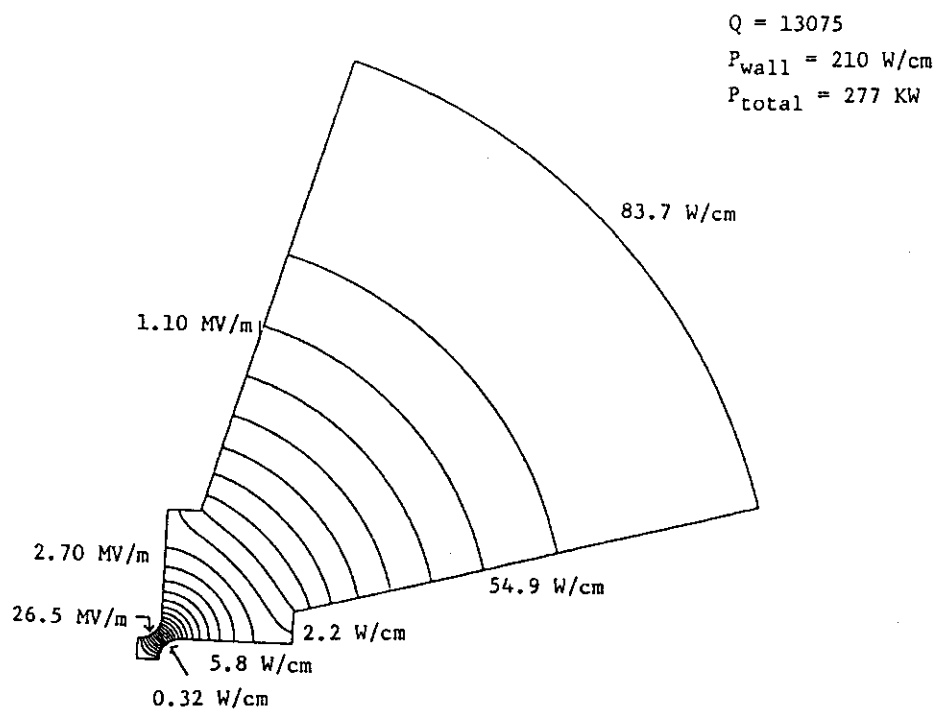


Fig. 11.3.2 Calculated results of the SUPERFISH  
 Strength of the electric field and  
 the power dissipations are indicated.



## 11.4 Study on a Drift Tube Linac of the Basic Technology Accelerator

H. Yokobori, M. Mizumoto, K. Hasegawa, H. Mino and Y. Kaneko

A drift tube linac (DTL) for the Basic Technology Accelerator (BTA) has been designed to meet the basic specification of the BTA<sup>1)</sup>. In this design study, extensive analyses were executed in order to optimize the beam optics and the mechanical structure of the DTL.

Through the beam optical analyses, the fundamental design parameters such as average electric field ( $E_0$ ), synchronous phase ( $\phi_s$ ), transverse phase advance induced by quadrupole magnetic focusing force ( $\mu$ ) have been optimized so that transverse emittance at the exit of the DTL should be minimized. As a result of the study using the beam simulation code, PARMILA<sup>2)</sup>, the following parameters are selected for the DTL:  $E_0 = 2$  MV/m,  $\phi_s = -30$  deg.,  $\mu = 90$  deg. The beam profiles are plotted in Fig. 11.4.1, and the design parameters for the DTL are shown in Table 11.4.1.

Based on the above fundamental structure of the DTL, some engineering studies for a heat removal system, a vacuum system, and an RF power supply system were performed. Heat dissipation in the structure wall was evaluated by electromagnetic field analysis code, SUPERFISH<sup>2)</sup>. Besides the RF power source, there are other heat sources caused by the Joule and eddy current in an electric quadrupole-magnet in the drift tube. The heat density is the most severe in the first cell of the DTL, because the strongest magnetic field gradient is necessary to focus the lowest energy beam. Therefore cooling of the first drift tube is the most difficult. The temperature distribution in the drift tube of the first cell caused by the above heat generation sources has been preliminary analyzed using a thermal conductivity and a stress/strain analysis code. Since the maximum temperature in the drift tube is estimated to be comparable to the upper limit for an epoxy-insulator, a further study should be continued to reduce the heat generation in the quadrupole magnet, and/or to improve the heat removal system of a drift tube.

As a vacuum of the order  $1 \times 10^{-7}$  Torr will be necessary at full power operation of the DTL, the following vacuum system consisting of three sub-systems is designed. Taking into account the gaseous production from the wall of the DTL's structure and incoming flow from the RFQ linac, the capacity of the pumps was roughly estimated. A vacuum of  $3 \times 10^{-7}$  Torr will be attained using a thousand liter per minute for a rotary

pump as an initial vacuum sub-system, 300 liter per second for a turbo molecular pump as an intermediate vacuum sub-system, and 4000 liter per second for a cryogenic pump as a main vacuum sub-system.

It is planned to supply RF power into a DTL tank through a co-axial LC input coupler. Because experiences in high duty and high power RF supply system are not enough, many R&D efforts with high RF power will be required in order to select an adequate material for the window of the input coupler, to suppress an electric discharge, and to remove a heat from the input coupler.

Since dimensional uncertainties by manufacturing and installation of the DTL are empirically estimated to be within several tens of micron, it has been assured by PARMILA simulation that the misalignment caused by these errors does not seriously affect to the beam optics.

It has been concluded that the fundamental structure of the DTL for the BTA is determined, however the followings are remained to be resolved by succeeding R&D:

1. to suppress a heat generation in the quadrupole magnet, and improve the heat removal system of it.
2. to improve the configuration of the input coupler through the high duty and high power RF test.

#### References

- 1) Mizumoto M., et al.: Reactor Engineering Department Annual Report (April 1, 1990 - March 31, 1991) (1991).
- 2) Los Alamos Accelerator Code Group: Computer Code for Particles Accelerator Design and Analysis, LA-UR-90-1766 (1990).

Table 11.4.1 Design parameters for the DTL

RF Frequency	201.25	MHz
Inlet/Outlet Energy	2.0-10.0	MeV
Beam Current	100	mA
Duty Factor	10	%
Average Axial Field	2.0	MV/m
Diameter of Tank	93.2	cm
Length of Tank	580.5	cm
Number of Cell	37	
Gap to Cell Length Ratio	0.235-0.302	
Inner/Outer Diameter of Drift Tube	2.5/18.0	cm
Synchronous Phase	-30	degree
Focusing Magnetic Field	81-31	T/m
Wall Loss Power (60%Q)	640	kW
Beam Power	800	kW

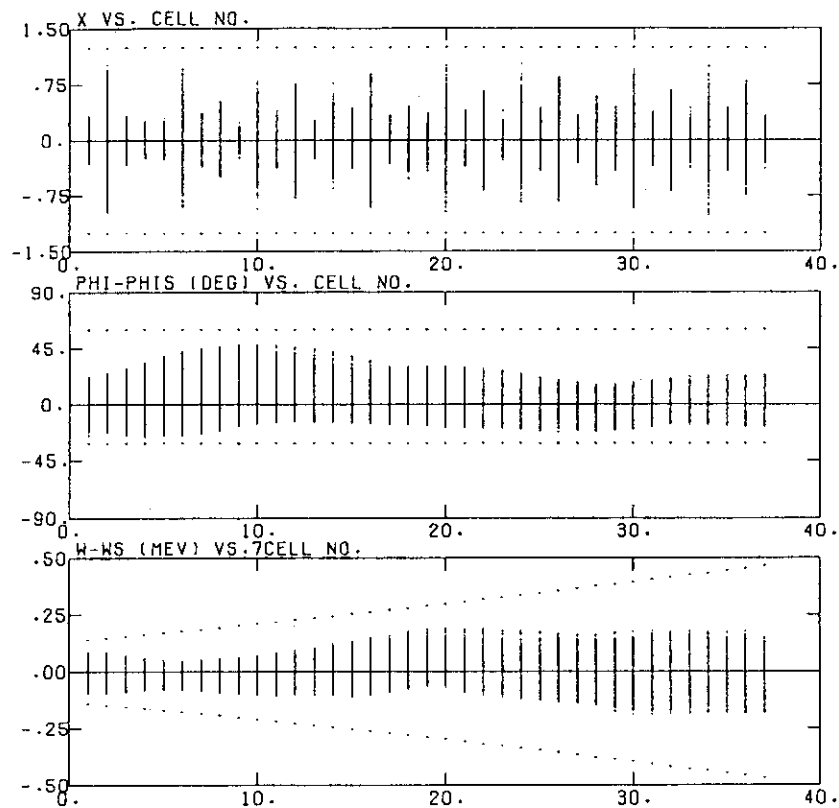


Fig. 11.4.1 Beam profiles in the DTL

## 11.5 Analysis of Time Evolution Process of Spallation Products

T. Nishida, Y. Nakahara, H. Takada, I. Kanno, H. Kadotani\* and  
T. Ishizuka\*

The basic researches about the spallation process of heavy nuclides such as actinides have been performed for developing the accelerator TRU transmutation system as a part of the OMEGA project. The SPCHAIN code system is being developed at JAERI to analyze the time evolution behavior of spallation products during irradiation and cooling times<sup>1)</sup>. The differential equations for the time evolution process of reaction products were formulated by adding the spallation reaction terms to the burnup equation of reactor fuel as in the following.

$$\begin{aligned} dN_i/dt = & \gamma_i F(t) + \beta_i G(t) + \sum_j f_{j,i} \lambda_j N_j + \sum_k g_{k,i} \sigma_k \phi_n N_k \\ & + \sum_l \alpha_{l,i} \sigma_l^s \phi_N N_l - (\lambda_i + \sigma_i \phi_n + \sigma_i^s \phi_N) N_i \end{aligned}$$

where the nuclide  $i = (A, Z)$ , the nuclide  $j = (A', Z')$  with mass number  $A$  and atomic number  $Z$  and,

- $N_i$  : concentration of  $i$  at time  $t$ ,
- $f_{j,i}$  : ratio for the production of  $i$  by the decay of  $j$ ,
- $g_{j,i}$  : ratio for the production of  $i$  by the neutron absorption of  $j$ ,
- $\lambda_i$  : decay constant of  $i$ ,
- $\alpha_{j,i}$  : production rate of  $i$  due to the spallation of  $j$ ,
- $\sigma_i^s$  : spallation cross section of the nuclide  $i$ ,
- $\sigma_i$  : neutron absorption cross section of the nuclide  $i$ ,
- $G(t)$  : number of spallation reactions (1/sec),
- $F(t)$  : number of fission reactions (1/sec),
- $\beta_i$  : production rate of  $i$  due to the spallation of a target nuclide,
- $\gamma_i$  : production rate of  $i$  due to fission of target nuclide,
- $\phi_n$  : neutron flux (neutrons/(cm<sup>2</sup> sec)),
- $\phi_N$  : high energy nucleon flux (nucleons/(cm<sup>2</sup> sec)).

The first version of the SPCHAIN code was programmed by expanding the one point depletion code DCHAIN2<sup>2)</sup> based on the Bateman method. Main modifications were carried out by rewriting the Bateman formula and making the interpolation routines of  $\alpha$ - and  $\sigma^s$ - tables. Figure 11.5.1 shows the code group for calculating some parameters needed for the SPCHAIN run. The spallation yields  $\alpha$  were computed using the spallation reaction code NUCLEUS<sup>3)</sup> for energies and nuclides as summarized in Table 11.5.1

\* CRC

and stored in the SPCHAIN data file. The table of inelastic scattering cross sections in the energy range of ~400 MeV to ~1800 MeV and for 12 elements with the atomic number of 4 to 92 given by Schimmering<sup>4)</sup> was used as the spallation cross section  $\sigma^S$ . When the half life time of a nuclide was unknown, it was calculated by using the  $\beta$  decay code SPD<sup>5)</sup> or guessed from data in Table of Isotope. The average fluxes  $\phi_N$  and  $\phi_n$  over the target can be computed using the spallation reaction-nucleon meson transport code NMTC/JAERI<sup>6)</sup>, and the neutron transport code MORSE-DD or ACCEL connected to NMTC/JAERI, respectively.

The yields and activities of spallation products (SP) in a  $^{244}\text{Cm}$  target irradiated by protons with the energies of 0.8, 1.0 and 1.5 GeV were calculated. Figure 11.5.2(a) and (b) show the activity rate distributions for SP elements accumulated in the target at the different times after one hour irradiation. As seen in the figure, just after irradiation, there are large overlapping peaks of activity at  $Z = \sim 80$  and  $\sim 90$  and the total activity of produced elements with the atomic number smaller than 70 is low. When most of activities in the overlapping zone have been lost after one year cooling due to their short half lives, two peaks are clearly separated. Then main residual nuclides around the smaller peak are  $^{194}\text{Au}$ ,  $^{185}\text{Os}$ ,  $^{181}\text{W}$  and  $^{172}\text{Lu}$  with half lifetimes shorter than ~3 year but actinides with relatively long half lifetimes are produced in the large peak. Table 11.5.2 summarizes the relative amounts of residual  $^{244}\text{Cm}$  and produced FPs, and the total relative activity of SP for three irradiation times, where the activity of SP was normalized to  $^{244}\text{Cm}$ 's one before the irradiation. While the target nuclides are remarkably reduced as the irradiation time increases, the total activity of SP has the increasing tendency mainly due to the buildup of actinides. In the second version of the SPCHAIN code the algorithm will be improved to take into account the continuous transmutation of buildup actinides through the multi-irradiation procedure.

#### References

- 1) Nishida T., et al.: JAERI-M 90-149, p.280 (1990).
- 2) Tasaka K.: JAERI-M 8727 (1980).
- 3) Nishida T., Nakahara Y. and Tsutsui T.: JAERI-M 86-116 (1986).
- 4) Schimmering W.: Physical Review C, 248 (1973).
- 5) Yoshida T.: JAERI-M 6313 (1975).
- 6) Nakahara Y. and Tsutsui T.: JAERI-M 82-198 (1982).

Table 11.5.1 Actinides and energies for which the yields of spallation product were calculated

Proton energy (GeV)	0.1, 0.2, 0.3, 0.5, 0.7, 0.9, 1.0, 1.1, 1.3, 1.5
Target actinides	U-235, -238 Np-237 Pu-238, -239, -240, -241 Am-241, -242 Cm-242, -244

Table 11.5.2 Dependences of amounts of  $^{244}\text{Cm}$  transmuted by 1 GeV protons and the relative activity of SP on the irradiation time at the time after one year cooling

	Irradiation Time			
	1 hour	1.0 hours	5.0 hours	
Target nuclides	0.861	0.223	0.0057	
Spallation Products (SP)	0.123	0.704	0.908	
Relative Activity of SP	0.15	4.02	5.52	

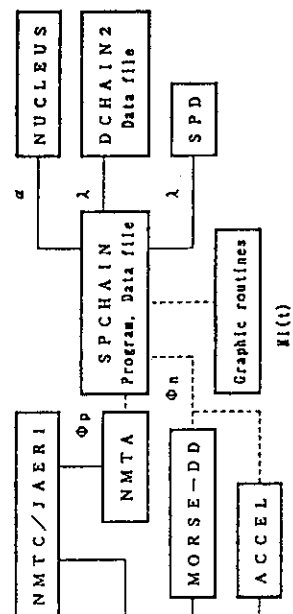


Fig. 11.5.1 Codes for calculating parameters used in SPCHAIN

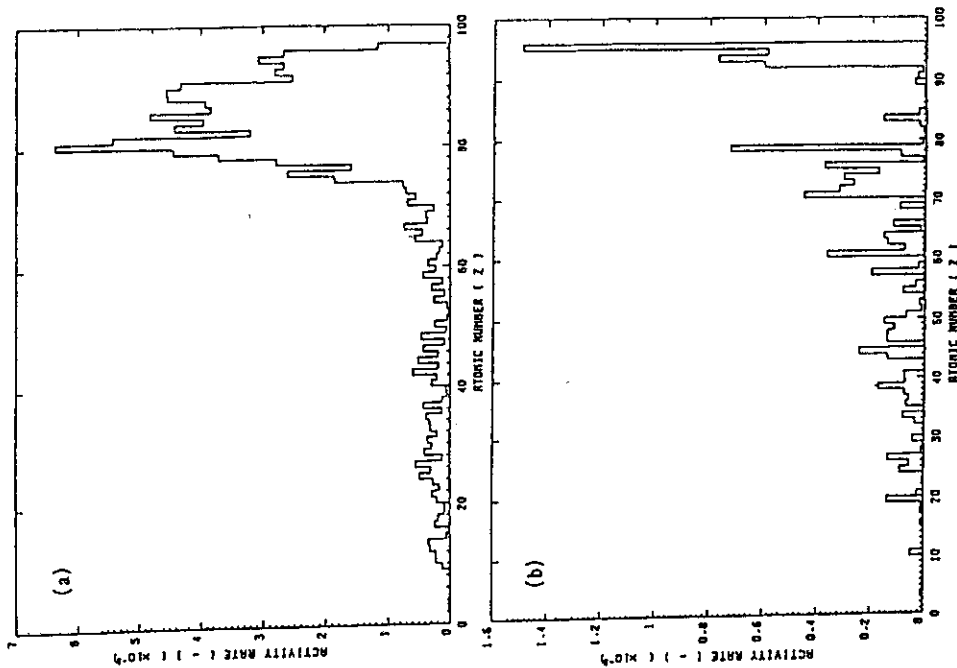


Fig. 11.5.2 Activity rate distribution for the SP element accumulation in a  $^{244}\text{Cm}$  target irradiated by 1 GeV protons (a) at the time just after one hour irradiation and (b) at the time after one hour irradiation and one year cooling

## 11.6 Conceptual Design Study on the TRU Incineration System Driven by a Proton Accelerator -- The Metal Fuelled Core --

H. Takada, T. Takizuka, I. Kanno, T. Nishida, M. Akabori,  
Y. Nakahara and Y. Kaneko

In order to achieve the transmutation rate higher than the one in the accelerator transmutation system already reported<sup>1),2)</sup>, we examined the technical feasibility of the most advantageous case (Na cooling, with a tungsten target) as an engineering facility. The direction of proton beam hitting the target in the core has been changed from the transverse direction to the vertical downward one. This means that we can utilize the information and technologies obtained in the development of the "MONJU" class fast reactor but that the large magnet system for bending the proton beam has to be newly equipped.

As shown in Fig. 11.6.1, the core consists of two regions; the tungsten target and the TRU fuel region. The target, which has a form nearly equal to a right circular cylinder, is installed at the center of the core and surrounded by the annular TRU fuel regions. The core is also surrounded by radial and axial reflectors of stainless steel. The beam window locates at the top of the target. The tungsten target acts as the spallation neutron source. The core design parameters are summarized in Table 11.6.1. Figure 11.6.2 shows the axial distribution of high energy neutrons and incident protons. A small fraction, about 0.3%, of the incident protons penetrate targets and reach the bottom reflector, still having the average energy of 70 MeV. The average neutron spectrum in the core is shown in Fig. 11.6.3. The neutron spectrum is much harder than that in LMFBR. Figure 11.6.4 shows the calculated power density distribution over the core and the target, where the maximum power densities are about 920 MW/m<sup>3</sup> and 360 MW/m<sup>3</sup>, respectively. Thermal hydraulics calculations have been performed to confirm that the fuel and cladding temperatures are below their limits. Figure 6.11.5 represents the temperature distribution along the fuel pin in the hot channel. The sodium temperature at the exit of hot channel is 473°C. The maximum temperature of the cladding is 528°C and well below its design limit. The maximum fuel center line temperature is 890°C. As this value is very close to the design limit, much more accurate thermal property data of the TRU fuel are required to confirm the design. The performance of the core is

summarized in Table 11.6.2. The subcritical performance was examined under the conditions that the maximum temperature should be below 900°C for the fuel meat and 650°C for the clad, respectively. The core with the effective multiplication factor of about 0.9 generates the thermal power of 820 MW within these temperature limits when it is driven by the 1.5 GeV, 39 mA proton accelerator. The present system can transmute about 250 kg of TRU annually, which corresponds to the TRU production in about ten units of 3000-MWt LWR. The plant generates electricity of 246 MW with a conventional steam turbine and supplies sufficient electricity to power the accelerator. As seen in Fig. 11.6.6, the  $k_{eff}$  of the core increases gradually with burn-up. In order to achieve the high performance by suppressing the increase of  $k_{eff}$ , there remain some possibilities for a further design optimization.

#### References

- 1) Takizuka T., et al.: "A Study of Incineration Target System", Proc. 5th Int. Conf. Emerging Nucl. Systems (Karlsruhe, 1989).
- 2) Takada H., et al.: Reactor Eng. Dep. Annal. Report, 238, JAERI-M 90-149 (1990).

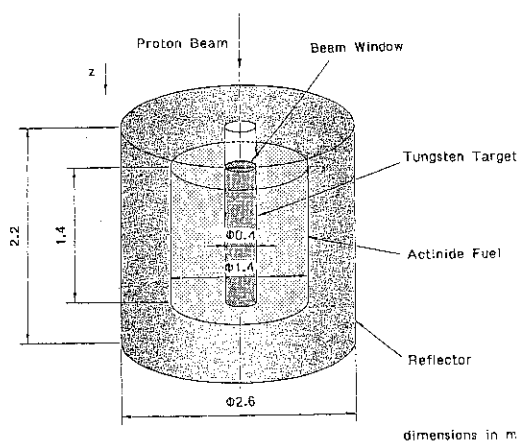


Fig. 11.6.1 Core configuration

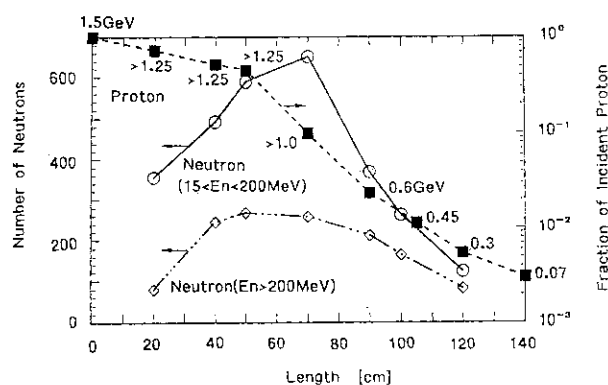


Fig. 11.6.2 Particle flux distributions above 15 MeV in the axis direction

Table 11.6.1 Core design parameters

Items	Specifications
Proton Energy	1.5 GeV
Beam Diameter	40 cm
Core	
Diameter	140 cm
Length	140 cm
Tungsten Target	
Diameter	40 cm
Length	140 cm
Reflector	
Composition	Stainless Steel
Thickness	40/60 cm
Coolant	Na



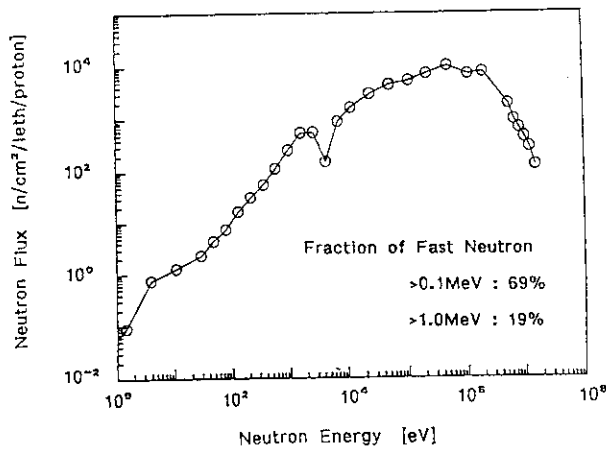


Fig. 11.6.3 Average neutron spectrum in the core. The fraction of fast neutrons is given.

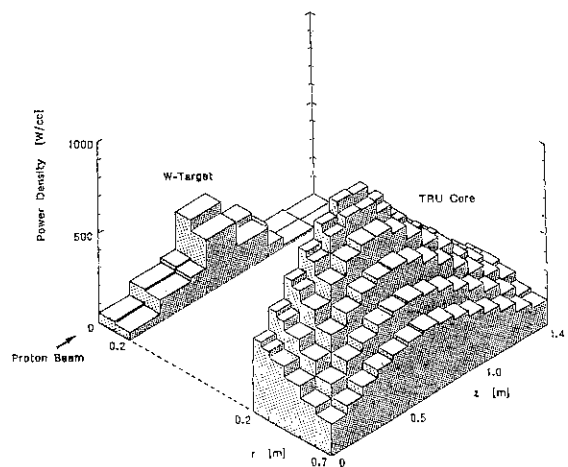


Fig. 11.6.4 Power distribution

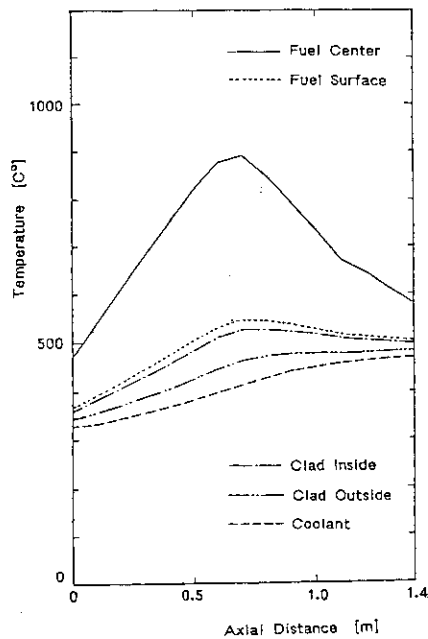


Fig. 11.6.5 Temperature distribution in the fuel pin installed in the hot channel

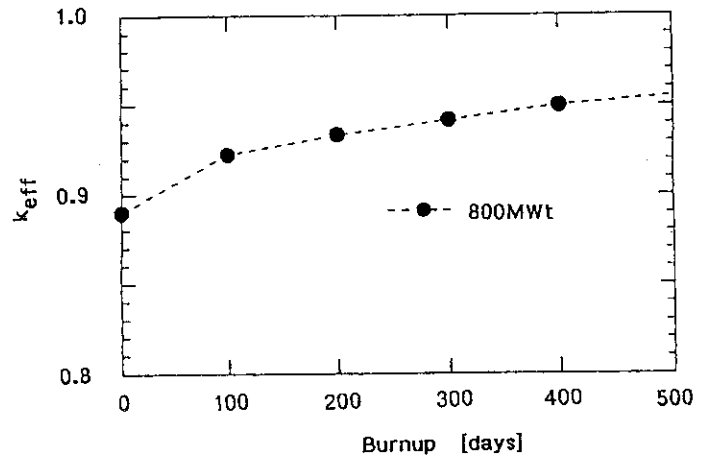


Fig. 11.6.6 Variation of  $k_{eff}$  with burnup

Table 11.6.2 Performance of the core

Items	Performances
Actinide Loading	3160 kg
Initial $k_{eff}$	0.89
Beam Current (max)	39 mA
Neutron Flux	$4.0 \times 10^{15}$ n/cm <sup>2</sup> /sec
(>0.1 MeV)	69%
Number of Neutron	40 neutrons/proton
Number of Fission(>15 MeV)	0.45 fissions/proton
(<15 MeV)	100 fissions/proton
Thermal Power	800 MWt
Power Density (max)	920 W/cc
(ave)	400 W/cc
Linear Power Rating (max.)	60 kW/m
Operating Rate (per year)	300 days (80%)
Burnup Weight	250 kg

# 11.7 Conceptual Design Study on the TRU Incineration System Driven by a Proton Accelerator -- The Molten Salt Core --

H. Takada, T. Takizuka, I. Kanno, T. Nishida, Y. Kato, K. Katsuta, M. Takano, Y. Nakahara and Y. Kaneko

As the another promising option of accelerator transmutation systems we started the conceptual design study on the transmutation system of a TRU molten salt core driven by a proton linac. This may be expected as an advantageous system to transmute continuously long-lived waste nuclides such as TRU, Tc and I, as described in Fig. 11.7.1, if it can achieve the reasonable transmutation rate in the fuel cycle.

Some reports<sup>1),2)</sup> about the accelerator-molten salt core hybrid system are mainly on the thermal core of thorium fuel for breeding fissile materials as well as the power generation. In the present study the TRU molten salt core with the hard neutron spectrum has been selected to increase the transmutation rate due to fast fissions induced by protons from an intense accelerator. The graphite reflector, which is currently used for the thermalization of neutrons in the breeder core, has been removed from this system. The solubilities of minor actinides (MA) are estimated from the data for plutonium and lanthanides, since there are few measured data for MA. It has been found that the fluoride molten salt such as  $\text{LiF-BeF}_2\text{-ThF}_4$  and  $\text{LiF-NaF}_2\text{-ThF}_4$ , which are currently proposed as the most excellent and stable molten salt but make the neutron spectrum soft, has less solubility for the TRU with three valences than the chloride one. Therefore we have examined the TRU chloride molten salt fuels, such as  $\text{NaCl-TRUCl}_3$  (64-36 mol%) and  $\text{PbCl}_2\text{-TRUCl}_3$  (60-40 mol%), for the molten salt core in the transmutation system. By our rough estimation it has been known that the chlorine reduction in the reaction with high energy particles may be neglected during the current cycle time of the system. The recent reports also inform us that the corrosion of structure materials due to chlorides can be suppressed by completely rejecting the oxide impurities except the case of  $\text{PbCl}_2$ . The Hastelloy N is considered to be the best structural material in the temperature range of 500°C to 600°C in coexistence with the chloride molten salt. However it is desirable that the maximum allowable temperature of structure materials is above 800°C from the view point of high transmutation rate and the new excellent structural material is expected.

The spallation reaction and the particle transport process occurring in the target molten salt above 15 MeV were calculated by the NMTC/JAERI code<sup>3)</sup>. The spallation neutrons slowed down below 15 MeV are treated as a fixed source in the successive neutron transport calculation using Sn codes ANISN and TWOTRAN-II. Figure 11.7.2 illustrates the concept of the molten salt transmutation system having eight compact inter heat exchangers. The core composed of NaCl-TRUCl<sub>3</sub> has dimensions of 170 cm in height and 105 cm in radius, and is surrounded by the stainless steel reflector with the thickness of 20 ~ 40 cm. The inner reflector made of Hastelloy N protects the heat exchanger from the strong irradiation due to the intense neutron flux generated in the central region of the core. Total TRU inventory at the initial stage is about 5.4 ton. This type of the system is expected to be able to reduce considerably the amount of TRU in the core. From the preliminary neutronics calculational results the proton beam with the energy of 1.5 GeV and the current of 1 mA produces ~40 spallation neutrons per incident proton in the target region and some protons with energy of ~500 MeV penetrate into the neighborhood of the bottom. The hard neutron spectrum is formed over the core, which produces the thermal power of ~11 MWt with  $k_{eff}$  of ~0.76 and the average power density of ~13 W/cc. From the result the system with the high beam power of 1.5 GeV and 100 mA can transmute about 260 kg TRU wastes per year, produced from ten units of 1 GWe LWR.

Further investigations should be carried out in more detail to achieve the high transmutation rate efficiently with the smaller beam current ~20 mA and the larger effective multiplication factor ~0.9 than ones in the present system by adjusting the geometry and the composition of molten salt core. In the next research plan the examination will be made of the process to remove continuously the fission products built up in the core due to burnup and the transmutation of long-lived FP such as <sup>99</sup>Tc and <sup>129</sup>I in this type of core.

#### References

- 1) Mynatt F.R.: ORNL/TM-5750 (1977).
- 2) Furukawa K., Lecocq A., Kato Y. and Mitachi K.: J. Nucl. Sci. Tech. Vol. 27, No. 12, p.1157 (1990).
- 3) Nakahara Y. and Tsutsui T.: JAERI-M 82-198 (1982).

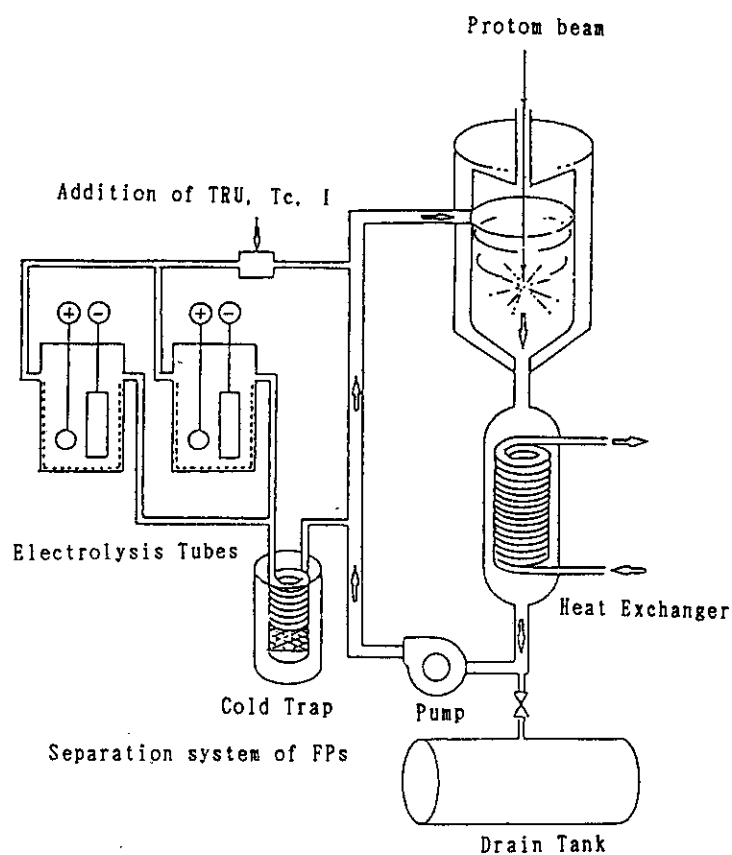


Fig. 11.7.1 Continuously processing transmutation system

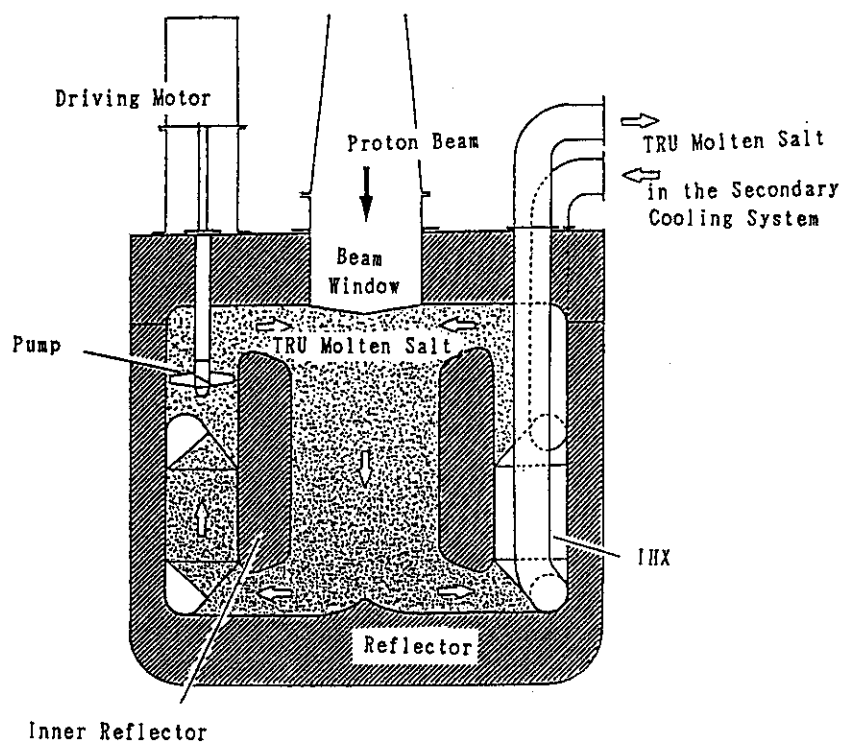


Fig. 11.7.2 Transmutation system of TRU molten salt core

## 11.8 Integral Experiment on a Lead Bulk System Bombarded with High Energy Protons

H. Takada, I. Kanno, K. Hasegawa, M. Mizumoto, T. Yamane,  
H. Yasuda, M. Takeuchi, T. Ono, M. Seki and Y. Kaneko

Transmutation of long-lived transuranic nuclides using the proton induced spallation reaction is a main theme in the OMEGA project promoted by Science and Technology Agency of Japan. From the view point of the reactor design and the radiation shielding for such a transmutation system, it is very important to know the transport process of the spallation neutrons in a thick medium.

We have performed an integral experiment with a lead bulk target to investigate the transport process of the particles produced by the spallation reaction. The experiment was performed in the beam dump room of the 500 MeV booster proton synchrotron facility of National Laboratory for High Energy Physics. Figure 11.8.1 shows the cross sectional view of the target. Protons come into the target through a 16 cm diameter  $\times$  20 cm long beam entrance hole. In order to install the activation samples, 9 holes were made along the lead bulk axis at the positions of 0, 3, 6, 10, 15, 20 and 25 cm in the radial distance.

The following high purity natural metals were used as the activation samples: Al(99.999%), Fe(99.99%), Ni(99.9%), Cu(99.99%) and Au(99.999%). The samples have the cylindrical configuration of 6 mm in diameter and 10 mm in length. The number of induced reactions were obtained by measuring  $\gamma$ -rays which were emitted from the samples.

The irradiation was carried out for about 45 minutes with the current of 200 nA. After 30 hours cooling, the  $\gamma$ -ray measurement was performed with a 100 cc Ge-detector. The reaction rate  $Y_{jexp}$  was obtained for the radioactive nuclide  $j$  by the following relation:

$$Y_{jexp} = \frac{\lambda_j I_j}{P N \epsilon_j \eta \delta (1 - e^{-\lambda_j T_r}) e^{-\lambda_j T_c} (1 - e^{-\lambda_j T_m})}, \quad (11.8.1)$$

where  $\lambda_j$  is the decay constant,  $I_j$  the peak area,  $P$  the number of photons,  $N$  the number of atoms in the activation sample,  $\epsilon_j$  the peak efficiency of the Ge-detector,  $\eta$  the number of photons in decay,  $\delta$  the self-absorption for photons in the sample,  $T_r$  the irradiation time,  $T_c$  the cooling time and  $T_m$  the measuring time.

The major source of the error comes from the statistics of the peak area and the number of protons. The statistical error of the peak area is from <1 to 35%, which depends on the sort of the nuclides and the position of in the lead bulk. The accuracy of the proton current was as large as 10%.

A preliminary nucleon transport calculation was performed to compare the results with the experimental ones. The Monte Carlo code MMTC/JAERI<sup>1)</sup> was used to evaluate the nucleon flux above 15 MeV in the lead bulk. The reaction rate  $Y_{jcal}$  was evaluated as follows:

$$Y_{jcal} = \sum_i \int_{E_{th}}^{500} \sigma^i_j(E) \phi^i_j(E) dE, \quad (11.8.2)$$

where  $i$  stands for protons or neutrons,  $\sigma^i_j(E)$  is the activation cross section for the nuclides  $j$ ,  $\phi^i_j(E)$  the flux of the nucleon  $i$  and  $E_{th}$  the threshold energy. As for the activation cross sections, the experimental data<sup>2),3)</sup> were employed for proton induced reaction. For the neutron induced reactions, the calculated values by NMTC/JAERI were employed above 20 MeV because of the lack of experimental cross sections.

The spatial distribution of the reaction rate is shown in Fig. 11.8.2 for  $^{57}\text{Ni}$  produced in the Ni samples. Since the protons were injected at 20 cm on the axis, the reaction rate shows peaks there and decreases exponentially along the beam line. Considering that the threshold energy for  $^{58}\text{Ni}(n,2n)^{57}\text{Ni}$  is about 12.4 MeV, the high energy neutrons seem to be transported to the surface of the lead bulk.

In Fig. 11.8.3, calculated results are compared with the experimental ones for  $^{56}\text{Ni}$  produced in the Ni samples. The calculated results were connected with the lines for eyeguide. On the axis, the calculated results agree well with the experimental ones at the depth between 25 cm and 40 cm. However, the calculated results decrease rapidly as the depth increases. For the results at 3 and 10 cm from the axis, on the other hand, the degree of the discrepancy was smaller than that on the axis.

## References

- 1) Nakahara Y. and Tsutsui T.: JAERI-M 82-198 (1982) (in Japanese).
- 2) Michel R., Weigel H. and Herr W.: Z. Phys. A286, 393 (1973).
- 3) Michel R. and Stuck R.: J. Geophys. Res. 89, B673 (1984).

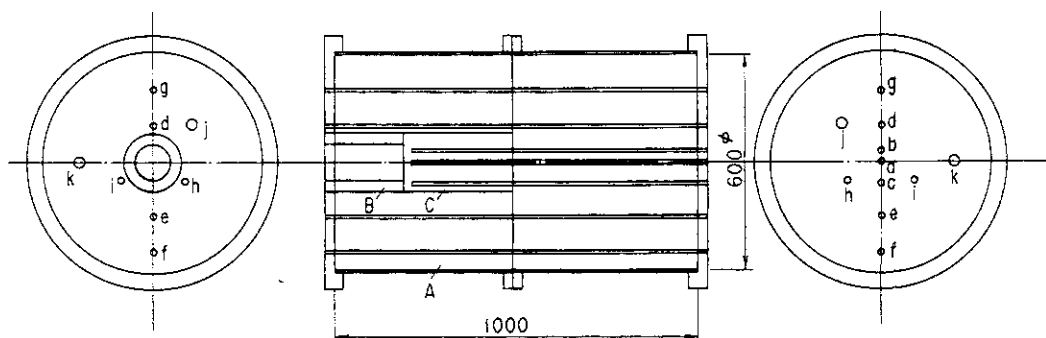


Fig. 11.8.1 Cross sectional view of the lead bulk. The small holes (a to i) indicate the places where activation samples are installed. The capitals A stands for lead bulk target, B the beam entrance hole, C the target region which can be replaced to another material.

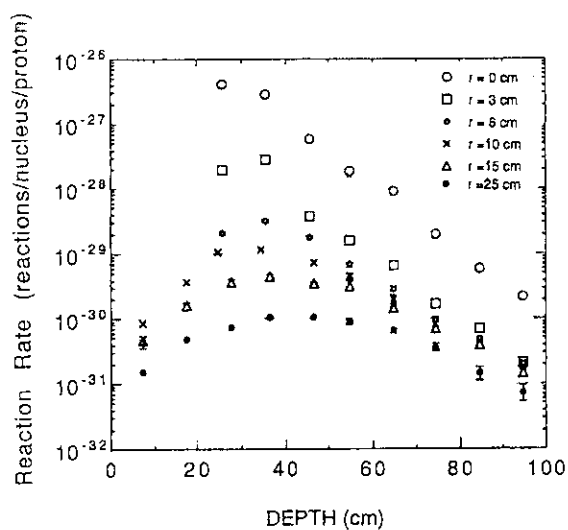


Fig. 11.8.2 Spatial distribution of the reaction rate for  $^{57}\text{Ni}$  produced in the Ni samples for the 500 MeV proton incident on the lead bulk target

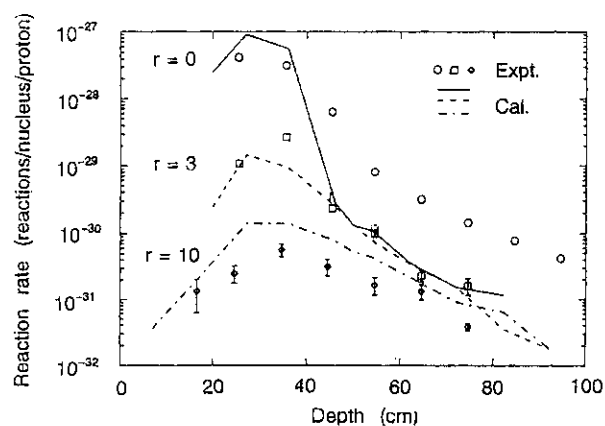


Fig. 11.8.3 Spatial distribution of the reaction rate for  $^{56}\text{Ni}$  produced in the Ni samples for the 500 MeV proton incident on the lead bulk target

## 12. Facility Operation and Technique Development

In FY-1990, operations of the Fast Critical Assembly (FCA), the Very High Temperature Reactor Critical assembly (VHTRC) and the Fusion Neutronics Source (FNS) were carried out without any major troubles disturbing the experiments. The FCA XVI-1 and XVI-2 cores were constructed to obtain benchmark data of the "Metallic Fuel FBR" core. Integral experiments were made on the VHTRC-4 and VHTRC-5 to verify the design accuracy of the HTTR. Including the Phase-IIIB experiments on the JAERI/US-DOE collaborative program, the fusion neutronics experiments were carried out at the FNS. The integrated operation time of 685 hours, 420 hours and 560 hours was recorded at the FCA, the VHTRC and the FNS, respectively.

To improve a reliability and safety of the facilities, feasibility test on nickel coatings of uranium metallic fuels at the FCA and the development of the newly neutron absorption rods at the VHTRC were carried out. Good performance results were obtained on both nickel coatings and neutron absorption. At the FNS, the development of Next Rotating Target assembly has progressed. In order to investigate the characteristics of 14 MeV neutron generation on the FNS Rotating Target, the diagnostic operations have been carried out at the FNS. A detail of the result of the examinations is described in section 5.9.

(Hideaki Watanabe)



## 12.1 Operation Report of FCA

K. Satoh, A. Ohno, K. Hayasaka, H. Sodeyama and H. Watanabe

The FCA XVI-1 and XVI-2 cores were assembled to obtain benchmark data on the "Metallic Fuel FBR" core. Operations have been performed as scheduled, without any major trouble.

Operations of 114 times were carried out in 105 days. No scram was recorded during the operations. The total operating time was 685 hours and the integrated power 5372.97 Wh. A total number of 4542 criticality operations has been recorded at the end of this fiscal year since the first achievement of criticality on 29 April 1967. Following to the safety regulation for operation, two days were devoted to the monthly inspection and about 7 weeks to the annual inspection from January to March in 1991 year. Routine maintenance activities were done in these days to provide maximum operation days for the experiments.

The maintenance activity was taken on the physical protection (P-P) system. The sensitivity and the function of the system were examined and calibrated.

In connection with safeguards, IAEA and NSB<sup>\*)</sup> carried out every month inspection under the international treaty. The Physical Inventory Taking (PIT) of the fuels was performed from June 18 to June 22 by means of item counting, weighing and non-destructive assay. IAEA and NSB made the Physical Inventory Verification (PIV) from June 25 to June 29. No anomaly was confirmed.

As for fuel management, examination of nickel coatings instead of the plastic coatings was carried out to solve contaminations caused by exfoliation of plastic coatings on uranium metallic fuels. Good compatibility of nickel coatings with metallic uranium plates was shown in a preliminary test carried out last year. In this year, 20 pieces of practical FCA uranium plates were coated with nickel coatings to test their feasibilities, the result shows sufficient strength and adhesion. The contamination could be solved by making all the FCA uranium plates with nickel coatings.

---

<sup>\*)</sup> NSB: Nuclear Safety Bureau

## 12.2 Operation Report of VHTRC

S. Fujisaki, M. Takeuchi, T. Ono, M. Seki and H. Watanabe

VHTRC-4 and VHTRC-5 cores were assembled to obtain experimental data for the verification of the HTTR design accuracy. The operations for this purpose were completed as scheduled without any problems disturbing execution of the experiment.

The experiment of water ingress simulation for the HTTR core was performed by using the various kinds of polyethylene which are like a urethane foam for the first time in July. The training experiment for the students of the nuclear engineering speciality of the university was performed for a week in August.

The results of the operation were as follows:

- 1) Operations of 248 times in 66 days,
- 2) Critical operations of 167 times,
- 3) Total operation time of 420 hours,
- 4) Integrated power of 109 WH.

No scram was recorded during the operations.

The integral operation time is 2,844 hours at the end of this fiscal year since the first achievement of criticality on May 13, 1985.

According to the safety regulation for operation, one day was devoted to the monthly inspection and about 8 weeks to the annual inspection from August to October.

The major activities relating to the maintenance were as follows;

- 1) Development of the newly neutron absorption rods for the control and safety rod drive mechanisms,
- 2) Installation of the automatic drive mechanism for the shield door into the fuel handling room in the reactor room.

By the installation of the automatic drive mechanism for the shield door, easiness operation and the improvement of safety were achieved.

As for fuel management, the book inventory was confirmed and Physical Inventory Taking (PIT) was carried out by item counting each fuel rod. IAEA and NSB made the Physical Inventory Verification (PIV) under the international treaty on May 9. No anomaly was confirmed. The maintenance activity was also taken on the physical protection (p-p) system. The sensitivity and function of the system were examined and calibrated.

### 12.3 Operation Report of FNS

J. Kusano, C. Kutsukake, S. Tanaka, Y. Abe and H. Watanabe

The Fusion Neutronics Source (FNS) marked tenth anniversary of operation period on FY-1990. The stable operation of FNS brought various Fusion Neutronics Experiments along the annual schedule. The integrated operation time was 560 hours for these experiments. As a regular maintenance work, a week-long inspection on the control circuit of the accelerator was carried out every four month. The manual drive mechanism of heavy shielding door at the 2nd target room was newly installed to prevent a trouble of personnel confinement by an accident of electric power failure. To improve a reliability of each beam line component, cooling water distribution instruments of the accelerator was replaced, and additional safety-interlock elements were installed.

According to a development of Next Rotating Target assembly of FNS, a test assembly of rotating vacuum seal by magnetic fluid seal mechanism achieved 300 hours of operation time on 1,100 rpm of rated value.

#### 0° beam line operation

Typical intensive beam operation of FNS realized the direct measurements of nuclear heating by 14 MeV neutron in a structural material of the fusion reactor. This operation contributes to one of the Phase-IIIB experiment on the JAERI/US-DOE collaborative program.

The diagnostic operations gave the characteristics of 14 MeV neutron generation on the FNS Rotating Target. The subject of the examination was a study to increase neutron generation as intensity 10 times maximum performance of current operation. A result of the examination, kind of the relation among beam intensity, neutron generation rate and tritium gas release rate, is shown in section 5.9.

#### 80° beam line operation

Seven week operation on the 80° beam line participated for the Phase-IIIB experiments on the JAERI/US-DOE collaborative program. During this operation period, the measurement of neutron spectrum was made using an NE-213 counter and using a small sized proton recoil counter under beam current of 10  $\mu$ A operation. The other operating activity aided to the proper experiments. There are cross-section measurements of second-

ary gamma-ray production, neutron spectroscopy in iron cylinder assembly, integral experiments on copper slab assembly and feasibility tests for detectors to measure d-D neutron. A diagnostic operation on the 80° beam line showed an energy effect of incident particle in d-T reaction for tritiated metal target. This operation made an investigation for an optimum thickness of tritide titanium layer, and the examination will be continued.

#### Tritium handling

The target exchange work for a water-cooled target, 370 GBq (10 Ci) of tritium, prepared to irradiation experiments frequently. To execute the d-D neutron experiments, deuteride metal target was mounted twice a year. The rotating target, 24 TBq (650 Ci) of tritium, on the 0° beam line was exchanged with a new one for a preparation work of the Phase-IIIIB experiments. The Tritium Adsorption Processor (TAP) system collected and processed the total amount of 1 TBq (27 Ci) tritium in the exhaust gas from the vacuum system of the accelerator.

The Isotope Distribution Office of Oak Ridge National Laboratory, United States, withdrew from the business of tritiated metal target since May 1990. The procurement program of tritiated metal target of FNS is looking for an alternative target supplier.

Ref. Outline of FNS; D-T 14 MeV neutron generator by particle acceleration

Accelerated Beam Energy; 350 keV nominal

Number of Beam Line; 2 ( 0° line and 80° line )

Number of Ion Source; 2 (Type 820A and Type 740A ; Duo-Plasmatron)

Maximum Beam Current; 20 mA at 0° Beam Line

3 mA at 80° Beam Line

Maximum Neutron Yield;  $7 \times 10^{12}$  n/s at 0° Beam Line

$4 \times 10^{11}$  n/s at 80° Beam Line

Pulse Neutron Performance ( on the 80° Beam Line )

Minimum Pulse Width; 2 nano second (FWHM)

Maximum Repetition Rate; 2 MHz

Maximum Peak Current; 80 mA

## 13. Activities of the Research Committee on Reactor Physics

Y. Kaneko, Y. Ishiguro, H. Maekawa and T. Suzuki

There were held two meetings of the Research Committee on Reactor Physics. The first one (the 57th meeting) was devoted to identify the future problems in the area of fusion reactor neutronics and also to prepare the 33rd meeting of the NEA Committee on Reactor Physics (NEACRP), which was held at Paris, France, 15-19 October, 1990. The following papers (one review paper and 17 technical papers) were presented in the NEACRP Meeting:

- L-322 : Reactor Physics Activities in Japan (October 1989 - September 1990) (Y. Kaneko and K. Shirakata)
- A-1066: Plutonium Generation Boiling Water Reactor Concept (R. Takeda et al.)
- A-1067: Utilization of MOX Fuel Assembly Containing Gd<sup>203</sup> in ATR (N. Kawata et al.)
- A-1068: Study on Enhanced Safety Core Characteristics of Nitride Fuel Core (Y. Ohkubo et al.)
- A-1069: Integral Experiments to Improve Tritium Breeding Ratio (A. Takahashi et al.)
- A-1070: Phase-IIIA Experiment of the JAERI/USDOE Collaborative Program on Fusion Neutronics (Y. Oyama et al.)
- A-1071: Benchmark Test of Be Nuclear Data in JENDL-3 Through Analyses of Time-of-Flight and Integral Experiments on Be Assemblies at FNS (H. Maekawa et al.)
- A-1072: Prediction Accuracies of Safety Related Core Design Parameters for FBR (K. Shirakata et al.)
- A-1073: Measurement of Void Reactivity Worth of HTTR Mockup Control Rod Hole in VHTRC-1 Core (F. Akino et al.)
- A-1074: Analysis of Temperature Effect of Reactivity for VHTRC and SHE with Nuclear Design Code System for High Temperature Engineering Test Reactor (HTTR) (I. Murata et al.)
- A-1075: Study of TRU Transmutation Plant with a Proton Accelerator (T. Nishida et al.)
- A-1076: TRU Transmutation in LMFBR(II) (M. Ishikawa et al.)
- A-1077: A Study of Regional Oscillation with TOSDYN-2 (Y. Takigawa et al.)

- A-1078: Examination of Nuclear Thermal Hydraulic Oscillation Modes in  
BWR Core (O. Yokomizo et al.)
- A-1079: Development of Non-Destructive Measuring Techniques for Trace  
Amount of Fissile and Fertile Materials in Drum-Sized Waste  
(H. Gotoh et al.)
- A-1080: International Comparison on Measuring Techniques of Tritium  
Production Rate for Fusion Neutronics Experiments  
(H. Maekawa et al.)
- A-1081: Progress Report of 3-D Neutron Benchmark Problems  
(T. Takeda et al.)
- A-1115: Analysis of JOYO Burnup Characteristics (A. Hara et al.)

In the 33rd NEACRP Meeting, was expressed such comments on the long-term programme of NEA by the Japanese delegate, the chairman of the Research Committee on Reactor Physics as given in the followings.

Nuclear energy developments have encountered a somewhat difficult situation (anti-nuclear power movements). What should be done hereafter is to provide much safer reactors and to establish nuclear waste management, with aiming at a social understanding that nuclear energy is clean. The reactor physics activity is expected to play an important and essential role to find solutions for the considerable problem. This is because one can think out the new type reactors through new knowledge of reactor physics. Therefore, I think we must devote much effort to keep and extend reactor physics activities. I think also that the NEACRP should take stronger actions to promote nuclear development area in cleaner and more integrated forms. In this context, closer coordination with other NEA committees is recommended.

The NEACRP has provided the forum of discussions on the future direction of reactor physics research and coordination on the fundamental problems through benchmarks and specialist meetings. The NEACRP is the only international committee that is also to address the problems. In Japan, the domestic Committee on Reactor Physics is well defined as the organization to coordinate the NEACRP. The NEACRP has given a good impact on the domestic Reactor Physics Committee, and contributed to encourage the scientists in this area.

The future targets of reactor physics are able to be seen, as follows:

1. Advanced reactor (very safe, economic and uranium resource saving)

2. Passive safety reactor
3. Industrial usage of accelerator (incineration of TRU elements)
4. Intense neutron source
5. Fusion reactor neutronics
6. Wider application of nuclear reactor
7. Advanced radiation protection
8. Physics problem related to improving reactor performance

In order to perform such tasks effectively, the NEACRP should still be positioned as one of the committees to cover the well-defined area.

The second one (the 58th meeting) of the Research Committee was held in November 1990 to review the 33rd NEACRP Meeting, where many technical papers were presented on the following 10 topics including 5 new topics;

- (1) Current Issues of Plutonium Recycling in LWRs
- (2) Review of Requirements for the Methods of Validating Neutronics Codes
- (3) Physics Related Safety Aspects of Fast Reactors
- (4) New Facilities of Importance for Neutronics and Reactor Physics Research
- (5) Fusion Blanket - Shield Neutronics with Emphasis on the Effects of Data Uncertainties
- (6) Evaluation of the Uncertainty in FBR Burn-up Reactivity Swing
- (7) The Reactor Physics of Advanced Gas-Cooled and Water Reactors
- (8) Engineering and Physics Aspects of Transuranium Burning by Reactors and Accelerators
- (9) Local Stability in LWRs and HWRs with Emphasis on 3D Effects
- (10) Physics Methods in Fuel Accountability

During the present fiscal year, there were held two meetings of the Research Committee on Reactor Physics as mentioned above, three meetings of the Subcommittee on Fusion Reactor, and two meetings each of the Subcommittees on Reactor System and on Shielding.

The Subcommittee on Reactor System held the 30th meeting in July 1990 to discuss the papers to be submitted to the 33rd NEACRP meeting. In the 31st meeting held in December 1990, was made a review on the papers presented at the 33rd NEACRP meeting. Also presented were the investigated results of the BWR stability in Japan.

The Subcommittee on Fusion Reactor held the 32nd meeting in July 1990. The followings were reported and discussed; a nuclear data library

for MCNP, the JAERI-USDOE collaborative experiment -Phase-IIIA-, integral experiment on graphite-reflected lithium sphere, the results for ANL samples under the NEACRP activity on international comparison of tritium production-rate measurements and benchmark test of Be nuclear data in JENDL-3. The 33rd meeting held in December 1990 dealt with the technical papers on the 33rd NEACRP meeting, the 9th ANS Topical Meeting on Technology of Fusion Energy, the Japan/US Workshop on Fusion Neutronics, the Japan/US Workshop on Tokamak-type Fusion Power Reactor, and the IAEA Advisory Group Meeting on Nuclear Data for Neutron Multiplication in Fusion Reactor First-Wall and Blanket Material. The 34th meeting was held in March 1991. The subjects were the reporting on the shielding design in ITER/CDA, the outline of coordinate research program on development fusion power under OECD-IEA, and IEA Workshop on Low Activation Material. A general discussion was also performed on the next fiscal year activities. The 2nd Specialists' Meeting on Nuclear Data for Fusion Reactor was held in December 1990, in order to discuss and assess the status of nuclear data in JENDL-3.

The Subcommittee on Shielding held the 30th meeting in October 1990, where a lecture was given by Dr. Robert W. Roussin, Head of the Radiation Shielding Information Center (RSIC) of ORNL, on "Present status and future prospect of codes/data development for high energy radiation transport". The summary of the lecture was published in JAERI-M 91-015. In the 31st meeting held in March 1991, two shielding benchmarks of the NEACRP were reported and discussed. One was the shielding experimental benchmark data base, and the other was the intercomparison of shielding codes for transport casks.



Publication List

(Less formal written materials not listed here can be referred in References of each chapter.)

## 1. Nuclear Data and Group Constants

- 1) Takano H., Kaneko K. and Nakagawa T.: "Benchmark Test of JENDL-3 for Thermal and Fast Reactors", Proc. Int. Conf. Physics of Reactors: Operation, Design and Computation, Marseille, France, April 23-27, 1990, Vol.3, I.21 (1990).

## 2. Theoretical Method and Code Development

- 1) Kugo T., Tsuchihashi K. and Kaneko K.: "Evaluation Methods of Resonance Absorption for System with Pellet Surrounded by Fuel Solution", J. Nucl. Sci. Technol., Vol.27, 870 (1990).
- 2) Asahi Y., Matsumoto K. and Hirano M.: "THYDE-W: RCS (Reactor Coolant System) Analysis Code", JAERI-M 90-172 (1990).
- 3) Tsuchihashi K., Nakagawa M., Mori T., Kugo T. and Fujita S.: "Development of Intellectual Reactor Design System: IRDS", JAERI-M 90-177 (1990) (in Japanese).
- 4) Nakagawa M., Mori T. and Sasaki M.: "Comparison of Vectorization Methods Used in a Monte Carlo Code", Nucl. Sci. Eng., 107, 58 (1991).

## 3. Reactor Physics Experiment and Analysis

- 1) Akino F., Yamane T., Yasuda H. and Kaneko Y.: "Critical Experiments at Very High Temperature Reactor Critical Assembly (VHTRC)", Proc. Int. Conf. Physics of Reactors: Operation, Design and Computation, Marseille, France, April 23-27, 1990, Vol.1, IV-13 (1990).
- 2) Iijima S., et al.: "Experimental Study of Physics Characteristics Related to Neutron Flux Distribution in an Axially Heterogeneous LMFBR", *ibid.*, V32-V40 (1990).
- 3) Osugi T., Okajima S., Sakurai T. and Oigawa H.: "Experimental Study on Criticality and Reactivity Worth in High Conversion Light Water Reactor Using FCA-HCLWR Core", *ibid.*, Vol.3, PI-93 (1990).
- 4) Okajima S., Osugi T., Sakurai T. and Tahara Y.: "Experimental Study

on Reactivity Worth for Absorber Material in High Conversion Light Water Reactor Using FCA-HCLWR Core Fueled with Enriched Uranium", J. Nucl. Sci. Technol., 27, 950 (1990).

- 5) Nakahara Y., Suzuki T., Takano H., et al.: "Amount of Nuclides Constituting PWR Spent Fuels: Comparison of Observed with Calculated Values", Radiochemica Acta, 50, 141 (1990).
- 6) Sakurai T., Okajima S. and Osugi T.: "Measurement of Infinite Multiplication Factor by Using Central Cell Reactivity Worth on FCA-XV-1 Core Simulating High Conversion Light Water Reactor", JAERI-M 91-014 (1991) (in Japanese).
- 7) Osugi T. and Nagatani M.: "Analysis on FCA-HCLWR Core Using JENDL-3", Proc. of The 1990 Symposium on Nuclear Data, JAERI-M 91-032, 159 (1991).
- 8) Akie H., Takano H. and Kaneko K.: "Burnup Calculation for the PWR Spent Fuels by JENDL-3", *ibid.*, 168 (1991).

#### 4. Advanced Reactor System Design Studies

- 1) Takano H., Akie H. and Kaneko K.: "Higher Actinides Confinement/Transmutation Fuel Cycles in Fission Reactors", Proc. Int. Conf. Physics of Reactors: Operation, Design and Computation, Marseille, France, April 23-27, Vol.3, III 145 (1990).
- 2) Okumura K., Akie H. and Ishiguro Y.: "The Concept for Axially Heterogeneous High Conversion Light Water Reactor and Its Application", *ibid.*, Vol.4, III 101 (1990).
- 3) Okumura K., Akie H., Mori T., Nakagawa M. and Ishiguro Y.: "Conceptual Design Study of High Conversion Light Water Reactor", JAERI-M 90-096 (1990).
- 4) Asahi Y., Sugawara I. and Kobayashi T.: "Conceptual Design of Integrated Reactor with Inherent Safety", Nucl. Technol., 91, 28 (1990).
- 5) Hiraoka T., Sako K., Takano H., et al.: "A High-Breeding Fast Reactor with Fission Product Gas Purge/Tube-in-Shell Metallic Fuel Assemblies", *ibid.*, 93, No.3 (1991).
- 6) Naito Y., Furuta T., Ichikawa H. and Takano H.: "Design Study on a Very Long Life Light Water Power Reactor Core", JAERI-M 91-028 (1991).
- 7) Akie H., Okumura K., Takano H. and Ishiguro Y.: "Studies of Neutronics Calculation of High Conversion Light Water Reactor", JAERI-M 90-109 (1990) (in Japanese).

## 5. Fusion Neutronics

- 1) Oyama N., Hatozaki O., Oyama Y., Nakamura T., et al.: "Electro-Chemical Calorimetry of D<sub>2</sub>O Electrolysis Using a Palladium Cathode -An Undivided Open Cell System-", Bull. Chem. Soc. Jpn., 63, 2659 (1990).
- 2) Oyama Y.: "Very Low Level Flux Neutron Measurement with an NE213 Liquid Scintillator", HOSHASEN, 16, 15 (1990) (in Japanese).
- 3) Noda K., Oyama Y., Yamaguchi S., Maekawa H. and Hishinuma A.: "Concept and Neutron-Field Characteristics of ESNIT", J. Nucl. Mat., 174, 319 (1990).
- 4) Ikeda Y., Smith D.L., Kumar A. and Konno C.: "Measurements of Long-Lived Activation Cross Sections by 14 MeV Neutrons at FNS", Proc. 1990 Symp. on Nuclear Data, JAERI-M 91-032, 272 (1991).
- 5) Ikeda Y., Konno C., Mizumoto M., Hasegawa K., Chiba S., Yamanouchi Y. and Sugimoto M.: "Activation Cross Section Measurement at Neutron Energy of 11.0, 12.0 and 13.2 MeV Using  $^1\text{H}(^{11}\text{B},n)^{11}\text{C}$  Neutron Source at JAERI", *ibid.*, 281 (1991).
- 6) Oyama Y., Kosako K. and Maekawa H.: "Self-shield Effect on Angular Neutron Flux Spectra Leaking from Thick Iron Slab", *ibid.*, 314 (1991).
- 7) Kosako K.: "MCNP Cross Section Library Based on JENDL-3", Proc. 2nd Specialists' Meeting on Nuclear Data for Fusion Reactors, JAERI-M 91-062, 26 (1991).
- 8) Nakagawa M.: "Integral Test of JENDL-3 through Analysis of Fusion Blanket Experiment Phase IIB", *ibid.*, 61 (1991).
- 9) Oyama Y.: "Experiments of Nuclear Heating by Gamma-Rays at FNS", *ibid.*, 106 (1991).
- 10) Ikeda Y.: "Activation Cross Sections for Fusion Structural Materials", *ibid.*, 140 (1991).
- 11) Nakagawa M.: "Benchmark Test through Analysis of Leakage Neutron Spectrum from Spherical Pile", *ibid.*, 218 (1991).
- 12) Oyama Y. and Maekawa H.: "Nuclear Data Test of JENDL-3 Using TOF Experiments at FNS", *ibid.*, 228 (1991).
- 13) Nakajima Y. and Maekawa H., Editors: "Proceedings of Specialists' Meeting on Nuclear Data for Fusion Reactor", *ibid.* (1991).
- 14) Oyama Y., Yamaguchi S. and Maekawa H.: "Experimental Results of Angular Neutron Flux Spectra Leaking from Slabs for Fusion Reactor

Candidate Materials (1)", JAERI-M 90-092 (1990).

- 15) Kosako K.: "INTERF: The Reaction Rate and Spectra Editing Code for Analysis of Fusion Neutronics Experiments", JAERI-M 90-199 (1990).
- 16) Oishi K., Ikeda Y., Konno C. and Nakamura T.: "Measurement and Analysis of Induced Activities in Concrete Components Irradiated by 14 MeV Neutrons", Fusion Technol., 18, 291 (1990).

## 6. Radiation Shielding

- 1) Takeuchi K. and Tanaka S.: "PALLAS-1D(V3): Variable Dimension of PALLAS-1D(VII)", JAERI-M 90-041 (1990).
- 2) Sasamoto N.: "Bulk Shielding Calculation of High Electron Accelerators with Line Source Assumptions", JAERI-M 90-095 (1990).
- 3) Sakamoto Y. and Tanaka S.: "QAD-CGGP2 and G33-GP2: Revised Versions of QAD-CGGP and G33-GP", JAERI-M 90-110 (1990).
- 4) Kotegawa H. and Tanaka S.: "Attenuation Data of Point Isotropic Neutron Sources in the Shielding Materials of Water, Concrete and Iron", JAERI-M 90-174 (1990) (in Japanese).
- 5) Sasamoto N. and Kurosaka N.: "QAD-SOR: An Interactive Shielding Calculation Code for High Energy Electron Accelerators", JAERI-M 90-229 (1990) (in Japanese).
- 6) Hasegawa A.: "Group Cross-section Processing Method and Common Nuclear Group Cross-section Library Based on JENDL-3 Nuclear Data File", Proc. 1990 Symp. on Nuclear Data, JAERI-M 91-032, 133 (1991).
- 7) Hasegawa A.: "JSSTD-295n-104γ; A Common Nuclear Group Cross-section Library Based on JENDL-3 Nuclear Data File", Proc. 2nd Specialists' Meeting on Nuclear Data for Fusion Reactors, JAERI-M 91-062, 15 (1991).
- 8) Hirayama H. and Tanaka S.: "Investigation of 1 cm Dose Equivalent for Photon behind Shielding Materials", ORNL/TR-90/28 (1990).
- 9) Tanaka S. and Suzuki T.: "A Calculational Method of Photon Dose Equivalent Based on the Revised Technical Standards of Radiological Protection Law", ORNL/TR-90/29 (1990).
- 10) Hirayama H., et al.: "Annotated References of Shielding Experiment and Calculation of High Energy Particles", KEK Report 90-18 (1990).
- 11) Tanaka S., et al.: "Practical Manual of Shielding Calculation of Radiation Facility (II)", Nucl. Safety Technol. Center Publication (1990) (in Japanese).

- 12) Cai S., Hasegawa A., Nakagawa T. and Kikuchi Y.: "Benchmark Test of Gamma-Ray Production Data in JENDL-3 for Some Important Nuclides", J. Nucl. Sci. Technol., 27(9), 844 (1990).
- 13) Harima R., Tanaka S., Sakamoto Y. and Hirayama H.: "Development of New Gamma-Ray Buildup Factor and Application to Shielding Calculations", *ibid.*, 28(1), 74 (1991).

## 7. Reactor and Nuclear Instrumentation

- 1) Sakasai K. and Ara K.: "Sensing of Induced Magnetic Field from a Cross Section of Ion-Beam Line by Utilizing Diamagnetic Parallel Plates and Magnetic Field Sensors", Proc. Tech. Meet. Magnetics, Paper Mag-90-177, November 30, 1990 (in Japanese).
- 2) Ara K. and Sakasai K.: "A Proposal for Measurement of Magnetic Field Produced by Human Body", *ibid.*, Paper Mag-91-100, March 12, 1991 (in Japanese).
- 3) Kanno I.: "A Model of Charge Collection Process in a Silicon Surface Barrier Detector", KEK Report 90-11, 113 (1990) (in Japanese).
- 4) Kanno I.: "Candidate for Residual Defect in Silicon Surface Barrier Detector", J. Nucl. Sci. Technol., 28, 87 (1991).

## 8. Reactor Control, Diagnosis and Robotics

- 1) Konno H., Hayashi K. and Shinohara Y.: "On the Origin of Power Oscillation in NSRR", Annals of Nuclear Energy, 17-6, 317 (1990).
- 2) Hayashi K. and Shinohara Y.: "Results of 1989 Reactor Analysis Noise Benchmark Test", Proc. OECD/NEA Reactor Noise Analysis Benchmark Test Meeting, Delft, The Netherlands, 1 (1990).
- 3) Sasaki S.: "A Method of Using the Inverse Matrix for Manipulator Kinematics", JAERI-M 90-064 (1990).
- 4) *idem*: "A Modelling of Robot Manipulator Dynamics Based on Newton-Euler's Equation", JAERI-M 90-147 (1990).
- 5) *idem*: "On the Non-trivial Kinematic Representations for Six-Link Manipulators", JAERI-M 90-227 (1990).
- 6) *idem*: "A Method of Solving the Inverse Kinematics Based on Separation of Articulated Variables", Trans. of the Society of Instrument and Control Eng., 26-6, 685 (1990).

## 9. Heat Transfer and Fluid Dynamics

- 1) Okubo T., et al.: "Evaluation Report on SCTF Core-III Test S3-20", JAERI-M 90-080 (1990).
- 2) Okubo T., et al.: "Analysis of SCTF/CCTF Counterpart Test Results", JAERI-M 90-083 (1990).
- 3) Hiraga F., et al.: "Small Break LOCA Analysis of Double-Flat-Core HCLWR", JAERI-M 90-085 (in Japanese).
- 4) Akimoto H., et al.: "Reflood Behavior at Low Initial Clad Temperature in Slab Core Test Facility Core-II", JAERI-M 90-106 (1990).
- 5) Adachi H., et al.: "Development of SCTF Cold Leg Injection Test Method for Eliminating U-Tube Oscillation during the Initial Period", JAERI-M 90-107 (1990).
- 6) Ohnuki A., Akimoto H. and Murao Y.: "Effect of Liquid Flow Rate on Film Boiling Heat Transfer during Reflood in Rod Bundle", J. Nucl. Sci. Technol., 27(6) (1990).
- 7) Iwamura T., Okubo T., Murao Y., et al.: "Evaluation of DNBR under Operational and Accident Conditions for Double-Flat-Core Type HCLWR", *ibid.*, 28(1) (1991).
- 8) Abe Y., Akimoto H. and Murao Y.: "Estimation of Shear Stress in Counter-current Annular Flow", *ibid.*, 28(3) (1991).
- 9) Adachi H., et al.: "Cold Leg Injection Reflood Test Results in the SCTF Core-I under Constant System Pressure", JAERI-M 90-129 (1990).
- 10) Adachi H., et al.: "Comparison of Facility Characteristics between SCTF Core-I and Core-II", JAERI-M 90-130 (1990).
- 11) Ohnuki A., et al.: "Evaluation Report on SCTF Core-II Test S2-08", JAERI-M 90-236 (1990).
- 12) Ohnuki A., et al.: "Study on ECC Injection Modes in Reflood Tests with SCTF Core-II", JAERI-M 91-001 (1991).
- 13) Ohnuki A., et al.: "Evaluation Report on SCTF Core-II Test S2-19", JAERI-M 91-033 (1991).
- 14) Akimoto H., Abe Y., Ohnuki A. and Murao Y.: "Implementation of an Implicit Method into Heat Conduction Calculation of TRAC-PF1/MOD2 Code", JAERI-M 90-122 (1990).
- 15) Abe Y., Akimoto H. and Murao Y.: "Analysis of Interfacial and Wall Friction Factors of Counter-current Flow in Vertical Pipe", Trans. Am. Nucl. Soc. 62, 719 (1990).
- 16) Iwamura T., Okubo T., Suemura T. and Murao Y.: "Thermal Hydraulic

Feasibility Study of a Double-Flat-Core Type HCLWR", ASME Winter Annual Meeting, HTD-Vol.150, 31 (1990).

- 17) Okubo T., Iwamura T., Suemura T., Hiraga F. and Murao Y.: "Accident Analysis for a Double-Flat-Core Type HCLWR", Proc. Sixth Nucl. Thermal Hydraulics, 79 (1990).

#### 10. Nuclear Energy Systems Analysis and Assessment

- 1) Takeda T., Tadokoro Y. and Yasukawa S.: "A Study on Steam Reforming Process Using Nuclear Heat of VHTR", JAERI-M 90-082 (1990).
- 2) Yasukawa S., Sato O., Tadokoro Y. and Kajiyama T.: "CO<sub>2</sub> Emission Reduction by High Temperature Nuclear Heat Application", Energy Conversion and Utilization with High Efficiency - Subarea A: Socio-Economic Aspects of Energy, Report on Researches Pursued under the Grant-in-Aid on Priority-Area Research Supported by the Ministry of Education, Science and Culture, Japan, 39-42 (1990).
- 3) Tadokoro Y., Kajiyama T., et al.: "Cycle Simulation of the 'UT-3' Thermochemical Hydrogen Production Process", Proc. 8th World Hydrogen Energy Conference, Honolulu and Waikoloa, Hawaii, USA, July 22-27, Vol.2, 513 (1990).
- 4) Yasukawa S., Tadokoro Y. and Kajiyama T.: "Reduction of CO<sub>2</sub> Emission by Nuclear Energy", Investigation on Responses to CO<sub>2</sub> Problem in Energy Related Industries, Japan Industrial Technology Association, 1 (1990) (in Japanese).
- 5) Tadokoro Y.: "High Temperature Gas-Cooled Reactor", Nuclear Almanac, the Japan Atomic Industrial Forum (1990) (in Japanese).

#### 11. Development of Proton Linear Accelerator and Transmutation Target System

- 1) Mizumoto M., Takada H., Nishida T., Kanno I., Yasuda H., Nakahara Y., Takizuka T., Akabori H., Okumura Y., Sugimoto M., Shirakata H., Jameson R.A. and Kaneko Y.: "Transmutation of Transuranium Waste with High Energy Proton Induced Spallation Reaction", Proc. European Particle Accelerator Conference EPAC90, Nice, France, June 12-16 (1991).
- 2) Kaneko Y.: "The Intense Proton Accelerator Program at JAERI", Proc. ICANS-XI, Tsukuba, Oct. 22-26, 1990, 210 (1991).

- 3) Nishida T., Takada H., Nakahara Y., Tsutsui T. and Kaneko Y.: "Calculation Code System for Fission and Spallation Products", *ibid.*, 300 (1990).
- 4) Mizumoto M. and Shikazono N.: "Development Plan of Basic Technology for a High Intensity Proton Linear Accelerator", *Bulletin of Institute for Chemical Research, Kyoto Univ.*, 68, 133 (1990).
- 5) Nishida T. and Nakahara Y.: "Mass Formula Dependence of Calculated Spallation Reaction Product Distributions", *Kerntechnik* 55, No.3, 147 (1990).
- 6) Takada H., Kanno I., Takizuka T., Akabori M., Nishida T. and Kaneko Y.: "Core Design Study for Hybrid Type Transuranium Nuclides Incineration Plant Part I. Concept", *JAERI-M 90-131* (1990).
- 7) Nishida T.: "Simulation Codes for Designing the TRU Transmutation System with Proton Accelerator", *Proc. Seminar on Software, Tokai, Japan*, 3 (in Japanese) (1990).
- 8) Nishida T., Mizumoto M., Takada H., Nakahara Y., Mukaiyama T. and Kikuchi Y.: "Nuclear Data on OMEGA Project", *Nuclear Data News*, No.37 (1990).



Author Index

ABDOU*,	Mohamed A.	5.5, 5.6
ABE,	Yuichi	5.9, 12.3
ABE,	Yutaka	9.1, 9.2, 9.3, 9.4, 9.5, 9.6, 9.7, 9.8, 9.9
ADACHI*,	Hiromichi	9.3, 9.4, 9.5
AKABORI <sup>+</sup> ,	Mitsuo	11.6
AKIE,	Hiroshi	1.3, 1.4, 4.2, 4.3
AKIMOTO,	Hajime	9.1, 9.2, 9.3, 9.4, 9.6, 9.7, 9.8, 9.9, 9.12, 9.13
AKIMOTO <sup>+</sup> ,	Masayuki	4.6
AKINO,	Fujiyoshi	3.8
ASAHI,	Yoshiro	2.7
ARA,	Katsuyuki	7., 7.2, 7.4, 7.8
ARAYA,	Fumimasa	4.6, 9.10, 9.11, 9.12, 9.13
BAN*,	Syuichi	6.1
BANDO*,	Masaru	3.1, 3.2, 3.5, 3.6
BENNETT*,	Edgar F.	5.1
DOI*,	Eiji	4.2
FUJII*,	Sadao	2.6
FUJII,	Yoshio	8.7
FUJISAKI,	Shingo	12.2
FUJITA*,	Shingi	2.5
FUKAKUSA*,	Shinji	7.1
FUKUSHIMA <sup>+</sup> ,	Masao	7.3
GIL*,	Choong-sup	4.4
GOTOH,	Hiroshi	7.6, 7.7
HARUYAMA,	Mitsuo	7.6, 7.7
HASEGAWA,	Kazuo	11.1, 11.2, 11.3, 11.4, 11.8
HASHIDATE*,	Koji	4.6
HAYASAKA,	Katsuhisa	3.3, 12.1
HAYASHI,	Koji	8.1, 8.2, 8.3, 8.4, 8.5
HIRAOKA,	Toru	4.1, 12.

HIRAYAMA*,	Hideo	6.1
IEKI*,	Hiroshi	7.1
IGUCHI,	Tadashi	9.1, 9.2, 9.3, 9.4
IIJIMA,	Susumu	3.1, 3.2, 3.3, 3.6
IKEDA,	Yujiro	1.1, 1.2, 5.1, 5.2, 5.5, 5.6
ISHIGURO,	Yukio	2.4, 4., 4.2, 4.4, 13.
ISHITUKA*,	Tatsuo	11.5
ITOH,	Hirokuni	7.3
ITOH,	Hiroshi	7.1
IWAMURA,	Takamichi	9.1, 9.2, 9.3, 9.4, 9.5, 9.10, 9.11, 9.12, 9.13
KADOTANI*,	Hiroyuki	11.5
KAJIYAMA,	Takeyoshi	10.2, 10.5, 10.6
KAKUTA,	Tsunemi	7.4
KANEKO*,	Kunio	1.3, 1.4, 4.1, 4.6
KANEKO,	Yoshihiko	Foreword, 3.8, 11.1, 11.3, 11.4, 11.6, 11.7, 11.8, 13.
KANNO,	Ikuo	7.5, 11.5, 11.6, 11.7, 11.8
KATAGIRI,	Masaki	7.3
KATO*,	Yoshio	11.7
KATSURAGI*,	Satoru	4.1
KATSUTA+,	Hiroshi	11.7
KAWAMURA,	Toshihide	7.7
KISHIMOTO,	Maki	7.3
KITAJIMA+,	Toshio	7.3
KONNO,	Chikara	1.1, 1.2, 5.1, 5.2, 5.5, 5.6
KONNO*,	Hidetoshi	8.3
KONTA,	Masahide	10.2
KOSAKO,	Kazuaki	5.1, 5.3, 5.4
KOTEGAWA,	Hiroshi	6.3
KUGO,	Teruhiko	2.1, 2.5
KUMAR*,	Anil	1.2, 5.5, 5.6
KUSANO,	Joichi	5.9, 12.3
KUTSUKAKE,	Chuzo	5.9, 12.3
MAEKAWA,	Hiroshi	5., 5.1, 5.3, 5.5, 5.7, 13.
MAEKAWA,	Fujio	5.5, 5.7, 5.8

MINO,	Hiroshi	11.1, 11.3, 11.4
MIZUMOTO,	Motoharu	11., 11.1, 11.3, 11.4, 11.8
MORI,	Takamasa	2.2, 2.3, 2.5, 2.6, 5.10
MORIMOTO*,	Yuichi	2.4, 4.2
MUKAIYAMA,	Takehiko	3.4
MURAO,	Yoshio	9., 9.1, 9.2, 9.3, 9.4, 9.5, 9.6, 9.7, 9.8, 9.9, 9.10, 9.11, 9.12, 9.13
NABESHIMA,	Kunihiko	8.1, 8.2, 8.5
NAGATANI*,	Mutsumi	3.7
NAKAGAWA,	Masayuki	2.2, 2.3, 2.5, 2.6, 5.10
NAKAHARA,	Yasuaki	11.5, 11.6, 11.7
NAKAMURA*,	Tomoo	5.1, 5.2, 5.6
NAKANO,	Masafumi	3., 3.4, 3.5
NAKASHIMA,	Hiroshi	6.1
NAMITO*,	Yoshihito	6.1
NARIYAMA*,	Nobuteru	6.1
NEMOTO,	Tatuo	3.1, 3.3
NISHIDA,	Takahiko	11.5, 11.6, 11.7
ODA*,	Junro	4.5
OHNO,	Akio	3.1, 3.5, 12.1
OHNUKI,	Akira	9.1, 9.2, 9.3, 9.4, 9.5, 9.6, 9.7, 9.8, 9.9
OIGAWA,	Hiroyuki	3.1, 3.2, 3.4, 3.6
OISHI*,	Koji	5.2
OKAZAKI,	Motoaki	9.2, 9.3
OKUBO,	Tsutomu	9.1, 9.2, 9.3, 9.4, 9.5, 9.10, 9.11, 9.12, 9.13
OKUMURA,	Keisuke	2.4, 4.4
OKUMURA+,	Yoshikazu	11.1, 11.2
ONO,	Toshihiko	3.8, 11.8, 12.2
OOKAWA+,	Hiroshi	7.3
OSUGI,	Toshitaka	3.5, 3.7
OYAMA,	Yukio	5.1, 5.3, 5.4, 5.5, 5.6, 5.8
SAITO*,	Jun	4.3
SAKAKI*,	Isao	9.4
SAKASAI,	Kaoru	7.1, 7.8
SAKURAI,	Takeshi	3.1, 3.3

SAKO,	Kiyoshi	4.5, 4.6
SANADA*,	Kazuo	7.4
SARUTA <sup>+</sup> ,	Tohru	7.3
SASAKI*,	Makoto	2.2
SASAKI,	Shinobu	8.8
SASAMOTO,	Nobuo	6.2
SATO,	Osamu	10.1, 10.2, 10.3, 10.4
SATOH,	Kunio	3.4, 12.1
SEKI,	Masakazu	11.8, 12.2
SHAMOTO*,	Naoki	7.4
SHIMAZAKI,	Junya	8.1, 8.2, 8.6
SHIMOYAMADA,	Yoshinori	10.1, 10.2, 10.3
SHINOHARA,	Yoshikuni	8., 8.1, 8.2, 8.3, 8.5, 8.6, 8.7
SHIRAKI,	Hajimu	10.1, 10.2
SOBAJIMA <sup>+</sup> ,	Makoto	9.5
SODEYAMA,	Hiroshi	3.5, 12.1
SUZUDO,	Tomoaki	8.4
SUZUKI,	Katsuo	8.2, 8.6
SUZUKI*,	Makoto	7.6
SUZUKI,	Tomoo	6., 13.
TADOKORO,	Yoshihiro	10.2, 10.5, 10.6
TAKADA,	Hiroshi	11.5, 11.6, 11.7, 11.8
TAKANO,	Hideki	1., 1.3, 1.4, 4.1, 4.3
TAKANO <sup>+</sup> ,	Makoto	11.7
TAKASE,	Misao	7.7
TAKEUCHI,	Motoyoshi	3.8, 11.8, 12.2
TAKIZUKA <sup>+</sup> ,	Takakazu	11.6, 11.7
TAMURA*,	Masakazu	7.1
TANAKA*,	Hideki	11.1, 11.2
TANAKA,	Shigeru	5.9, 12.3
TANAKA,	Shun-ichi	6.1, 6.3
TERANISHI*,	Kazuo	7.6
TOBITA <sup>+</sup> ,	Tsutomu	7.3
TOUGASAKI*,	Masashi	4.5
TSUCHIHASHI,	Keichiro	2., 2.5
UNO*,	Masayuki	2.6

USUI,	Hozumi	8.7
WAKAYAMA <sup>+</sup> ,	Naoaki	7.1
WATANABE,	Hideaki	12.1, 12.2, 12.3
WATANABE,	Hironori	9.10, 9.11
WATANABE,	Koichi	8.5
YAMADA,	Masaharu	7.2
YAMAGISHI,	Hideshi	7.1
YAMANE,	Tsuyoshi	11.8
YAMASHITA <sup>*</sup> ,	Shin-ichi	7.1
YAMAZAKI <sup>*</sup> ,	Shigeki	10.4
YASUDA,	Hideshi	11.8
YASUKAWA,	Shigeru	10., 10.1, 10.2, 10.3, 10.4, 10.5
YOKOBORI,	Hitoshi	11.1, 11.2, 11.3, 11.4
YOSHIDA,	Hiroshi	7.3
YOSHIZAWA <sup>+</sup> ,	Michio	6.1
YOUSSEF <sup>*</sup> ,	Mahmoud Z.	5.6

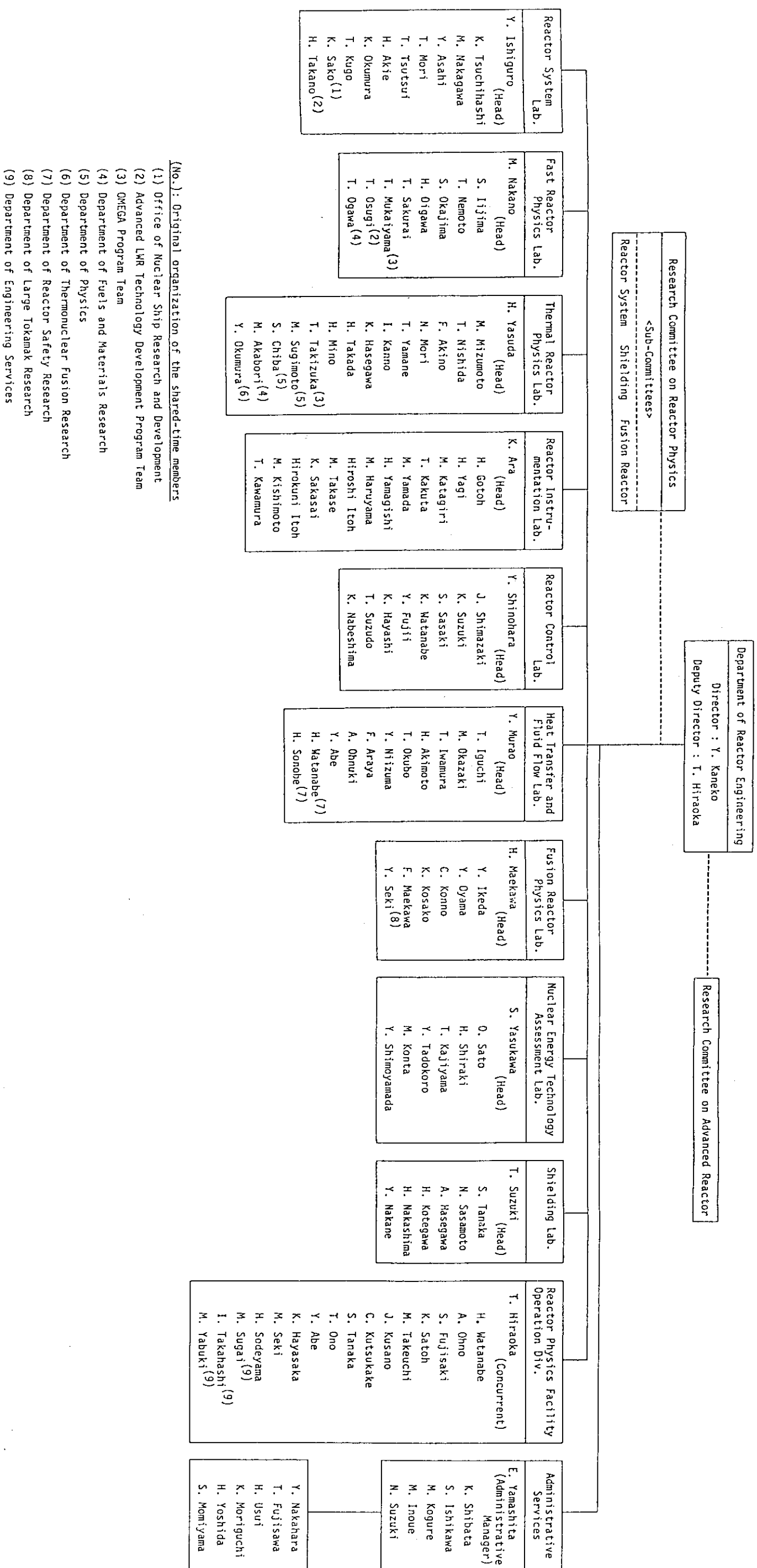
---

+ Contributors attached to JAERI but not to Department of Reactor Engineering

\* Contributors attached not to JAERI

## Appendix I Department of Reactor Engineering Organization Chart

March 1991



## Appendix II Abbreviations

CCTF : Cylindrical Core Test Facility

ECCS : Emergency Core Cooling System

FCA : Fast Critical Assembly

The FCA is a split-table type facility of horizontal matrix structure designed for studying nuclear characteristics of fast reactor. The construction of the FCA was started in 1965 and the first core went critical on 29th April, 1967.

The main features of the facility are summarized as follows:

Type : Split-table type of horizontal matrix structure

Size : 2.8 m × 2.8 m × 1.3 m (each half assembly)

Fuel : Enriched uranium and plutonium  
(Plate type)

Other material: Sodium, stainless steel, aluminum  
oxide ( $\text{Al}_2\text{O}_3$ ), polystyrene etc.  
(Plate type)

Maximum power : 2 kW

Assembly name constructed: FCA I ~ FCA XVI

Critical experiments using enriched uranium cores were made in 1960s for investigating basic characteristics of fast reactor cores. Mock-up experiments were extensively made in 1970s for the Fast Experimental Reactor JOYO and the Prototype Fast Breeder Reactor MONJU. In 1980s, the main subjects of experiments were the investigation of the core characteristics of an axially heterogeneous large fast breeder reactor and the core physics study on a high conversion light water reactor. From 1989, the reactor physics experiments of metallic-fueled LMFBR have been carried out using the FCA-XVI cores.

FER : Fusion Experimental Reactor

A next fusion device designed and planned at JAERI.

FNS : Fusion Neutronics Source

The FNS is an accelerator based D-T neutron source installed for the purpose of investigating the neutronics on the D-T fusion reactor blanket and shielding. It provides following three functions to meet experimental requirements:

- 1) High intensity DC point source
- 2) DC point source with wide variation of neutron yield rate
- 3) Pulsed neutron source

The D-T neutrons are generated via  ${}^3\text{T}(\text{d},\text{n}){}^4\text{He}$  reaction. There are two beam lines; one is so called  $0^\circ$  line for high current operation, and the other is so called  $80^\circ$  line for rather low current operation. The major specifications of the FNS accelerator are shown in the following Table.

« Table »

Items	$0^\circ$	$80^\circ$
• Beam current	>20 mA	3 mA
• Beam size	<15 mm $\phi$	<15 mm $\phi$
• Pulse width	--	< 2 ns
• Frequency	--	2 MHz
• Peak current	--	40 mA
• Target assembly	Rotating (Water cooled)	Stationary (Water cooled, Air cooled)
• Amount of ${}^3\text{T}$	<37T Bq	370G Bq
• Neutron Yield	$4 \times 10^{12}/\text{s}$	$5 \times 10^{11}/\text{s}$

The major experimental subjects are as follows:

- 1) Tritium production rate in the various blanket configurations
- 2) Nuclear heating rate in the structural materials
- 3) Shielding performance for D-T neutrons in the various structure configurations
- 4) Induced effects on the structural materials by D-T neutrons

HCLWR : High Conversion Light Water ReactorHTTR : High Temperature engineering Test Reactor

JAERI is to construct and operate the HTTR, to carry out the necessary R&D for establishing and upgrading the HTGR (High



Temperature Gas-cooled Reactor) technology basis, and to conduct various innovative basic researches on high-temperature technologies such as ceramics and fusion reactor materials. The HTTR consists of a core of 30 MWt, a main cooling circuit, an auxiliary cooling circuit and related components. The reactor pressure vessel is 13.2 m high and 5.5 m in diameter and contains the core graphite reflectors, metallic core support structure and radial restraining devices.

« Table » Specification of HTTR

Thermal power	30 MW
Outlet coolant temperature	850°C/950°C
Inlet coolant temperature	395°C
Fuel	Low enriched UO <sub>2</sub>
Fuel element type	Prismatic block
Direction of coolant flow	Downward-flow in core
Pressure vessel	Steel
Number of main cooling loop	1
Heat removal	IHX and PWC(parallel loaded)
Primary coolant pressure	4 MPa
Containment type	Steel containment
Plant lifetime	20 years

ITER : International Thermonuclear Experimental Reactor

A next fusion device. The ITER Project is conducted by four parties, i.e., Japan, U.S.A., U.S.S.R. and E.C. under the framework of IAEA.

JENDL-3 : The Japanese Evaluated Nuclear Data Library, version 3, released in 1989.

JENDL-3T : A temporary file of JENDL-3, released in 1987.

LOCA : Loss of Coolant Accident

NSRR : Nuclear Safety Research Reactor

SCTF : Slab Core Test Facility

TRU : Trans-Uranium element (Transuranic nuclide)

VHTRC : Very High Temperature Reactor Critical assembly

1. Purpose

Neutronics design verification of Very High Temperature Reactor

2. Main features of VHTRC

Type : Split table type of hexagonal graphite block structure

Size : Height; 2.4 m

Length; 2.4 m (Each half)

Fuel : Coated particle fuel compact (pin in block)

<size> 36, 18 mm outer, inner diameters,  
36 mm height

<coated particle> 920  $\mu\text{m}$  overall diameter  
(600  $\mu\text{m}$   $\text{UO}_2$  kernel coated with pyrolytic carbon and SiC)

<Enrichment> 2, 4 and 6wt%

Moderator and reflector : Graphite

Core temperature : Room temperature to 210°C by  
electric heaters

Maximum power : 10 W

Auxiliary equipments :

(1) Sample heating device (Up to 800°C)

(2) Pulsed neutron source

3. Main items of experiments

(1) Critical mass

(2) Reactivity worth of control and burnable poison rods

(3) Power distribution

(4) Temperature coefficient of reactivity of the whole  
core up to 200°C

(5) Doppler effect of a sample fuel rod up to 800°C

(6) Cell spectrum indices